UNIVERSITY OF ICELAND

Ph.D. Dissertation
in Physics

The impact of Self-Interacting Dark Matter and Warm Dark Matter in dwarf galaxies

Tamar Meshveliani

June 2024

FACULTY OF PHYSICAL SCIENCES

The impact of Self-Interacting Dark Matter and Warm Dark Matter in dwarf galaxies

Tamar Meshveliani

Dissertation submitted in partial fulfillment of a
Philosophiae Doctor degree in Physics

Ph.D. Committee
Jesús Zavala Franco (Chair)
Gunnlaugur Björnsson
David James Edward Marsh

Opponents
Azadeh Fattahi Savadjani
Camila Correa

Faculty of Physical Sciences
School of Engineering and Natural Sciences
University of Iceland
Reykjavik, June 2024

The impact of Self-Interacting Dark Matter and Warm Dark Matter in dwarf galaxies

Dissertation submitted in partial fulfillment of a *Ph.D.* degree in Physics

Faculty of Physical Sciences
School of Engineering and Natural Sciences
University of Iceland
Dunhagi 5
107, Reykjavik Reykjavik
Iceland

Telephone: 525-4000

Bibliographic information:
Tamar Meshveliani, 2024, *The impact of Self-Interacting Dark Matter and Warm Dark Matter in dwarf galaxies*, Ph.D.Dissertation, Faculty of Physical Sciences, University of Iceland, 117 pp.

Author ORCID: 0000-0002-2250-7633
ISBN: 978-9935-9768-4-0

Printing: Háskólaprent ehf.
Reykjavik, Iceland, June 2024

Abstract

The ΛCDM model is the most widely accepted model of cosmological structure formation and evolution. It includes a form of Cold Dark Matter (CDM), which is non-quantum, non-relativistic and collisionless. It settles into extended and dense self-gravitating haloes as a result of cosmic structure formation. CDM haloes act as a stabilizing agent for galaxies, while the late-time accelerating expansion of the Universe is sourced by a cosmological constant Λ. Due to the disagreement between ΛCDM-based simulations and observations on galactic and sub-galactic scales and the fact that traditional dark matter candidates remain undetected, the theoretical space for alternatives has been widening, making the particle nature of dark matter a fundamental question in Physics. This thesis revolves around this question in the context of two proposed modifications to the CDM cosmology: Self-interacting dark matter (SIDM) and Warm Dark Matter (WDM). In the former, strong self-interactions modify the inner dynamics of dark matter haloes, while in the latter, non-negligible thermal velocities in the early Universe suppress the abundance and inner densities of low-mass haloes. These modifications have been proposed to solve outstanding inconsistencies between CDM and observations of dwarf galaxies.

In the WDM project, we use a high-resolution hydrodynamical simulation that includes the EAGLE galaxy formation model to understand how the properties and statistics of the dwarf galaxy population are related to the ∼Mpc-scale environment in our Local Group. We are interested in a cosmologically underdense region that has been relatively unexplored to uncover divergent predictions of CDM and WDM. We find that the cumulative stellar mass function is almost identical for high stellar mass systems ($M_* > 10^7$ $\mathrm{M}_\odot$), while it is suppressed below this mass, where WDM predicts fewer dwarf galaxies than CDM.

In the SIDM project, we use a semi-analytic framework calibrated to simulations to study the final stage of the SIDM halo evolution - the "gravothermal collapse" phase. We show that in certain region of the parameter space of SIDM models, dwarf-size SIDM haloes have a bimodal distribution, with some having central density cores and others being centrally cuspy, the latter being those that have collapsed and contain an intermediate-mass black hole. This offers a promising solution to the so-called "diversity problem" in Milky-Way satellites. Finally, we extend the analysis of the core-collapse phase in SIDM haloes, including the impact on the baryonic component. In particular, we discuss how the use of adiabatic invariants can be exploited to predict the response of stellar orbits to the collapsing SIDM core.

Ágrip

Í heimsfræði er svonefnt ΛCDM-líkan hin viðtekna lýsing á myndun og þróun stærri efniseininga í alheimi. Það samanstendur að megninu til af köldu hulduefni (CDM), sem er óskammtað, hægfara og árekstralaust. Við myndun stærri kerfa, safnast hulduefnið undan eigin þyngdarverkun, í víðfema en þétta hjúpa. Hulduefnishjúparnir hafa styrkjandi áhrif á stöðugleika vetrarbrauta, en aukinn útþennsluhraði alheims á síðari stigum stafar af heimsfasta, Λ. Hermanir ΛCDM-líkana hafa oft ekki samræmst niðurstöðum mælinga á vetrarbrautum og grunneiningum þeirra, sér í lagi hafa hefðbundnar hulduagnir ekki fundist. Þar með hefur svigrúm aukist til að kanna aðra möguleika og á þann hátt hefur spurningin um gerð og eiginleika huldusefnis orðið ein af meginráðgátum eðlisfræðinnar. Þessi ritgerð tekur þessa spurningu til umfjöllunar og skoðar samhengið á milli tveggja tilgáta um breytta heimsmynd hulduefnis: Annars vegar eiginvíxlverkandi hulduefni (e. Self-Interacting Dark Matter - SIDM) og svo heitt hulduefni (Warm Dark Matter - WDM). Í fyrra tilvikinu breytir sterk eiginvíxlverkun hreyfifræði hulduefnishjúpanna, en hið síðara veldur því að varmafræðilegur hraði í ungum alheimi dregur úr fjölda og innri þéttleika hjúpa með lítinn massa. Þessi tilvik hafa verið innleidd til að leysa ósamkvæmni á milli hulduefnis og mælinga á dvergvetrarbrautum. Í WDM-hlutanum byggjum við á hermireikningum í hárri upplausn, sem innihalda EAGLE líkanið af myndun vetrarbrauta til að varpa ljósi á hvernig tölfræðilegir eiginleikar safns dvergvetrarbrauta tengjast nánasta ($\sim$Mpc) umhverfi í Grenndarhópnum. Við beinum sjónum að heimsfræðilegum svæðum með undirþéttleika sem lítt hafa verið könnuð með tilliti til forspáa CDM og WDM. Í ljós kemur að dreifingarfall massa stjarna í vetrarbrautum er í þessum tveimur tilfellum eins ef massinn er hár ($M_* > 10^7\ \mathrm{M}_\odot$), en fyrir lægri massa spáir WDM færri dvergvetrarbrautum en CDM.

Í SIDM-hlutanum nýtum við aflfræðilega framsetningu sem er kvörðuð við hermireikninga til að kanna lokaskeið í þróun SIDM hjúpa, skeið þyngdarvermins hruns. Við sýnum að á vissu svæði í stikarúmi SIDM-líkananna, hafa dvergvetrarbrautir tvítindadreifingu þar sem sumar hafa þéttann kjarna á meðan aðrar eru yddar. Þeir hjúpar sem hafa þegar fallið saman innihalda miðlungsstór svarthol. Þessar niðurstöður varða leið að lausn svonefnds margbreytileika í fylgiþokum vetrarbrautarinnar. Loks útvíkkum við greiningu á skeiði kjarna-hruns í SIDM-líkönum, með því að taka einnig tillit til áhrifa þungeinda í hjúpnum. Sér í lagi hugum við að því hvernig nýta má óvermióbreytur til að spá fyrir um svörun og breytingu á brautum stjarna þegar SIDM-kjarninn fellur saman.

To my son Niko, who has effortlessly taken up all the personal space Iceland could provide and made this unbearable stuffiness utterly lovable.

Table of Contents

List of Publications

Paper I: **Tamar Meshveliani**, Jesús Zavala, and Mark R. Lovell, 2023, Gravothermal collapse of self-interacting dark matter halos as the origin of intermediate mass black holes in Milky Way satellites. *Physical Review D*, Vol. 107, Issue 8, 083010. Accessed at `https://journals.aps.org/prd/abstract/10.1103/PhysRevD.107.083010`.

Paper II: **Tamar Meshveliani**, Mark R. Lovell, Robert A. Crain, Joel Pfeffer, 2024, The impact of free-streaming on dwarf galaxy counts in low-density regions. *Monthly Notices of the Royal Astronomical Society*, Accessed at `https://doi.org/10.1093/mnras/stae1519`.

Paper III: Jesús Zavala, **Tamar Meshveliani**, Naoki Yoshida Ayuki Kamada. Star clusters in Self-Interacting Dark Matter haloes: the adiabatic regime. *To be submitted to Physical Review D*.

I am the leading author of the first two projects. I was involved in the project's conception, design and performance of numerical simulations, data analysis, building (semi-)analytical models, and manuscript writing. In the third project, the numerical work and results were performed by me, and the theoretical derivations were done by the lead author. Paper I is presented in Chapter 3. Paper II is presented in Chapter 5, and partial results of Paper III are presented in Chapter 4.

Acknowledgements

I am absolutely thrilled to express my utmost gratitude and appreciation to the wonderful individuals who have played an instrumental role in shaping me into the physicist I am today.

First and foremost, I cannot thank my PhD advisor, Jesús Zavala Franco, enough for his unwavering support and guidance throughout my academic journey. Working alongside him has been an absolute privilege, and I can only hope that other students are as fortunate as I was to have such an amazing mentor.

A huge shoutout goes to Mark Lovell. I had the pleasure of working with him and sharing an office for two years. I cannot recall a single day when he did not ask if I had any questions before leaving. His constant support made my PhD years a breeze. I am incredibly grateful to him for always lending an ear whenever I needed to vent about the challenges of raising a baby. And believe me, that was quite often!

I would like to express my sincere gratitude to Mark Vogelsberger for believing in me and endorsing my abilities. He went above and beyond to help me kickstart my project, including sharing internet data to check the code during a dinner at the restaurant, asking about the project while on a plane, and staying up late on Zoom calls to provide the final word.

I would like to thank my loving husband, Mirian, who has been my rock throughout this journey. His support, hilarious encouragement, and incredible insight have been invaluable to me. I am also incredibly grateful to our families for their willingness to come to Iceland to lend a helping hand whenever we needed it.

To my dearest friends, Alexia and Evan, you have been the cherry on top of this beautiful adventure. Your constant encouragement to stay sane has been a lifeline, and I am endlessly grateful that you have still travelled with me through my alternate realities and dreams. You are the absolute best!

This work was supported by a Project Grant from the Icelandic Research Fund (grant number 206930). For the paper presented in Chapter 5, simulations were performed on resources provided by LJMU's central high performance computing (HPC) facility. For the upcoming paper discussed in Chapter 4, simulations were performed on resources provided by MKI cluster computing.

1 Dark Matter

One of the fundamental questions in cosmology and astrophysics is how the Universe evolved from a mostly homogeneous state into a complex system containing many structures on different scales, from correlated large-scale structures of order 10 Mpc in size to $\sim$ Mpc galaxy clusters, individual galaxies in the $1 - 100$ kpc regime, all the way down to the sub-pc scale into the regime of stars. Various observations indicate that to explain our Universe, a large amount of an unknown type of "invisible" matter is needed. It does not interact with light or ordinary matter in any measurable way thus far, and therefore, it has not been directly observed by telescopes or any other experiment in spacer or on Earth; hence, it is referred to as "dark matter". It makes up about 26 per cent of the current matter-energy density in the Universe, which is five times as much as ordinary matter, and it plays a pivotal role in the formation and evolution of cosmic structure. Although we know little about the nature of dark matter, we have inferred its existence through its gravitational effects. The evidence of such gravitational impact is overwhelming and comes from a wide variety of astrophysical measurements (see below). These findings and independent theoretical models have led the scientific community to incorporate dark matter as a fundamental component within the standard cosmological model.

1.1 Observational evidence

Galaxy Clusters. One way to determine the mass of a self-gravitating astrophysical system is to observe the motion of objects/tracers within this system. Then, the mass needed to reproduce such motion can be calculated from Newton's law of gravity. When a system is in equilibrium, the virial theorem can be used to simplify the calculations. This theorem states that if a system is gravitationally bound and in steady-state, then $2\langle T\rangle + \langle U\rangle = 0$, where $\langle T\rangle$ and $\langle U\rangle$ are the average kinetic and average potential energies, respectively. This can help us understand the relationship between the velocity dispersion (related to the kinetic energy) and the total mass and size of the system (related to the potential energy). In 1933, by adopting the virial theorem, Fritz Zwicky first computed the mass of the Coma Cluster from the observed velocity dispersion of galaxies within the cluster. He found that the mass he obtained was 400 times larger than expected from luminosity measurements of all visible galaxies in the cluster (Zwicky, 1933, 2009). It provided the first evidence that there might be a large amount of invisible/dark matter in the Coma Cluster. Another piece of gravitational evidence came decades later with measurements of the hot gas in the Coma Cluster inferred through its X-ray emission. It is found that the mass of the luminous galaxies in the cluster is only $\propto 10\%$ of the gas mass (Briel and Henry, 1998). By assuming hydrostatic equilibrium, it is found that the combination of the gravitating baryonic (gas+stars) mass cannot provide the required gravitational potential to hold such a huge amount of gas at such high temperatures $\sim 8\mathrm{keV}$. This implies that a vast amount of dark matter is needed to be the main source of the gravitational potential.

Gravitational Lensing. Lensing measurements confirm the existence of enormous quantities of dark matter in galaxies and clusters of galaxies. Distant bright objects, such as galaxies and quasars, act as a background source of light that can be bent along the line of sight as it crosses intervening matter, which acts as a gravitational lens amplifying the source and distorting/shearing it (weak lensing) or possibly creating multiple images if the alignment is right (strong lensing). It is typical for the modelling of the lensing signals to require dark matter. For instance, using statistical analysis of weak lensing from the Sloan Digital Sky Survey, it was concluded that galactic systems, including the Milky Way, are even larger and more massive than previously thought and require even more dark matter out to greater distances from their centres. A prominent/classic example of a lensing system that provides strong evidence for the existence of dark matter is the Bullet Cluster, which shows the interaction of two colliding galaxy clusters. Lensing measurements show that the bulk of the (gravitational) mass is spatially separated from the bulk of the baryonic mass (most of which is in a hot gas component visible through X-ray emission). This separation is expected since the hot gas in the clusters interacts strongly and lags behind the dominant gravitational component, which needs to be mostly non-interacting/collisionless, i.e., dark matter.

Rotation Curves. For disk galaxies, the mass distribution can be inferred from the rotation velocity of visible stars or gas around the galaxy centre by applying Kepler's second law. The improvement in spectroscopic techniques made it possible to accurately measure galaxies' rotation velocity to large radii (known as rotation curves) with optical and radio telescopes using the Doppler effect. In 1970, Vera Rubin and Kent Ford discovered the first compelling evidence for dark matter in the rotation curve of the M31 Andromeda galaxy (Rubin and Ford, 1970). Later, in 1978, they measured the rotation curves for ten spiral galaxies and found they are mostly flat even out to the outermost radii (Rubin et al., 1978). These results are inconsistent with the predictions from Newtonian dynamics, where the circular velocity of a tracer of the gravitational potential is given by

$$v_{\rm circ}^2 = \frac{GM(<r)}{r}, \tag{1}$$

where $M(<r)$ is the enclosed mass given by $M(<r) = 4\pi \int_0^r \rho(r')r'^2\,dr'$, r is the distance from the center and G is the gravitational constant. If a galaxy contains only luminous/baryonic matter, such as stars and gas, then the density of the luminous matter is observed to decrease progressively at larger radii. Thus, the enclosed mass, $M(<r)$, should approach a constant value, which would imply the velocity $v_{\rm circ}$ to decrease as $1/\sqrt{r}$, as opposed to being roughly constant as observed. A way to address this inconsistency is to introduce more matter that does not produce significant electromagnetic radiation, i.e., dark matter.

Expansion of the universe and Nucleosynthesis. Another indirect evidence of dark matter comes from measurements of the Universe's expansion history. As was first discovered by Hubble in 1929 Hubble, 1929, the Universe is expanding, and in fact, it is expanding at an accelerated rate as was discovered in 1998 (Perlmutter et al., 1998, Riess et al., 1998). The expansion history of the Universe depends on its global matter-energy components, as well as its spatial curvature. For instance, since gravity is attractive, the expansion of the Universe should be slowed down by matter components: the larger the amount of matter, the greater the deceleration. Therefore, by measuring the expansion of the Universe, we can constrain the global matter density in the Universe and check whether it is consistent with independent measurements of the global density of ordinary/baryonic matter.

One way to measure the expansion history of the Universe is to look at Type Ia supernovae. Type Ia supernovae produce nearly universal light curves (brightness as a function of time) with consistent peak luminosities during their explosions. They thus can be used as standard candles (an object whose intrinsic luminosity is well known). Comparing the brightness of a supernova with its intrinsic luminosity, its (luminosity) distance to us can be derived using Gauss's law, which states that $\text{intensity} \propto 1/\text{distance}^2$. On the other hand, the redshift of the supernova can be obtained from its spectrum. The redshift is a measure of how much the Universe has expanded since the explosion of the supernova. Thus, comparing the distances and redshifts of different supernovae gives information about the expansion history of the Universe, which can then be used to constrain the parameters of the cosmological model using Friedmann's equations; more importantly, its curvature, matter density and dark energy density (vacuum energy, cosmological constant Λ in its simplest form).

In 1998, two groups, the High-Z Supernova Search Team (Riess et al., 1998) and the Supernova Cosmology Project (Perlmutter et al., 1998), independently discovered that the expansion of the Universe is currently accelerating and thus giving evidence of a significant contribution of the cosmological constant that opposes the decelerating effect of gravitating matter. The implications of this discovery and other recent analyses are that the Universe is made up of about $1/4$ of matter and $3/4$ of dark energy.

Although the expansion history cannot directly measure how much of the matter in the Universe is baryonic and how much is dark, other independent estimates (such as those based on Big Bang nucleosynthesis) indicate that the contribution of baryons to the matter-energy density is around 5 per cent Copi et al., 1995. This implies dark matter is the dominant form of matter, constituting over 80 per cent of the matter density.

Cosmic Microwave Background. The most compelling evidence for the existence of dark matter is the Cosmic Microwave Background (CMB). It is a remnant radiation from the earlier epoch when the Universe was roughly 380,000 years old, discovered in 1964 by Penzias and Wilson (Penzias and Wilson, 1965). The temperature before the CMB emission was so high that electrons could not be bound to nuclei, and photons interacted strongly with free electrons, establishing thermodynamic equilibrium and creating a perfect black-body spectrum for the photons. As the universe expanded, its temperature decreased until finally, free electrons were able to become bound to nuclei to form neutral hydrogen (an epoch referred to as recombination), making the Universe neutral and transparent to photons. Thus, photons decoupled and began to travel freely from a last scattering surface, which is the CMB radiation we observe today (redshifted). The temperature of the CMB is nearly isotropic, with only very small variations across the sky. But these small anisotropies contain crucial details about the Universe's primordial composition as well as encoding statistically the initial conditions for the formation of cosmic structures across different scales (Miller et al., 1999). The temperature anisotropies/fluctuations in the CMB are connected to matter density fluctuations at the time of the CMB emission, both of which can be modelled by the well-understood linear perturbation theory. In its simplest form, this theory uses the so-called ΛCDM model (Cold Dark Matter, see below, plus a non-zero cosmological constant), which, using only six independent parameters, can describe the statistical properties of the CMB anisotropies, commonly studied through its angular power spectrum. Crucially, among these parameters are the global baryonic and dark matter contents in the Universe. The latest results from the Planck satellite indicate that dark matter makes up about 26 per cent of the current Universe while baryonic matter only makes up around 5 per cent (Planck Collaboration,

2020).

Baryon Acoustic Oscillations. Another way to constrain the expansion history is to search for the signature of Baryon Acoustic Oscillations (BAOs), i.e., density peaks and valleys caused by sound waves propagating in the primordial plasma caused by the interplay between radiation pressure and gravity before decoupling at the time of the emission of the CMB. Before recombination, baryons coupled with photons gave rise to an effective pressure that opposed the clustering of matter due to gravity; this interplay created oscillations of the density fluctuations, resulting in sound waves that travelled at $c/\sqrt{3}$ with c the speed of light. After recombination, the universe became neutral, and baryons decoupled from photons, losing their pressure support. Thus, the sound waves were frozen. In particular, decoupling leaves behind an overdense shell at a characteristic radius called the sound horizon, set by the distance sound waves can travel until the epoch of decoupling. Thus, a peak in the correlation function of the density field is expected to be seen at the scale of the sound horizon. This is observed in the angular power spectrum of the CMB as a harmonic sequence of oscillations. At later times (lower redshifts), the primordial overdense regions (imprinted in the CMB) collapse to eventually form galaxies (this is a process studied in cosmological structure formation (Sec. 1.3). The signature of BAOs is predicted to survive this process, with the sound horizon peak still appearing in the correlation function of the number density field of galaxies, but the position of the peak shifted to a larger scale due to the expansion of the Universe. By measuring this shift relative to the sound horizon at recombination (measured from the CMB), we can obtain information about the expansion history of the Universe. BAOs were detected in the SDSS galaxy survey in 2005 (Eisenstein et al., 2005), and their measurement provides an independent constraint to cosmological parameters, with an overall picture that supports the existence of dark matter (Aubourg et al., 2015).

1.2 Dark Matter particle models and categories

As is shown in the previous section, dark matter is necessary to explain the discrepancy between the matter density estimated from gravitational effects and the density of visible baryonic matter. However, beyond its gravitational effects, little is known about the nature of dark matter; thus, there is a variety of possible (particle) dark matter candidates.

Cold Dark Matter. From the observational point of view, it would be sufficient for most cases to assume that dark matter is made of particles that, for cosmological structure formation, have the following properties:

- cold, i.e., its thermal velocity must be very small at early times;
- collisionless, i.e., it only interacts gravitationally, or, at most, it only weakly interacts (i.e. with an amplitude given by the weak force) with particles in the Standard Model of particle physics, and with itself;
- classical, i.e., with negligible quantum effects.

This is the so-called cold dark matter (CDM) model of structure formation, which, together with a non-zero cosmological constant, i.e., the ΛCDM model, has successfully explained many current observations from galactic to cosmological scales. It has been well tested on scales larger than few 100 kpcs and as small scales as 10 kpcs using Lyman-alpha

forest constraints (Viel et al., 2013), and it shows excellent agreement with observations of the large-scale structure of the Universe over distances greater than > 1 Mpc.

However, from the particle physics point of view, such a model remains incomplete since it does not tell us much about the nature of dark matter as a particle. The properties described above only imply that dark matter must be mostly composed of new undiscovered particle(s) (beyond the Standard Model), which is electrically neutral, stable and weakly interacting (at the most) on cosmological time scales. This leaves a broad spectrum of possible CDM candidates with vast differences in mass and particle interactions. These particle candidates have unique characteristics that typically lead to distinct predictions of new phenomena/signals (uncorrelated/separated from the astrophysical evidence of dark matter we have thus far), which can be tested through experiments. On the other hand, if we observe any deviations from the CDM model in astrophysical/cosmological scales, it would give us the first (non-gravitational) clues about the nature of dark matter that could be searched for in particle physics experiments.

Among the most favoured CDM candidates are Weakly Interacting Massive Particles (WIMPs) and axions. In the standard WIMP scenario, these particles can self-annihilate, which provides a natural thermal production of dark matter: initially, in thermal equilibrium with other species, WIMPs decouple as the universe cools down, and their self-annihilation rate naturally produces the observed global abundance of dark matter if their masses and interactions are set by the weak force; hence their name. Their high masses make them non-relativistic at very early times, and thus, besides being collisionless, they are also cold for the purpose of structure formation. In addition, WIMPs can belong to a class of well-motivated dark matter models that include particles borne out of symmetries proposed to address inconsistencies in the Standard Model of particle physics. For example, the lightest neutralino is a well-known WIMP candidate motivated by Supersymmetry (Jungman et al., 1996). On the other hand, axions stand out as an especially well-motivated dark matter candidate. They are light pseudoscalar particles that appear in a wide variety of extensions of the Standard Model. For instance, they may arise as Goldstone bosons of a spontaneous symmetry breaking at a high energy scale f_a, leading to a small mass m_a and weak couplings to photons, gluons, leptons, and nucleons. Axions possess a unique property that cancels out the CP-violating term in the QCD Lagrangian, thereby addressing the strong CP problem without requiring fine-tuning. Unlike WIMPs, axions have very light masses, typically on the order of microelectronvolts (μeV) to millielectronvolts (meV). However, axions with very low masses have correspondingly large de Broglie wavelengths, which can exhibit wave-like behaviour on large scales. This wave-like behaviour may result in unique large-scale structures that differ from those predicted by standard CDM models, where the structure formation is primarily governed by the gravitational collapse of classical particles (Chadha-Day et al., 2022).

Despite extensive experimental searches in laboratories on Earth and by looking at signals of their interactions in astrophysical sources, WIMPs or axions have not yet been detected (see Aprile et al., 2018, Lanfranchi et al., 2021 for WIMPs and see Rosenberg, 2015, Du et al., 2018 for axions). This lack of detection has increased the interest among particle physicists in other classes of models, which deviate from the CDM hypotheses and, in some cases, include a richer phenomenology, such as new dark/hidden forces. Furthermore, while the ΛCDM model has been successful in explaining the large-scale structure of the universe and a variety of properties of the galactic population, it encounters enduring challenges at smaller

subgalactic scales (Sec. 1.5). This has led to a growing interest in alternative dark matter models among the astrophysical community. Studying alternative/competing dark matter models to CDM and their impact on structure formation is thus a fundamental task in particle physics and astrophysics.

Self-interacting Dark Matter (SIDM). In structure formation, SIDM generically describes dark matter particles that have strong self-interactions, significant enough to relax the collisionless nature of CDM and impact the formation, evolution and structure of galactic-scale dark matter structures. Although we refer to Sec.2 for a more detailed description of the particle physics of the SIDM model, we mention here briefly that the SIDM self-interaction is commonly mediated by new dark/hidden forces beyond the SM. Typically, SIDM interactions are mediated by a particle with a MeV-scale mass through an attractive Yukawa-type potential. Such Yukawa models have as a natural feature a cross section with a steep velocity-dependence, which makes them promising CDM alternatives since self-interactions are suppressed at large velocities/scales where CDM is a good match to observations, while at small velocities/scales, they can significantly deviate from CDM to alleviate some of its challenges. Self-interactions between dark matter particles with typical timescales of 1 scattering per $\sim$ Gyr are sufficient to allow energy and momentum transfer across different parts of the dark matter structures, particularly in the densest regions, transforming their distribution and dynamics relative to CDM. This is especially significant for dwarf galaxies and has the potential to explain some of the puzzling properties of this class of galaxies (Sec. 1.5, see a review Tulin and Yu, 2018).

Warm Dark Matter (WDM). This type of dark matter has a significant velocity dispersion in the early Universe. This velocity induces collisionless damping in the linear/primordial matter power spectrum (i.e. a measure of the clustering of dark matter as a function of scale, which is determined using linear perturbation theory) through the free-streaming mechanism, where the random motions of WDM particles flow between over- and under-dense regions, setting a characteristic length scale. On scales smaller than this free-streaming length, the formation of structures is significantly suppressed, while on larger scales, WDM behaves similarly to CDM. For the purposes of galactic structure formation, the relevance of WDM rests on models that have an effective free-streaming length corresponding to scales of dwarf galaxies and, hence, can deviate distinctly from CDM and address its problems at these scales (1.5.1). Among the potential candidates for WDM, sterile neutrinos stand out. They are hypothetical right-handed neutrinos capable of interacting with Standard Model neutrinos (and thus offering the possibility of searching for decay byproducts) while being effectively collisionless in structure formation. Sterile neutrinos are additionally attractive since they offer a mechanism to explain the small masses of the Standard Model neutrinos (for a review, see Boyarsky et al., 2019).

Fuzzy Dark Matter (FDM). It is proposed as an alternative to CDM that relaxes the hypothesis of dark matter being made of classical/non-quantum particles. In essence, if dark matter is made of extremely light scalar bosons, then their de Broglie wavelengths can be macroscopic, even reaching astrophysical scales. This means that wave-like properties can be significant for structure formation. On large scales, FDM behaves like CDM, producing large-scale structure of the Universe consistent with current observations. But on scales below the Jeans length, quantum pressure arising from coherent oscillations of the scalar field counters gravity, leading to a large suppression in structure formation at the scale of dwarf galaxies, while self-bound dark matter structures (haloes) are expected to form Bose-Einstein-Condensates in their centres. Both of these properties are distinct from CDM and

can potentially solve some of its challenges.

1.3 Dark Matter in structure formation

At large scales, the evolution of structures in the Universe is primarily controlled by the force of gravity in an expanding background, described by Einstein's theory of general relativity. The gravitational force tends to amplify relative overdensities in dense regions over time, which explains how small perturbations observed in the CMB radiation can form giant (10's of Mpc) correlated structures observed in the cosmic web. The ΛCDM model explains the large-scale structure of the Universe remarkably well. In particular, numerical simulations of cosmological structure formation and evolution agree with large-scale observations of the cosmic web (such as CfA Great Wall (Geller and Huchra, 1989) and Sloan Great Wall (Gott et al., 2005)); (see Springel et al., 2005a)).

The goal of structure formation is to trace the evolution of structures across cosmic time from the CMB to the present day. At the time of the last scattering, the density fluctuations are small (compared to the average density), similar to the magnitude of the temperature anisotropies in the CMB, and therefore, can be studied analytically using linear perturbation theory over a homogeneous, isotropic and expanding background. Using this framework, which involves a linearized version of the Boltzmann equation, it is possible to calculate the linear matter power spectra of both CDM and baryons.

For Gaussian random fields, the density and velocity fields of dark matter in the linear regime are described by the linear power spectrum $P(k)$, where k represents the wavenumber of a mode. This spectrum encapsulates all statistical information regarding the spatial clustering of dark matter at all scales. Expressed as the dimensionless power spectrum $\Delta^2(k) = k^3P(k)/(2\pi^2)$, i.e., $\Delta(k)$ is a measure of the amplitude of a perturbation of a characteristic physical scale l, inversely proportional to a given mode k. More formally, $\Delta(k)$ quantifies the contribution to the density field's variance per logarithmic bin of k. The power spectrum predicted by inflation is nearly scale-invariant with $\Delta^2(k) \propto k^{3+n_s}$, where n_s is the spectral index. When a perturbation of a given size enters the horizon, it is amplified by gravity according to linear perturbation theory. Thus, the k-dependence of the power spectrum depends on the predictions of this theory, given the different parameters of the model.

During the epoch of radiation domination, the rapid expansion rate of the universe inhibits the growth of perturbations that enter the horizon (Mészáros effect). On the other hand, baryonic perturbations cannot grow due to the baryonic acoustic oscillations phenomena; this gives dark matter an additional growth period, allowing small initial perturbations to grow, albeit only logarithmically. At approximately $z \sim 3400$, the Universe becomes matter-dominated, allowing more rapid growth of the dark matter perturbation, while the baryonic perturbations continue oscillating until they decouple with photons at $z \sim 1100$ when the CMB is emitted. During the so-called dark ages period in cosmic history (from the time of the CMB emission until the first stars began to form), the gravitational potential was mainly sourced by dark matter, causing baryonic matter to fall into the potential wells created by growing dark matter perturbations. The perturbations (dark matter and baryons) continue growing until they reach the non-linear regime of evolution. At this stage, linear perturbation theory is no longer applicable (modes of different scales are no longer decoupled), and alternative methods have to be used to describe structure formation. In summary, by the end

of the linear regime, when it comes to dark matter perturbations, their statistical properties are fully determined by the (nearly) scale-free inflation power spectrum processed/convolved by the Mészáros effect and the (gravitational) imprint of the baryonic acoustic oscillations. The latter leaves a signature at the sound-horizon scale (measurable in the large-scale distribution of galaxies, as mentioned earlier), while the former impacts the initial conditions for the formation of all dark matter structures that will eventually become self-bound (dark matter haloes) from the scale of galaxy clusters to the lowest-mass galaxies we observe today. Current constraints on the matter power spectrum inferred from different observations, e.g. the CMB and the Lyman-alpha forest, constrained dark matter to behave like CDM up to $k \sim 10$ h/Mpc (Viel et al., 2013). At smaller scales, deviations from the CDM model are less constrained and harder to probe due to non-linear process, both gravitational (taken care of by $N-$body simulations; see sec. 1.3.1) and baryonic (gas hydrodynamics, cooling, star formation and evolution, among others).

Since the physics of the latter remains an open avenue of research, it becomes complicated to distinguish CDM from alternative theories that, due to new (i.e. non-gravitational) dark matter physics, suppress the power spectrum at galactic scales, below current constraints (e.g. WDM and FDM).

For models that only deviate from CDM in the initial (i.e. linear) power spectrum, only linear perturbation theory is needed to obtain this initial condition. The subsequent evolution is given by the same $N-$body equations and methods used for CDM. This is true as long as the dark matter behaves as a non-quantum collisionless system and the simulation starts well after the dark matter particles have become non-relativistic. If dark matter is non-quantum and non-relativistic but particles experience collisions (like in SIDM), then the collisionless Boltzmann equation (valid for CDM) needs to be replaced by the full collisional Boltzmann equation, which has an extra term on the right-hand side of eq. 2 (see sec. 1.3.1) to account for the effect of dark matter collisions according to a SIDM self-scattering cross section. The case of FDM will not be discussed further, but both the initial conditions and the subsequent evolution are affected by non-quantum effects.

1.3.1 Cosmological simulations

The most powerful method to follow the formation of non-linear structures is cosmological $N-$body simulations. It calculates the gravitational forces of a sample of N particles at a given timestep, and then it computes the dynamical evolution using Newtonian Mechanics (in most $N-$body simulations, relativistic effects only impact the background evolution of the expanding Universe). Therefore, the dark matter distribution function can evolve self-consistently from the linear perturbation era to the present day.

For non-relativistic, collisionless particles, CDM N-body simulations follow the evolution of the dark matter phase-space distribution function, $f(\vec{x}, \vec{v}, t)$, which is given by the collisionless Boltzmann equation coupled with the Poisson equation for the gravitational field, $\Phi(\vec{x,}t)$, known as the Vlasov-Poisson equation:

$$\frac{df}{dt} = \frac{\partial f}{\partial t} + \sum_{i=1}^{3} v_i \frac{\partial f}{\partial x_i} - \sum_{i=1}^{3} \frac{\partial \Phi}{\partial x_i} \frac{\partial f}{\partial v_i} = 0 \tag{2}$$

$$\nabla^2 \Phi(\vec{x}, t) = 4\pi G \int f(\vec{x}, \vec{v}, t) d^3\vec{v} \tag{3}$$

Directly solving this pair of equations is computationally impractical. Instead, $N-$body simulations follow the evolution of a set of N macro particles, which sample the distribution function randomly from the statistics of the linear Gaussian density field given by the linear power spectrum. Macro particles have a much larger mass than the actual dark matter particle, and they serve as a statistical representation of the true system, averaged at their resolved scales. To solve macro-scale problems, coarse-graining techniques are used. While this approach enhances computational efficiency by reducing the number of particles, it comes at the cost of diminished resolution, particularly on smaller scales. The dark matter phase space distribution function, f, can be effectively understood as a coarse-graining distribution function, given by:

$$\tilde{f}(\vec{x}, \vec{v}) = \sum_{i=1}^{N} m_i W(|\vec{x} - \vec{x}_i|, \epsilon)\delta(\vec{v} - \vec{v}_i), \tag{4}$$

where m_i is the mass of a dark matter particle, $\delta(\vec{v} - \vec{v}_i)$, is the Dirac delta function, and W is a softening kernel with a softening length ϵ. The softening kernel smooths the close-encounter two-body gravitational interactions and removes the gravitational singularities from point-like density spikes. The evolution of the coarse-grained function is calculated in a comoving reference frame for the N particles, which factors out the expansion of the universe solved separately using Friedmann's equations.

As mentioned above, for SIDM simulations, the full collisional Boltzmann equation should be considered to take into account the self-scattering of dark matter particles. Since this is computationally prohibitive, a probabilistic Monte Carlo approach is used instead, which assigns a probability of scattering between a particle and its immediate neighbours, which depends on the local density, SIDM cross-section and relative velocity between the interacting particles (Vogelsberger et al., 2012a).

Methods to compute gravitational forces.

A primary task in $N-$body simulations is to efficiently calculate gravitational forces for a large number of macro particles. One common method used is called the particle-mesh (PM) technique. It calculates the smoothed density field on a pre-defined grid from the N particles and then solves Poisson's equation (Eq. 3) for the potential Φ in Fourier space. Then, the potential and force acting on individual particles are obtained with the inverse Fourier transform and interpolation. (Klypin and Shandarin, 1983). This method is, however, limited by the mesh size, restricting the effective resolution.

Another algorithm is the hierarchical tree method, which divides the simulation volume recursively into cubes in a tree structure (Barnes and Hut, 1986). The tree gets fully "opened" for nearby particles, and each force pair is precisely computed. For distant particles, instead of computing each individual force pair, all particles within the respective cube are grouped together to act as a macro particle for the gravitational force.

Many modern $N-$body codes use a hybrid approach combining the PM and tree methods to exploit their advantages at large and small scales, respectively. One such example is the code AREPO (Springel, 2010) used in this Thesis, which uses the treePM algorithm on a moving Voronoi mesh (AREPO is built upon the widely used GADGET code; Springel, 2005).

Timestep evolution. Accurate time integration is critical for obtaining reliable results

in cosmological simulations that aim to follow the evolution of the distribution function over a Hubble time. The Kick-drift-kick (KDK) leapfrog algorithm is commonly used in $N-$body simulations. The KDK is advantageous for accurately modelling dynamical systems with high accuracy over long integration times. For a fixed timestep, the KDK leapfrog is time-invariant and symplectic, which means that total angular momentum and phase space volume are conserved. However, the typical timescales of particles in cosmological $N-$body simulations can vary a lot between them depending on their orbits, and thus, a single fixed timestep hardly seems like the best choice for an efficient time integration scheme.

CDM $N-$body simulations typically use adaptive and variable time-stepping schemes that enable each simulation particle to have an independent, time-dependent timestep, which is usually based on particles' accelerations. This violates the assumptions made when formulating a symplectic integrator, and simulations may suffer from secular energy and momentum error accumulation. The acceleration-based timestep:

$$\Delta t = \sqrt{\frac{2\eta\epsilon}{|a|}} \tag{5}$$

is based on the magnitude of the gravitational acceleration $|a|$ of the particle and the particle's softening length ϵ. The aim of this assignment is to ensure that the timestep is small enough to accurately integrate rapidly accelerating particles. The dimensionless parameter η is selected as needed to scale the timestep size; it describes the fraction of the force-softening length the particle is allowed to move in the given timestep.

For CDM and WDM simulations, the relevant timescales are set by gravity, but for SIDM simulations, another timescale enters into the problem, the relaxation timescale (sec. 2), which is related to the self-interacting cross section. The SIDM timestep in AREPO is designed to avoid multiple scatterings within a timestep in the individual neighbourhoods where the probabilistic approach for scattering is evaluated (see above). Otherwise, it would be difficult to determine the chronological order of scattering events or pose computational challenges in processor communication in parallel computing environments. AREPO implements SIDM timesteps as follows:

$$\Delta t_{\rm SIDM} = \frac{\texttt{DtimeFac}}{\bar{\rho} \times (\sigma/m) \times \sigma_{\rm vel}}, \tag{6}$$

where $\sigma_{\rm vel}$ is the local velocity dispersion, $\bar{\rho}$ is the local matter density measured for each particle by determining the density of the sphere enclosing the 32 nearest neighbours of the test particle. (σ/m) is the self-interaction cross-section per unit mass. `DtimeFac` is a normalization parameter or the mean scattering probability that is set by default to 0.0025. It establishes a maximum scattering probability for particles at each timestep. This commonly used value limits this probability to 0.25%.

1.4 Dark Matter haloes

$N-$body simulations are used to create virtual universes that can be used to study the clustering of dark matter at all scales, from cosmological scales to analyse the (linear and quasi-linear) large-scale structure of the Universe to the highly non-linear small-scales. The latter regime is more relevant for this thesis, particularly in regard to the development of

gravitationally self-bound dark matter structures called haloes. $N-$body CDM simulations have by now achieved the resolution that allows us to understand the phase-space structure of dark matter haloes completely for the purposes of galaxy formation and evolution.

1.4.1 Virialized haloes

Although $N-$body simulations offer the complete picture of halo formation, a simplified picture emerges from simple considerations. Dark matter overdensities start out as very small perturbations on top of the smooth average density. They grow over time until they reach the critical density, after which they decouple from the expansion of the Universe and collapse due to gravity into self-bound structures called haloes; it is the (gravitational) energy exchange across the different sections of the perturbation as they collapse that results in virial equilibrium. These haloes are the final stage of the evolution of the primordial dark matter density perturbations inferred from the CMB. According to the spherical collapse framework, which models the formation and growth of such haloes in a simplified way, virialized haloes in a matter-only Universe have an overdensity of $\Delta(z) \approx 178$ with respect to the background. However, a common choice is to approximate the halo as a sphere of radius r_{200} within which the average density is given by 200 times the critical density $\rho_{\rm c}$, and then the corresponding virial mass is M_{200}, the enclosed mass within this radius. After haloes become virialized structures, they continue growing and increasing their mass over time, either through mass accretion or through merging with other haloes.

1.4.2 Halo abundance

The CDM model predicts a hierarchical formation of dark matter haloes, with low-mass haloes forming first and more massive haloes later, mostly through the merger of small haloes. With this hierarchical scenario, the CDM model predicts an ever-increasing amount of haloes towards smaller masses. Using the statistics of Gaussian random fields and the spherical collapse model, Press & Schechter (Press and Schechter, 1974) proposed an analytical model called the Press–Schechter formalism (PS) that predicts the abundance of dark matter haloes as a function of mass. This formalism assumes that collapse occurs when the smoothed density field, δ, exceeds the critical overdensity for collapse, $\delta_{\rm c}(t) = 1.686/D(t)$, where $D(t)$ is the linear growth factor. It qualitatively predicts halo abundances that are comparable to numerical simulations. Based on PS formalism, Bond et al., 1991, Bower, 1991 and Lacey and Cole, 1993 extended the analysis to include predictions for the halo abundance and assembly history in different environments. Thereafter, several studies have attempted to provide accurate and universal fitting formulae for halo mass functions from numerical simulations. Since the advent of simulations that can resolve a large dynamical range (many orders of magnitude in halo mass), it has been possible to have a complete picture of the halo mass function across all scales relevant to galaxy formation and evolution. Qualitatively, there are two relevant regimes we can mention for the CDM model; at the low-mass end, the halo mass function is given by a featureless power-law (Boylan-Kolchin et al., 2009):

$$\frac{dn}{dM} \propto M^{-1.9}, \tag{7}$$

where n is the number density of haloes, and M is the virial mass. On the other hand, at the high-mass end, there is a natural exponential cut-off set by the characteristic halo mass/scale that, at a given redshift, has just become sufficiently non-linear to collapse into virialized structures. At $z = 0$, this is the scale of massive galaxy clusters $M \gtrsim 10^{14}{\rm M}_{\odot}$.

The question of what the physical mechanism that sets the minimal scale for galaxy formation is remains open. This is an important question in the context of the halo mass function since it would naturally set the minimum halo mass one should care about in this context. For CDM, this question only depends on baryonic physics, in processes such as supernova feedback, and more importantly, reionization, which is known to severely suppress galaxy formation below $\sim 10^9 \mathrm{M}_\odot$ haloes (e.g. Sawala et al., 2016a). For certain alternative dark matter models, however, the relevant mechanism to suppress galaxy formation might not only depend on baryonic physics but also on the particle nature of the dark matter. For instance, in the WDM model, collisionless damping (free streaming) in the early Universe introduces a sharp cut-off at a certain wavenumber $k_{\rm fs}$, suppressing perturbations with $k > k_{\rm fs}$. In allowed WDM models, this free-streaming scale is comparable to those scales affected by reionization, while in CDM, $k_{\rm fs} \longrightarrow \infty$ in principle. In practice, its value depends on the exact CDM particle model, but it is many orders of magnitude below galactic scales. The free-streaming scale is related to the time at which the dark matter particles become non-relativistic and is given by:

$$\lambda_{\rm fs} = \frac{2ct_{\rm nr}}{a_{\rm nr}} \left[1 + \ln \frac{a_{\rm eq}}{a_{\rm nr}} \right], \tag{8}$$

where $t_{\rm nr}$ is the time dark matter particles become non-relativistic, $a_{\rm nr}$ is the scale factor at that time and $a_{\rm eq}$ is the scale factor at the the matter-radiation equality. For collisionless dark matter, the free-streaming length scales roughly as $\lambda_{\rm fs} \propto m_\chi^{-1}$, where m_χ is the mass of the dark matter particle and thus, lighter dark matter particles are more strongly affected by free-streaming damping. The free-streaming length directly corresponds to a lower limit on the size of gravitationally bound structures (haloes) that can eventually form from the collapse of growing dark matter density perturbations. Currently allowed WDM models have a cutoff at galactic scales, corresponding to masses of dwarf galaxies, which in WDM cosmogony, determines the abundance and structure of small-mass dark matter haloes.

1.4.3 Halo structure

Perhaps the most significant result found with $N-$body simulation is the near-universality of their inner distribution. In particular, the spherically averaged density profile of CDM haloes is well described by a two-parameter function, referred to as the Navarro-Frenk-White (NFW) profile (Navarro et al., 1997, 1996a):

$$\rho_{\rm NFW}(r) = \frac{\rho_{\rm s}}{r/r_{\rm s}(1 + r/r_{\rm s})^2}, \tag{9}$$

where $\rho_{\rm s}$ and $r_{\rm s}$ represent the scale density and radius, respectively, the latter of which corresponds to the radius where the logarithmic slope of the profile is equal to -2. The density of CDM haloes asymptotically increases towards a halo's centre as r^{-1} and steepens towards the outskirts, with an asymptotic behaviour of $\rho \propto r^{-3}$ at large radii. The NFW profile is called 'universal' because of its remarkable regularity across 20 orders of magnitude in halo mass, covering the entire hierarchy expected in WIMP CDM models (Wang et al., 2020), which goes well beyond the ~ 7 orders of magnitude that are relevant for galaxies and galaxy clusters.

The concentration parameter, defined as $c = r_{200}/r_{\rm s}$, is more commonly used as a measure of the inner density of haloes, where a low concentration means lower central densities. The

scale density can then be fixed by the requirement that $M(< r_{200}) = M_{200}$, i.e., the definition of the virial mass. Integrating over the NFW density profile and using the definition of the virial mass allows us to write:

$$\rho_{\rm s} = \delta_{\rm c}\rho_{\rm crit} \tag{10}$$

$$\delta_{\rm c} = \frac{200}{3}\frac{c^3}{\ln(1+c) - c/(1+c)} \tag{11}$$

where $\rho_{\rm crit}$ is the critical density of the Universe. Thus, the halo's mass density profile is fully defined by its virial mass and concentration. The concentration of a halo, in turn, depends on the average matter density in the Universe at the epoch of assembly of its central region. In hierarchical structure formation, small haloes have larger concentrations than larger ones since they collapse earlier at a time when the average matter density of the Universe was larger. Furthermore, halo assembly can be analysed as a process of progressive mass aggregation of shells, each having a characteristic density set by the average density of the Universe at the time when a given shell is assembled. The central regions assemble earlier, and thus are denser, than the outer material, which is assembled later. Ludlow et al., 2014 presented a formalism that connects the density at a given radius from the halo centre to the average density of the universe at the time material at that radius was accreted. This can be used to explain (after calibration) the correlation between halo mass and halo concentration measured in $N-$body simulations, which is known as the mass-concentration relation Navarro et al., 1996a, Bullock et al., 2001, Neto et al., 2007, Ludlow et al., 2014, 2016. This correlation is strong, with a relatively small scatter, connected to the variance in assembly time for haloes of a fixed mass. Since the scatter is small, CDM haloes are mainly characterised effectively by a one-parameter (halo mass) density profile.

New dark matter physics, beyond CDM, can impact the structure of dark matter haloes, changing the CDM predictions. High-resolution simulations of WDM have shown that WDM haloes retain the universality of CDM haloes, following an NFW profile but with a lower concentration for low-mass haloes, those affected by the cutoff in the power spectrum, which not only suppresses their abundance but also delays their early assembly (Lovell et al., 2014, Ludlow et al., 2016). On the other hand, SIDM disrupts the universality of haloes, which is a result of gravitational assembly, by introducing another timescale set by the physics of self-scattering (this will be discussed in more detail in Chapter 2). SIDM haloes develop quasi-stable isothermal density cores with a size of the order of the scale radius. During the long-lived core stage, the central density continues to increase relatively slowly until the gravothermal collapse is triggered. This causes instability that results in ever larger densities tending to infinity, forming a central black hole.

1.4.4 Subhaloes

According to the hierarchical structure formation theory, haloes grow by merging with other smaller haloes and by accreting surrounding unbound mass. When small haloes cross the virial radius, they are called subhaloes since the vast majority of them will become bound to the larger host due to environmental (gravitational) effects. They exhibit structural properties similar to isolated haloes but are influenced by several relevant physical processes. A subhalo experiences tidal forces due to the gravitational potential produced by the host halo and the host galaxy; the strength of this tidal interaction depends on the orbit of the subhalo. A subhalo orbit passing close to the halo's centre will be strongly affected due to the steep changes in the central density of the halo and the presence of the central galaxy. This can cause a strong

gradient in the host's gravitational field over the subhalo's spatial extent, which, depending on the duration of the tidal forces and the strength of the gradient, the effect can either be approximated as continuous or instantaneous/impulsive. The first phenomenon is known as tidal stripping, while the second one is called tidal shock heating (when the tidal force acts on a timescale much shorter than the orbital timescale of the subhalo). Both tidal stripping and tidal heating play significant roles in shaping the inner structure, morphology and kinematics f subhaloes, and thus in the galaxies that inhabit them. $N-$body Simulations (e.g. Kazantzidis et al., 2004) have shown that due to these processes, subhaloes can lose substantial mass from their outskirts, experience (transitory) disturbances in their central densities, and can eventually be completely disrupted as self-gravitating structure, finally merging with the host halo. As long as they remain self-bound, however, the asymptotic behaviour of the NFW profile in the centre remains unchanged. In addition, as a subhalo moves through the host's dark matter halo, it experiences the phenomenon known as dynamical friction due to interactions with the surrounding dark matter particles. This gravitational drag transfers energy and momentum from the subhalo to the surroundings, causing the subhalo's orbit to decay, leading it to spiral inward toward the centre of the host halo. The strength of dynamical friction experienced by a subhalo depends on several factors, including the mass of the subhalo, its velocity relative to the surrounding medium, and the density distribution of the medium. Generally, more massive subhaloes experience stronger dynamical friction and, therefore, decay faster than less massive ones. Additionally, subhaloes moving at higher velocities experience less dynamical friction compared to slower-moving ones. The dynamical friction affects the spatial distribution of subhaloes, which is key to ultimately determining the timescale for the final merger with the host.

1.5 Dwarf galaxies

Since dark matter cannot be observed/measured directly, it is only possible to infer the properties of dark matter haloes indirectly through their influence in the galaxies that reside within. Galaxies are gravitationally bound systems of stars, gas and dust. The galaxy in the central halo is called the host or central galaxy, while galaxies inhabiting subhaloes are referred to as satellite galaxies. Small galaxies with the stellar mass of $M_* \lesssim 10^9\,\mathrm{M}_\odot$ are called dwarf galaxies. Dwarf galaxies have a wide range of stellar masses and origins. In this Thesis, we do not consider the highest mass end of the dwarf galaxy population and concentrate mostly on the so-called classical dwarfs and ultra-faint dwarfs (UFDs). Those with stellar mass $M_* \gtrsim 10^{5-7}\,\mathrm{M}_\odot$ residing in haloes with masses of order $M_{\rm vir} \sim 10^{9-10}\,\mathrm{M}_\odot$ known as classical dwarfs, often exhibit active star formation in the present day when they are central/field galaxies characterized by a substantial gas-to-stellar mass ratio (Geha et al., 2012), they are commonly known then as dwarf irregulars (dIrrs) in this case. On the other hand, dwarf galaxies typically lack gas and recent star formation if they are satellites of larger galaxies (Spekkens et al., 2014); the latter class is commonly known as dwarf spheroidal galaxies (dSphs). Due to their low luminosity, dSphs and UFDs have been primarily observed and studied in the immediate vicinity of the Milky Way or in the Andromeda (M31) galaxy. Dwarf galaxies are the most dark matter-dominated systems in the Universe, with stellar-to-halo mass ratios reaching 1000 or above, with UFDs having the highest values. UFDs represent ancient relics of star formation predating the reionization of the Universe (Benson et al., 2002). Reionization heats the intergalactic medium so that it cannot condense into

small haloes, highly suppressing star formation in $10^9\,\mathrm{M}_\odot$ haloes and thus shaping the UFDs as witnesses to early cosmic epochs that can be used for both to test our understanding of baryonic physics at the faintest galaxy scales and to look for clues for new dark matter physics.

1.5.1 CDM small-scale challenges

The properties of dwarf galaxies have been harder to understand in the context of the CDM model. In particular, there have been a series of puzzling observations that are a challenge to the model. Whether this challenge has its roots in baryonic physics or in dark matter physics remains an open question. The following are four of these challenges that are more significant for the purposes of this Thesis.

Core-cusp problem

Starting with the observations of large gas-rich dwarfs, such as Low Surface-Brightness galaxies (LSBs) (de Blok and McGaugh, 1997) and later, classical dwarf satellites of the Milky Way and late-type spiral dwarfs, astronomers discovered that inferred dark matter central densities in these galaxies are lower than anticipated the CDM-only $N-$body simulations (that is without modelling the impact of baryonic physics). For example, LSBs have diffuse disks with low baryonic density, suggesting that rotation curves should be strongly dominated by dark matter in the centre.

However, observations indicate that many LSBs have rotation curves that rise linearly as a function of radius in the inner region, which, according to Eq. 1, implies a constant central density, i.e., the presence of cores rather than the NFW cusps expected in CDM (see Eq. 9). It is challenging to infer the inner dark matter distribution of haloes due to the incomplete kinematical information we have from gravitational traces, such as stars and gas. For larger dwarfs with high gas fractions, it is common to find systems with central densities that are lower than the CDM-only prediction, generally with $\alpha < 1$ where $\rho \propto r^{-\alpha}$ (e.g. see results from the `LITTLE THINGS` survey Hunter et al., 2012, Oh et al., 2015). The UFDs and dSphs remain particularly elusive in regards to inferring their dark matter density profile.

These galaxies lack significant rotating gas components making it impossible to measure their rotation curves, which could be used to trace the underlying dark matter potential. Instead, they are, in the best of cases, spheroid-like systems in dynamical equilibrium, primarily supported by the velocity dispersion of their stars. This makes the inference of the dark matter potential more complicated since 6D phase-space information is needed, while only 3D information is typically present (2D spatial projection and line-of-sight velocities). This leads to degeneracies in inferring the density profile that, in some cases, can be broken by, e.g. using multiple populations. Studies in the past have found that some dSphs have central cores (e.g. Walker and Peñarrubia, 2011a), but such results remain controversial.

Missing-satellites problem

The number of small satellite galaxies around the Milky-Way galaxy is much less than predicted by the high-resolution cosmological simulations of Milky Way-sized haloes in the CDM model without considering baryonic physics (Klypin et al., 1999, Moore et al., 1999). As we mentioned in Sec. 1.4.2, CDM predicts dark matter clumps to exist at all resolved masses (Eq. 7). CDM simulations predict a vast abundance of low-mass haloes, which should, in principle, host dwarf galaxies all the way down to the mass scale where galaxies can form, i.e., to the limits set by relevant baryonic physics processes such as atomic and molecular gas

cooling, and heating during reionization. Although the minimum halo mass for a galaxy to form remains uncertain, dark matter haloes are expected to become increasingly inefficient at making galaxies at smaller halo masses. The limit of $M_{\rm vir} \leq 10^9$ $\rm M_\odot$ is the threshold beyond which gas accretion is suppressed by reionization UV feedback (Bullock et al., 2000, Benson et al., 2002, Sawala et al., 2016a), while $M_{\rm vir} \leq 10^8$ $\rm M_\odot$ represents the minimum mass needed for atomic cooling in the early universe.

Too-Big-To-Fail Problem

Although inferring the inner dark matter density profile of haloes in dwarf galaxies is complicated and results remain controversial (see core-cusp problem above), inferring average central densities is a less complicated task, and is now well-accepted that many dwarf galaxies have a central deficit of dark matter relative to CDM expectations. Comparing the central densities of observed satellites with those predicted by simulations gave rise to the "Too Big to Fail" (TBTF) problem. The TBTF problem is the observation that the largest subhaloes in CDM dark matter-only simulations have circular velocities larger than those inferred from the stellar kinematics of large Milky Way classical dwarfs (Boylan-Kolchin et al., 2011, 2012). This implies that the CDM model predicts a subhalo population that overall has higher central densities of dark matter than those observed in the Milky Way satellites.

The name comes from the fact that it is the most massive CDM subhaloes that should be the most efficient at forming stars and thus should host the brightest visible satellites. Instead, these subhaloes seem to have no observational counterpart.

The TBTF problem has by now been identified for dwarf galaxies in the Local Group (Garrison-Kimmel et al., 2014) as well as in the field (Papastergis et al., 2015).

Diversity problem

In some sense, the current perspective on the CDM TBTF problem described above has shifted from a problem of the surprising deficit of dark matter in the centres of dwarf galaxies to a problem of the overall wide range of inner densities that dwarf galaxies exhibit in a relatively narrow range of halo masses. This was first firmly established by noticing the large observed diversity of rotation curves (at a fixed maximum rotation speed, which is a proxy for halo mass) that exists in higher-mass, gas-rich field dwarf galaxies (Oman et al., 2015, Relatores et al., 2019). This is at odds with predictions based on the CDM model, contrary to the TBTF and cusp-core problems above, including the modelling of baryonic physics. CDM plus baryonic physics systematically predict a narrow diversity/scatter in the shape of rotation curves at a fixed maximum circular velocity (Santos-Santos et al., 2020). A likely implication of the diversity problem in rotation curves is that galaxies, at a fixed maximum circular velocity, inhabit haloes with a diverse range of density profiles, from cored to very cuspy. A similar diversity is present at lower scales in the Milky Way satellites, which exhibit a wide range of dark matter densities at sub-kpc scales, with some satellites being consistent with large cores while others have cuspy centres, out of which some are consistent with NFW, and some are even denser (Fattahi et al., 2018, Zavala et al., 2019, Errani et al., 2018).

1.5.2 Possible solutions to the CDM small-scale challenges

Proposed solutions to explain the puzzling properties of dwarf galaxies described above are divided into two main avenues: explaining them with baryonic physics processes and/or new dark matter physics, which deviates from CDM on small scales.

Core-cusp problem

Baryonic solution. The complex (stellar + gas) physics of galaxy formation and evolution has several mechanisms that can alter the inner structure of the halo. In the following, we describe some of the most relevant ones. In the simplest picture of galaxy formation, gas settles into the dark matter halo in hydrostatic equilibrium. Afterwards, it loses energy due to radiative cooling and sinks into the inner halo until the gas density is high enough to trigger star formation. This process has a gravitational impact on the inner structure of the halo. The deepening gravitational potential of baryons causes dark matter's central density and velocity dispersion to increase through a process known as adiabatic contraction (it's adiabatic because the potential changes slowly relative to the typical orbital times of the dark matter particles). This tends to make the central dark matter density profile steeper than NFW.

On the other hand, the final stage in the evolution of massive stars causes supernova-driven gas outflows, which are an effective form of non-adiabatic dynamic feedback into the dark matter distribution. A fraction of the energy released in supernovae is deposited as a momentum exchange in the surrounding interstellar medium. This can cause rapid gas outflows which impulsively change the local gravitational potential. It has been shown that repeated episodes of this nature can result in an irreversible reduction of the central halo density (Navarro et al., 1996b, Governato et al., 2010). In general, the ability of baryons to affect the central density of dark matter depends on the complex interplay between adiabatic contraction and impulsive supernova feedback across the assembly history of the galaxy, with not only the stellar-mass ratio playing a role, but also how concentrated the stellar distribution is within the halo and how impulsive and episodic the feedback process is, among other factors. Hydrodynamical simulations suggest that supernova feedback transforms cusps into cores most efficiently in bright dwarf galaxies (Benítez-Llambay et al., 2019, Dutton et al., 2020). This method is less efficient for faint dark matter-dominated systems with low stellar-mass ratios (like dSphs and UFDs; see e.g. Peñarrubia et al., 2012, Amorisco et al., 2014), but the minimum halo mass from efficient baryonic cusp-core transformation remains an open question (Read et al., 2016, Bose et al., 2019, Robles et al., 2017, Macciò et al., 2017). Thus, whether or not supernova feedback can explain the presence of cores in dwarf galaxies remains an active topic of research (Genina et al., 2022, Wheeler et al., 2019, Orkney et al., 2021).

Dark matter solutions. SIDM can change the central dynamics of the halo and create large dark matter cores through a redistribution of energy between the inner and outer regions of the halo through elastic scattering between dark matter particles (Spergel and Steinhardt, 2000, Davé et al., 2001, Vogelsberger et al., 2012a, Rocha et al., 2013). SIDM haloes have two sequential phases along their evolution. The first (and long-lived) is the creation of an isothermal core, which can be up to the size of the scale radius of the halo, and the second is the gravothermal collapse, which results in cuspier centres than CDM and/or in the formation of a black hole. Whether a SIDM halo is in the cored phase or in the collapsed phase depends on the timescales for relaxation (set by the SIDM cross-section and the characteristic central densities) and halo assembly (set by the halo concentration). The cusp-core-collapse evolution in SIDM haloes is discussed in detail in Sec. 3.2.1. In broad terms, SIDM offers a simple mechanism to naturally created cored haloes without the need of efficient supernova feedback, which is particularly appealing to explain the presence of cores in galaxies that are strongly dominated by dark matter.

Missing-satellite problem

Baryonic solutions.

The missing-satellite problem was originally formulated based on dark matter-only simulations and highlighted the discrepancy between the number of satellites predicted in CDM and observed in the Milky Way. Significant progress has been made in observing many ultra-faint satellite galaxies in the Local Group in recent years through increasingly sensitive surveys that expanded the observed satellite count (Simon, 2019, Kim et al., 2018, Drlica-Wagner et al., 2020). However, correcting for those satellites that have not yet been detected is required, and it is necessary to make assumptions regarding the distribution of satellites both radially and on the size-luminosity plane, neither of which is accurately known. It is thought that with reasonable theoretical and observational uncertainties, observations and high-resolution simulations, including baryonic physics are consistent with each other (Sales et al., 2022). Including baryonic physics is expected to alleviate this problem. The reason is a combination of effects. On the one hand, mergers between haloes during the cosmological assembly result in the disruption of low-mass haloes due to the processes described in Sec. 1.4.4. This is, of course, captured by $N-$body simulations, but when galaxies are added into the picture, the expectation is that the disruption might be more severe since the host produces a stronger tidal field in its central reason due to the central galaxy. In addition, if supernova-driven feedback has been efficient in reducing the central densities of the merging subhaloes, then they will be more prone to tidal heating and disruption (Garrison-Kimmel et al., 2017, Errani et al., 2018, Dooley et al., 2016, Zolotov et al., 2012). Current high-resolution simulations that incorporate these effects and, in addition, consider observational incompleteness show a reasonable agreement with the abundance of satellites in the Milky Way (Sawala et al., 2016b, Fattahi et al., 2016a, Nadler and DES Collaboration, 2020, Manwadkar and Kravtsov, 2022, Garrison-Kimmel et al., 2019a). The key solution to this problem involves identifying which haloes are occupied by visible baryons, an approach especially important for UFDs.

Dark matter solutions. The missing-satellite and core-cusp problems inspired the development of WDM (Colín et al., 2000, Bode et al., 2001) and SIDM models (Spergel and Steinhardt, 2000). As discussed in Sec. 1.4.2, the free-streaming mechanism in the WDM model erases small perturbations in the early universe and suppresses the formation of low-mass haloes and, thus, of dwarf galaxies. With an appropriate free-streaming/cutoff scale (which translates to a certain WDM particle mass), WDM can alleviate the missing-satellite problem (Bose et al., 2016a, Lovell et al., 2019). In SIDM models, the dark matter particle self-interactions can cause smaller subhaloes to evaporate due to energy exchange between particles in the subhalo with those in the host halo; this can result in fewer visible satellite galaxies. However, recent SIDM simulations have shown that SIDM can only substantially reduce the abundance of subhaloes for large (nearly-)velocity-independent cross sections $\gtrsim 10\text{cm}^2/\text{gr}$ (Vogelsberger et al., 2012a). Models with such cross-sections are ruled out by observational constraints based on ellipticals (e.g. Peter et al., 2013) and galaxy clusters (e.g. Robertson et al., 2019). Therefore, currently allowed SIDM models can not offer an alternative solution to the missing satellite problem; they rely on the same solutions provided within CDM.

TBTF and diversity problems

Baryonic solutions. As mentioned above, baryonic physics, both internal to galaxies (i.e.

processes such as adiabatic contraction and supernova-driven feedback) and environmental (i.e. processes such as tidal heating), play an important role in shaping the central densities of the Milky Way satellites. This can certainly alleviate the TBTF problem with supernova-induced cores being produced in those systems with a significant fraction of concentrated baryons, while tidal effects can help explain the diversity problem due to the different orbits that the satellites might experience (citeZolotov2012, GK2019). However, CDM + baryonic simulations still struggle to account for low-density, big Milky Way satellites like Fornax, Sextans and Canis Venatici I (Simon and Geha, 2007, Walker et al., 2009, Sawala et al., 2016b). Furthermore, the discovery of Crater II (Torrealba et al., 2016a) and Antlia II (Torrealba et al., 2019a) has posed new challenges to existing models. Studies by Errani et al., 2022 and Borukhovetskaya et al., 2022 suggested that matching the observed mass and size of Crater II without disrupting the satellite entirely may require modifications to the dark matter profile, such as introducing a baryonic core or considering novel dark matter physics. Meanwhile, Ji et al., 2021 presented evidence indicating that Antlia II is undergoing disruption, suggesting that Crater II may be experiencing a similar fate. A similar difficulty exists in comparing the CDM model to the diversity of rotating curves in gas-rich dwarf galaxies (Santos-Santos et al., 2020). However, for this type of galaxies, the presence of non-circular motions should be considered carefully since they can account for a considerable fraction of the observed diversity (Oman et al., 2019).

Dark matter solutions. The TBTF problem motivated a resurgence of the WDM and the SIDM models. WDM simulations result in less abundant and less concentrated haloes with a mass/scale near the free-streaming scale. This implies that the population of dwarf galaxies in WDM would inhabit haloes with a broader distribution of inner densities with an overall reduced normalization relative to CDM; both of these help with the TBTF problem (Lovell et al., 2012) and the diversity problem in Milky Way galaxies Zavala et al., 2019, Lovell and Zavala, 2023. On the other hand, dark matter self-interactions can redistribute the dark matter in haloes and reduce their central densities, which can significantly alleviate the TBTF problem for allowed SIDM models (Zavala et al., 2013). Furthermore, a velocity-dependent SIDM model with large effective cross section at small scales (low subhalo masses) combined with tidal effects produces a large diversity in the Milky Way satellite population, with some dwarf-size suhaloes predicted to be cored, while others are expected to be very dense driven by the phenomenon of gravothermal collapse (Zavala et al., 2019, Nadler et al., 2023, Correa, 2021, Kahlhoefer et al., 2019, Kaplinghat et al., 2019, Sameie et al., 2020, Yang et al., 2023a). A similar diversity in cores and cusps can be achieved for more massive dwarf galaxies in the field, enhancing the diversity of rotation curves (Creasey et al., 2017, Correa et al., 2022). The role of SIDM in the diversity of the Milky Way satellite population is a significant component of this Thesis (Meshveliani et al., 2023).

1.6 Context and outline of the Thesis

Observational context: dwarf galaxies. Advancements in observations of dwarf galaxies have provided opportunities to better understand the nature of dark matter. The census of ultra-faint satellite galaxies in the Local Group has been significantly enhanced in recent years through optical imaging surveys, such as the Dark Energy Survey (Dark Energy Survey Collaboration, 2016, Bechtol et al., 2015, Drlica-Wagner et al., 2015, 2020), the Panoramic Survey Telescope and the Rapid Response System (Laevens et al., 2015a,b) and others

(Torrealba et al., 2016a, 2019a). In the nearby Universe, the Legacy Survey of Space and Time (Ivezić et al., 2019) at the Vera Rubin Observatory has the potential to greatly enhance our knowledge of faint dwarf galaxies, as this survey is capable of detecting galaxies that are one hundred times fainter and at the same distance (Bullock and Boylan-Kolchin, 2017a) as those detected by the Sloan Digital Sky Survey (York and SDSS Collaboration, 2000). On the other hand, the Dark Energy Camera (Flaugher et al., 2015) and Subaru (Hyper) Suprime-Cam (Miyazaki et al., 2018) are being used to search for faint companions of nearby galaxies as well as the LSBs and ultra-diffuse dwarf galaxies in a cluster environment (Koda et al., 2015, Eigenthaler et al., 2018, van Dokkum et al., 2015). On the other hand, HI observations will also extend the survey of gas-rich galaxies in the nearby Universe currently set by the ALFALFA survey (Oman, 2022) into even lower-mass systems and in bigger volumes (e.g. WALLABY Koribalski et al., 2020). Ongoing surveys, like DELVE (Drlica-Wagner et al., 2021, 2022) and UNIONS (Ibata et al., 2017), continue to expand our knowledge of Milky Way satellite dwarf galaxies (Mau et al., 2020, Cer, Cerny and Delve Collaboration, 2023a,b, Smith et al., 2023). The Gaia space telescope (Gaia Collaboration et al., 2016, 2021) has revolutionized our understanding by providing proper motion measurements, which constrain the characterization and discovery of dwarf galaxies (e.g., Torrealba et al., 2019a, Pace and Li, 2019, McConnachie and Venn, 2020a,b) and globular clusters (e.g., Torrealba et al., 2019b, Pace et al., 2023. Expanding the census of Local Group galaxies will constitute a stringent test on dark matter models where the abundance of haloes is, e.g. allowing for more detailed/refined comparisons between CDM and WDM.

The measured structural and dynamical properties of nearby dwarf galaxies with resolved stellar populations play a key role in understanding the structural CDM challenges: core-cusp, TBTF and diversity. On the one hand, for field dwarf galaxies in the Local Universe, radio observations have reported the HI rotation curves and mass models of 160 massive late-type disky dwarfs (Lelli et al., 2016, Oh et al., 2011, 2015, Ott et al., 2012). Other recent compilations are extending the census of rotation curves in nearby galaxies (see PROBES catalogue Frosst et al., 2022). The detection of HI in UFDS, even in small amounts, can have a significant impact in characterizing the inner gravitational potential in the smallest dwarf-size haloes. Rotation curve analysis is possible if HI can be used as a tracer. This would be a relevant advance since baryonic physics plays a diminishing role in the structure of haloes with ever-low mass (Rey et al., 2024). WALLABY and the Five-hundred-meter Aperture Spherical radio Telescope (Kang et al., 2022) are expected to provide several new candidates for HI-rich, low-mass dwarfs. Additionally, there has been an increase in the detection of such objects, especially in sensitive hydrogen surveys that are cross-matched with deep imaging like MHONGOOSE and MIGHTEE on MeerKAT. Even though these new catalogues and detections may not have the necessary angular and spectral resolution to obtain reliable hydrogen kinematics, they will be very useful in identifying the most promising targets for high-quality rotation curve follow-ups with deep interferometry from VLA and MeerKAT (de Blok et al., 2020, Maddox et al., 2021).

Finally, spectroscopic follow-ups of the galaxies that will be discovered with LSST might yield line-of-sight velocity measurements for a fraction of them, while the next generation of Extremely Large Telescopes (such as ESO's ELT) will extend this coverage (Drlica-Wagner et al., 2019). This will make it possible to study stellar kinematics, which can be used to constrain the inner dark matter densities. Furthermore, precise stellar proper motions for Milky Way satellites using spectroscopy and high-precision astrometry based on the next

generation of ELTs promise to give definitive answers on the inner dark matter densities in MW satellites (Simon et al., 2019). With these advancements, it is now the opportune moment to generate testable predictions from different dark matter models.

Theoretical context: SIDM. SIDM is an important category of competing dark matter models that have been proposed and discussed in the literature for about three decades (Spergel and Steinhardt, 2000). It is well motivated by hidden dark sectors as extensions to the Standard Model (Feng et al., 2009, Loeb and Weiner, 2011, Tulin et al., 2013), in addition to potentially solving some of the CDM small-scale problems Tulin and Yu, 2018, Adhikari et al., 2022. Dark matter self-interactions of $\sim 1\mathrm{cm}^2\mathrm{g}^{-1}$ enable effective heat conduction and could result in an isothermal distribution of dark matter with cores at halo centres, which alleviates the core-cusp problem, and the TBTF problem (Vogelsberger et al., 2012a, Rocha et al., 2013, Zavala et al., 2013, Elbert et al., 2015). In addition, SIDM with comparable cross sections also has the potential to explain the diversity of rotation curves of dwarf galaxies (Kamada et al., 2017, Sameie et al., 2020, Creasey et al., 2017). Constraints on SIDM based on studies at larger scales, particularly focusing on the morphology of elliptical galaxies (Peter et al., 2013 and more recently Despali et al., 2019) and galaxy clusters (Kaplinghat et al., 2016, Elbert et al., 2018, Robertson et al., 2017, 2018 have suggested limits on the cross section that are to close, or even below the $\sim 1\mathrm{cm}^2\mathrm{g}^{-1}$ value needed for SIDM to be a distinct alternative to CDM.

The gravothermal collapse of SIDM haloes. The context described above has strengthened the need for SIDM models with strong velocity-dependence. Furthermore, larger cross sections, $\gtrsim 10\mathrm{cm}^2\mathrm{g}^{-1}$, are required in order to trigger the gravothermal collapse phase at the scale of the Milky Way satellites (Zeng et al., 2022, Silverman et al., 2022). This disfavours SIDM models with a constant cross section where the acceleration of core-collapse due to tidal effects was invoked in order to make them remain viable (Nishikawa et al., 2020). Therefore, SIDM models with a strong velocity-dependence and large cross section at the scale of Milky Way satellites offer a promising explanation of the diversity of halo profile shapes, as demonstrated in analytical works as well as in N-body simulations (Nadler et al., 2023, Sameie et al., 2020, Turner et al., 2021, Zavala et al., 2019, Kahlhoefer et al., 2019). The previous context makes it necessary to quantify in detail the parameter space of SIDM models where the diversity is possible and to find specific signatures of gravothermal collapse, distinct from baryonic solutions to the diversity problem. In Meshveliani et al., 2023, we studied the gravothermal collapse phase in SIDM haloes and estimated the timescales and mass scales of collapse-driven black holes. Gravothermal collapse formalism in detail is presented in Sec. 2.2, while in Chapter 3.2, I present the result of this study, one of the main works of this Thesis.

The gravothermal collapse of SIDM haloes: impact on baryons. In Chapter 4, we extend the analysis to study the impact of the core collapse of SIDM haloes in the assembly and dynamics of the baryonic galaxy. This project is ongoing and presented here in its preliminary stage. We study how stars, modelled as a population of point collisionless tracers, respond dynamically to the gravothermal collapse phase. It has been shown that stellar orbits exhibit distinct responses to different cusp-core transformation mechanisms (e.g. SIDM cores formed adiabatically vs supernova-driven cores formed impulsively, then observables can be used to constrain these mechanisms and thus indirectly put constraints on DM/baryonic physics (Burger et al., 2022). We are looking to extend these ideas to the core-collapse phase in dwarf-size haloes where the potential is dominated by DM, and the collapse itself is unperturbed

from the presence of baryons. The ultimate goal is to identify the unique signature of the SIDM core-collapse in the dynamics of stars. In our first results, we proved that stellar orbits should respond adiabatically to the core-collapse of dwarf-size SIDM haloes. Using this approximation, we can estimate how a stellar distribution would evolve as the gravitational potential evolves in time using adiabatic invariants. The project concentrates on central compact star clusters (e.g. globular clusters) as a good target to either search for signatures of the gravothermal collapse or indirectly constrain the cross section of SIDM models.

Theoretical context: (sub)halo abundance and environment in WDM. The efficiency of galaxy formation is greatly influenced by the surrounding environment (Maulbetsch et al., 2007, Hellwing et al., 2021). Perturbations located in larger-scale overdense regions, such as galaxy clusters, experience earlier collapse times due to the presence of stacked perturbations, while those situated in underdense regions (at large scales), like cosmic voids, undergo delayed collapse. Consequently, the interplay between the large-scale structure of the universe and the properties of dark matter significantly influences the timing and efficiency of halo formation across cosmic environments. As we mentioned in sec. 1.4.2, the suppression of small-scale perturbations due to the cutoff in the primordial power spectrum in WDM models also impacts the formation and properties of WDM haloes close to the cutoff scale. The specific WDM model we study is characterized by the resonantly produced sterile neutrino, which is well motivated by particle physics, as it can potentially explain baryogenesis and neutrino flavour oscillations (Asaka and Shaposhnikov, 2005, Boyarsky et al., 2009). Several studies have reported constraints on corresponding thermal-relic WDM (Schneider, 2016, Cherry and Horiuchi, 2017, Iršič et al., 2017, 2024, Hsueh et al., 2020, Gilman et al., 2020, Banik et al., 2021, Nadler and DES Collaboration, 2021, Nadler et al., 2021a, Enzi et al., 2021, Newton et al., 2021, Zelko et al., 2022, Villasenor et al., 2023). However, these constraints suggest that a 3.55 keV line sterile neutrino model to be compatible with observations, particularly the inferred number of MW satellite galaxies, should be, in the allowed range of the half-mode mass, $2.5 \times 10^7 < M_{\rm hm} < 8.5 \times 10^8\,{\rm M}_\odot$ (Lovell, 2023a). It is in this context that in Chapter 5 we study the connection between the local environment and halo abundance in CDM and WDM models. Currently allowed WDM models have a cutoff scale roughly corresponding to the scale of dwarf galaxies, and therefore, the abundance and properties of dwarf-size haloes and the galaxies they host are distinct relative to CDM. In Section 5, I present Paper II of this Thesis, where we use hydrodynamical cosmological simulations that include a full modelling of baryonic physics to study the WDM model and its impact on the abundance of haloes and galaxies.

2 Self-interacting Dark Matter

2.1 SIDM particle models and the transfer cross section

Self-interacting dark matter (SIDM) is well motivated by *hidden dark sectors* as extensions to the Standard Model (SM) (Spergel and Steinhardt, 2000, Loeb and Weiner, 2011, Tulin et al., 2013, Feng et al., 2009, Tulin and Yu, 2018). It could be composed of one or more particles that may interact with each other through new interactions in a hidden sector. Among the most well-studied models of SIDM postulates that these new interactions are mediated by a light mass mediator (massive hidden/dark photon), typically in the mass range of $1 - 100$MeV (Kaplinghat et al., 2014, Smolinsky and Tanedo, 2017). A simple model with a light mediator can be described by a vector boson where dark matter particles are charged under a spontaneously broken U(1) symmetry and interact through gauge boson exchange or a scalar boson that mediates self-scattering between dark matter particles. These interactions can be represented as follows:

$$\mathcal{L}_{\rm int} = \begin{cases} g_\chi \bar{\chi}\gamma^\mu \chi \phi_\mu & \text{(vector mediator)} \\ g_\chi \bar{\chi}\chi\phi & \text{(scalar mediator)}\,, \end{cases} \tag{12}$$

where χ is the dark matter particle (assumed to be a fermion), γ^μ is the gamma matrix, ϕ is the mediator, and g_χ is the coupling constant. In the non-relativistic limit (applicable for the regime of cosmological structure formation we are interested in), self-interactions are described by the Yukawa potential

$$V(r) = \pm \frac{\alpha_\chi}{r} e^{-m_\phi r}. \tag{13}$$

The model parameters are the *dark* fine structure constant $\alpha_\chi \equiv g_\chi^2/4\pi$, the mediator mass m_ϕ, and the dark matter mass m_χ. The $+(-)$ sign indicates that the interactions are attractive (repulsive); (for a scalar mediator, the potential can only be attractive). Although this particle physics model has a rich phenomenology, we restrict it to the simplest kind of interactions between dark matter particles, that is, elastic self-scattering. The relevant quantity to characterize this interaction is then the cross section, in its differential form $d\sigma/d\Omega$ (where Ω is the solid angle), if one is interested in preserving/studying angular dependence, or in its integral form if isotropic scattering is assumed; the latter is the case we study in this Thesis. Since we are ultimately interested in capturing the effects of self-scattering in the macroscopic properties of the dark matter halo, it is appropriate to refer to an integral cross section that is relevant for heat conduction. For this purpose, it is common to use the transfer cross section:

$$\sigma_T = 2\pi \int_0^\pi \frac{d\sigma}{d\Omega} \left(1 - \cos\theta\right) \sin\theta d\theta \tag{14}$$

where θ is the scattering angle in the center of mass frame. This definition helps suppress small-angle scatterings, which would contribute heavily to the total cross section but that do

not physically contribute significantly to heat conduction. Another cross section commonly used is the viscosity cross section, but in the isotropic scattering limit, it is of the same order as the transfer cross section, which is the one used here (Tulin and Yu, 2018).

There are two widely used formulas in the literature for the transfer cross section. The first is an analytic formula based on the Born approximation (perturbative limit when $\alpha_\chi m_\chi / m_\phi \ll 1$) and is given by (Feng et al., 2010):

$$\sigma_T^{\rm Born} = \frac{8\pi\alpha_\chi^2}{m_\chi^2 v^4}\left[\log(1+R^2) - R^2/(1+R^2))\right], \tag{15}$$

where $R = m_\chi v / m_\phi$ with v being the relative velocity between dark matter particles. In the classical regime, where quantum effects are not relevant and the de Broglie wavelength is much shorter than the characteristic range of the interaction $\sim m_\phi^{-1}$, i.e. $R \gg 1$, elastic scattering through a massive mediator is equivalent to screened Coulomb scattering in a plasma (Khrapak et al., 2003). A good empirical fit to the transfer cross section in these conditions has been found to be given by (e.g. Loeb and Weiner, 2011):

$$\frac{\sigma_{\rm T}}{\sigma_{\rm T}^{\rm max}} \approx \begin{cases} \dfrac{4\pi}{22.7}\beta^2 \ln\left(1+\beta^{-1}\right), & \beta < 0.1 \\ \dfrac{8\pi}{22.7}\beta^2 \left(1+1.5\beta^{1.65}\right)^{-1}, & 0.1 < \beta < 10^3 \\ \dfrac{\pi}{22.7}\left(\ln\beta + 1 - 0.5\ln^{-1}\beta\right)^2, & \beta > 10^3, \end{cases} \tag{16}$$

where $\sigma_{\rm T}^{\rm max} = 22.7/m_\phi^2$ and β is the ratio of the potential energy at the scale characteristic range of the interaction, to the kinetic energy of the dark matter particle:

$$\beta = \frac{\pi v_{\rm max}^2}{v^2} = \frac{2\,\alpha_\chi\, m_\phi}{m_\chi v^2}, \tag{17}$$

where $v_{\rm max}$ is the velocity at which $(\sigma_{\rm T} v)$ peaks at a transfer cross section equal to $\sigma_{\rm T}^{\rm max}$. The functional form of the scattering cross section governed by Yukawa potential, Eq. 16, ensures that the scattering rate decreases rapidly for velocities larger than $v_{\rm max}$. Therefore, the choice of $v_{\rm max}$ essentially sets the circular velocity scale (and hence the mass/distance scale) at which the self-interactions become important. This formula can then be used to naturally satisfy the astrophysical requirement of SIDM to be close to collisionless (i.e. close to CDM) at large velocities/scales while being significantly collisional at smaller scales, particularly at the scale of galaxies where deviations from CDM are crucial for SIDM to present viable solutions to the CDM challenges at the scale of dwarf galaxies.

2.2 Gravothermal evolution of SIDM haloes

The gravothermal fluid formalism was initially introduced to study compact self-gravitating stellar systems, such as globular clusters where (gravitational) scattering between stars plays an important role (Lynden-Bell and Wood, 1968a, Lynden-Bell and Eggleton, 1980). The formalism was later adapted to isolated SIDM haloes where the gravitational two-body scattering of stars is replaced by the two-body contact interactions between SIDM particles

(Balberg et al., 2002, Balberg and Shapiro, 2002). A finite self-gravitating system has negative specific heat in the inner region and positive specific heat in the outskirts (for example, the inner and outer regions of a globular cluster, respectively). This results in a redistribution of mass and energy from the (hotter) centre towards the (colder) outskirts where the "heat conduction" is driven by two-body scattering of stars. If the outskirts is effectively a large reservoir with very high specific heat, the heat transfer from the centre outwards can never increase the temperature of the outskirts to that in the centre, and thus, equilibrium cannot be reached with the centre shrinking and becoming ever hotter. This phenomenon is called gravothermal catastrophe since the thermodynamic description breaks down once the densities and velocities diverge in the centre. In the case of globular clusters, this runaway instability of the central core stops since, in close proximity, stars can form bound binaries, which then act as an energy sink. For SIDM haloes, the evolution is analogous with self-scattering driving the heat conduction, but in this case, the formation of bound systems is not possible, and the collapse of the core continuous until a black hole is eventually formed.

The gravothermal fluid model contains the following Newtonian fluid conduction equations, which describe the behaviour of an isolated spherically symmetric halo, initially in equilibrium (Lynden-Bell and Eggleton, 1980, Balberg and Shapiro, 2002, Pollack et al., 2015, Koda and Shapiro, 2011, Shapiro, 2018):

$$\text{Mass Conservation} : \frac{\partial M}{\partial r} = 4\pi r^2 \rho \tag{18}$$

$$\text{Hydrostatic Equilibrium} : \frac{\partial \left(\rho \sigma_{\rm vel}^2\right)}{\partial r} = -\frac{GM\rho}{r^2} \tag{19}$$

$$\text{Heat Flux/Fourier's Law} : \frac{L}{4\pi r^2} = -\kappa \frac{\partial T}{\partial r} \tag{20}$$

$$\text{The first law of Thermodynamics} : \frac{\partial L}{\partial r} = -4\pi r^2 \sigma^2 \frac{D}{Dt}\left[\ln\left(\frac{\sigma_{\rm vel}^3}{\rho}\right)\right] \tag{21}$$

where $\rho,\ M,\ L$ and $\sigma_{\rm vel}$ represent the halo's density, the enclosed mass, luminosity, and one-dimensional velocity dispersion, respectively, and the dark matter temperature is given by $T = m_\chi \sigma_{\rm vel}^2(r)/k_{\rm B}$. The heat conductivity term, κ, which relates the luminosity to the temperature gradient, is where the physical mechanism of heat conduction is introduced, whether it is two-body gravitational scattering or dark matter self-interactions.

For the SIDM case, It is not possible to derive analytically the effective thermal conductivity since there are two relevant characteristic lengths/timescales across different regions of the halo, and their relative importance changes as the halo evolves. The two scales are the mean free path due to self-scattering $\lambda = 1/(\rho\sigma_T/m_\chi)$ and the gravitational (Jeans) scale $H = \sqrt{\sigma_{\rm vel}^2/(4\pi G)}$. In the short mean free path (SMFP) regime, $\lambda \ll H$, collisions are very relevant and transport theory can be used to estimate κ, while in the long mean free path (LMFP) regime, $\lambda \gg H$, the behaviour is nearly collisionless, and gravity is the dominant interaction, one can then use the analogy with globular clusters and use the results by Lynden-Bell and Eggleton, 1980. In order to capture the whole evolution and the transitions between the LMFP and SMFP regimes as the halo evolves, a semi-empirical relation must be used to

interpolate between both regimes. In the fluid approximation where heat conduction is due to thermal redistribution of energy and mass due collisions between gas particles, the kinetic theory of gases provides a formula for the heat conductivity:

$$\kappa_{\rm SMFP} \propto \frac{n\lambda^2 k_{\rm B}}{t_r} \tag{22}$$

where the numerical constant of proportionality is given by transport theory (Balberg and Shapiro, 2002) so that $\kappa_{\rm SMFP} = 2.1\sigma_{\rm vel}k_{\rm B}/\sigma_T$. Here, $n = \rho/m_\chi$ is the local dark matter particle number density, and $t_r = \lambda/\sigma_{\rm vel}$ is the relaxation time. In low-density and low-cross section gravothermal systems, where particles orbit several times before colliding with each other, we need to replace the mean free path λ with the Jeans' scale height H:

$$\kappa_{\rm LMFP} \propto \frac{nH^2 k_{\rm B}}{t_r} \tag{23}$$

In this case, the constant of proportionality cannot be found using transport theory; instead, it is conventional to write $\kappa_{\rm LMFP} = (3/2)C(nH^2k_{\rm B})/t_{\rm r} = 0.27Cn\sigma_{\rm vel}\sigma_T k_{\rm B}/({\rm G}m_\chi)$, where C is an adjustable parameter derived from interpolating the conductivity between the SMFP and LMFP regimes and calibrating to SIDM N-body simulations (Koda and Shapiro, 2011, Pollack et al., 2015, Nishikawa et al., 2020, Outmezguine et al., 2022, Yang et al., 2024, Essig et al., 2019). Based on previous studies, this parameter has a plausible range between $0.4 - 0.75$, indicating a strong similarity to the transport equation. The thermal conductivity that is then used in the gravothermal fluid model (Eq. 20) is an interpolation between Eqs. 22 and 23, which is done in reciprocal to ensure the correct behaviour in the limiting cases: $\kappa^{-1} = \kappa^{-1}_{\rm SMFP} + \kappa^{-1}_{\rm LMFP}$.

All SIDM haloes are expected to begin their evolution in the LMFP regime, and then the central regions transition to the intermediate regime $\lambda \gtrsim H$ as the cusp transforms into a core. This region spends the majority of their time in this intermediate regime, while the outskirts remain firmly in the LMFP regime. Once the gravothermal catastrophe is triggered, the centre collapses, and eventually, it reaches the SMFP at the very late stages of the collapse. We can divide a halo undergoing gravothermal collapse into two regions: the outer halo and the central core. As gravothermal evolution progresses, the core contracts and heats up, becoming denser and hotter. This causes dark matter self-interactions to transport heat and mass to the outer halo. The outer halo surrounding the core remains relatively dilute and acts as a heat sink. The thermal evolution timescale of the outer halo is much longer than that of the core, so the outer halo changes temperature very slowly while the core temperature increases rapidly. The outer halo remains in the LMFP regime, while the core begins in the LMFP regime, then moves to the intermediate regime (during the isothermal core phase) and then eventually reaches the SMFP regime in the very last stages of the core collapse. The evolution of the two regimes differs substantially.

In the LMFP regime, dark matter particles are dilute enough to make many orbits before scattering. While the outer halo is always in the LMFP regime, the very central region transitions from the LMFP, the intermediate regime and eventually the SMFP regime, although the more extended cored region might not reach the SMFP regime.

During the core formation phase, the cores of haloes evolve increasingly farther from the LMFP regime into the intermediate regime ($\lambda \gtrsim H$), where they spend most of the time of

their evolution. Initially, heat is transferred inward from the hotter outer halo to the colder inner core, causing the core to expand until it reaches a maximum size, which is limited by the peak in the velocity dispersion (temperature) profile of the halo, roughly occurring at the scale radius. Then, the core starts transferring heat and mass to the outer (colder) halo and shrinks, becoming denser and hotter. This runaway (gravothermal catastrophe) process inevitably drives the core ever closer to the SMFP regime, with the inner region of the core shrinking and drastically increasing in density (Gad-Nasr et al., 2023).

In the SMFP regime, particles are so dense that collisions are extremely frequent. The dense core interferes with the heat and mass transfer from the core to the outer halo, which, in effect, separates the evolution of the SMFP core from the outer regions; the core can then be treated approximately independently. Shortly after this transition, the core falls into a phase of constant thermal energy, rapidly heating up and increasing in density by several orders of magnitude.

The thermal evolution timescale of the dense core is much shorter than that of the extended halo, which acts as a static heat sink. As the core evolves, it shrinks in size and mass, but its density and temperature increase. When the temperature increases, more heat is transferred to the halo. This heat loss in the core results in DM particles moving to the tightly bound orbits and causing thermal instability on a collisional relaxation timescale. With the assumption that the dynamical instability occurs when the particle velocities in the core, or central potential, become relativistic, this instability signals the end of the epoch of gravothermal contraction and leads to the collapse of a finite mass core, ultimately resulting in the formation of a black hole.

Recent studies of the gravothermal fluid model have been extended to velocity-dependent cross sections (Gad-Nasr et al., 2023, Outmezguine et al., 2022, Yang and Yu, 2022, Yang et al., 2023b). The gravothermal equations admit an approximate universality In the LMFP regime, which can be transformed into a velocity-independent model with an appropriate averaging (Outmezguine et al., 2022). This has also been shown in idealized N-body simulations (Yang and Yu, 2022). There is also the universality in the deep SMFP core-collapse regime, but it is argued that the intermediate regime needs more careful treatment (Gad-Nasr et al., 2023). However, further work with idealized and cosmological N-body simulations is required to study this intermediate regime and potentially simplify it.

3 Gravothermal collapse of SIDM Dark Matter halos

This chapter is based on the following article:

Gravothermal collapse of Self-Interacting Dark Matter halos as the Origin of Intermediate Mass Black Holes in Milky Way satellites

Published in Phys. Rev. D 107, 083010 – 6 April 2023

Authors:

Tamar Meshveliani[1], Jesús Zavala[1], Mark R. Lovell[1]

[1] Centre for Astrophysics and Cosmology, Science Institute, University of Iceland, Dunhagi 5, 107 Reykjavik, Iceland

Abstract

Milky Way (MW) satellites exhibit a diverse range of internal kinematics, reflecting in turn a diverse set of subhalo density profiles. These profiles include large cores and dense cusps, which any successful dark matter model must explain simultaneously. A plausible driver of such diversity is self-interactions between dark matter particles (SIDM) if the cross section passes the threshold for the gravothermal collapse phase at the characteristic velocities of the MW satellites. In this case, some of the satellites are expected to be hosted by subhalos that are still in the classical SIDM core phase, while those in the collapse phase would have cuspy inner profiles, with a SIDM-driven intermediate mass black hole (IMBH) in the centre as a consequence of the runaway collapse. We develop an analytical framework that takes into account the cosmological assembly of halos and is calibrated to previous simulations; we then predict the timescales and mass scales ($M_{\rm BH}$) for the formation of IMBHs in velocity-dependent SIDM (vdSIDM) models as a function of the present-day halo mass, M_0. Finally, we estimate the region in the parameter space of the effective cross section and M_0 for a subclass of vdSIDM models that result in a diverse MW satellite population, as well as their corresponding fraction of SIDM-collapsed halos and those halos' inferred IMBH masses. We predict the latter to be in the range $0.1 - 1000$ M$_\odot$ with a $M_{\rm BH} - M_0$ relation that has a similar slope, but lower normalization, than the extrapolated empirical relation of super-massive black holes found in massive galaxies.

3.1 Introduction

The cold dark matter (CDM) model is highly successful at explaining observations of the large-scale structure of the Universe (e.g. Springel et al., 2005b). However, it has challenges in matching

observations on small scales, such as in the regime of dwarf galaxies (for a recent review see e.g Bullock and Boylan-Kolchin, 2017b). Observationally, these challenges have been established prominently for dwarf galaxies in the Local Group, and particularly within the Milky Way (MW) satellites. For instance, the dynamical mass is dominated by dark matter (DM) in the inner region of several bright MW satellites, yet is low compared to the inner densities of the plausible subhalo hosts of MW-analogues found in collisionless CDM simulations; this is the *classical* too-big-to-fail (TBTF) problem (Boylan-Kolchin et al., 2011, 2012). Another recurrent challenge is that several of the MW satellites are best explained by density profiles of constant density, known as "cored" density profiles, rather than the steep inner density slope found in CDM simulations, referred to as "cuspy" profiles; satellites that are reported to have cored profiles include Fornax, Sculptor, Crater II and Antlia II (Walker and Peñarrubia, 2011b, Agnello and Evans, 2012, Breddels et al., 2013, Torrealba et al., 2016b, 2019a). Overall, it is now well established that the MW satellites have a diverse range of internal kinematics, which is likely associated with a subhalo population that exhibits a considerable diversity of inner density profiles, from large cores to dense cuspy systems (Fattahi et al., 2018, Errani et al., 2018, Read et al., 2019, Zavala et al., 2019, Kaplinghat et al., 2019). This diversity is analogous to that of rotation curves observed in higher mass, gas-rich dwarf galaxies (Oman et al., 2015, Santos-Santos et al., 2020).

It is important to emphasize that such dwarf-scale challenges are only insurmountable within CDM if no other physical mechanisms related to gas/stellar (*baryonic*) physics are considered. There are in fact several baryonic processes that are known to exist that can alleviate these challenges. For instance, supernova feedback can inject energy into the inner DM halo, reducing its density (Navarro et al., 1996b). If impulsive enough, this is an efficient and irreversible cusp-core transformation mechanism in dwarf galaxies (Pontzen and Governato, 2012, Burger and Zavala, 2019, 2021). In addition, tidal forces on the satellite by the MW DM halo and the MW disk can effectively lower the densities of MW subhalos if their orbits pass sufficiently close to the disk (Zolotov et al., 2012). The diverse orbits of the MW satellites combined with this effect enhance the diversity of inner DM densities relative to the CDM-only expectations (Garrison-Kimmel et al., 2019a). However, how efficient these processes are in creating the observed diversity of the MW satellite population remains uncertain since, for example, the impact of supernova feedback is expected to be small in very faint DM-dominated systems with low stellar-mass ratios (Di Cintio et al., 2014a). On the other hand, it has been argued that the tidal field of the MW system might not be strong enough to explain the extremely low densities of bright satellites such as Crater II and Antlia II (Errani et al., 2022, Lovell and Zavala, 2023).

One exciting possibility is that the properties of the MW satellites provide clues about the DM nature beyond CDM. In particular, if DM particles have strong self-interactions, they can impact the non-linear evolution of halos, significantly reducing their inner densities (Spergel and Steinhardt, 2000). Modified N-body simulations that incorporate self-interacting DM (SIDM) have shown that the collisions experienced by DM particles with each other lead to significant momentum exchange. This process effectively transfers heat from the dynamically hot outer regions of the halo to the colder central regions, thus lowering the central density of halos and creating constant (isothermal) density cores (Davé et al., 2001, Colín et al., 2002, Vogelsberger et al., 2012b, Rocha et al., 2013, Dooley et al., 2016, Robles et al., 2019, Tulin and Yu, 2018, Vogelsberger et al., 2019). SIDM models can create sizeable DM cores and alleviate the *classical* TBTF problem if the transfer cross section per unit mass, $\sigma_{\rm T}/m_\chi$, is $\gtrsim 1\ {\rm cm}^2{\rm g}^{-1}$ at the characteristic scales/velocities of MW satellites $\lesssim 50{\rm km/s}$ (Zavala et al., 2013). It is also possible to alleviate significantly the diversity of rotation curves in higher mass dwarf galaxies (characteristic velocities $> 50{\rm km/s}$) if $\sigma_{\rm T}/m_\chi \gtrsim 2-3\ {\rm cm}^2{\rm g}^{-1}$ (Creasey et al., 2017, Ren et al., 2019).

Constant cross section SIDM models have been constrained more strongly at large scales/velocities. Particularly, $\sigma_{\rm T}/m_\chi$ is required to be $\lesssim 0.1-1\ {\rm cm}^2{\rm g}^{-1}$ at the scale of clusters based on gravitational lensing, X-ray morphology, and dynamical analysis in cluster mergers (Robertson et al., 2017, 2019,

Harvey et al., 2019, Andrade et al., 2022, Eckert et al., 2022, Shen et al., 2022). At scales corresponding to massive elliptical galaxies, previous constraints based on X-ray morphology have been shown to be weaker than anticipated by DM-only simulations (Peter et al., 2013) once baryonic effects are included. Current simulations including baryons have shown that $\sigma_{\rm T} m_\chi \sim 1$ cm^{2}g^{-1} is consistent with the morphologies of elliptical galaxies (Despali et al., 2022). With such constraints at larger scales, a constant cross section SIDM model is already only narrowly viable as an alternative to CDM to explain the properties of dwarf galaxies. Recent developments regarding the diversity in the inner densities of the MW satellites virtually rule out this possibility since with such a low cross section, it is not possible to generate very high density satellites such as Willman I (Valli and Yu, 2018, Read et al., 2018, Zavala et al., 2019, Kim and Peter, 2021).

Remarkably, what is needed for SIDM models to remain an interesting, viable alternative to CDM is to have even larger cross sections (> 10 cm^{2}g^{-1}) at the scale of the MW satellites in order to trigger the gravothermal collapse phase (see below). Such large cross sections can be naturally accommodated by particle models with a velocity-dependent cross section (e.g. through Yukawa-like interactions, see e.g. Feng et al., 2009, Buckley and Fox, 2010, Loeb and Weiner, 2011), where DM behaves as a collisional fluid on small scales and is essentially collisionless at cluster scales. Long after the core-formation phase, further DM particle collisions lead to heat outflow from the hotter inner region to the colder outskirts of the halo. Since gravitationally bound systems have negative specific heat, mass/energy is continuously lost from the inner region, while the density and temperature continue to grow in a runaway instability that drives the collapse of the inner core. This phenomenon is known as the gravothermal catastrophe (Lynden-Bell and Wood, 1968a) and is observed in globular clusters, where the collapse is mainly halted by the formation of binary stars, which act as energy sinks (Hut et al., 1992). For SIDM halos, the physical mechanism is the same, but without the formation of bound DM states to act as energy sinks, the collapse continues, eventually reaching a relativistic instability that results in the formation of a black hole (Colín et al., 2002, Balberg et al., 2002, Balberg and Shapiro, 2002, Koda and Shapiro, 2011, Pollack et al., 2015). If the core-collapse phase has been reached at the scales of the MW satellites, then the SIDM predictions become radically different with some of the satellites expected to be hosted by (sub)halos with SIDM cores, while those in the collapse phase would have cuspy (collapsed) inner DM regions (Zavala et al., 2019).

Given the problems with constant cross section SIDM models mentioned above, it has been argued recently that such models could be reconciled with the MW satellite population by suggesting that the collapse phase might be accelerated in the host (sub) halos of MW satellites by mass-loss via tidal stripping (Nishikawa et al., 2020), since mass-loss enhances the negative temperature gradient in the outskirts of the (sub)halo and makes the heat outflow more efficient. Accelerated core-collapse has been invoked to explain the diversity of the MW's dwarf spheroidal galaxies in constant cross section models with $\sigma_{\rm T}/m_\chi \gtrsim 2 - 3$ cm^{2}g^{-1} (Kahlhoefer et al., 2019, Nishikawa et al., 2020, Kaplinghat et al., 2019, Sameie et al., 2020). However, Ref. Zeng et al., 2022 recently simulated SIDM subhalo satellites as they orbit the MW system and found that energy gain due to collisions between particles in the subhalo and the host instead inhibits core-collapse in subhalos.

Another study, Ref. Silverman et al., 2022, showed that subhalos in models with constant cross sections between 1 and 5 cm^{2}g^{-1} are not dense enough to match the densest ultra-faint and classical dwarf spheroidal galaxies in the MW, and 5 cm^{2}g^{-1} is not sufficient to enforce collapse even with the tidal effect of a MW disk and bulge. This seemingly closes the last possibility for velocity-independent SIDM models (see also discussion in Section 3.3.1 below). On the other hand, this result motivates the exploration of velocity-dependent SIDM models, where recent full cosmological simulations with a specific benchmark model (Zavala et al., 2019, Turner et al., 2021) have shown that cross sections $\gtrsim 50$ cm^2/g at velocities $\lesssim 30$ km/s naturally result in a diverse bimodal population of MW satellites, predicting both cuspy, high velocity dispersion subhalos, consistent with dense systems (particularly ultra-faint satellites), and cored, low velocity dispersion subhalos, consistent with brighter low-density

satellites. These results have been confirmed and expanded to generic velocity-dependent SIDM models by the recent cosmological simulation suite TangoSIDM (Correa et al., 2022).

In this work, we adopt the benchmark SIDM model presented in Zavala et al., 2019, Turner et al., 2021 to explore the consequences of gravothermal collapse for the formation of intermediate mass black holes (IMBHs) in the MW satellite population. Our goal is twofold: (i) to compile a simple analytical framework (calibrated to the simulations in Zavala et al., 2019, Turner et al., 2021) that provides predictions for the formation timescales and mass scales of IMBHs in SIDM halos under arbitrary velocity-dependent cross sections, and (ii) to provide the range of IMBH masses that is expected given the plausible range of cross sections that produce a diverse MW satellite population, i.e., a bimodal – core-cusp – satellite distribution.

This paper is organised as follows. In Section 3.2, we describe our model for the evolution of SIDM halos. We start with our adopted primordial halo density profile and the concentration–mass relation, describe our computation of the threshold time for the cusp-core transformation, and finally estimate the timescales and masses of IMBHs expected in the SIDM model due to gravothermal collapse. We also include the impact of tidal stripping. In Section 3.4, we present our results, discuss how they are impacted by the various properties of the model, and put our work in the context of other related studies. Finally, we draw conclusions in Section 3.5.

3.2 Gravothermal collapse in SIDM halos

Our goal in this section is to follow the relevant stages in the evolution of an SIDM halo: i) formation of the progenitor cuspy (i.e. CDM-like) halo, ii) development of the central core and iii) gravothermal collapse of the core and formation of the black hole. In addition, we discuss how tidal stripping might affect the gravothermal collapse timescale.

3.2.1 Cosmic evolution of SIDM halos

In an SIDM halo where thermalization occurs due to close, rare interactions with large momentum transfer, a relaxation time can be defined due to self-scattering at the characteristic radius[1] r_{-2}, which is given by:

$$t_{\rm r} = \frac{\lambda}{a\sigma_{\rm vel}}, \tag{24}$$

where $\sigma_{\rm vel}$ is the characteristic velocity dispersion, $a = \sqrt{16/\pi}$ for hard-sphere scattering of particles with a Maxwell–Boltzmann velocity distribution (Balberg et al., 2002) and $\lambda^{-1} = \rho(r_{-2})\sigma_{\rm T}/m_\chi$ is the mean free path, which is inversely proportional to the local density $\rho(r_{-2})$ and the cross section per unit mass $\sigma_{\rm T}/m_\chi$ (evaluated at the characteristic velocity $\sigma_{\rm vel}$ in the case of velocity-dependent SIDM models). Therefore, the scattering rate (mean free path) is higher (shorter) in denser regions. Within the region where the age of the inner halo is comparable to the relaxation time, self-scattering has a significant impact on the inner DM structure turning the cusp into a core.

In CDM, where DM is collisionless, the velocity dispersion peaks near the scale radius, r_{-2}. By contrast, in SIDM elastic scattering leads to momentum exchange between DM particles, which, given the positive gradient of the velocity dispersion profile within r_{-2}, effectively results in heat transfer from the outside-in, up to the radius where the velocity dispersion peaks. As a result, a central isothermal core is formed, which continues to grow until it is roughly the size of the scale radius and thus reaches a quasi-equilibrium state. After core formation, subsequent collisions lead

[1]From here on in, we assign the characteristic radius to the scale radius of the halo, which for the NFW profile is equal to r_{-2}, the radius at which the logarithm slope of the profile is -2; see Section 3.2.2.

to momentum/energy flow from the center to the outskirts of the halo, where the velocity dispersion profile has a negative slope. Heat loss in the core results in the infall of DM particles to more tightly bound orbits, where they experience more interactions and are heated further due to the negative heat capacity of the self-gravitating system; a similar phenomenon occurs in globular clusters (Lynden-Bell and Wood, 1968b). Without energy sinks, the core suffers a runaway instability, transforming the core into an ever denser cusp, which ultimately results in the formation of a black hole (Balberg et al., 2002).

An SIDM halo undergoes gravothermal collapse in a timescale $t_{\rm coll} \approx 382 t_{\rm r}$, as described in Section 3.3. The relaxation time depends on the halo mass and time of assembly/formation (described in Sections 3.2.2− and 3.2.4) as well as the SIDM cross section at the characteristic velocity of the halo (Section 3.2.5).

3.2.2 Primordial density profile

We assume that in the SIDM cosmology DM assembles into spherical self-gravitating halos in virial equilibrium, with a *primordial* structure that is the same as that of CDM halos. This is a reasonable assumption at sufficiently high redshift when the average number of collisions in the center of halos is still well below one per Hubble time, and thus the structure of the halo has been affected only minimally. Cosmological simulations have shown that DM core sizes are only a small fraction of their value at $z = 0$ when the Universe is around 1 Gyr old ($z \sim 5$), e.g. Vogelsberger et al., 2014.

The spherically averaged density profiles of equilibrium collisionless CDM halos are well approximated by a two-parameter formula known as the Navarro, Frenk & White (NFW) profile (Navarro et al., 1997, 1996a):

$$\rho_{\rm NFW}(r) = \rho_{\rm crit} \frac{\delta_{\rm char}}{r/r_{-2}(1 + r/r_{-2})^2}, \tag{25}$$

where r_{-2} is the radius at which the logarithmic slope of the profile is -2, $\rho_{\rm crit}$ is the critical density of the Universe and the characteristic overdensity $\delta_{\rm char}$ is given by:

$$\delta_{\rm char} = \frac{200}{3} \frac{c^3}{k(c)}, \tag{26}$$

where $k(c) = \ln(1 + c) - c/(1 + c)$ and the concentration c is defined as $c = r_{200}/r_{-2}$ with r_{200} being the virial radius, which is defined in this work as the radius where the mean density of the halo is 200 times $\rho_{\rm crit}$.

3.2.3 Concentration-Mass relation and formation redshift

The NFW profile is to first order a one free parameter profile since the virial mass of the halo and its concentration are strongly correlated, with a 1σ scatter in $\log c$ of order 0.1 (Navarro et al., 1996a, Bullock et al., 2001). We use the concentration-mass relation modeled in Ludlow et al., 2014, 2016, where the authors link the enclosed mass profile of a halo at a given time with the prior mass aggregation history of the halo. In particular, following Ludlow et al., 2016, we can define an *assembly/formation* redshift of a halo of mass M_0 at a redshift z_0 as the redshift z_{-2} when the enclosed mass within r_{-2} at z_0, M_{-2}, was first assembled into progenitors more massive than a certain fraction f of M_0. M_0 is defined as the mass within the virial radius $M_0 = (4\pi/3) r_{200}^3 200 \rho_{\rm crit}$. The virial mass of the halo at z_{-2} is equal to M_{-2} and can be computed from the assembly history:

$$M_{-2} = M_0 \times {\rm erfc}\left(\frac{\delta_{\rm c}(z_{-2}) - \delta_{\rm c}(z_0)}{\sqrt{2(\sigma^2(f \times M) - \sigma^2(M))}} \right), \tag{27}$$

The expression in parentheses on the right hand side corresponds to the collapsed mass fraction in Extended Press-Schechter theory (Lacey and Cole, 1993), where $\delta_{\rm c}(z_{-2}) = \delta_{\rm c}/D(z)$ is the redshift

dependent critical density for collapse with the linear growth factor $D(z)$, and $\sigma(M)$ being the rms mass variance. For the NFW profile, the mass is connected to the concentration by:

$$\frac{M_{-2}}{M_0} = \frac{k(1)}{k(c)}, \tag{28}$$

$$\frac{\langle \rho_{-2} \rangle}{\rho_{\rm crit}(z_{-2})} = 200 c^3 \frac{k(1)}{k(c)}. \tag{29}$$

The key assumption in the model is that the mean density inside r_{-2} is directly proportional to the critical density of the Universe at an assembly redshift z_{-2}:

$$\frac{\langle \rho_{-2} \rangle}{\rho_{\rm crit}(z_{-2})} = C \left(\frac{H(z_{-2})}{H(z_0)} \right)^2, \tag{30}$$

where C is a free parameter. Throughout this paper we use $f = 0.02$ and $C = 575$ Bohr et al., 2021. Inserting Eqs. 28−29 into Eq. 27, we have a transcendental equation for the formation redshift $z_{\rm form} = z_{-2}$ as a function of M_0, which can then be used to obtain the concentration c.

3.2.4 Threshold time for the cusp-core transformation

As a benchmark case, we set the halo formation time z_{-2} of an SIDM halo extant at the present day to be the threshold epoch at which the cusp-core transformation begins, $z_{\rm cc} = z_{\rm form} = z_{-2}$. At this epoch, we assume that the SIDM halo has an NFW profile with a virial mass equal to the enclosed mass within r_{-2} at $z_0 = 0$, $M(z_{-2}) = M_{-2}|_{z_0}$. The concentration of this *primordial* SIDM halo is calculated by repeating the method described in Section 3.2.3, but this time setting $z_0 = z_{-2}$. The range of z_{-2} values for the range of present-day halo masses that we are interested in, $10^8 \leq M_0 \leq 10^{12} M_\odot$, is given by $6.1 \geq z_{-2} \geq 3$. As we noticed earlier, given this relatively high redshift range, our choice of setting $z_{\rm cc} = z_{-2}$ is reasonable because the effect of collisions in the inner halo is minimal at early times.

The next step is to develop a method to calculate the relevant timescale for gravothermal collapse (Section 3.3), for which we build a simplified model in which the evolutionary stages of the SIDM halo occur in isolation. This approach is somewhat different to the full cosmological setting, where halo mergers are an active mechanism of halo growth with transitory stages that affect the inner centre of the halo. Although the cuspy NFW profile of CDM halos is resilient to merger activity e.g. Kazantzidis et al., 2006, the situation might in principle be more complex in an SIDM scenario with gravothermal collapse for the following reason. In the standard SIDM model without core-collapse, the merger between a small halo with a larger one is that of two shallow (core-like) profiles with the smaller one having progressed further in its core development since it forms earlier; the result of this merger is a DM profile that is also cored (Boylan-Kolchin and Ma, 2004). Thus, we would naively expect that halo mergers will not delay the cusp-core transformation. However, cosmological mass infall in general might delay the core-collapse phase by pumping energy into the central region to stabilize the core (Ahn and Shapiro, 2005). Moreover, in a velocity-dependent SIDM halo with a sharp difference between the cross section of low-mass halos to that of large mass halos, the former are expected to go through the cusp-core-collapse stages much faster than the latter, resulting in a scenario in which mergers between low-mass core-collapsed (cuspy) halos and high-mass cored halos are possible. This has the potential to delay the core-collapse phase.

Since our goal is to provide a simple, first-order estimate for the black hole formation time, rather than a comprehensive calculation, we assume that in a relatively extreme scenario, a significant merger would reset the clock for the cusp-core-collapse stage. For this event we adopt the last major merger (LMM), which we define as a mass ratio of 10:1 or higher between the two merging halos, and we label the corresponding redshift as $z_{\rm LMM}$. In order to calculate $z_{\rm LMM}$, we use the fitting formula for

the mean merger rate $dN_{\rm m}/d\xi/dz$ – in units of mergers per halo per unit redshift per unit of mass ratio ξ – for a halo of mass $M(z)$ at redshift z obtained from the combined Millennium and Millennium II data sets in Fakhouri et al., 2010:

$$\frac{dN_{\rm m}}{d\xi dz}(M(z),\xi,z) = A\left(\frac{M(z)}{10^{12}{\rm M}_\odot}\right)^{\alpha}\xi^{\beta}\exp\left[\left(\frac{\xi}{\tilde{\xi}}\right)^{\gamma}\right]\times(1+z)^{\eta}, \tag{31}$$

where the best-fit parameters are $(\alpha,\beta,\gamma,\eta) = (0.133,-1.995,0.263,0.0993)$ and $(A,\tilde{\xi}) = (0.0104, 9.72\times 10^{-3})$. The mass $M(z)$ is given by integrating the mean mass growth rate of halos, taken from Fakhouri et al., 2010:

$$\frac{dM}{dt} = \left\langle \dot{M}\right\rangle_{\rm mean} = 46.1{\rm M}_\odot{\rm yr}^{-1}\left(\frac{\rm M}{10^{12}{\rm M}_\odot}\right)^{1.1} \times(1+1.11z)\sqrt{\Omega_{\rm m}(1+z)^3+\Omega_\Lambda}. \tag{32}$$

where Ω_m and Ω_Λ are, respectively, the DM and dark energy density parameters evaluated at the present day.

The cumulative number of mergers $N_{\rm m}(\xi_{\rm min}, M_0, z_0, z)$ for a halo of mass M_0 at redshift z_0 is then given by:

$$N_{\rm m}(\xi_{\rm min}, M_0, z_0, z) = \int_{z_0}^{z} dz \int_{\xi_{\rm min}}^{1} d\xi \frac{dN_{\rm m}}{d\xi dz}[M(z),\xi,z]. \tag{33}$$

where we use the minimum mass ratio for a major merger to be $\xi_{\rm min} = 0.1$. When the above equation equals to 1, meaning that the halo experienced one major merger event, we find the corresponding $z_{\rm LMM}$ for given halo of mass M_0; we therefore only consider the properties of halos extant at $z_0 = 0$.

Having adopted all these considerations, we assume that a viable range for the threshold epoch of the cusp-core transformation is given by $z_{-2} < z_{\rm cc} < z_{\rm LMM}$. The corresponding cosmic time for this epoch is given by:

$$t(z) = t_0\int_0^{1/(1+z)}\frac{da}{\dot{a}} = \frac{2\sinh^{-1}\left(\sqrt{\frac{\Omega_\Lambda}{\Omega_{\rm m}}}(1+z)^{-3/2}\right)}{3H_0\sqrt{\Omega_\Lambda}}. \tag{34}$$

where t_0 is the age of the Universe and H_0 is the Hubble parameter. For reference, Fig. 3.1 shows the range of plausible threshold times as a function of halo mass M_0.

3.2.5 Velocity-dependent SIDM cross section

The cross section per unit mass, σ/m_χ, is the key physical property that characterizes a specific SIDM model. We consider a class of models where self-scattering between DM particles is mediated by a massive force carrier of mass m_ϕ through an attractive Yukawa potential with coupling strength α_c (Vogelsberger et al., 2012b, Feng et al., 2010, Loeb and Weiner, 2011). Furthermore, we assume that the elastic scattering between SIDM particles can be modeled by the screened Coulomb scattering interaction observed in a plasma, which in the classical regime is well fitted by the transfer cross section:

$$\frac{\sigma_{\rm T}}{\sigma_{\rm T}^{\rm max}} \approx \begin{cases} \frac{4\pi}{22.7}\beta^2\ln\left(1+\beta^{-1}\right), & \beta<0.1 \\ \frac{8\pi}{22.7}\beta^2\left(1+1.5\beta^{1.65}\right)^{-1}, & 0.1<\beta<10^3 \\ \frac{\pi}{22.7}\left(\ln\beta+1-0.5\ln^{-1}\beta\right)^2, & \beta>10^3, \end{cases} \tag{35}$$

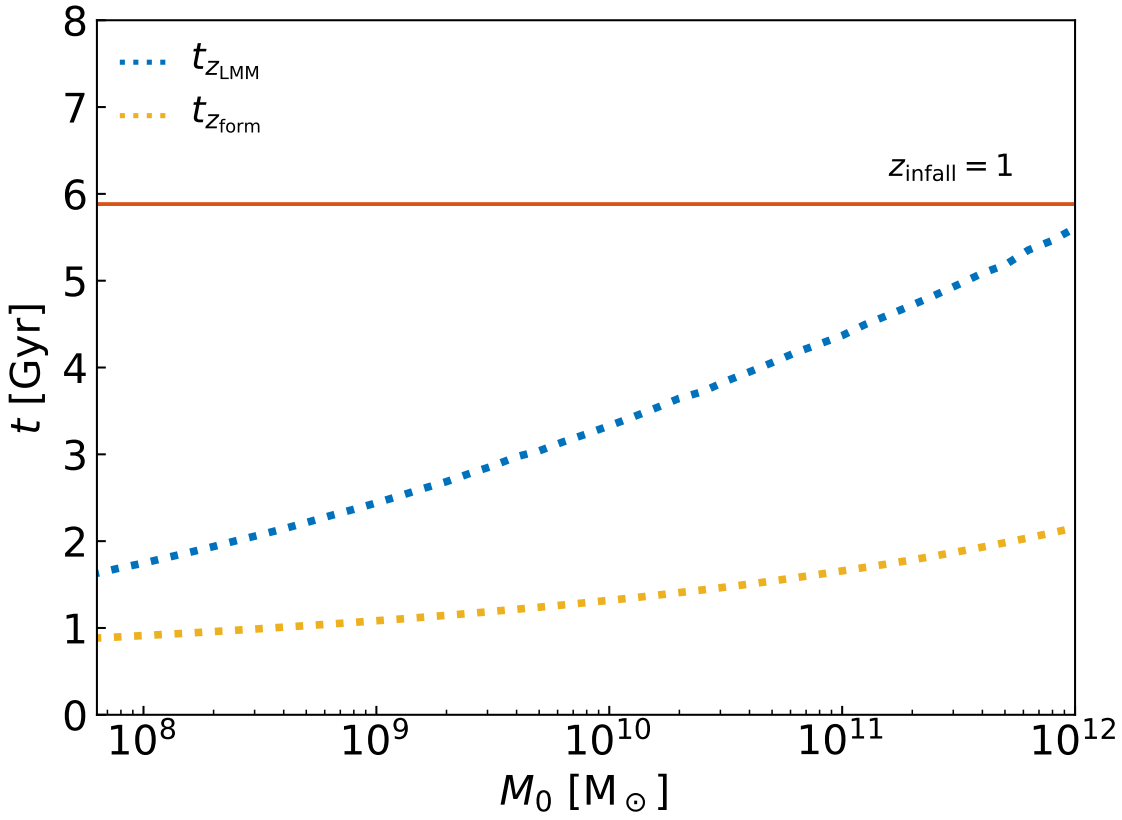

Figure 3.1: Cosmic time for the cusp-core transformation threshold of SIDM halos as a function of the present-day halo mass M_0. The blue dotted line is the function of $z_{\rm LMM}$ and the yellow dotted line is the function of $z_{\rm form}$. The horizontal line indicates the *infall* time of subhaloes, which we fix to $z_{\rm infall} = 1$ (see Section 3.3.1).

where $\beta = \pi v_{\rm max}^2/v^2 = 2\,\alpha_c\,m_\phi/(m_\chi v^2)$ and $\sigma_{\rm T}^{\rm max} = 22.7/m_\phi^2$, and v is the relative velocity of the DM particles. Here $v_{\rm max}$ is the velocity at which $(\sigma_{\rm T} v)$ peaks at a transfer cross section equal to $\sigma_{\rm T}^{\rm max}$.

In this work, we use the benchmark velocity-dependent SIDM model introduced in Zavala et al., 2019 with $v_{\rm max}$ = 25 km/s and $\sigma_{\rm T}^{\rm max} = 60{\rm cm}^2{\rm g}^{-1}$. Ref. Zavala et al., 2019 used SIDM cosmological zoom simulations of a MW-size halo to show that self-interactions are frequent enough in the center of dwarf-scale (sub)halos to trigger the gravothermal catastrophe phase in a fraction of the subhalo population, and thus constitutes an alternative explanation to the diverse distribution of inner DM densities found in the MW satellite population (see Section 3.1).

In our idealised model, we are interested in the characteristic scales of a given halo that are relevant to set a single characteristic cusp-core-collapse timescale. In particular, we assign a single relaxation timescale for a halo due to self-scattering using Eq. 24. We set a single characteristic velocity dispersion $\sigma_{\rm vel}$, which is given by the the maximum of the velocity dispersion profile $\sigma_{\rm vel} = \sigma_{\rm r}(r_{\rm max})$ of the primordial NFW halo at the beginning ($z_{\rm cc}$) of the cusp-core transformation. The radius at which this maximum occurs is of $\mathcal{O}(1)$ of the maximum size of the SIDM core that eventually develops, and the value of $\sigma_r(r_{\rm max})$ sets the *temperature* of the fully developed isothermal core. We now describe in detail how we calculate $\sigma_r(r_{\rm max})$.

We start by referring to the local radial velocity dispersion $\sigma_{\rm r}(r)$, which can in principle be obtained self-consistently by solving the Jeans equation:

$$\frac{1}{\rho}\frac{{\rm d}}{{\rm d}r}(\rho\sigma_{\rm r}^2) + 2\beta\frac{\sigma_{\rm r}^2}{r} = -\frac{{\rm d}\Phi}{{\rm d}r}\,, \tag{36}$$

where $\beta = 1 - \sigma_\theta^2/\sigma_{\rm r}^2$ is the velocity anisotropy parameter and Φ is the gravitational potential, which for the NFW profile is given by:

$$\frac{\Phi(s)}{V_{200}^2} = -\frac{1}{k(c)}\frac{\ln(1+cs)}{s}\,, \tag{37}$$

where $s = r/r_{200}$ and V_{200} is the circular velocity at $r = r_{200}$:

$$V_{200}^2 = G\left({\rm M_0}^2 \times \frac{4}{3}\pi 200\rho_{\rm crit}\right)^{1/3}. \tag{38}$$

Here we assume the simplest case of isotropic orbits, where $\sigma_\theta(r) = \sigma_{\rm r}(r)$ and $\beta = 0$. In this case, the solution to the Jeans equation can be computed analytically (Łokas and Mamon, 2001), giving the 1D velocity dispersion:

$$\begin{aligned}\frac{\sigma_{\rm r}^2}{V_{200}^2}(s,\beta=0) = \frac{1}{2k(c)}c^2 s(1+cs)^2[\pi^2 - \ln(cs) - \frac{1}{cs}\\ -\frac{1}{(1+cs)^2} - \frac{6}{1+cs} + \left(1 + \frac{1}{c^2s^2} - \frac{4}{cs} - \frac{2}{1+cs}\right)\\ \times \ln(1+cs) + 3\ln^2(1+cs) + 6{\rm Li}_2(-cs)],\end{aligned} \tag{39}$$

where ${\rm Li}_2(x)$ is the dilogarithm. Using Eq. 39, we compute $\sigma_{\rm vel} = \sigma_r(r_{\rm max})$ for a given value of M_0 and c.

Finally, we compute a characteristic value for the transfer cross section $\langle\sigma_{\rm max}\rangle$ by computing the thermal average of the transfer cross section at $r_{\rm max}$, i.e., within the SIDM core. We assume that the velocity distribution of DM particles can be approximated by a Maxwell-Boltzmann distribution. Although such a distribution is not self-consistent with the NFW profile e.g. Petač et al., 2018, it

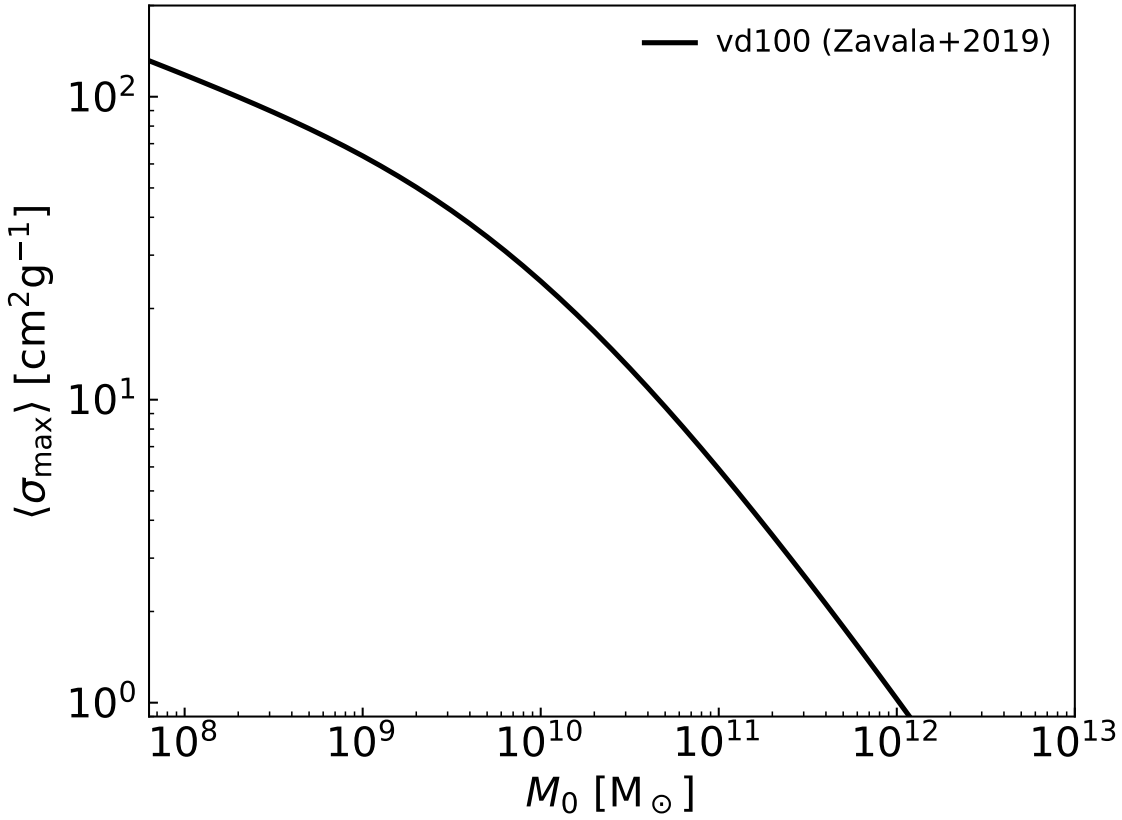

Figure 3.2: Characteristic transfer cross section per unit mass as a function of a halo mass at $z = 0$ (Eq. 40) for the benchmark SIDM model (vd100) from Zavala et al., 2019.

is a reasonable approximation for our purposes, because the distribution within the SIDM core will eventually become Maxwellian (Vogelsberger and Zavala, 2013). Therefore:

$$\langle\sigma_{\rm max}\rangle = \frac{1}{2\sigma_{\rm vel}^3\sqrt{\pi}} \int (\sigma_{\rm T}) v^2 e^{-v^2/4\sigma_{\rm vel}^2}\, {\rm d}v. \tag{40}$$

For reference, Fig. 3.2 shows the characteristic value for the transfer cross section per unit mass as a function of halo mass M_0 today for the benchmark SIDM model (vd100) from Zavala et al., 2019 that we use for calibration in our work.

3.3 Mass and time scales for black hole formation

We estimate the timescale for the formation of a black hole in the center of an SIDM halo following the procedure laid out by Outmezguine et al., 2022. This timescale applies after the threshold time for the cusp-core transformation $z_{\rm cc}$ of the primordial NFW halo as discussed in Section 3.2.4. The formula from Outmezguine et al., 2022 is based on the (spherical) gravothermal fluid model, which has been used in the past to study the gravothermal catastrophe in SIDM halos e.g. Balberg et al., 2002, Koda and Shapiro, 2011, Essig et al., 2019, Pollack et al., 2015, Xiao et al., 2021, Choquette et al., 2019, Feng et al., 2021. The recent study by Outmezguine et al., 2022 is particularly suitable for our work since, contrary to previous papers, they consider velocity-dependent cross sections. In Appendix 3.6 we make a comparison between their estimate of the collapse time and that made in

Pollack et al., 2015. Before describing the key equation, we present a short summary of the physical process based on Balberg et al., 2002.

In the gravothermal evolution of an SIDM halo, we can distinguish between a long mean free path (LMFP) regime, where the typical distance a particle travels is much longer than the gravitational Jeans scale and the short mean free path (SMFP) regime, where the situation is reversed. In the LMFP regime, particles orbit the inner halo many times unperturbed before being scattered, while in the SMFP regime particle motions in the core are constrained by multiple collisions. In these two regimes, the heat conduction and the mass transfer between the core and the extended halo are different.

Initially, as the core is growing in size, both the core and extended halo are firmly in the LMFP limit; during this phase, the inner core is approaching the transitional regime, in between the LMFP and the SMFP where the Knudsen number is of $\mathcal{O}(1)$. While the extended halo remains nearly collisionless, with nearly the same primordial NFW density profile, the core evolves and, as the gravothermal collapse is triggered, it transitions into the SMFP regime where it essentially behaves as a fluid. Although the velocity dispersion and the density of the core both increase, the latter increases much faster with time, $\mathrm{d}\log(\sigma_\mathrm{r}^2)/\mathrm{d}\log(\rho_\mathrm{core}) \approx 0.1$ (Balberg et al., 2002), and it drives the core into two components: a dense SMFP inner core that continues to evolve, and a more dilute LMFP outer core, with a nearly constant density, which connects to the extended nearly unperturbed NFW halo. Eventually, the temperature in the inner core is so high that it enters the relativistic regime and dynamical instability occurs that leads to the formation of the black hole (Balberg et al., 2002, see also Feng et al., 2022). The *classical* gravothermal fluid formalism cannot be used once the system becomes relativistic. However, the classical formalism in the LMFP regime allows us to follow the evolution of the core to high central densities, and in fact since most of the evolution occurs in the LMFP regime, with only the last instants prior to collapse being in the SMFP regime, the timescale for collapse is dominated by the LMFP evolution of the core, and thus, the classical approach can be used to estimate the timescale of interest.

According to Outmezguine et al., 2022, the amount of time required for the primordial NFW to evolve from a central cusp to an SIDM core and then to a fully collapsed cored when a black hole forms – i.e. the cusp-core-collapse timescale – is given by:

$$t_\mathrm{coll} \approx 382 t_\mathrm{r}(z_\mathrm{cc}). \tag{41}$$

where $t_\mathrm{r}(z_\mathrm{cc})$ is the relaxation time, defined as the mean time between individual collisions, which we introduced briefly at the beginning of Section 3.2.1 (see Eq. 24). Ref. Outmezguine et al., 2022 gives a formula for $t_\mathrm{r}(z_\mathrm{cc})$ based on the properties of the primordial NFW halo:

$$\begin{aligned} t_r(z_\mathrm{cc}) \simeq 1.47\mathrm{Gyr} \times \left(\frac{0.6}{C}\right) \times \\ \times \left(\frac{\mathrm{cm}^2/\mathrm{g}}{\sigma_{\mathrm{c},0}(z_\mathrm{cc})}\right) \left(\frac{100\mathrm{km/s}}{\sigma_\mathrm{vel}(z_\mathrm{cc})}\right) \left(\frac{10^7 \mathrm{M}_\odot \mathrm{kpc}^{-3}}{\rho_\mathrm{s}(z_\mathrm{cc})}\right), \end{aligned} \tag{42}$$

where C is a fitting parameter, which we set to 0.57 following Outmezguine et al., 2022. The parameter $\sigma_{c,0}$ is a type of cross section average given by:

$$\sigma_{c,0}(z_\mathrm{cc}) = \frac{3}{2}\frac{\langle \sigma_\mathrm{visc} v^3 \rangle}{\langle v^3 \rangle}, \tag{43}$$

where $\sigma_\mathrm{visc} = \int \mathrm{d}\sigma \sin^2\theta$ is the viscosity cross section with the scattering deflecting angle θ. The difference between σ_visc and σ_T is small and depends on the SIDM particle physics model, which gives the specific angular dependence for the differential cross section (Tulin and Yu, 2018). We assume that $\sigma_\mathrm{visc} \approx \sigma_\mathrm{T}$ for isotropic scattering, since our results are calibrated on the SIDM simulations by Zavala

et al., 2019, which use elastic isotropic scattering using $\sigma_{\rm T}$. The cosmic time from the Big Bang until the formation of the black hole is finally given by:

$$t_{\rm BH} = t(z_{\rm cc}) + 382 t_r(z_{\rm cc}), \tag{44}$$

where $t(z_{\rm cc})$ is the time at which the core-collapse transition begins, and is computed with Eq. 34.

The black hole is expected to form from material in the SMFP region. Ref. Balberg and Shapiro, 2002 estimates the mass of this seed black hole $M_{\rm BH}$ based on the mass in the core, $M_{\rm core}$, that is in the SMFP regime. In the late stages of the core evolution, the $M_{\rm core}$ - $\sigma_{\rm vel}$ relation determines the mass of the core at the relativistic instability, which occurs when $\sigma_{\rm vel} \approx c/3$. When the inner core is sufficiently dense, mass is continuously lost from its surface as outer layers cool and expand to join the outer core, with Balberg et al., 2002 predicting that the $M_{\rm core}$ - $\sigma_{\rm vel}$ relation settles to: $\mathrm{d}\log \mathrm{M_{core}}/\mathrm{d}\log(\sigma^2_{\rm vel}) \approx -0.85$. Therefore, the seed black hole mass is predicted to be:

$$M_{\rm BH}(z^*) = M_{\rm core}(z^*) \left(\frac{\sigma^2_{\rm vel}(z^*)}{(c/3)^2 \mathrm{km^2 s^{-2}}} \right)^{0.85}. \tag{45}$$

The region outside the collapsed core relaxes to a dynamically stable equilibrium system of particles that continue to orbit the central black hole and subsequent interactions in this region will feed the black hole.

We should note that the behaviour above has been developed for a system in isolation. In an evolving halo growing in a cosmological scenario, mass accretion might modify this behaviour as we described in Section 3.2.4. A detailed treatment of the impact of cosmological accretion in the gravothermal fluid equations, and in particular on the scale of the SMFP region, goes beyond the scope of this work. Instead, we consider a simple approach in which we establish a range of plausible black hole masses by considering the epoch z^* at which Eq. 45 should be evaluated. A lower estimate for the seed black hole mass would be to set $z^* = z_{\rm cc}$, that is to assume that the scale of the core (LMFP region), and thus the scale of the collapsing SMFP region, is set by the properties of the halo, essentially its mass $M(z_{\rm cc})$, at the threshold time for the cusp-core transformation. This, however, ignores the fact that the halo mass grows during the cusp-core transformation and up to the point of collapse ($z_{\rm BH}$ given by Eq. 44), the size of the core should thus grow as well, affecting the scale of the collapsing region. An upper estimate for the seed black hole mass can then be given by setting $z^* = z_{\rm BH}$, that is to assume that the size of the SMFP region is set by the last stages of the cusp-core-collapse evolution when the LMFP region (core) has grown to a size set by $M(z_{\rm BH})$. We then bracket the plausible range of black hole masses by:

$$M_{\rm BH}(z^* = z_{\rm cc}) < M_{\rm BH} < M_{\rm BH}(z^* = z_{\rm BH}). \tag{46}$$

To estimate the core mass $M_{\rm core}$ in Eq. 45, we use the results of the gravothermal fluid approach in Outmezguine et al., 2022 (the same reference we use in Eq. 42) where is estimated that the maximal core size of the halo is:

$$r_{\rm core} \simeq 0.45 r_{-2}, \tag{47}$$

before the collapse regime begins. This core radius is defined as the radius at which the local density is half that of the central density. The core size estimate in Eq. 47 is roughly consistent with simulation results where the core size is found to be $\lesssim r_{-2}$ (Rocha et al., 2012, Vogelsberger et al., 2014). Assuming that the region beyond the core remains essentially collisionless and with a profile that matches the NFW distribution we then have:

$$M_{\rm core}(z^*) = M_{\rm NFW}(r_{\rm core}; z^*), \tag{48}$$

where $M_{\rm NFW}(r)$ is given by the NFW radial density profile (Eq. 25) for a halo with a mass $M_0(z^*)$ given by the mass accretion history formula (Eq. 32) evaluated at z^*, and a concentration $c(z^*)$ obtained from this mass using the model described in Section 3.2.3.

3.3.1 Impact of tidal stripping in the core-collapse phase

Tidal stripping is the process by which DM in the outskirts of a smaller halo is removed by tidal forces as it orbits within a larger host. It has been argued that the tidal interactions with the halo and central galaxy of the host accelerate the core-collapse timescale by increasing the *temperature* (velocity dispersion) gradient outside the core, making heat outflow more efficient (Kaplinghat et al., 2019, Nishikawa et al., 2020, Kahlhoefer et al., 2019, Sameie et al., 2020). These previous works have invoked tidal acceleration of core-collapse as an explanation for the diversity of the MW's dwarf spheroidal galaxies (dSphs), based on constant cross section SIDM models with relatively low cross sections $\sigma_{\rm T}/m_\chi \sim 1-5$ cm^{2}g^{-1}, while the velocity-dependent model presented in (Zavala et al., 2019) see also Correa, 2021, Turner et al., 2021 relies on large cross sections $\sigma_{\rm T}/m_\chi > 10$ cm^{2}g^{-1} at the characteristic velocities of the dSphs to ensure core-collapse.

In order to take into account the impact of tidal stripping in accelerating the core-collapse phase, we use the results presented in Nishikawa et al., 2020, where tidal stripping is assumed to modify the NFW profile for $r > r_t$ in the following way: $\rho_{\rm NFW}(r_t) \times (r_t/r)^{p_t}$ where p_t = 5 (based on Peñarrubia et al., 2010) and r_t is a truncation radius. This modified profile is a simple way to incorporate the impact of mass loss from the outer region in the timescale for collapse. We use the case of $r_t = r_{-2}$, and estimate the acceleration of the gravothermal catastrophe due to tidal stripping as:

$$t_{\rm coll,t} \approx \frac{1}{10} t_{\rm coll}, \tag{49}$$

where $t_{\rm coll}$ is the timescale for core-collapse without the tidal effects (see Eq. 41). We only apply Eq. 49 for (sub)halos after the infall redshift into the MW halo, which for simplicity, we fix to be $z_{\rm infall} = 1$ for the entire (sub)halo mass range we consider in this work[2].

3.4 Results and Discussion

Our main goal is to investigate the consequences for velocity-dependent SIDM models, which invoke core-collapse to explain the diversity of the MW satellite population (such as that in Zavala et al., 2019), on the formation timescales for IMBHs and their masses.

Fig. 3.3 shows the gravothermal collapse timescale – which is approximately the BH formation timescale – as a function of the halo's present day mass M_0 (Eq. 44). The solid lines – together with their shaded regions, which are given by the scatter in the cosmological concentration–mass relation – bracket the range of possible threshold epochs for the cusp-core-collapse evolution to begin (see Section 3.2.4), with the yellow corresponding to the assembly redshift of the primordial NFW halo $z_{\rm cc} = z_{\rm form} = z_{-2}$, while the blue corresponds to the epoch of the last major merger $z_{\rm cc} = z_{\rm LMM}$. The points where the right edge of the blue region, $t_{\rm BH}(z_{\rm LMM})$, and the right edge of the yellow region, $t_{\rm BH}(z_{\rm form})$, cross the $z = 0$ horizontal line roughly indicate the maximum mass of an isolated SIDM halo that could undergo core-collapse by the present day, for both of these cases. For the case where $z_{\rm cc} = z_{\rm LMM}$, the maximum mass is $\sim 3 \times 10^9 {\rm M}_\odot$ and for $z_{\rm cc} = z_{\rm form}$, it is $\sim 5 \times 10^{10} {\rm M}_\odot$.

Since we are interested in the (sub)halos that could host the MW satellites, we have considered the impact of tidal effects in the timescale for black hole formation. As discussed in Section 3.3.1, for simplicity we assume that all (sub)halos in the mass range considered in Fig. 3.3 become satellites at an infall redshift $z_{\rm infall} = 1$, and that tidal forces by the host halo strip the material from the subhalo

[2]We note that although the subhalo infall redshift distribution is broad, depending on the mass and orbit of individual subhalos, it roughly has a median value of $z \sim 1$ for the subhalo population of MW-size halos (Rocha et al., 2012, Jiang et al., 2015). Since this is the population we are interested in, and since we are not considering detailed orbital properties, we fix $z_{\rm infall} = 1$.

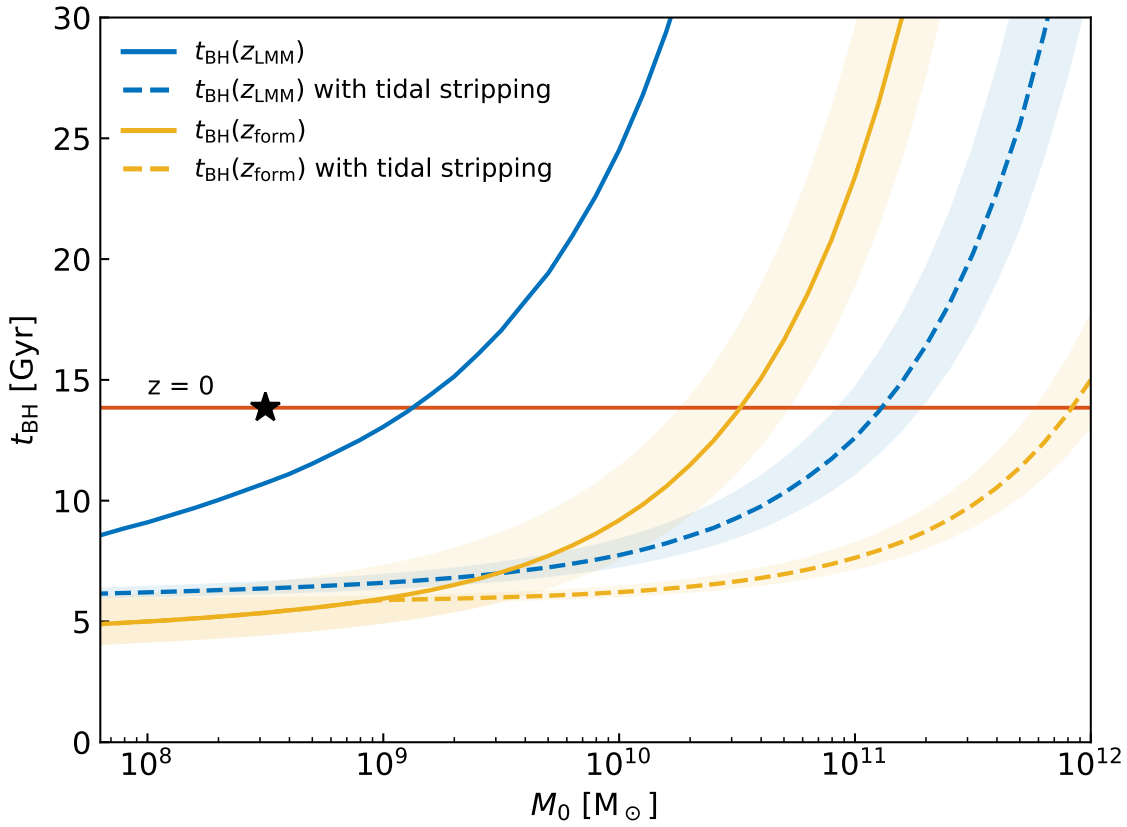

Figure 3.3: The timescale to form a black hole (Eq. 44) in SIDM halos as a function of the present-day halo mass M_0 (in isolation) for the velocity-dependent model vd100 (Zavala et al., 2019, Turner et al., 2021) shown in Fig. 3.2. The yellow solid line shows the case where the starting time for the cusp-core-collapse evolution is set to the assembly/formation time of the primordial (pre-SIDM) CDM NFW halo: $z_{\rm cc} = z_{\rm form}$ (see Section 3.2.3 and Fig. 3.1 where the yellow dotted line marks the cosmic time corresponding to $z_{\rm form}$), while the blue solid line brackets the impact of cosmological accretion by setting $z_{\rm cc} = z_{\rm LMM}$, which is the epoch of the last major merger for given halo of mass M_0 (see Section 3.2.4 and Fig. 3.1 where the blue dotted line marks the cosmic time corresponding to $z_{\rm LMM}$). Shaded regions indicate a scatter of $\pm 10\%$ in the concentration-mass relation e.g. Sánchez-Conde and Prada, 2014. Dashed lines are the corresponding cases including the acceleration of the collapse time driven by tidal stripping (Nishikawa et al., 2020) assuming a mass-independent infall epoch of $z_{\rm infall} = 1$ (see Section 3.3.1). The horizontal orange line indicates the age of the Universe. The black star symbol marks the transition mass where 50% of the subhalo population is estimated to be in the core-collapse regime according to Lovell and Zavala, 2023; (see also Zavala et al., 2019, Turner et al., 2021).

making the heat outflow from the center to the outskirts of the subhalo much more efficient, and thus reduces the timescale for collapse by a factor of ten (see Eq. 49). This significant acceleration of the core-collapse phase is shown as dashed lines in Fig. 3.3, which shifts the upper limit of the mean mass of a halo that could undergo the core-collapse to $\sim 2 \times 10^{11} \mathrm{M}_{\odot}$ and $\sim 10^{12} \mathrm{M}_{\odot}$ for the $t_{\mathrm{BH}}(z_{\mathrm{LMM}})$ and $t_{\mathrm{BH}}(z_{\mathrm{form}})$ cases, respectively.

The black star symbol in Fig. 3.3 indicates the halo mass at which 50% of (sub)halos are estimated to undergo core-collapse by $z = 0$ according to the results in Ref. Lovell and Zavala, 2023, which is based on the simulation of the vd100 model presented in Zavala et al., 2019. The simulation results are not compatible with our modelling of an early cusp-core transformation (yellow lines), and/or the acceleration effect due to tidal stripping (dashed lines). In the following, we discuss the effects that are likely behind this result.

Tidal acceleration of core-collapse? The impact of additional environmental effects taking place between a (sub)halo and the host halo during mergers, such as the evaporation of subhalo particles due to interactions with particles in the host, have been found to counteract the tidal stripping effect, delaying – or even disrupting – the core-collapse phase in models with low cross sections $\sigma_{\mathrm{T}}/m_{\chi} \lesssim 10$ cm^{2}g^{-1} (Zeng et al., 2022). Recent $N-$body cosmological SIDM simulations of a MW-size halo and its subhalos with a cross section in the range $\sigma_{\mathrm{T}}/m_{\chi} \sim 1 - 5$ cm^{2}g^{-1} confirm that subhalos do not experience core-collapse, thus larger values are required (Silverman et al., 2022). These recent results essentially rule out the constant cross section SIDM model as a viable possibility to explain the diversity of the MW satellite population, and therefore strengthen the case for a velocity-dependent SIDM model with core-collapse such as the one explored here based in Zavala et al., 2019 (see also Correa, 2021). Moreover, these results indicate that core-collapse is not accelerated in the manner anticipated by the tidal stripping model in Nishikawa et al., 2020, and thus the dashed lines in Fig. 3.3 are likely overestimating its effectiveness. *Cosmological accretion.* Based on the previous discussion, the likely range of validity for our modelling is shown in Fig. 3.4, where we have omitted the concentration–mass relation scatter for clarity. It is clear that the simulation result (black star symbol) is closer to the model where the cusp-core transformation begins later, at $z_{\mathrm{cc}} = z_{\mathrm{LMM}}$. This finding supports the case for cosmological accretion increasing the time of the evolution of a SIDM halo spent in the cored, quasi stable regime, possibly due to energy injection from infall material into the central core as discussed in Section 3.2.4. A good match to the simulation results can then be achieved by setting $z_{\mathrm{cc}} = z_{\mathrm{LMM}}$ in our model and adjusting the C parameter in Eq. 42 to $C \approx 0.42$, which is shown as a dashed line in Fig. 3.4. We note that C is a calibration factor which, following Outmezguine et al., 2022, we had set to $C = 0.57$ in Fig. 3.3. This agrees with Essig et al., 2019 who calibrated this parameter to a very similar value using the *isolated* SIDM simulations in Ref. Koda and Shapiro, 2011. We can then model the impact of cosmological accretion by either setting z_{cc} to z_{LMM} and make a small modification to C (which is the case we adopt), or by modifying the value of C significantly (starting from $z_{\mathrm{cc}} = z_{\mathrm{form}}$) and invoking a needed re-calibration of the parameter based on cosmological simulations. For our model, the latter case can be achieved by setting $z_{\mathrm{cc}} = z_{-2}$ and fixing $C \approx 0.19$.

3.4.1 IMBHs in the ultra-faint galaxies

One consequence of invoking core-collapse of SIDM halos to explain the diversity of inner DM densities in the MW satellite population is that those collapsed satellites will host central black holes. In particular, the vd100 model explored in Zavala et al., 2019 predicts that the dense ultra-faint galaxies, specifically, Segue I, Segue II, Willman I and Boötes II will be hosted by gravothermally collapsed subhalos (see Fig. 3 in Zavala et al., 2019). We can compute the expected seed black hole mass for a collapsed SIDM halo in the vd100 model using our framework (see Eq. 45). This is shown in Fig. 3.5 as a function of M_0, the halo mass in isolation. We use our calibrated model with $z_{\mathrm{cc}} = z_{\mathrm{LMM}}$ and

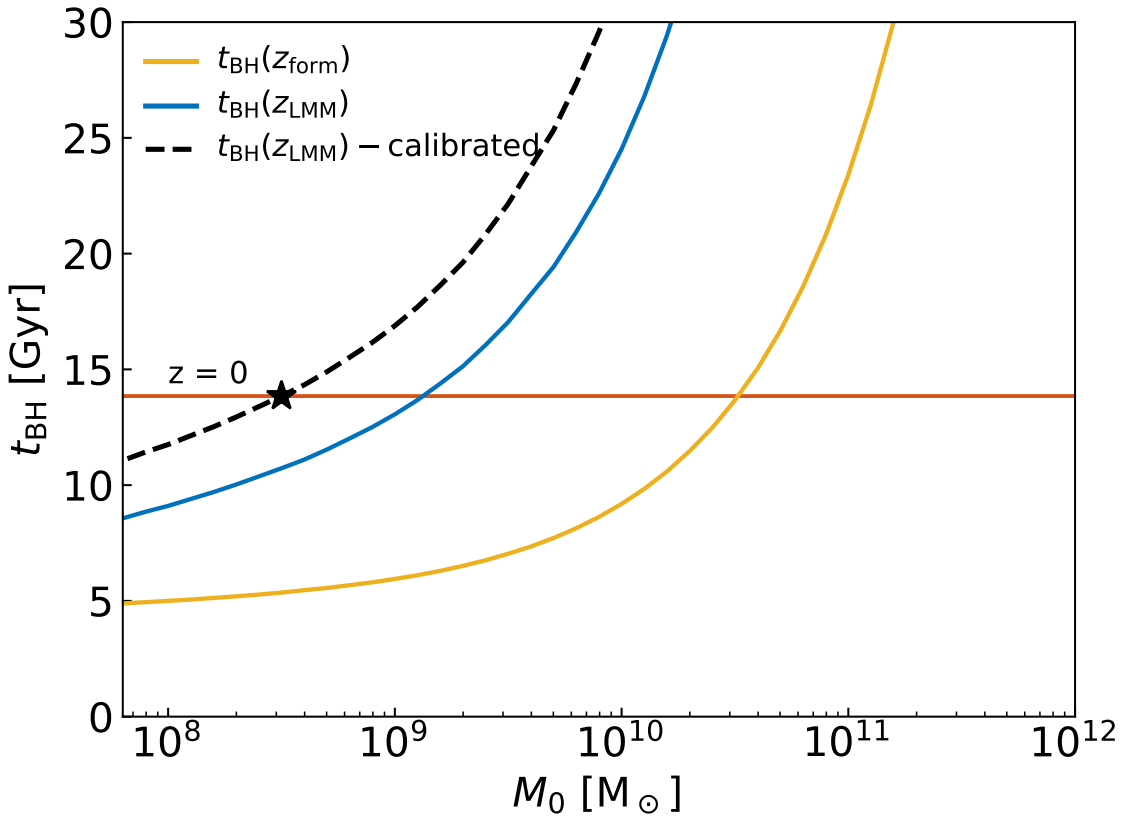

Figure 3.4: Timescale for black hole formation in SIDM halos as a function of the present-day SIDM halo mass M_0 in isolation. The solid blue and yellow lines are the same as those in Fig. 3.3, which bracket the range of the possible threshold epochs for the cusp-core-collapse evolution to begin (for mean values of the concentration-mass relation). The dashed black line is $t_{\rm BH}(z_{\rm LMM})$ (i.e., the blue line) re-calibrated to the simulation-based result of Ref. Lovell and Zavala, 2023 (black star) with the calibration factor $C = 0.42$ (see Eq. 42).

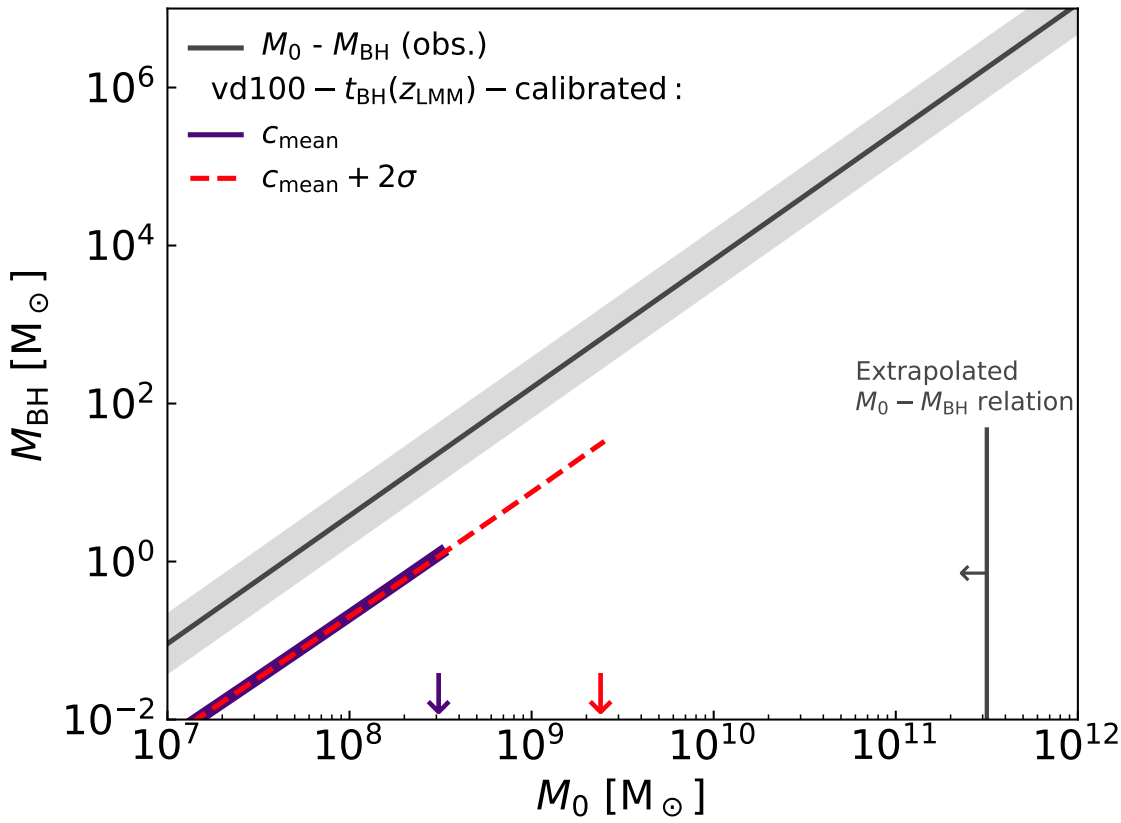

Figure 3.5: Black hole mass–halo mass relation. The violet and red lines follow the estimate of the SIDM-core-collapse formula (Eq. 45) with the former using the mean concentration-mass relation, while the latter uses a $+2\sigma$ value over the mean. For these cases, the arrows indicate the corresponding halo mass at which $t_{\rm BH} = 0$, i.e., the mass at which 50% and 2.5% of the halo population at that mass is in the core-collapse regime, violet and red, respectively. The gray line is the extrapolation towards lower masses of the empirical relation for SMBHs in galaxies with halo masses $> 10^{11.5}\mathrm{M}_\odot$, while the gray band represents the intrinsic scatter on this relation; adopted from Marasco et al., 2021.

$C = 0.42$ and consider two cases to illustrate the impact of halo concentration in our results: i) the solid violet line where halos have a mean concentration at M_0 ($c_{\rm mean}$) and ii) the dashed red line for halos with a concentration in excess[3] to the mean by 2σ ($c_{\rm mean} + 2\sigma$). We first notice that although the two lines representing these cases almost overlap with each other in Fig. 3.5, they in fact have a different slope and normalization since Eq. 45 depends (weakly) on concentration[4]. The net impact of concentration in the value of $M_{\rm BH}$ for a given halo mass is up to 5%.

Secondly, these predicted $M_{\rm BH} - M_0$ relations are truncated at different halo masses, represented by the vertical downward arrows of the respective color. In the first case (using $c_{\rm mean}$), this cutoff mass occurs at $M_0 \sim 3 \times 10^8$ $\mathrm{M}_\odot$ (violet arrow), and can be interpreted as the mass at which 50%

[3]Recall we are using a mass-independent spread of the distribution of halos in the concentration-mass relation equivalent to 0.1 dex for 1σ of the distribution.

[4]This dependence is not strong because $z_{\rm BH}$ decreases with M_0, thus the halo mass at this redshift, $M(z_{\rm BH})$, increases with M_0, which makes the relevant concentration, $c(M(z_{\rm BH}))$, almost independent of present day halo mass M_0.

of the halos have core-collapsed and 50% of the halos are still in the core phase. At higher (lower) masses, the fraction of core-collapsed halos is lower (higher) depending on halo concentration. For example, SIDM halos with $M_0 \sim 2 \times 10^9$ M$_\odot$ are only expected to have collapsed by the present day if they have a concentration larger than the mean by 2σ (red arrow), which represents only a small fraction (2.5%) of the halos at this mass. Therefore, in the vd100 model, only a small fraction of the massive (sub)halos in a MW-size system, which are expected to host the MW satellites, would have undergone core-collapse.

As we discussed in Section 3.3, the range of plausible BH masses depends on the epoch (z^*) at which one should evaluate the relevant properties of the core that determine the SMFP region that collapses (Eq. 46). We established $z^* = z_{\rm BH}$ as a reasonable choice and it is the one that appears in Fig. 3.5 and in subsequent figures. Modifying this choice to the earliest plausible epoch $z^* = z_{\rm cc}$ results instead in a smaller BH mass. For our default choice of $z_{\rm cc} = z_{\rm lmm}$ the difference is up to 30% over the relevant mass range with a weak dependence on halo mass.

The gray line in Fig. 3.5 represents the observed supermassive black hole (SMBH)-mass–halo-mass relation for massive galaxies extrapolated to low masses (Marasco et al., 2021), while the shaded gray band represents the intrinsic observational scatter. This relation and its spread have only been measured in halos larger than $10^{11.5}$ M$_\odot$, and therefore we plot the extrapolated values down to 10^7 M$_\odot$ in Fig. 3.5. Such an extrapolation of the empirical $M_{\rm BH} - M_0$ relation to the regime of dSphs ($M_0 \leq 10^{10}$M$_\odot$) would imply IMBHs in the range between $4 - 7 \times 10^3$ M$_\odot$. Remarkably, the slope of the predicted SIDM-driven $M_{\rm BH} - M_0$ relation by (Eq. 45) is very similar to that of the SMBH–halo mass relation, while the normalization is approximately two orders of magnitude lower.

An important aspect of our model is that it aims to explain the diversity of MW satellite population, by invoking a velocity-dependent SIDM model. This model predicts that only a fraction of the satellites have undergone collapse, and therefore only a fraction host IMBHs, specifically the least massive (in a model like vd100, those with $M_0 \lesssim 3 \times 10^9M_\odot$). For instance, the massive central black hole inferred recently in the dSph Leo I with $M_{\rm BH} \sim 3 \times 10^6M_\odot$ (Bustamante-Rosell et al., 2021) is too massive to lie in the extrapolated $M_{\rm BH} - M_0$ relation, and the properties of the halo associated with Leo I, being one of the brightest satellites of the MW, would likely put it in a range of M_0 values close to, but nevertheless above, the threshold for collapse in the vd100 model. The significance of this issue depends on the specific velocity-dependent SIDM model assumed. For instance, in Correa, 2021, Leo I is associated with a halo of an initial mass of $M_{200} \sim 3 \times 10^9M_\odot$ that has gravothermally collapsed, according to the inferred velocity-dependent SIDM model tuned to explain the diversity of the dSph satellite population in that work. Nevertheless, the central black hole mass inferred for Leo I in Bustamante-Rosell et al., 2021 is several orders of magnitude larger than can be explained by gravothermal collapse alone and a significant growth of the seed black hole by other means would be required. For other bright dSphs, there might be a different type of conflict; for instance, Fornax and Ursa Minor have upper limits to the presence of a central black hole of around $M_{\rm BH} \sim 3 \times 10^4M_\odot$ Jardel and Gebhardt, 2012, Lora et al., 2009. These systems have M_0 values likely in the range around the threshold for core-collapse. The precise value of M_0 inferred from the observed kinematics of the dSph depends on several quantities, such as the modelled DM profile and the orbital parameters, but being both associated to cored systems in Zavala et al., 2019 for the vd100 model, they are not expected to be associated with collapsed subhalos.

We can classify SIDM models in the cross section–halo mass parameter space as to whether they generate a combination of cored and gravothermally collapsed halos in the dwarf galaxy regime. More specifically, we determine the normalization boundaries of the self-interacting cross section according to whether or not the gravothermal collapse regime is expected to occur in a fraction of the MW satellites' host subhalos. In practice, and for simplicity, we only consider SIDM models described by the classical velocity-dependent formula for a Yukawa-like interaction model $\sigma_{\rm T}$ – i.e. Eq. 35 –

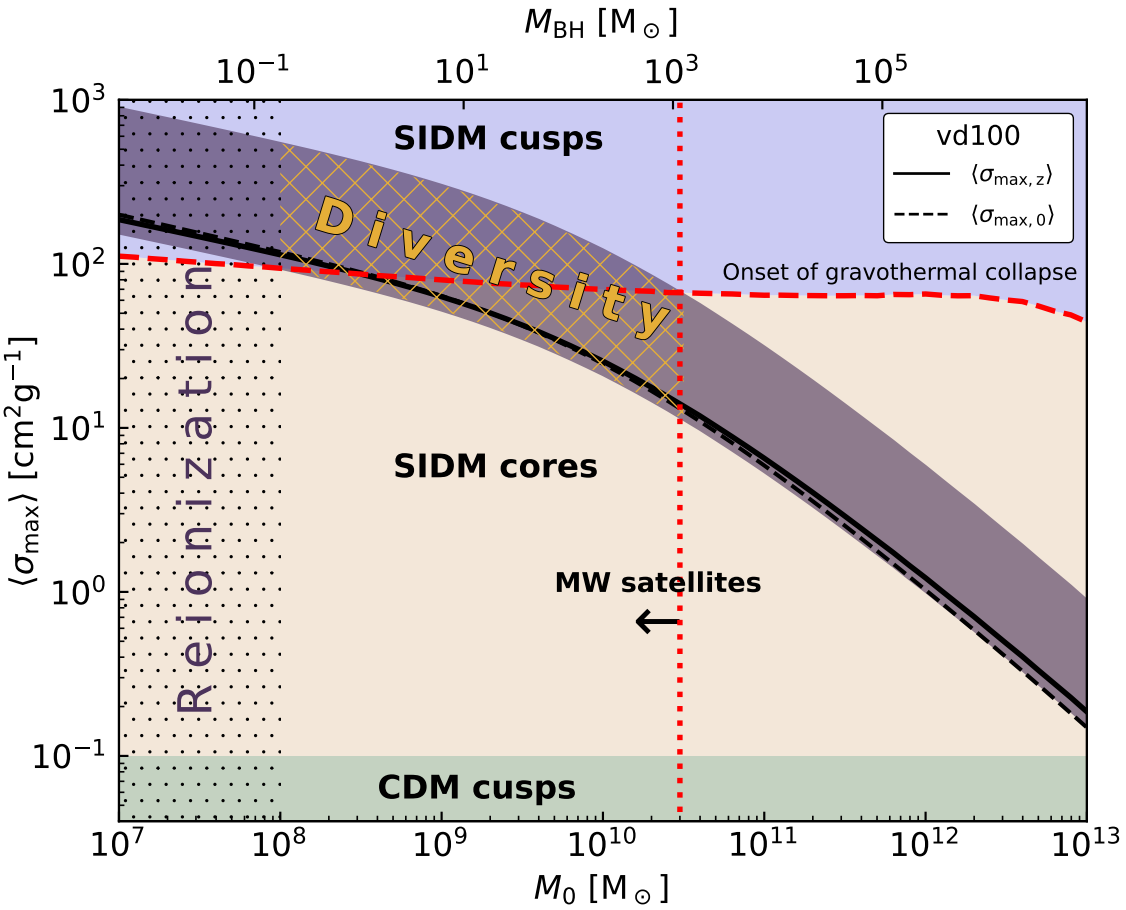

Figure 3.6: The effective cross section as a function of a present-day SIDM halo mass M_0 in isolation. The black solid and dashed lines represent the effective cross section for the vd100 model evaluated at $z_{\rm LMM}$ and $z = 0$, respectively; we use our default model with $z_{\rm cc} = z_{\rm LMM}$ and calibrated to the simulation analysis in Lovell and Zavala, 2023. The x−axis on the top shows the corresponding (SIDM-driven) black hole mass for a given M_0. The red dashed line (nearly horizontal) indicates the required cross section value for the onset of gravothermal collapse: SIDM-driven cuspy halos lie above (light violet), while SIDM cores lie below (beige) down to the point where the cross section is so low that halos are essentially CDM-like (light green). The red dotted line marks the upper mass for the dSph MW satellites to reside e.g. Errani et al., 2022, while the hashed/dotted region to the left starts at the mass where reionization significantly suppresses galaxy formation. The dark violet band indicates the region where vdSIDM models like vd100 but with different normalization, produce a diverse MW satellite population hosted by halos that could either be cored or cuspy.

and, at first, we fix the relative velocity $v_{\rm max}$ at which $(\sigma_{\rm T} v)$ peaks; in this way, we only vary the normalization $\sigma_{\rm T}^{\rm max}$.

Fig. 3.6 shows the effective cross section $\langle \sigma_{\rm max} \rangle$ (thermal average of $\sigma_{\rm T}/m_\chi$ at $r_{\rm max}$; see Eq. 40) as a function of a halo mass at the present day, M_0. The corresponding BH masses for a given M_0 are plotted on the top x−axis using Eq. 45. The vd100 model results for the cases in which $\langle \sigma_{\rm max} \rangle$ is computed at $z = z_{\rm cc} = z_{\rm LMM}(M_0)$ and at $z = 0$ are shown as the black solid and dashed lines, respectively. The former is the relevant cross section to set the core-collapse timescale – notice that the relevant epoch is a function of mass – while the latter is shown as reference to make the connection with Fig. 3.2 where the thermal average is evaluated at $z = 0$ for all halos.

The hashed/dotted region at $M_0 \leq 10^8 M_\odot$ marks an approximate lower limit on the mass of halos where galaxy formation is efficient; below this mass, heating during the epoch of reionization severely reduces the efficiency of cooling and subsequent star formation e.g. Sawala et al., 2016a. The vertical dotted red line is an approximate upper limit on the mass of possible halo hosts for the population of dSph MW satellites e.g. Errani et al., 2018. Thus, the mass range $10^8 - 3 \times 10^{10} M_\odot$ represents the region inhabited by the MW satellites. Different colored regions indicate the range of cross section values where halos with different inner density profiles reside. The light-green region at < 0.1 cm^{2}g^{-1} is where DM is effectively collisionless, and thus the structure of all halos is indistinguishable from CDM (i.e. cuspy)[5]. The light brown region in the middle is where SIDM models deviate significantly from CDM and predict quasi-equilibrium cored halos. The red dashed line marks the effective cross section for the onset of gravothermal collapse to occur by $z = 0$; it demarcates the transition from cores to SIDM-driven core-collapsed (cuspy) halos (light violet region on the top of Fig. 3.6).

The violet band in Fig. 3.6 denotes the set of cross section normalization values ($\sigma_{\rm T}^{\rm max}$ in Eq. 35) in vd100-like models that generate a diverse population of MW satellites, i.e., where halos with cored and cuspy profiles coexist. This section of parameter space is highlighted with a yellow hatched region within the range of halo masses expected for the MW satellites. Given that the timescale for core-collapse depends on halo mass and concentration, we can estimate the fraction of halos of a given mass M_0 that have undergone gravothermal collapse by considering the probability distribution (PDF) of concentrations for halos at a fixed mass, which according to simulations follows a log-normal distribution e.g. Neto et al., 2007:

$$P(\log_{10} c) = \frac{1}{\sigma\sqrt{2\pi}} \exp\Big[-\frac{1}{2}\Big(\frac{\log_{10} c - \langle \log_{10} c \rangle}{\sigma}\Big)^2\Big]. \tag{50}$$

where $\langle \log_{10} c \rangle$ is the median value of the concentration (in logarithm) and σ is its standard deviation. In our framework, the former is given by the concentration–mass relation model described in Section 3.2.3, while the latter is taken to be mass-independent and fixed to 0.1 dex based on simulations.

Fig. 3.7 shows the fraction of core-collapsed halos as a function of M_0 for the vd100 model (black solid line) and for its variations with different cross section normalizations that result in a diverse MW satellite population (dark violet), i.e., for the corresponding models shown in dark violet in Fig. 3.6. For a model with the normalization of vd100, most of the massive (sub)halos ($> 10^9$ M$_\odot$) that are expected to host the MW satellites are predicted to be cored, with only $\sim 30\%$ having undergone core-collapse. However, the breadth of the potential collapsed fraction values indicates that even a small re-normalization of the model will significantly increase this fraction. We note that the prediction in Fig. 3.7 needs to be tested with MW-size simulations with a wide range of cross sections and with enough massive subhalos to sample the high-mass end of the subhalo population, and subsequently recalibrated to match the full range of vd100-style models.

[5]The upper boundary here is approximate since small cores are expected even at such low cross sections; however, simulation results e.g. Zavala et al., 2013 have shown that these cores are too small at the scale of MW satellites to constitute a significant deviation from the CDM case (see also Zavala and Frenk, 2019).

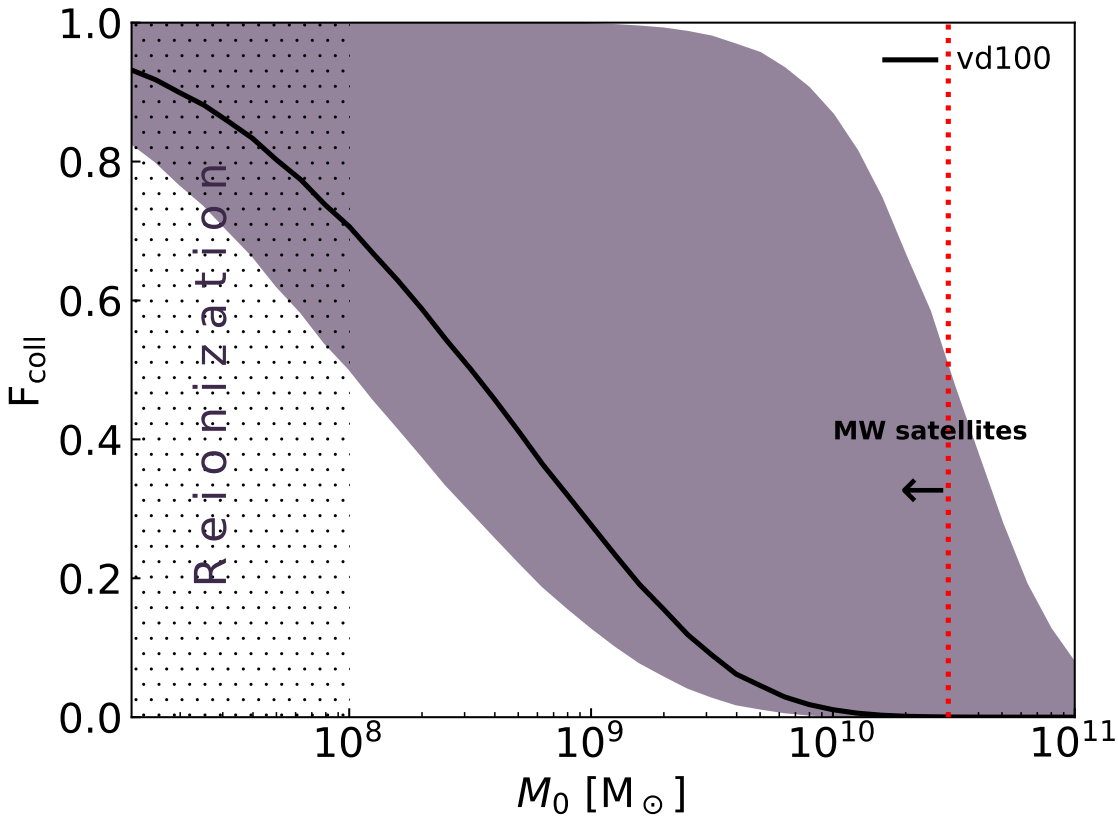

Figure 3.7: The fraction of core-collapsed halos as a function of M_0 for the vdSIDM models shown in Fig. 3.6, which have a diverse range of halo profiles (dark violet). The black solid line represents the benchmark vd100 model. As in Fig. 3.6, we use our default model with $z_{\rm cc} = z_{\rm LMM}$ and calibrated to the simulation analysis in Lovell and Zavala, 2023.

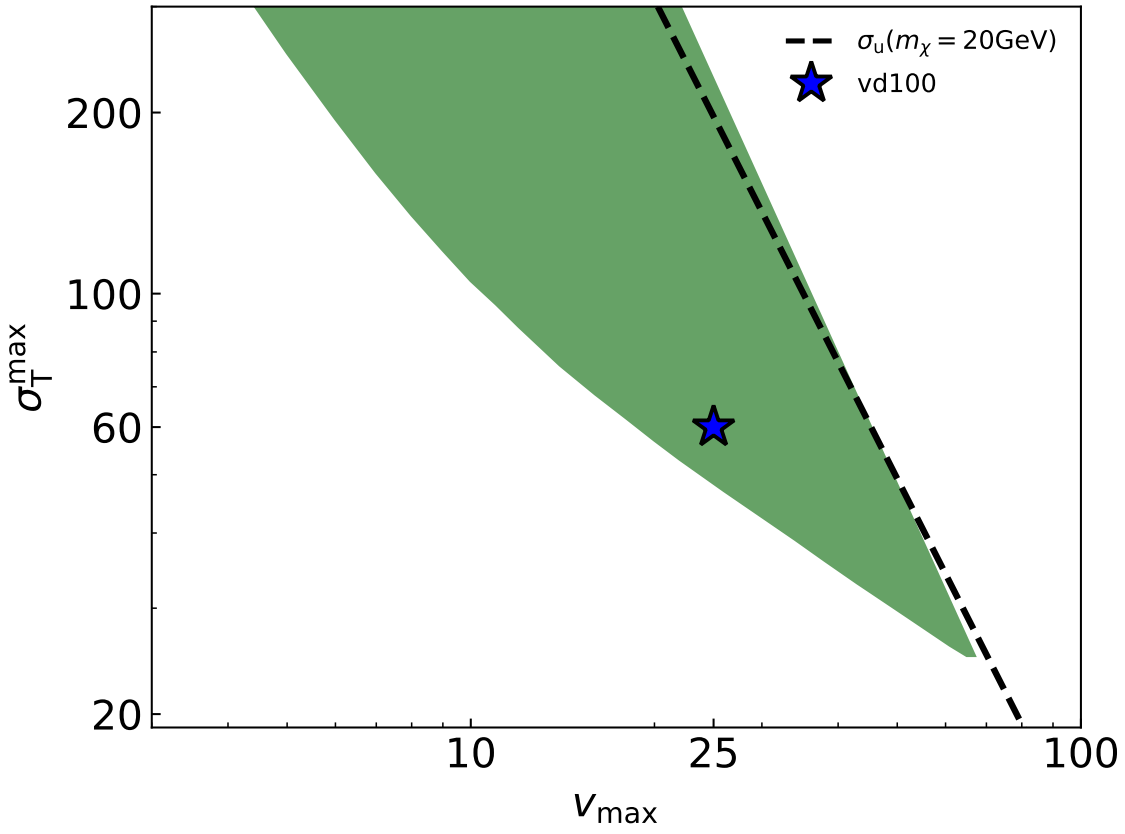

Figure 3.8: The viable values of the parameter space that define the vdSIDM models studied here (Eq. 35): the relative velocity $v_{\rm max}$ where the transfer cross section $\sigma_{\rm T}^{\rm max}$ peaks. The highlighted region is that of models that produce a bimodal distribution of halos (green area) and satisfies the constraint from elliptical galaxies $\langle\sigma_{\rm max}\rangle \leq 1{\rm cm}^2{\rm g}^{-1}$ for a halo mass of $M_0 = 10^{13}{\rm M}_\odot$. The black dashed line is the unitarity bound for the SIDM cross section for a particle mass $m_\chi = 20{\rm GeV}$. The blue star marks the vd100 model.

In principle, a complete exploration of the Yukawa-like interaction SIDM model in the classical regime requires variations of two parameters, $v_{\rm max}$ and the normalization $\sigma_{\rm T}^{\rm max}$. In addition, the family of SIDM models that generate gravothermally collapsed halos as well as cored halos is restricted by a couple of additional factors we have yet to consider. First, the impact of SIDM in DM structures at larger scales can be compared with observational probes of morphology based on lensing and X-rays. These observations have constrained the transfer cross section $\sigma_{\rm T}/m_\chi \lesssim 0.1 - 1$ cm^{2}g^{-1} on massive galaxies and galaxy cluster scales (see Section 3.1 for references). In particular, we take the approximate constraint on the cross section in massive ellipticals set in Peter et al., 2013 and more recently in Despali et al., 2022 of $\langle \sigma_{\rm max} \rangle \leq 1 {\rm cm}^2{\rm g}^{-1}$ at halo mass $M_0 = 10^{13} {\rm M}_\odot$. Second, the SIDM cross section is subject to an upper limit set by the quantum zero-energy resonance, known as the unitarity bound e.g. Kamada et al., 2020. When the cross section saturates the unitarity bound, it is parameterized solely by the DM mass and is given by:

$$\sigma_{\rm u} = \frac{4\pi}{k^2} \tag{51}$$

where the relative momentum of the scattering particles k is defined as $k = (m/2)v$. We can then use $\sigma_{\rm u}$ to set an upper bound for the cross section $\sigma_{\rm T}^{\rm max}$ that peaks at $v_{\rm max}$:

$$(\sigma_{\rm T} v) \leq \sigma_{\rm T}^{\rm max} v_{\rm max} \leq \sigma_{\rm u} v_{\rm max} \tag{52}$$

In Fig. 3.8 we show the range of viable parameter space, in peak relative velocity $v_{\rm max}$ and normalization $\sigma_{\rm T}^{\rm max}$, of the Yukawa-like SIDM models (Eq. 35) that satisfy two conditions: a diverse halo population (i.e. cored and gravothermally-collapsed halos) in the range of masses suitable to host the MW satellite population, and that satisfy the constraint from elliptical galaxies. The unitarity bound (for $m_\chi = 20$ GeV as a reference) is marked as a dashed line and the pair of $\sigma_{\rm T}^{\rm max}$ and $v_{\rm max}$ corresponding to vd100 is marked with the blue star.

3.5 Conclusions

If dark matter (DM) is made of particles that can strongly self-interact and therefore can be described as self-interacting DM (SIDM), the non-linear evolution of DM halos consists of two phases: a cusp-core transformation in which the originally cuspy halo develops a central isothermal core that is in quasi-equilibrium and remains in cored configuration for several Gyr followed by a rapid gravothermal core-collapse phase. The ultimate consequence of this SIDM-driven collapse is the formation of a black hole with a mass that is a fraction of the central DM core mass (Balberg et al., 2002). If the cross section is strongly velocity dependent – and thus halo mass dependent – then the population of halos today is expected to exhibit a wide diversity of central density profiles. This behaviour has been invoked as a viable way to explain the diversity of inner DM densities in the Milky Way (MW) satellites (Zavala et al., 2019, Correa, 2021, Correa et al., 2022).

Velocity-dependent SIDM models are the natural result of several particle physics models, e.g. those with new light mediators that produce an effective Yukawa-like interaction between DM particles (for a review see e.g. Tulin and Yu, 2018). These models also have the advantage of avoiding the stringent constraints on the cross section from gravitational lensing, X-ray morphology and dynamical analysis in cluster mergers and elliptical galaxies, which limits $\sigma_{\rm T}/m_\chi \lesssim 1$ cm^{2}g^{-1} at these scales (Peter et al., 2013, Robertson et al., 2017, 2019, Harvey et al., 2019, Andrade et al., 2022, Eckert et al., 2022, Shen et al., 2022, Despali et al., 2022), well below the threshold for gravothermal collapse. In this SIDM scenario, the structure of DM today is indistinguishable from the cold dark matter (CDM) scenario at cluster scales. The deviation from CDM grows at smaller scales, starting with the development of spherical isothermal cores in the center of $10^{11} - 10^{12}\,{\rm M}_\odot$ halos, and followed by the

onset of gravothermal collapse for the halos of dwarf spheroidal galaxies, a fraction of which should host SIDM-generated intermediate mass black holes (IMBHs).

In this work, we develop an analytical framework to predict the timescales and mass scales for the formation of IMBHs in SIDM halos, which includes the different stages in the cusp-core-collapse evolution of SIDM halos in a cosmological setting (Section 3.2). This framework is calibrated to a high-resolution simulation of a benchmark velocity-dependent SIDM model (vd100; see Fig. 3.2), which has been tuned to produce a large diversity in the MW satellite population (Zavala et al., 2019, Turner et al., 2021, Lovell and Zavala, 2023). Our main results are summarized as follows:

- The black hole formation (gravothermal collapse) timescale as a function of present day halo mass (in isolation) is shown in Fig. 3.3. We consider two starting redshifts that bracket the range of the possible threshold epochs ($z_{\rm cc}$) when the cusp-core-collapse evolution starts (see Section 3.2.4). The assembly/formation redshift of the primordial CDM NFW halo $z_{\rm cc} = z_{\rm form} = z_{-2}$ (yellow lines; defined as the time of assembly of the central region of the halo within its scale radius according to the model by Ref. Ludlow et al., 2016), and the redshift of the last major merger of the halo $z_{\rm cc} = z_{\rm LMM}$ (blue lines; takes into account cosmological accretion and it is computed using the simulation results of Fakhouri et al., 2010). We also consider the possible acceleration of the collapse timescale driven by tidal stripping following Nishikawa et al., 2020 (dashed lines in Fig. 3.3; see Section 3.3.1).

- We compare our results with the mass threshold ($\sim 3 \times 10^8 {\rm M}_\odot$), where most of the MW (sub)halos are observed to have undergone gravothermal collapse according to the vd100 SIDM simulation analyses made in Turner et al., 2021 and more recently in Lovell and Zavala, 2023. We find that our modelling can be fitted to this result by a small re-calibration of the free parameter C in the gravothermal fluid formalism (Eq.42) by choosing $z_{\rm cc} = z_{\rm LMM}$ and by assuming that tidal stripping has no impact on the collapse time (see Fig. 3.4). This choice is seemingly consistent with previous expectations that the core phase is delayed by cosmological infall Ahn and Shapiro, 2005, and supports the recent detailed simulation work by Zeng et al., 2022 that suggests the impact of tidal stripping in accelerating core collapse is likely overestimated in Nishikawa et al., 2020 – from which we developed our incorporate tidal stripping model – due to the competing environmental effect of subhalo heating through collisions with host halo particles.

- We show the black hole mass $M_{\rm BH}$ as a function of the present day halo mass M_0 in Fig. 3.5 (violet and red lines). This estimated seed black hole mass is obtained with Eq. 45, which is derived by following the evolution of the part of the core that collapses to high central densities within the gravothermal fluid formalism. The development of the relativistic instability ultimately leads to the formation of the black hole (Balberg and Shapiro, 2002). Remarkably, the slope of the $M_{\rm BH} - M_0$ SIDM-core-collapse relation is similar to that of the extrapolated SMBH–halo mass empirical relation found in massive galaxies (Marasco et al., 2021). This mechanism could then potentially constitute a continuation of the empirical relation towards the regime of dSphs, although the normalization is two orders of magnitude below the expectation, and thus the seed SIDM-driven black hole would need to grow substantially to satisfy such a scenario and would have to be rapidly accelerated compared to our predictions.

- We also consider the impact of the cosmological scatter in the concentration–mass relation in our results by first considering a 10% scatter on the concentration at a fixed mass (today) e.g. Sánchez-Conde and Prada, 2014. We find that more concentrated halos have their core collapse several Gyrs earlier (shaded areas in Fig. 3.3). The fraction of halos that is expected to collapse strongly depends on the range of concentrations available to the halo population at a given mass

(see Fig. 3.7). The predicted black hole mass is however, mainly set by halo mass, and is only weakly affected by concentration (at the percent level).

- Finally, we estimated the range of self-scattering cross sections that result in a diverse MW satellite population, i.e., that generate both cored and core-collapsed host halos for MW satellites. We first consider SIDM models with the same velocity dependence as vd100 but with different normalization (see Eq. 35). The results are shown in Figs. 3.6 and 3.7. We found that the vd100 model has a normalization that is close to the lower limit to exhibit diversity with most of the subhalos in MW-size systems being cored, especially for halos $M_0 > 10^{10}\,\mathrm{M}_\odot$, of which $\sim 70\%$ are cored. The latter is expected since our default choice of parameters is calibrated to the recent results in Lovell and Zavala, 2023, who agree qualitatively on the scarcity of massive core-collapsed subhalos in vd100. As noted by Lovell and Zavala, 2023, this represents a potential issue with models such as vd100 since it would be more natural to expect the bright MW dSphs to be assigned to the most massive subhalos, which in this case are likely to be cored, and thus inconsistent with the properties of dense bright dSphs. We show that such a potential issue can be alleviated by a relatively small increase in the cross section normalization of the vd100 model, since the fraction of massive core-collapsed halos increases rapidly with larger cross sections (see Fig. 3.7). To expand upon this result, we explore in Fig. 3.8 the parameter space of the Yukawa-like SIDM model (Eq. 35) to find the viable values of the peak velocity $v_{\rm max}$ and the normalization $\sigma_{\rm T}^{\rm max}$ that satisfy: i) having a diverse MW satellite population (as described before); ii) satisfy constraints at larger scales, in particular those set by elliptical galaxies (Peter et al., 2013, Despali et al., 2022); and iii) satisfy the constraint set on the cross section by the unitarity bound. These conditions set an upper bound for $v_{\rm max}$ to be $v_{\rm max} < 70 {\rm kms}^{-1}$ with a very narrow range of possible $\sigma_{\rm T}^{\rm max}$ values, while an ever wider range of $\sigma_{\rm T}^{\rm max}$ is suitable for smaller $v_{\rm max}$ values down to $v_{\rm max} \sim 5 {\rm kms}^{-1}$. To ascertain whether a single SIDM model can fit all MW satellites simultaneously requires much more precise estimates for the fraction of collapsed-to-total MW satellites.

In Appendix 3.7, we discuss different values of calibration parameter C in the gravothermal fluid model and their impact on our results. Based on previous studies this parameter has a plausible range between $0.4 - 0.75$, with our calibrated value being at the low end. However, such a value seems to be appropriate/favored by analyses based on cosmological simulation (Yang et al., 2023a, see also Essig et al., 2019). Nevertheless, we explore in Appendix 3.7 how choosing a value at the high end $C = 0.75$ would impact our key results. We find that although the timescale for black hole formation significantly changes with such a value of C, (see Fig. 3.10), the impact on our key result is modest, that is the region in the plane $\sigma_{\rm max} - M_0$ that would result in a diverse (i.e. cuspy and cored) MW satellite population, is shifted downward overall by about a factor of ~ 1.5 in the normalization of the cross section (see Fig. 3.11).

If SIDM is to be invoked to explain the diversity of the dSph MW satellite population, then the presence of IMBHs in the center of cored-collapsed (cuspy) halos is unavoidable. Based on our work, the range of seed IMBH masses for the dSph MW satellites that can potentially be hosted by cored-collapsed SIDM halos is in the range $0.1 - 1000$ M$_\odot$ (Fig. 3.6). The existence of such IMBHs may be verified by detailed observations of dSph kinematics with the upcoming generations of extremely large telescopes (Greene et al., 2020). Due to their high spatial resolution, they should be able to find $< 10^5\,\mathrm{M}_\odot$ black holes in $< 10^9\,\mathrm{M}_\odot$ in nearby galaxies through high-precision proper motion measurements (Greene et al., 2020). For example, to reach the range of $10^3 - 10^4\,\mathrm{M}_\odot$ Ref. MacLeod et al., 2016 suggest looking at the disruption of stars passing close to IMBHs. Under certain conditions, IMBHs should typically acquire companions with orbital periods of years, corresponding to semi-major axes of $\sim 5 - 10$ mas for $\sim 10^3 M_\odot$ IMBHs.

More precise observational kinematic data for the dSphs in the future will constraint further the

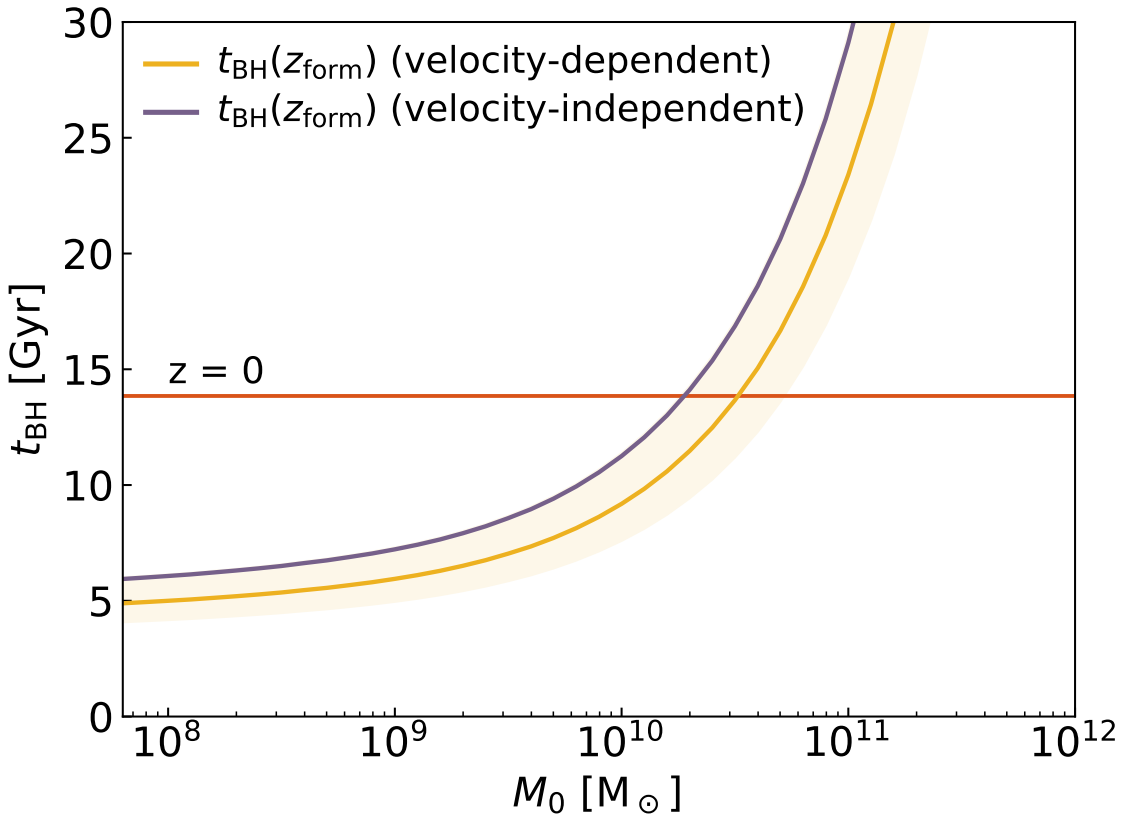

Figure 3.9: Timescale to form a black hole in SIDM halos as a function of the present-day halo mass M_0 (in isolation). The yellow line (Eq. 44) represents the cusp-core-collapse evolution timescale chosen for this work (equal to the curve of the same color in Fig. 3.3), and the violet line (Eq. 55) is based on Pollack et al., 2015. As in Fig. 3.3, shaded bands indicate a concentration scatter of $\pm 10\%$ in the concentration-mass relation e.g. Sánchez-Conde and Prada, 2014. The horizontal line indicates the age of the Universe at $z = 0$.

inner DM content of these systems, possibly establishing their inner DM profile. This will conclusively determine the significance of the diversity problem and constrain different classes of solutions. On the theoretical side, the predictions of vdSIDM models such as those considered in this work need to be complemented with more dedicated simulations that explore the relevant parameter space of cross sections that contain the gravothermal collapse regime (Zavala et al., 2019, Correa et al., 2022), and can be complemented with a semi-analytical revision of the predicted seed black hole mass in the seminal work by Ref. Balberg et al., 2002 within a full cosmological setting. Finally, a key aspect to explore is the interplay between the formation and evolution of the visible baryonic galaxy with the collapsing SIDM core and its central black hole.

Acknowledgments

TM, JZ, and MRL acknowledge support by a Project Grant from the Icelandic Research Fund (grant number 206930).

3.6 Appendix A

In this work, we computed the relaxation timescales for self-scattering and core-collapse using Eqs. 42 and 41 respectively. These equations are adapted from Outmezguine et al., 2022, which incorporates a velocity-dependent SIDM cross section into the gravothermal fluid formalism. In this Appendix, we consider the impact on our results of using an alternative set of formulae developed by Ref. Pollack et al., 2015, where the SIDM cross section is assumed to be constant. According to this reference, the cusp-core-collapse timescale is given by:

$$t_{\rm coll} = 455.65 t_r(z_{\rm cc}), \tag{53}$$

where $t_r(z_{\rm cc})$ is the relaxation time derived for velocity-independent cross sections:

$$\begin{aligned} t_r(z_{\rm cc}) &= \frac{1}{a\sigma_{\rm max}} \left(\frac{k(c)^2}{4\pi {\rm G}^3}\right)^{1/6} \delta_{\rm char}^{-7/6} \rho_{\rm crit}(z_{\rm cc})^{-7/6} M_0^{-1/3} \\ &= 0.310 \text{ Myr} \times \left(\frac{M_0}{10^{12}{\rm M}_\odot}\right)^{-1/3} \left(\frac{k(c(z_{\rm cc}))}{k(9)}\right)^{3/2} \\ &\left(\frac{c(z_{\rm cc})}{9}\right)^{-7/2} \left(\frac{\rho_{\rm crit}(z_{\rm cc})}{\rho_{crit}(z=15)}\right)^{-7/6} \left(\frac{\langle\sigma_{\rm max}\rangle}{1 \text{ cm}^2/\text{g}}\right)^{-1}. \end{aligned} \tag{54}$$

Then the time to form a black hole is given by:

$$t_{\rm BH}(M_0, \sigma_{\rm max}) = t(z_{\rm cc}) + 455.65 t_r(z_{\rm cc}). \tag{55}$$

In Fig. 3.9 we compare the black hole formation timescale derived self-consistently for velocity-dependent cross sections (Eq. 44) with the case derived assuming the velocity-independent cross section (Eq. 55). For this comparison, we have used the case with $z_{\rm cc} = z_{\rm form} = z_{-2}$ un-calibrated and without tidal stripping (i.e. equivalent to the solid yellow line in Fig. 3.3). The $t_{\rm BH} - M_0$ curves have a similar shape in both cases across all the explored mass range, but with a ~ 1 Gyr difference in normalization. For the purposes of this work, such a difference could be absorbed almost completely in the calibration factor C in Eq. 41.

3.7 Appendix B

In the gravothermal fluid formalism, the heat conductivity κ is a key quantity in the time evolution of the SIDM halo. In the LMFP regime, it can be derived by dimensional analysis but it carries an unknown parameter C that is the order of unity, which cannot be derived from first principles e.g. Balberg et al., 2002, Koda and Shapiro, 2011, Pollack et al., 2015, Essig et al., 2019, Nishikawa et al., 2020, Outmezguine et al., 2022. To determine C all these studies compared the evolution of the halo density profile given by the gravothermal fluid model to that obtained from different types of $N-$body simulations, where hard-sphere elastic scattering interactions were implemented. Most of these studies used isolated idealized simulations with only Refs. Essig et al., 2019, Nishikawa et al., 2020, Outmezguine et al., 2022 using the cosmological constant-cross section SIDM simulations presented in Elbert et al., 2015 and Koda and Shapiro, 2011. For large cross sections that have entered the regime of core-collapse, the latter studies suggest that a value of $C = 0.45$ is a better fit to cosmological simulations, while previous analyses based on isolated simulations preferred values around $0.6 - 0.75$.

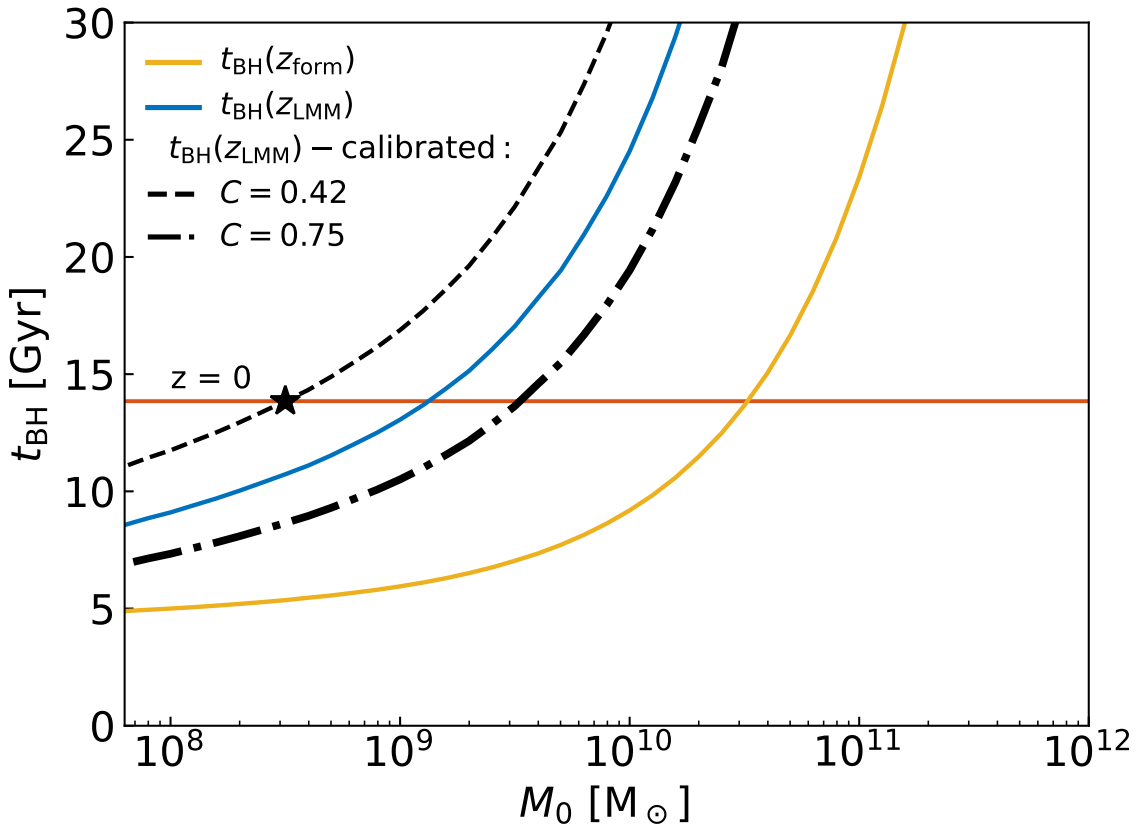

Figure 3.10: The same as Fig. 3.4, but with the addition of the thick dot-dashed black line, which is the same as the calibrated model used for our key results (thin dashed black line) but with $C = 0.75$ instead.

In this work, we used the formula for the relaxation time (Eq. 42) and, initially, the fitting parameter $C = 0.57$ calibrated for the velocity-dependent SIDM model in Ref. Outmezguine et al., 2022 using isolated simulations. This value was roughly in between the values explored in the literature as discussed above. After comparing the timescale for gravothermal collapse (black hole formation) with the results from Lovell and Zavala, 2023 based on the high-resolution velocity-dependent SIDM simulation performed in Zavala et al., 2019, we found that a value of $C = 0.42$ is a more accurate fit (see Fig. 3.4). This is in qualitative agreement with the analysis in Essig et al., 2019, who found $C = 0.45$ consistent with the cosmological simulation they analyzed. However, we note that there are different methods used for calibration. Our calibration is based on comparing the mass threshold where $\geq 50\%$ subhalos of a MW-size host have collapsed, while Essig et al., 2019 uses the density profile of dwarf-size main host halo. More recently, a new velocity-dependent SIDM cosmological simulation with a similar resolution to the one we used has been performed (Yang et al., 2023a). Using a similar comparison to ours, albeit with a different methodology, between the gravothermal fluid model and the simulation, they find that a value of $C = 0.75$ overestimates the number of subhalos that should collapse by $z = 0$ by around a factor of 2. Thus, this result also suggests that a lower value of C fits cosmological simulations better, which is qualitatively in agreement with our finding.

In order to obtain a precise value of the parameter C that is appropriate for subhalos in a cosmological setting, it would be necessary to perform a detailed analysis across multiple high-resolution simulations that considers variations across different velocity-dependent cross sections and a large exploration across different host halo masses. This hypothetical study requires many more

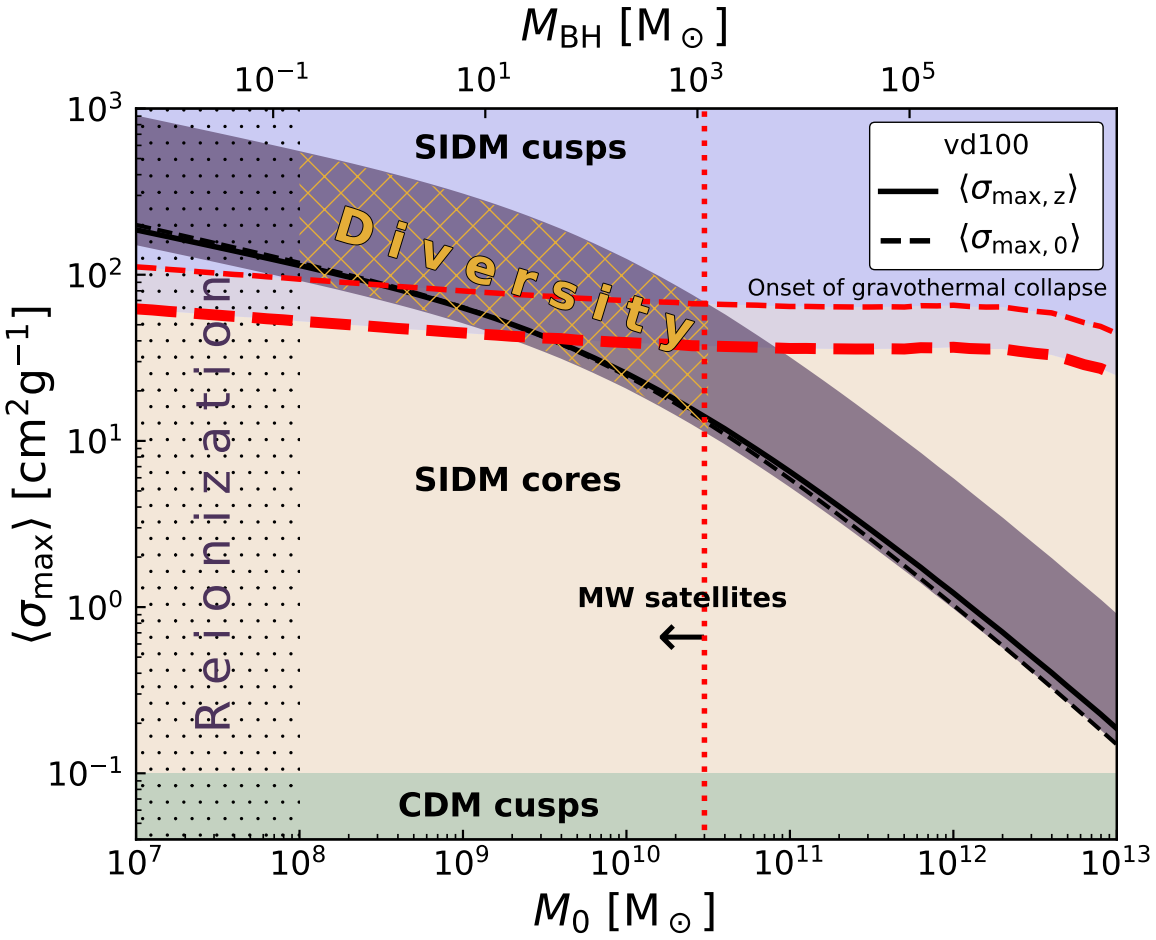

Figure 3.11: The same as Fig. 3.6, but with the addition of the nearly horizontal thick red dashed line – the required cross section value for the onset of gravothermal collapse when $C = 0.75$ is used instead of $C = 0.42$, which is the calibrated value used for our key results (thin red dashed line).

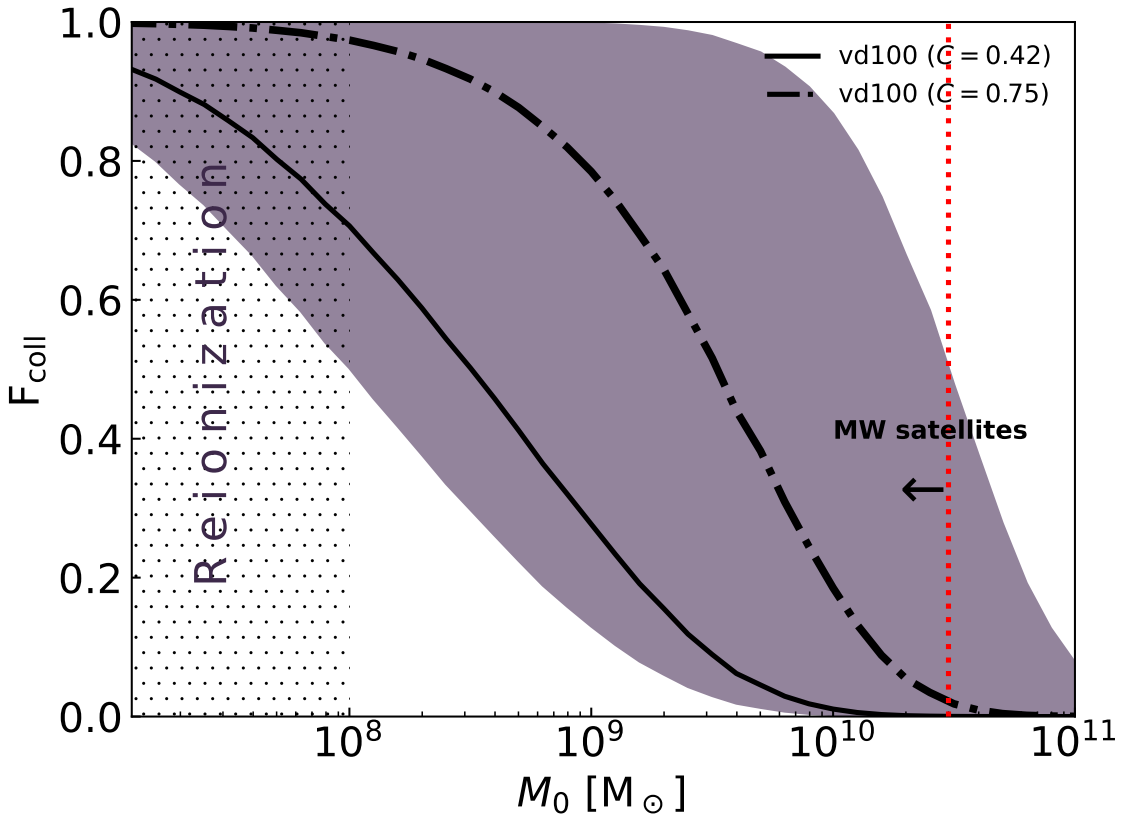

Figure 3.12: The same as Fig. 3.7, but with the addition of the thick black dot-dashed line – the fraction of core-collapsed halos as a function of M_0 when $C = 0.75$ is used instead of $C = 42$, as in our key result (solid black line).

simulations than have been performed to date; currently only two exhibit the required mass resolution (Zavala et al., 2019 and Yang et al., 2023a). Such an analysis is beyond the scope of this paper. Nevertheless, we can take into account the uncertainty in the value of C by considering its impact on the key results of our work. We do this in this appendix by comparing the predictions of our model with the calibrated $C = 0.42$ value we have used in our key results, and with a value of $C = 0.75$. The latter is the highest value for this parameter explored in Balberg et al., 2002, Nishikawa et al., 2020 and as we argued before is at the high end of plausible values as found in Yang et al., 2023a.

The impact on the timescale for black hole formation due to variations in C across this plausible range of values is shown in Fig. 3.10, specifically as the range between the dashed and thick dot-dashed black lines. We note that the resulting range is similar to the spread observed due to the 10% cosmological scatter in the concentration–mass relation (see Fig. 3.3) with an increase in the threshold mass that divides subhalos that have collapsed from those that have not by about an order of magnitude. Naturally, setting a higher value for the C parameter lowers the cross section values required to reach the threshold for the onset of gravothermal collapse by about a factor of 1.5; this is shown in Fig. 3.11 through the difference between the thin and thick red dashed lines. The overall change would then be a shift downwards of the region that is expected to have a diverse MW subhalo satellite population of cores and cusps. We conclude that the overall impact of the C parameter uncertainty on our key plot Fig. 3.6 is a factor of ~ 1.5 on the normalization of the transfer cross section that results in a diverse MW satellite population. Finally, we show in Fig. 3.12 the fraction of core-collapsed halos as a function of M_0 when setting $C = 0.75$ instead of our default value of $C = 0.42$ as a thick dot-dashed

black line. With this highest value of C, 80% of the (sub)halos with $> 10^9 M_\odot$ are expected to have undergone core collapse. This is around 50% higher than in the case of $C = 0.42$. Setting other values of C in the plausible range would result in different core-collapsed halo fractions in between the two black solid and dot-dashed lines.

4 Dynamical response of stars to the evolution of SIDM halos

The internal evolution of haloes in SIDM should in principle produce a distinct dynamical impact in the evolution of galaxies. As a SIDM halo transitions from its primordial cuspy CDM-like density profile to the development of the long-lasting SIDM core and finally to the gravothermal collapse of the core, the baryons within the central region of the halo must experience a dynamical response to these changes. This dynamical response could leave unique signatures that could be searched for in observations to either find evidence of the SIDM model or constrain it. Although by now, there are a number of cosmological simulations with full baryonic physics (e.g. REFs: Vogelsberger et al., 2014, Robles et al., 2017, Robertson et al., 2019, Despali et al., 2019, Correa et al., 2022, Robles et al., 2023), it remains necessary to understand the impact of the evolving SIDM potential in the baryons in a fundamental way, particularly in the gravothermal collapse phase, which remains largely unexplored. To advance in this direction, one can remove the complications of cosmological assembly and baryonic physics present in full hydrodynamical simulations and reduce the problem to that of the response of a population of tracer particles responding to a time-dependent SIDM potential. Such a configuration would be particularly useful in understanding the behaviour of baryonic systems devoid of a gaseous component and within a gravitational potential strongly dominated by dark matter, for example, UFDs and central globular clusters (GCs).

This Chapter presents a preliminary study in this direction, particularly its ultimate goal is to develop an analytical framework to predict changes in the main properties (density, velocity dispersion and half-mass radius) of a stellar population during the two key phases of a SIDM halo: cusp-core (expansion) and core-cusp (collapse). As mentioned above, we will focus on two types of stellar systems, UFDs and central GCs, in order to quantify the corresponding expansion and collapse of stars as they respond to the SIDM evolution. GCs located in the centre of dwarf-size haloes are a particularly promising target to maximize the SIDM effect given how compact they are; studying the stability of GCs in these conditions can lead to relevant constraints in the nature of dark matter (see, for example, REF. Marsh and Niemeyer, 2019 in regards to fuzzy DM). Since this project is still in development, we present in this Chapter the framework and results only for the first cusp-core phase and for an example of GC system. At the end of the Chapter, we discuss future analyses of this project.

We study how an SIDM halo evolution affects a population of stars embedded in dwarf-size haloes. We make two key assumptions: i) both the dark matter halo and the stellar distribution are spherically symmetric, and ii) the gravitational potential is dominated by dark matter at all radii and across all times. The latter of these assumptions implies that we can model the evolution of the SIDM halo independently using the gravothermal fluid model described in sec. 2.2. The former of these assumptions means that we can treat the evolution of the stellar distribution as a collection of tracers (we can ignore their self-gravity) responding gravitationally to a time-dependent external gravitational potential, given by the gravothermal fluid model of the SIDM halo.

4.1 Initial conditions and evolution of the SIDM halo

The evolution of the halo is governed by equations 18− 21, which considers a spherically symmetric halo made of a self-gravitating, self-collisional fluid, which is initially under hydrostatic equilibrium. For sufficiently large cross sections, the central region of the SIDM halo, during its evolution, will transition from the LMFP initially and during the cusp-core transformation to the SMFP regime deep in the gravothermal collapse regime. Then, we can write the general expression for conductivity that captures both the LMFP and SMFP stages by combining the respective conductivities from the LMFP (Eq. 23) and SMFP (Eq. 22) regimes to achieve an empirical interpolation which is in principle valid at all regimes:

$$\kappa^{-1} = \kappa_{\rm SMFP}^{-1} + \kappa_{\rm LMFP}^{-1} = \frac{3}{2}\rho \left[\left(a^{-1} b \frac{\lambda^2}{t_r} \right)^{-1} + \left(C \frac{H^2}{t_r} \right)^{-1} \right]^{-1}. \tag{56}$$

with $a = \sqrt{16/\pi}$ for hard-sphere interactions and the coefficient $b = 25/\sqrt{\pi}/32$ calculated perturbatively in Chapman-Enskog theory (Lifshitz and Pitaevskii, 1981).

The set of gravothermal fluid equations, with the conductivity given by Eq.56, can be solved numerically given an initial condition for the radial density profile of the halo $\rho_{\rm ini}(r)$, which then determines directly the initial enclosed mass $M_{\rm ini}(r)$ (through Eq. 18) and velocity dispersion profiles $\nu_{\rm ini}(r)$ (through Eq. 19). The key assumption to set this initial density profile is that dark matter self-scattering is not significant in the first stages of structure formation when the halo first reaches virial equilibrium. This means that the *primordial* SIDM halo is assumed to have the same structure as a CDM halo of the same virial mass. Specifically, CDM haloes are well described by the well-known two-parameter NFW profile (Eq. 9), and thus, we assume:

$$\rho_{\rm ini}(r) = \rho_{\rm NFW}(r) = \frac{\rho_s}{r/r_s(1 + r/r_s)^2}. \tag{57}$$

We can rewrite Eq. (57) in terms of the average halo density $\rho_{\rm avg}$ and the concentration parameter c:

$$\rho_{\rm avg} = \frac{M_{200}}{(4\pi/3) r_{200}^3} = 200 \rho_{\rm crit}, \tag{58}$$

$$\text{and } c = \frac{r_{200}}{r_s}, \tag{59}$$

where the virial quantities, radius and mass, are set by an average density being 200 times the critical density $\rho_{\rm crit}$; the virial mass of the halo, M_{200}, given by:

$$M_{200} = 4\pi \rho_s r_s^3 g(c) = 4\pi \rho_s r_s^3 \left(\ln(1 + c) - \frac{c}{1 + c} \right) \tag{60}$$

Eq. (57) can then be written as:

$$\rho_{\rm ini}(r) = \rho_{\rm NFW}(x) = \left(\frac{c^2}{3g(c)} \right) \frac{\rho_{\rm avg}}{x(1 + cx)^2} \tag{61}$$

where $x = r/r_{200}$. This reparameterization of the density profile (in terms of M_{200} and c) will be more convenient later on, and it also shows more clearly how the NFW profile can be reduced to a one-parameter profile once we consider the tight mass-concentration relation, discussed in detail in Chapter 3.

As a benchmark, we select an SIDM halo with the typical mass and concentration for dwarf galaxies in the field at the edge of the classical dSphs mass-scale. The halo has a mass $M_{200} =$

$10^{10.1}\,\mathrm{M}_\odot$, corresponding to a concentration $c = 12.97$, then the scale density and the scale radius are given by $\rho_\mathrm{s} = 0.0107\ \mathrm{M}_\odot\,/\,\mathrm{pc}^3$ and $r_\mathrm{s} = 3.79$ kpc, respectively. For simplicity, we choose a constant cross section SIDM model with $\sigma_T/m_\chi = 100\ \mathrm{cm}^2\mathrm{g}^{-1}$. The code to solve the gravothermal fluid equations was obtained through direct collaboration with A. Kamada, in preparation for an article with the contents of this Chapter forming an integral part. The code is described in ref. Kamada et al., 2020.

4.2 Time evolution of the SIDM halo: the adiabatic regime

The time evolution of the halo density profile, as well as the evolution of the central density, defined as the density at $r = 10^{-2}r_s$, are shown in Fig. 4.1. In the lower panel, in particular, three stages are distinctive: the initial rapid cusp-core transformation in the first ~ 1 Gyr, the long-lasting quasi-equilibrium cored stage (up to ~ 5 Gyr), and the rapid gravothermal collapse after ~ 9 Gyr.

The ultimate goal is to describe how a gravitational tracer (star) located in the central regions would respond to the evolution of the SIDM halo. To accomplish this, we first need to obtain a simple measure of how fast this evolution occurs since which technique to use to estimate the impact on a tracer depends on such timescale. We construct a simple local timescale that captures how quickly the gravitational potential changes by defining t_ϕ as:

$$t_\phi(r) = \left| \frac{1}{\phi(r)} \frac{d\phi(r)}{dt} \right|^{-1} \tag{62}$$

where $\phi(r)$ is the gravitational potential at the radius r. To obtain $\phi(r)$ due to a spherical mass distribution $\rho(r')$, we sum the contributions from all shells with mass $dM(r') = 4\pi\mathrm{G}\rho(r')r'^2dr'$ inside and outside of r as follows (Binney and Tremaine, 2008):

$$\phi(r) = -4\pi\mathrm{G}\left[\frac{1}{r}\int_0^r dr'\rho(r')r'^2 + \int_r^\infty dr'\rho(r')r'\right]. \tag{63}$$

The gravitational potential as a function of radius and the timescale for its change in time across the evolution of the SIDM halo is shown in the upper and lower panels of Fig. 4.2, respectively. The timescale is quite short at the beginning in the central region, gradually increasing until the core is formed. This quantifies the rapid cusp-core transformation seen in Fig. 4.1 to be of the order of 400 Myrs at $r/r_s = 10^{-2}$. Afterwards, it remains quite long (of order 400 Gyrs) while the core is in the isothermal quasi-equilibrium state. The timescale drops again during the core-cusp collapse, reaching once more sub-Gyr values in the central region.

The period of a circular orbit within the potential ϕ, t_orb, is a relevant characteristic timescale to compare to t_ϕ, since it is a simple measure of the time it takes for a tracer (star) to make a complete orbit. This orbital time is defined as follows:

$$t_\mathrm{orb} = \frac{r}{V_\mathrm{c}(r)} = \frac{r}{\sqrt{\dfrac{\mathrm{G}M(<r)}{r}}} \tag{64}$$

where $V_c(r)$ is the circular velocity. Fig. 4.3 shows the orbital timescale as a function of radius. This timescale shows less variation than t_ϕ across the evolution of the halo. In the central region, $r/r_s = 10^{-2}$, it changes from around 40 Myrs at $t = 0$ to around 200-300 Myrs during the isothermal core phase. Once the gravothermal collapse phase is triggered, t_orb drops quickly down to 10 Myrs by the end of the evolution at $t = 10$ Gyr.

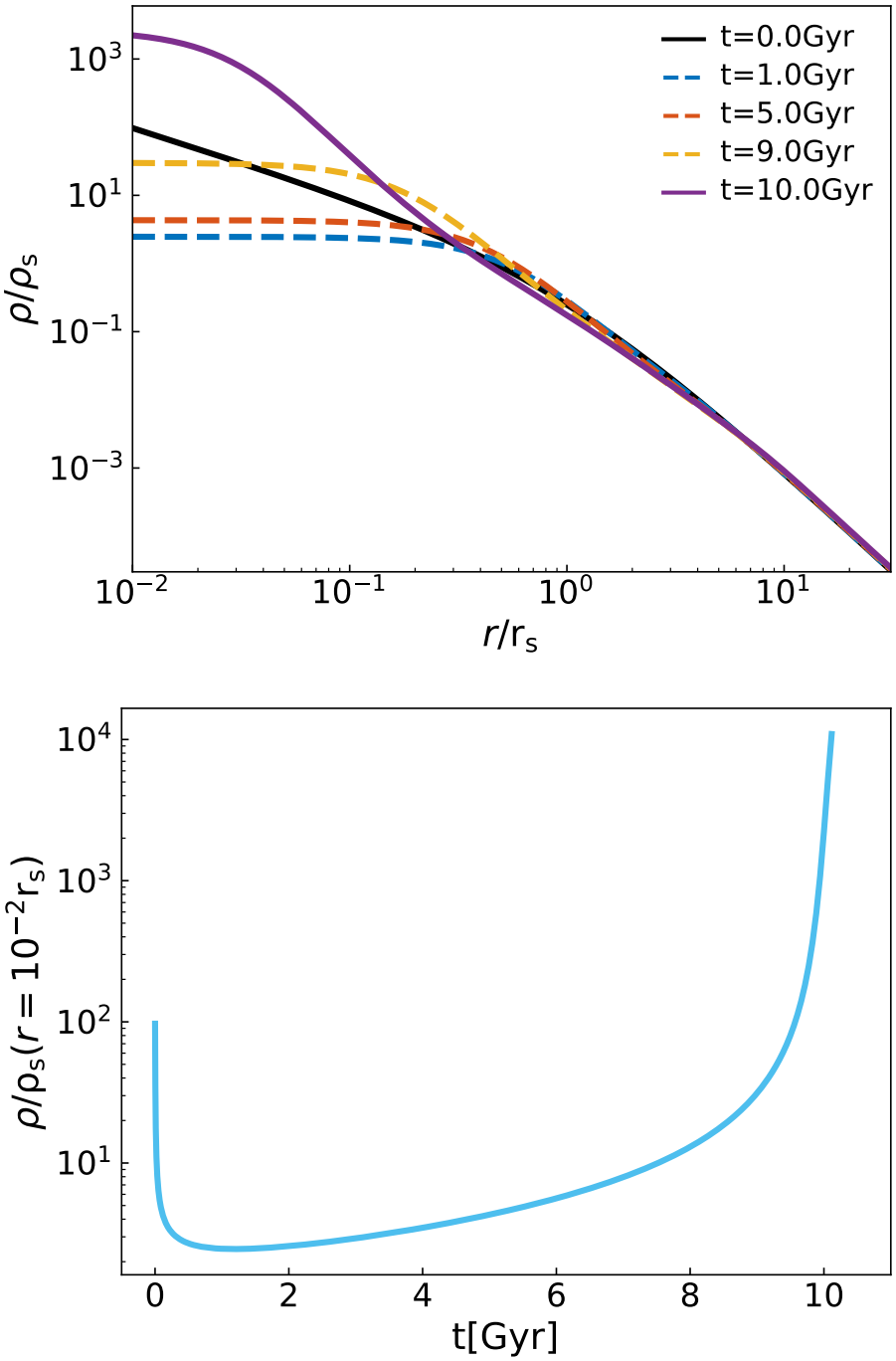

Figure 4.1: *Upper panel:* Evolution of the density profile of SIDM halo of $M_{200} = 10^{10.1}\,\mathrm{M}_\odot$ and $c_{200} = 12.97$. The density and radius are dimensionless, scaled by the characteristic density ρ_s and scale radius r_s, respectively, of the initial NFW profile shown as a black solid line. Dashed lines show the evolution at different timescales: blue (1 Gyr, roughly corresponding to the epoch when the core has its maximum size), orange (5 Gyr, corresponding to the epoch where the long-lived quasi-equilibrium state of the isothermal core begins to end), and yellow (9 Gyr, when the collapse phase is well underway). The solid violet line at 10 Gyr corresponds to a stage where the very central regions have entered the SMFP regime. *Lower panel:* Evolution of the central density defined at $r/r_s = 10^{-2}$, scaled to the characteristic density of the initial NFW halo.

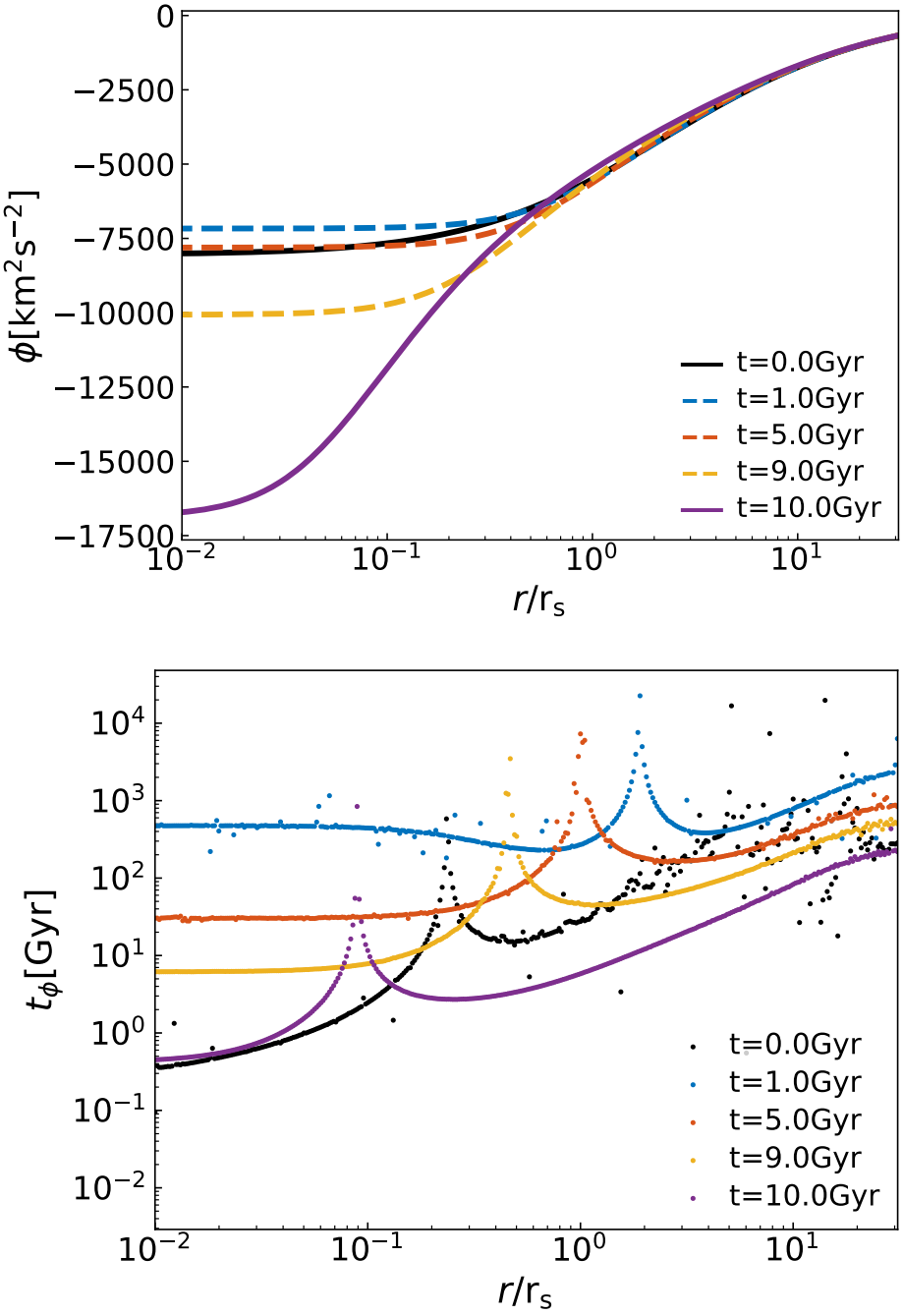

Figure 4.2: *Upper panel:* Evolution of the gravitational potential corresponding to the SIDM halo profile shown in Fig. 4.1 (at the same corresponding times) as a function of the dimensionless radius (Eq. 63). *Lower panel:* The local timescale measuring the change in gravitational potential as defined in Eq. 62. Notice that the timescale tends to infinity at a characteristic radius where the potential is essentially fixed across consecutive timesteps. Such a characteristic radius is related to the core radius in the density profile. The noise in the data is caused by numerical errors in calculating the derivative due to the sparsity in the data across the radial direction and across time. The "peaks" occur at the points where the derivative equals zero, i.e. at the radii where the gravitational potentials at two consecutive time steps intersect.

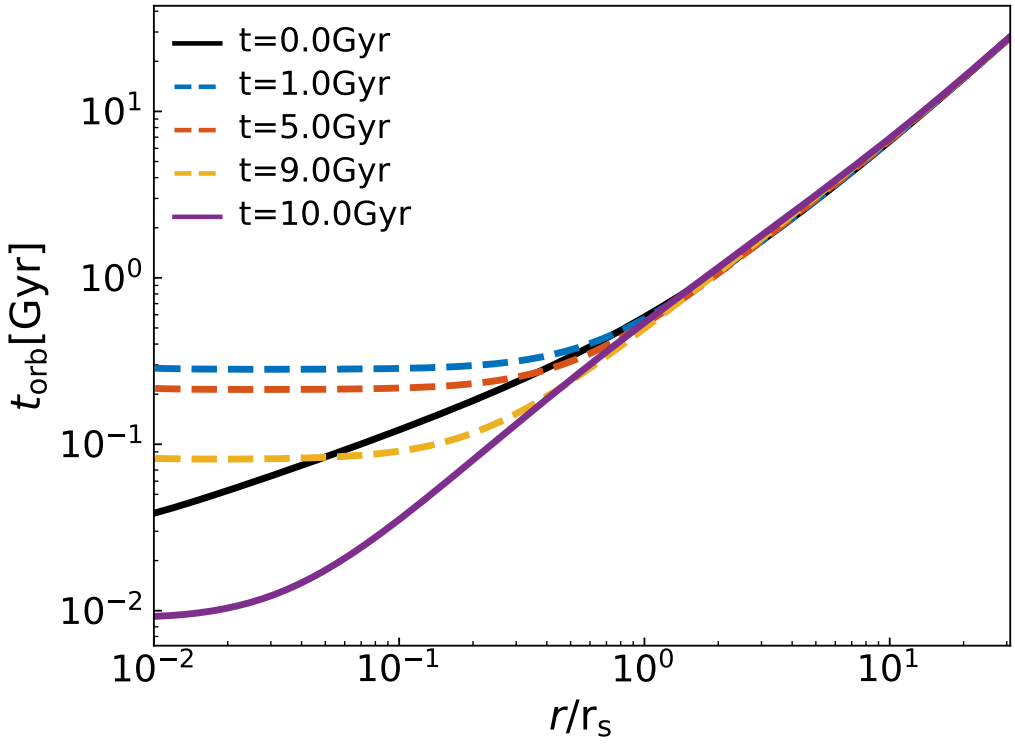

Figure 4.3: Orbital timescale (Eq. 64) corresponding to the SIDM halo profile shown in Fig. 4.1 (at the same corresponding times) as a function of the dimensionless radius.

We calculate the ratio of the timescales for the change in time of the gravitational potential and the orbital timescale:

$$\Delta \equiv \frac{t_\phi}{t_{\rm orb}} \tag{65}$$

and present it in Fig. 4.4. When a particle's orbital timescale is shorter than the timescale for the change in gravitational potential, we assume that the evolution is adiabatic; otherwise, it is impulsive. We can see that across all times and all radii, the evolution is firmly in the adiabatic regime: although t_phi is short during the initial cusp-core transformation, it is never as short as $t_{\rm orb}$, even deep within the central region, during the core collapse phase, the core-collapse phase, t_ϕ becomes shorter and shorter, but it does not catch up with $t_{\rm orb}$.

This can be clearly seen in the lower panel of Fig. 4.4, where we compare the two timescales deep in the halo centre where $r/r_{\rm s} = 10^{-2}$; one can see that for most of the time $\Delta > 10$, which strongly suggests that stellar orbits would respond adiabatically to the evolution of SIDM haloes both within the cusp-core transformation and during the gravothermal collapse phases) at least within the order of magnitude of the cross sections of interest and within a Hubble time.

4.3 Stellar response in the cusp-core transformation: the adiabatic regime

Having established that the tracers would respond adiabatically as the SIDM halo evolves, it is then possible to calculate analytically how a stellar distribution with a certain initial profile would evolve using adiabatic invariants. Although the adiabatic regime is valid across the whole evolution,

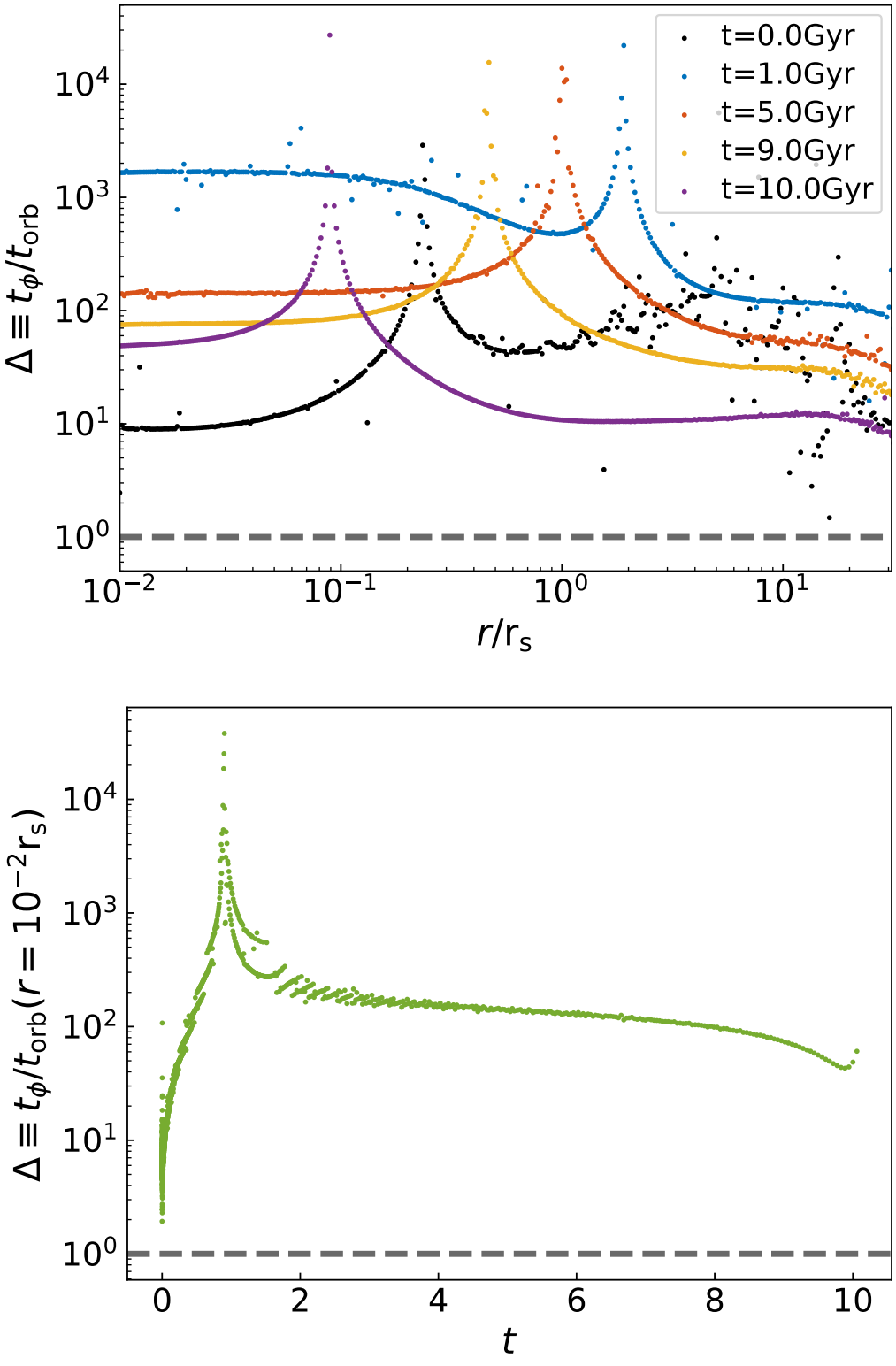

Figure 4.4: *Upper panel:* Ratio of the timescale for changes in the potential and the orbital timescale (Δ in Eq. 65) corresponding to the SIDM halo profile shown in Fig. 4.1 (at the same corresponding times) as a function of the dimensionless radius. The horizontal dashed grey line corresponds to $\Delta = 1$ and represents the threshold above which we define the evolution to be adiabatic and below it to be impulsive. *Lower panel:* Time evolution of Δ at $r/r_s = 10^{-2}$.

we concentrate in this Thesis only on the first cusp-core transformation phase since the results for the gravothermal collapse phase were still in preparation by the time this Thesis was written. The procedure described below follows closely Section 4.6.1 of Binney and Tremaine, 2008, where a similar problem is discussed: the adiabatic evolution of an isothermal distribution of stars to the growth in time of a point mass (black hole).

To simplify the calculations, we assume that the initial distribution of stars is isothermal with a distribution function given by:

$$f_{\rm in} = \frac{\rho_{0,\rm in}}{(2\pi\sigma^2_{0,\rm in})^{3/2}} e^{-H_{in}/\sigma^2_{0,\rm in}}, \tag{66}$$

where $\rho_{0,\rm in}$ and $\sigma_{0,\rm in}$ are the initial central values of the density and velocity dispersion for the stellar distribution, respectively, and H_{in} is the initial Hamiltonian. Notice that the assumption of an isothermal distribution is a good assumption in the innermost regions of dSphs and Globular Clusters, which are typically well-fitted by a Plummer profile, which is asymptotically isothermal at $r \to 0$.

The initial gravitational potential, which we assume to be dominated by dark matter and given by the NFW profile $\phi_{\rm TOT,in} \sim \phi_{\rm DM,in} \sim \phi_{\rm NFW}$. Since we are only interested in the evolution of the central regions ($r \ll r_{200}$), the NFW potential can be approximated as a linear function of the radius:

$$\phi_{\rm TOT,in}(r \ll r_{200}) \sim \phi_{\rm NFW}(r \ll r_{200}) \sim Ar = \left(\frac{c^2}{2k(c)}\frac{V^2_{200}}{r_{200}}\right) r \tag{67}$$

where $k(c)$ is a function of concentration given below Eq. 26 in Chapter 3, and $V^2_{200} = GM_{200}/r_{200}$ is the virial velocity of the halo.

Expressions for the Hamiltonian in terms of action-angle variables for power-law potentials were derived by Williams et al., 2014. For the NFW case, a good approximation to the Hamiltonian is given by (with a maximum of $\sim 1\%$ errors):

$$H_{\rm in}(J_r, L) = H_{\rm NFW}(J_r, L) \sim \frac{3}{2} A^{2/3} \left(L + \frac{\pi}{\sqrt{3}} J_r\right)^{2/3} \tag{68}$$

where J_r is the radial action and L is the total angular momentum of the tracer particle.

The relevance of writing the Hamiltonian in terms of action-angle variables is clear in the adiabatic regime since both J_r and L are adiabatic invariants for spherical potentials (Chapter 3.6 of Binney and Tremaine, 2008). This means that we can assume $L = L_{in} = L_{end}$ and $J_r = J_{r,in} = J_{r,end}$ where the subscript "end" refers to any time during the entire evolution of the halo. In this case, we are discussing only the cusp-core transformation phase. Thus, we take the "end" time to be the time when the SIDM core has reached its maximum size. At this time, the gravitational potential is no longer given by Eq. 67, but it still has a power law form since now the dark matter distribution is isothermal $\rho_{\rm DM,end}(r \ll r_{200}) \sim \rho_{\rm core}$, where $\rho_{\rm core}$ is the core density of the SIDM halo when it reaches its maximum size, which is given by (Outmezguine et al., 2022):

$$\rho_{\rm core} \sim 2.4\rho_s \tag{69}$$

A concern here could be that since the central dark matter density has dropped substantially relative to the original values in the NFW cusp, it might drop below the value of the central stellar density $\rho_{0,\rm end}$, but even if that were to be the case, the total central density would remain flat and thus, the total potential would still be harmonic, i.e., given by:

$$\phi_{\rm TOT,end}(r \ll r_{200}) \sim \frac{1}{2}\Omega^2 r^2 \tag{70}$$

where Ω^2 is related to the final total central density through Poisson's equation:

$$\nabla^2\phi_{\rm TOT,end}(r \ll r_{200}) = 3\Omega^2 = 4\pi G\rho_{0,\rm end}\Delta_\rho \tag{71}$$

where $\Delta_\rho = (1+\rho_{\rm core}/\rho_{0,\rm end})$. The Hamiltonian for the harmonic potential in Eq. 70 is fully analytical and is given (Binney and Tremaine, 2008):

$$H_{\rm end}(J_r, L) = \Omega\,(2J_r + L) \tag{72}$$

On the other hand, in terms of the phase-space variables of the tracer particle:

$$H_{rmend}(r \ll r_{200}, \vec{v}) = \frac{1}{2}v^2 + \phi_{\rm TOT,end}(r \ll r_{200}) \tag{73}$$

Combining Eqs. 72 and 73, we can write the radial action as:

$$J_r = \frac{1}{2\Omega}\left(\frac{1}{2}v^2 + \frac{1}{2}\Omega^2 r^2\right) - \frac{L}{2} \tag{74}$$

Since radial actions are adiabatic invariants and since $L = rv\sin\Psi$ where Ψ is the angle between the radius and velocity vectors, we can substitute Eq. 74 in 68:

$$H_{\rm in}(r \ll r_{200}, \vec{v}) \sim \frac{3}{2}A^{2/3}\left[\left(1 - \frac{\pi}{2\sqrt{3}}\right)rv\sin\Psi + \frac{\pi}{2\Omega\sqrt{3}}\left(\frac{1}{2}v^2 + \frac{1}{2}\Omega^2 r^2\right)\right]^{2/3} \tag{75}$$

We can simplify this expression further by noticing that the first anisotropic term, proportional to the angular momentum, has a much smaller prefactor than the isotropic term; in addition, L will be small for the tracers within the innermost regions (see also Williams et al., 2014). Finally, since we are interested if we only consider the limit $r \to 0$ to zeroth order, we can finally approximate:

$$H_{\rm in}(r \to 0, \vec{v}) \sim \frac{3}{2}A^{2/3}\left[\frac{\pi}{2\Omega\sqrt{3}}\left(\frac{1}{2}v^2\right)\right]^{2/3} \tag{76}$$

Notice that it should be possible to make a Taylor expansion of Eq 75 on radius to expand the radial range of validity of our final results. Since the changes in the gravitational potential of the SIDM halo are adiabatic, and thus J_r and L are adiabatic invariants, the distribution function preserves the same form as it had initially. Thus, we can write:

$$f_{\rm end} = f_{\rm in} \sim Ce^{-Gv^{4/3}} \tag{77}$$

where C and G are given by:

$$C = \frac{\rho_{0,\rm in}}{(2\pi\sigma^2_{0,\rm in})^{3/2}} \tag{78}$$

$$G = \frac{3}{2\sigma^2_{0,\rm in}}\left(\frac{\pi A}{4\Omega\sqrt{3}}\right)^{2/3} \tag{79}$$

Since Eq. 77 gives the asymptotic distribution of stars (treated as tracers) in the innermost region at the end of the cusp-core transformation of the SIDM halo (maximum core size), we can then compute the central density of the stars $\rho_{0,\rm end}$ at this epoch:

$$\rho_{0,\rm end} = \int f_{\rm end}d^3\vec{v} = 4\pi\int_0^\infty v^2 f_{\rm in}dv \sim 4\pi C\int_0^\infty v^2 e^{-Gv^{4/3}}dv \tag{80}$$

where in the middle equality, we are using the fact that the distribution function is isotropic (as described above) and for simplicity, we do not put a cutoff to the maximum velocities in the central

regions since the integral is dominated by a relatively narrow region around the integrand. The integral in Eq. 80 is analytical, and after using the equations for A, C and G we find:

$$\left(\frac{\rho_{0,\mathrm{end}}}{\rho_{0,\mathrm{in}}}\right) = \left(\frac{2^{21/4}}{\sqrt{3}\pi^2}\Gamma\left(9/4\right)\right)\left(\frac{k(c)}{c^2}\frac{\Omega\sigma_{0,\mathrm{in}}r_{200}}{V_{200}^2}\right)^{3/2} \tag{81}$$

where Γ is the gamma function. This equation can be rewritten in a more convenient form by using the equation that relates Ω to the central total density (Eq. 71) and by using the average density of the halo (Eq. 58):

$$\left(\frac{\rho_{0,\mathrm{end}}}{\rho_{0,\mathrm{in}}}\right) = \left(\frac{2^{21/4}}{\sqrt{3}\pi^2}\Gamma\left(9/4\right)\right)^4\left(\frac{\rho_{0,\mathrm{in}}}{\rho_{\mathrm{avg}}}\right)^3\Delta_\rho^3\left(\frac{\sigma_{0,\mathrm{in}}}{V_{200}}\right)^6\left(\frac{k(c)}{c^2}\right)^6 \tag{82}$$

Notice that this equation is written in a form that can give a prediction for $\rho_{0,\mathrm{end}}$ in terms of the initial conditions for the SIDM halo (i.e. the NFW parameters) and for the stellar distribution ($\rho_{0,\mathrm{in}}$ and $\sigma_{0,\mathrm{in}}$) *if* the term Δ_ρ can be ignored (see discussion further below).

Although Eq. 82 could, in principle, be used given the initial conditions for the stellar distribution, it is important to take into account that in the systems of interest (e.g. dSphs and GCs), the stars are in dynamical equilibrium within the halo. A simple way to introduce this condition is discussed in Amorisco and Evans, 2011 who found that for power-law potentials, there is a simple power-law correlation between the central velocity dispersion of the stellar distribution and its half-mass radius $r_{1/2}$ with a constant of proportionality that only depends on the properties of the halo. For an isothermal distribution function for an NFW-like potential in the centre, they find:

$$\left(\frac{r_{1/2}}{r_{\mathrm{s}}}\right) \sim 2.027\left(\frac{\sigma_0^2}{\phi_0}\right) \tag{83}$$

where $\phi_0 = cV_{200}^2/2k(c)$; we can then write for the initial conditions:

$$\sigma_{0,\mathrm{in}}^2 = \left(\frac{1}{2.027}\right)\left(\frac{c^2V_{200}^2}{2k(c)}\right)\left(\frac{r_{1/2}}{r_{200}}\right) \tag{84}$$

A final consideration is to note that we can write:

$$\frac{k(c)}{c^2} = \frac{c}{3}\left(\frac{\rho_{\mathrm{avg}}}{\rho_{\mathrm{s}}}\right) \tag{85}$$

Using Eqs. 84 and 85 in Eq. 82 we can finally write:

$$\begin{aligned}\left(\frac{\rho_{0,\mathrm{end}}}{\rho_{0,\mathrm{in}}}\right) &= \left(\frac{2^{21/4}}{\sqrt{3}\pi^2}\Gamma\left(9/4\right)\right)^4\left(\frac{1}{216}\right)\left(\frac{1}{2.027}\right)^3\left(\frac{\rho_{0,\mathrm{in}}}{\rho_s}\right)^3\Delta_\rho^3\left(\frac{r_{1/2}}{r_s}\right)^3 \\ &\sim 0.0225\left(\frac{\rho_{0,\mathrm{in}}}{\rho_s}\right)^3\Delta_\rho^3\left(\frac{r_{1/2}}{r_s}\right)^3,\end{aligned} \tag{86}$$

which gives the final prediction in terms of the characteristic densities and scales of the halo and the stellar distribution.

In our assumptions, the stellar distribution must be spherically symmetric and centred in the halo, we could then consider dSphs or central star clusters as good targets that satisfy this condition. In addition, since Eq. 86 scales strongly with the size of the stellar system, $\propto r_{1/2}^3$ for a fixed halo, a compact star cluster would have a stronger reduction of $(\rho_{0,\mathrm{end}}/\rho_{0,\mathrm{in}})$ compared to a more extended dSph. We then consider the specific example of the globular cluster in the dwarf galaxy Eridanus II, which is close to its centre and has a half-mass radius $r_{1/2} = 13$ pc and a stellar mass

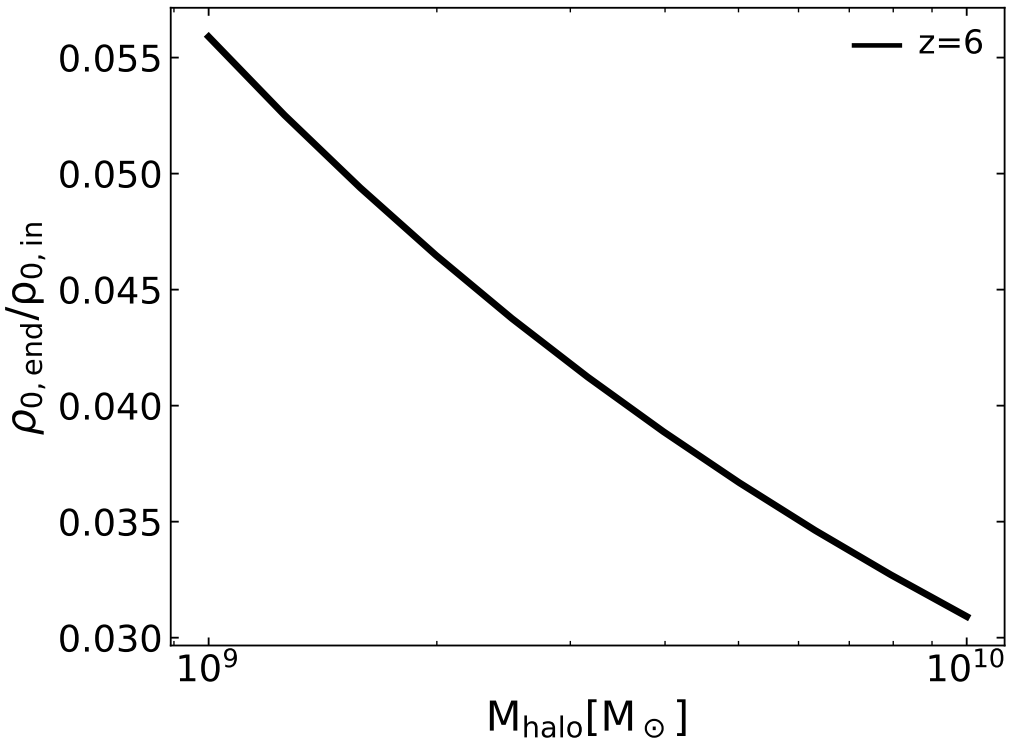

Figure 4.5: The change in the central density of stars (assumed to be isothermal) in the central globular cluster in Eridanus II ($M_{\rm GC} \sim 5.2 \times 10^3\,{\rm M}_\odot$ and $r_{1/2}$ pc) calculated using the adiabatic approximation (Eq. 82). The horizontal axis is the halo mass of the progenitor of Eridanus II at $z = 6$, roughly corresponding to the estimated age of the globular cluster.

of $M_{\rm GC} \sim 5.2 \times 10^3\,{\rm M}_\odot$ (Weisz et al., 2023). The age of the Eridanus II cluster is found to be very old, ~ 13 Gyr, and thus is considered a relic from the reionization era. In addition, ref. Simon et al., 2021 found that the structure of the GC is well fitted by a Plummer profile, which means that we can connect its stellar mass and half-mass radius to its central density:

$$\rho_0 = \frac{3M_{\rm GC}}{4\pi\left(r_{1/2}/1.3\right)^3} \tag{87}$$

Given the old age of the GC in this example, we consider, as a first simplification, that the GC had the same properties observed today as it did in formation time. Thus we can use Eq. 87 to set $\rho_{0,\rm in} = \rho_0$ as an input in Eq. 86 (and we set $r_{1/2} = 13$ pc). For the properties of the halo, we consider a range of masses between $10^9\,{\rm M}_\odot$ and $10^{10}\,{\rm M}_\odot$, which covers a broad range of expected halo masses for the progenitor of the dwarf galaxy Eridanus II. This is estimated given the inferred halo mass of this galaxy today ($7 \times 10^9 - 3 \times 10^{10}\,{\rm M}_\odot$; see ref. Boylan-Kolchin, 2017), and given the estimated age of its central GC (~ 13 Gyr, i.e., $z \sim 6-7$); we can thus assume that the halo mass of the progenitor of Eridanus II is closer to $10^9\,{\rm M}_\odot$. To be specific, we estimate the concentration of haloes at $z = 6$ using the model by Ludlow et al., 2016 described in Chapter 3 and then use masses and concentration to obtain r_s and ρ_s, which are then used as input in Eq. 86. Fig.4.5 shows the result of this exercise where the ratio of final to initial densities for the GC in Eridanus II is shown. The predicted decrease in central density due to the cusp-core transformation is substantial, about a factor of 20.

Based on these preliminary results, the plan is to use the same formalism of adiabatic invariants to compute the change in the stellar density during the second stage of the evolution of the SIDM halo:

core-cusp transformation (gravothermal collapse). The procedure, in this case, is entirely analogous to the one described here with a few differences: i) the initial condition is now given by the final configuration in the previous stage; ii) we need to find the appropriate formula for the Hamiltonian of the final stage based on the asymptotic behaviour of the power-law density profile in the inner part of the collapsed core. We also plan to compute the impact on the central velocity dispersion and half-mass radius in both stages of the SIDM halo evolution, i.e., the equations for these two quantities that are analogous to Eq. 86. This can be done by noticing that the velocity dispersion can be found from the second moment of the distribution function, while the half-mass radius can be connected to the velocity dispersion using a similar relation to that in Eq. 86 for the appropriate potential following Amorisco and Evans, 2011.

After completing the tasks in the previous paragraph, we will have a complete formalism that can predict the adiabatic evolution of the central properties of stellar systems in SIDM-dominated potentials. We plan to apply this formalism across a parameter space of stellar masses and sizes covering the relevant region for central GCs and UDFs. With the predicted changes in density, velocity dispersion, and size, we plan to obtain constraints for the SIDM model, particularly based on the stability of central GCs.

5 Free-streaming in voids

This chapter is based on the following article:

The impact of free-streaming on dwarf galaxy counts in low-density regions

Published in Monthly Notices of the Royal Astronomical Society, stae1519, 18 June 2024

Authors:

Tamar Meshveliani[1], Mark R. Lovell[1,2,3], Robert A. Crain[4] and Joel Pfeffer[5]

[1]Centre for Astrophysics and Cosmology, Science Institute, University of Iceland, Dunhagi 5, 107 Reykjavik, Iceland
[2] Institute for Computational Cosmology, Durham University, South Road, Durham DH1 3LE, United Kingdom
[3] Department of Physics, Durham University, South Road, Durham DH1 3LE, United Kingdom
[4]Astrophysics Research Institute, Liverpool John Moores University, 146 Brownlow Hill, Liverpool L3 5RF, UK
[5]Centre for Astrophysics & Supercomputing, Swinburne University, Hawthorn, VIC 3122, Australia

Abstract

We study the statistics of dwarf galaxy populations as a function of environment in cold dark matter (CDM) and warm dark matter (WDM; sterile neutrino model mass $M_{\rm s} = 7.1$ keV; half-mode mass $M_{\rm hm} = 6.3 \times 10^8$ $\mathrm{M}_\odot$; thermal relic equivalent mass $m_{\rm th} = 2.8$ keV) cosmogonies, using the EAGLE galaxy formation model in two counterpart simulations. We measure the abundance of dwarf galaxies within 3 Mpc of DM haloes with a present-day halo mass similar to the Milky Way, finding that the number of galaxies $M_* > 10^7$ $\mathrm{M}_\odot$ is nearly identical for WDM and CDM. However, the cumulative mass function becomes shallower for WDM at lower masses, yielding 50 per cent fewer dwarf galaxies of $M_* \gtrsim 10^5$ $\mathrm{M}_\odot$ than CDM. The suppression of low-mass halo counts in WDM increases significantly from high-density to low-density regions for haloes in the $[0.5, 2] \times M_{\rm hm}$ range. The fraction of haloes hosting resolvable galaxies ($M_* \gtrsim 10^5$ $\mathrm{M}_\odot$) also diverges from overdense to underdense regions for $M > 2M_{\rm hm}$, as the increased collapse delay at small densities pushes the collapse to after the reionization threshold. However, the stellar mass of WDM haloes at $[0.5, 2] \times M_{\rm hm}$ is 30 per cent higher per unit halo mass than CDM haloes in underdense regions. We conclude that the suppression of galaxies with $M_* \gtrsim 10^5\,\mathrm{M}_\odot$ between WDM and CDM is independent of density: the suppression of halo counts and fraction of luminous haloes is balanced by an enhancement in stellar mass–halo mass relation.

5.1 Introduction

The cold dark matter (CDM) model has been highly successful in explaining the Universe's large-scale structure, including the predictions for the cosmic microwave background (Planck Collaboration, 2014) and the large scale distribution of galaxies (Eisenstein et al., 2005). One of its key predictions is the existence of dark matter (DM) particles whose streaming velocities are negligible for most astrophysical considerations. The greatest uncertainty in the zero-streaming velocity paradigm is expected for dwarf galaxies, where the constraints on free-streaming are weakest. Compared to other classes of galaxies, it is also the case that the halo density profiles of faint dwarf galaxies are subject to a weaker influence from supernova feedback (Di Cintio et al., 2014b). Therefore, the dwarf galaxies of the Local Group (LG) and their haloes have become popular test cases for the impact of cosmological models on small-scale structures (Polisensky and Ricotti, 2011, Lovell et al., 2014, Vogelsberger et al., 2012a, Bozek et al., 2016, Horiuchi et al., 2016, Cherry and Horiuchi, 2017, Kim et al., 2018, Newton et al., 2018, Macciò et al., 2019, Nadler and DES Collaboration, 2020, Enzi et al., 2021, Nadler et al., 2021b).

For instance, there is a reported mismatch between observations and the predictions of CDM N-body simulations for the abundance and kinematic properties of the Milky Way's (MW's) satellites. The inner regions of several bright MW satellite galaxies are measured to be DM-dominated yet are less dense than is predicted by N-body CDM simulations of MW-analogue haloes, the well-known 'Too Big To Fail' problem (Boylan-Kolchin et al., 2011, 2012). Another challenge, known as the cusp-core problem, states that central regions of several MW satellites are more accurately described by roughly constant radial density profiles than the steep inner density slope predicted for standard CDM haloes (Walker and Peñarrubia, 2011a). Finally, it is also unclear whether galaxy formation models based on CDM can predict accurately the number of faint, isolated dwarf galaxies in the LG (Kim et al., 2018). It is anticipated that astrophysical processes, including reionization and feedback from the formation and evolution of stars will play a crucial role in shaping the LG dwarf population (e.g. Governato et al., 2012, Sawala et al., 2016c, Lovell et al., 2017), but the simulations representing the current state-of-the-art, such as APOSTLE (Fattahi et al., 2016b) overpredict the number of LG galaxies of stellar mass $> 10^5$ $\mathrm{M}_\odot$ by over 50 per cent (Fattahi et al., 2020). In practice, modelling these astrophysical processes on small scales is very complex, and a substantial number of studies have indicated that the inclusion of baryons alleviates the small scale-problems (Brooks et al., 2013, Di Cintio et al., 2014b, Wetzel et al., 2016, Bullock and Boylan-Kolchin, 2017a, Kim et al., 2018, Garrison-Kimmel et al., 2019b, Nadler and DES Collaboration, 2020, Sales et al., 2022).

A further challenge to the CDM model is that none of its particle physics candidates have been directly observed or detected by experiments. Collider searches have yet to show any evidence for DM production *Aaboud et al., 2018, Sirunyan and CMS Collaboration, 2018) and similarly underground direct detection experiments have not identified a conclusive set of DM collision events, either for supersymmetric weakly interacting massive particles (Aprile et al., 2018, Lanfranchi et al., 2021) or for QCD axions (Rosenberg, 2015, Du et al., 2018). Taken together with the inconclusive nature of gamma-ray indirect detection efforts (Hooper and Goodenough, 2011, Albert et al., 2017), the identification of DM in experiments remains an outstanding problem.

Given the dual challenges posed to CDM – the discrepancies at small scales and the lack of evidence for its DM particle in experiments – there is strong motivation to consider other DM candidates that can address these challenges simultaneously. One such candidate is the resonantly-produced sterile neutrino (Shi and Fuller, 1999). This candidate is part of a standard model extension called the neutrino Minimal Standard Model (νMSM; Asaka and Shaposhnikov, 2005, Boyarsky et al., 2009), which is well motivated from a particle physics perspective in that it has the potential to explain baryogenesis and neutrino flavour oscillations as well as supply a DM candidate. It belongs to the warm DM (WDM) subset of DM candidates in that it exhibits a significant primordial velocity distribution,

erases small dwarf galaxy-mass perturbations in the early Universe, and subsequently produces a cutoff in the linear fluctuation power spectrum. This cutoff impacts the properties of dwarf galaxies in several ways relevant to the CDM small-scale challenges, including delaying their formation time (Lovell et al., 2012), lowering their central densities (Lovell et al., 2012), and reducing their number density (Colín et al., 2000, Bode et al., 2001, Polisensky and Ricotti, 2011).

Another compelling aspect of the resonantly-produced sterile neutrino is that it has a decay channel that generates an X-ray photon and is, therefore, subject to indirect detection constraints. The decay rate of the sterile neutrinos is set in part by their mixing angle, $\sin^2(2\theta)$, which also plays a role in setting the free-streaming length. The detection of an X-ray decay signal, therefore, determines the power spectrum cutoff, enabling this detection to be probed with measurements of dwarf galaxy counts and densities. One such signal is an unexplained 3.55 keV X-ray line reported in galaxy clusters, the M31 galaxy, and the Galactic Centre (Bulbul et al., 2014, Boyarsky et al., 2014, Hofmann and Wegg, 2019; see Anderson et al., 2015, Jeltema and Profumo, 2016, Dessert et al., 2020, 2023 for alternative interpretations that include uncertainties in the X-ray background modelling and the proposed contribution of charge exchange). The sterile neutrino decay interpretation is consistent with a mixing angle in the range $[2, 20] \times 10^{-11}$, which corresponds to a cutoff scale wavenumber $k \sim [7, 13]\ h\mathrm{Mpc}^{-1}$ (Lovell, 2023b), therefore adopting this model we have a fixed WDM scale at which to test the sterile neutrino as an alternative solution to the CDM small-scale challenges. We note that multiple papers have reported thermal-relic WDM constraints that indicate our sterile neutrino model may be proved to be incompatible with observations, particularly the inferred number of MW satellite galaxies (see Schneider, 2016, Cherry and Horiuchi, 2017, Iršič et al., 2017, 2024, Hsueh et al., 2020, Gilman et al., 2020, Banik et al., 2021, Nadler and DES Collaboration, 2021, Nadler et al., 2021a, Enzi et al., 2021, Newton et al., 2021, Zelko et al., 2022, Villasenor et al., 2023, for a comprehensive list). The future Vera C. Rubin Observatory will play a crucial role in verifying these satellite count estimates and thus determine whether resonantly produced sterile neutrinos are indeed a viable dark matter candidate.

Cosmologically underdense regions present an attractive and relatively unexplored regime in which to uncover divergent predictions of CDM and WDM. This regime is of interest because the absence of large scale overdensities means the collapse of DM haloes is governed by small-scale fluctuations, whose absence differentiates WDM from CDM. Lovell, 2024 demonstrated explicitly that halo collapse time – the time at which a halo first becomes massive enough to undergo atomic hydrogen cooling – is delayed in WDM relative to CDM, and the delay becomes longer for progressively lower-mass haloes. It has been shown that the general delay in WDM halo formation leads to lower halo densities (Lovell et al., 2012) and to later reionization times (Bose et al., 2016b); therefore, it may lead to a further suppression over and above that of the halo mass function in voids that could be detected by deep surveys such as Vera C. Rubin Observatory (Ivezić et al., 2019). This change would be relevant for LG dwarf count analyses (e.g. Fattahi et al., 2020), and we should expect the suppression of dwarf galaxies to differ as a function of the local density between different subregions of the LG. In this paper, we will present a qualitative examination of this hypothesis and discuss in our conclusions how to provide a more quantitative test.

The relatively recent emergence of galaxy formation models capable of yielding galaxy populations with broadly realistic properties (see, e.g. Crain and van de Voort, 2023, and references therein) affords an exciting opportunity to compare the outcomes of 'paired' simulations that use a fixed galaxy formation model, and whose initial conditions have matched phases thus differing only in terms of the adopted power spectrum. Here, we use such simulations to understand the relationship between the statistics and properties of dwarf galaxy populations as a function of the local overdensity in the CDM and WDM cosmogonies, with a particular focus on how this change may alleviate the discrepancy between observed dwarf galaxy counts and the predictions of CDM simulations of the LG highlighted by (Fattahi et al., 2020). We select our WDM model from the set of models favoured by the reported

3.55 keV line, which yields a preferred halo suppression scale independent of structure formation considerations, and conduct a new cosmological hydrodynamical simulation of galaxy formation that is a WDM partner to an existing CDM simulation from the EAGLE project. We consider the impact of changes to the halo mass function, to the fraction of haloes that generate resolvable galaxies (stellar mass $> 10^5$ $\mathrm{M}_\odot$), and the stellar mass–halo mass relation on the likelihood of detecting faint dwarf galaxies with future surveys. We thus test the hypothesis that the abundance of low-mass galaxies is suppressed even further between CDM and WDM in low-density regions than is the case in high-density regions. This potential disparity could be an additional factor contributing to the absence of dwarf galaxies in the LG (see also Bose et al., 2016a, Lovell et al., 2019). The paper is structured as follows: in Sec. 5.2, we present the numerical simulations, the LG galaxy sample and describe our methods; in Sec. 5.3, we present our results, and we draw our conclusions in Sec. 5.4.

5.2 Methods

In Sec. 5.2.1, we provide a brief overview of the simulations we examine. Many aspects of simulations have been described in detail elsewhere, so we restrict ourselves to a brief overview and discuss primarily the novel initial conditions of the WDM simulations. We discuss the WDM model we adopt in Sec. 5.2.2. We briefly outline our Local Group galaxy sample in Sec. 5.2.3.

5.2.1 Numerical simulations

We analyse a pair of high-resolution cosmological hydrodynamical simulations adopting initial conditions with matched phases but differing power spectra, one corresponding to CDM and one to WDM. The simulations were evolved with the EAGLE galaxy formation model (Schaye et al., 2015, Crain et al., 2015), which comprises a suite of subgrid models built into a modified version of the N-body Tree-PM smoothed particle hydrodynamics (SPH) code GADGET-3 (last described by Springel et al., 2005b). The simulations were evolved with mass resolution $8\times$ better than the flagship Ref-L100N1504 EAGLE simulation, yielding a baryon particle mass of $m_\mathrm{g} = 2.26 \times 10^5\,\mathrm{M}_\odot$ and DM particle mass $m_\mathrm{dm} = 1.2 \times 10^6\,\mathrm{M}_\odot$, and hence adopt the 'Recal' model (see Schaye et al., 2015, for further discussion). The CDM simulation, introduced by Bastian et al., 2020 and recently examined in the study of Mason et al., 2023, is a $(34.4\,\mathrm{Mpc})^3$ volume realised at the same resolution as the Recal-L025N0752 simulation introduced by Schaye et al., 2015, thus corresponding to $N = 1034^3$ and adopting the same cosmogony (that of the Planck Collaboration, 2014). This simulation also includes the E-MOSAICS globular cluster formation and evolution model (Pfeffer et al., 2018, Kruijssen et al., 2019), implemented as subgrid routines within EAGLE, but since these routines impart no 'back-reaction' on the galaxy properties we do not discuss them here.

The WDM counterpart simulation, which we introduce in this paper, adopts initial conditions generated using a modified power spectrum (see Sec. 5.2.2), but which are otherwise identical to those of the CDM simulation. The WDM simulation uses the same galaxy formation model adopted as the CDM simulation, with no recalibration of the feedback parameters: it nevertheless yields a present-day galaxy stellar mass function consistent with observations (Oman et al., 2024). WDM simulation consists of 48 MW-analogue haloes. To the best of our knowledge, the WDM simulation is the first cosmological, hydrodynamical simulation of a uniform resolution volume within a WDM cosmogony that is broadly consistent with extant observational constraints. Both simulations adopt a Plummer-equivalent gravitational softening length of $\epsilon_\mathrm{com} = 1.33$ ckpc, limited to a maximum proper length of $\epsilon_\mathrm{prop} = 0.35$ ckpc.

A key aim of our paper is to compare the dwarf galaxy counts of the WDM simulation with those reported by (Fattahi et al., 2020). Those authors analysed the APOSTLE zoom simulations

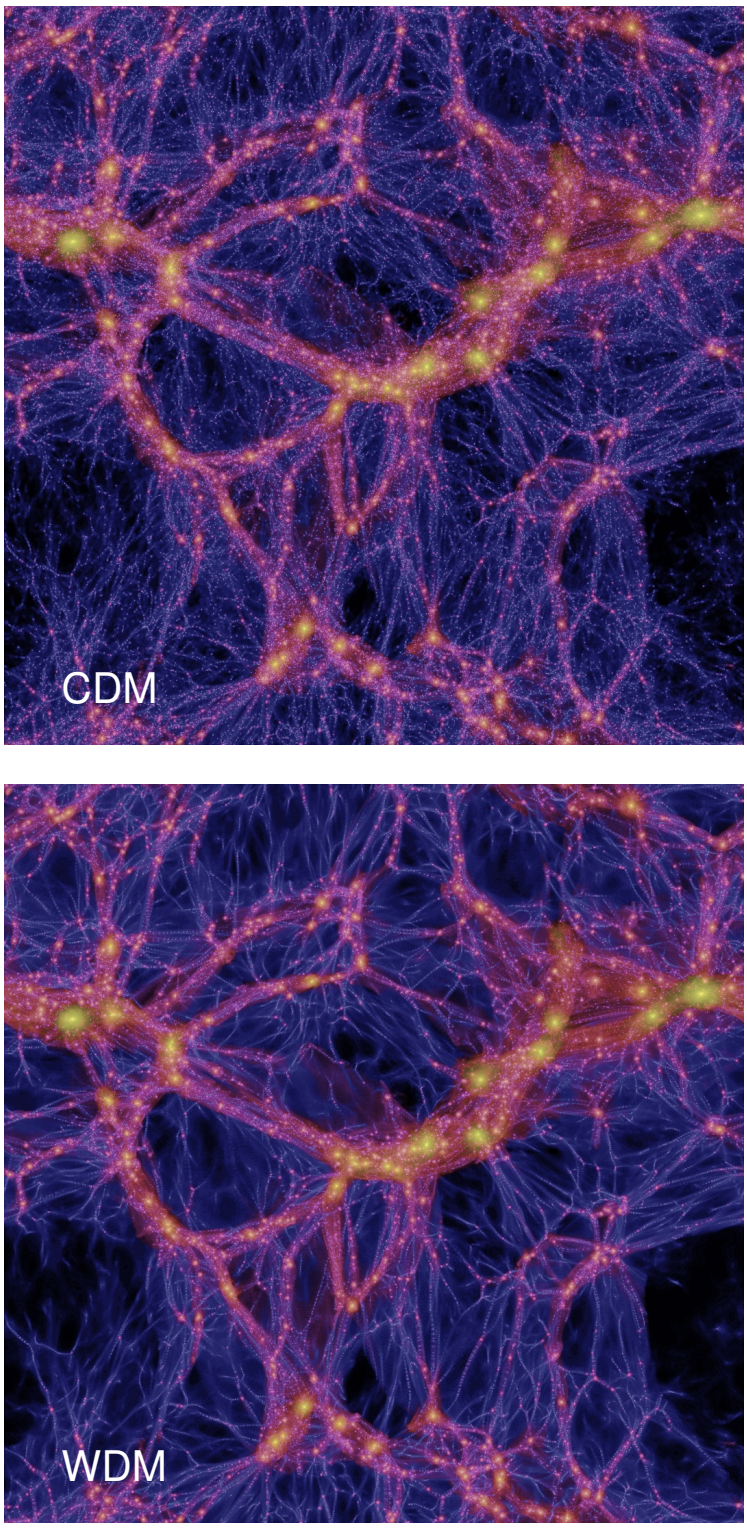

Figure 5.1: Visualization of present-day DM distribution of the two simulations analysed here, CDM (top) and WDM (bottom). Each image is $L = 34.4$ Mpc on a side. Image intensity indicates DM comoving density, and colour indicates velocity dispersion, with blue denoting low-velocity dispersion ($< 5\mathrm{kms}^{-1}$) and yellow high-velocity dispersion ($> 200\mathrm{kms}^{-1}$). The switch from a CDM to a WDM power spectrum clearly preserves large-scale structure but erases small-scale fluctuations.

(Fattahi et al., 2016b, Sawala et al., 2016c) of LG analogues, considering galaxies with stellar mass $> 10^5$ $\mathrm{M}_\odot$. The mass resolution of the simulations considered here is $\simeq 10\times$ poorer than the APOSTLE simulations at their resolution level 'L1'. We must, therefore, be cautious when comparing galaxy counts at a mass scale close to the resolution limit of the simulations. Schaye et al., 2015 showed that resolution-related sampling effects result in an over-abundance of galaxies in EAGLE with fewer than 100 baryonic particles. Lovell et al., 2020 found that the total stellar mass varies significantly with resolution: massive galaxies, with the stellar mass $M_* > 10^9\,\mathrm{M}_\odot$, form over twice as many stars at medium resolution than at high resolution, while the opposite is true for dwarf galaxies, with the high-resolution stellar mass in the range $M_* = [10^7, 10^8]$ $\mathrm{M}_\odot$. In our study, the mass resolution is slightly worse than in Lovell et al., 2020. Therefore, the subhaloes of dwarf galaxies are resolved with 1000 particles. Where galaxies contain only one star particle, we can be confident that the halo does indeed host a galaxy but cannot be confident of its mass. We discuss convergence issues further in the results and conclusions where relevant.

5.2.2 WDM model

The WDM candidate sterile neutrino is characterized by three parameters: its mass, M_s, the mixing angle θ_1, and the lepton asymmetry, L_6, which we define as $L_6 \equiv 10^6(n_{\nu_\mathrm{e}} - n_{\bar{\nu}_\mathrm{e}})/s$, where n_{ν_e} is the lepton number density, $n_{\bar{\nu}_\mathrm{e}}$ the anti-lepton number density and s the entropy density. In principle, setting the value of two of these parameters uniquely determines the value of the third in order to obtain the correct DM abundance. Performing this calculation in practice is complicated by uncertainties in the computation of the lepton asymmetry at a fixed M_s and θ_1 (Ghiglieri and Laine, 2015, Venumadhav et al., 2016, Lovell, 2023b). We adopt $\sin^2(2\theta_1) = 2 \times 10^{-11}$ and $M_\mathrm{s} = 7.1$ keV, as this model is the warmest model consistent with the decay interpretation of the 3.55 keV line. We compute the lepton asymmetry and the momentum distribution using the Lovell et al., 2016 implementation of Laine and Shaposhnikov, 2008, which gives the lepton asymmetry $L_6 = 11.2$. Note that more recent codes return very different L_6 values as well as different momentum distributions (Ghiglieri and Laine, 2015, Venumadhav et al., 2016). We then compute the linear matter power spectrum for this model using a modified version of the CAMB Boltzmann solver code (Lewis et al., 2000).

WDM introduces a cutoff to the linear matter power spectrum, $P(k)$, at small scales, which significantly affects early structure formation. Computing the ratio of the two power spectra and taking its square root defines the transfer function:

$$T(k) \equiv \left(\frac{P_\mathrm{WDM}(k)}{P_\mathrm{CDM}(k)}\right)^{1/2}. \tag{88}$$

The difference between CDM and WDM can then be parametrized using the half-mode mass, M_hm, defined as:

$$M_\mathrm{hm} = \frac{4\pi}{3}\bar{\rho}\left(\frac{\pi}{k_\mathrm{hm}}\right)^3, \tag{89}$$

where $\bar{\rho}$ is the average density of the Universe, and k_hm is the half mode wavenumber, which is the scale where the transfer function drops by a factor of 2 and can therefore be thought of as the characteristic scale of the damping. We compute the half-mode mass for our model to be $M_\mathrm{hm} = 6.3 \times 10^8\,\mathrm{M}_\odot$. This is equivalent to the mass of a thermal relic particle $m_\mathrm{th} = 2.8$ keV using the approximation of Viel et al., 2005. The transfer function amplitudes of our model and those of its corresponding thermal relic differ by less than 10 per cent for wavenumbers $< 30\ h/\mathrm{Mpc}$ Lovell, 2020.

Visualisations of the CDM and WDM present-day matter distributions in the two simulations are shown in Fig. 5.1. The images demonstrate how WDM preserves the characteristic CDM matter distribution on large scales, but smooths density fluctuations on small scales. The projected density is encoded using brightness and the projected average three-dimensional velocity dispersion using the

colour. The location of the massive haloes and the structure of the filaments that join them together are identical in the two models, highlighting that the formation time of massive haloes does not change significantly in response to the power spectrum alteration. The thermal motions of WDM particles at very early times erase low-mass structures leading to a paucity of low-mass haloes compared to CDM. We note that we do not include thermal motions in the creation of the initial conditions.

It has been shown that WDM simulations contain spurious haloes, which are numerical/resolution-dependent artefacts and, therefore, are not predictions of the underlying physical model. In simulations in which the initial power spectrum has a resolved cutoff, the small-scale structure is seeded in part by the discreteness of the particle set and generates spurious subhaloes. A significant fraction of spurious haloes can be identified and removed by performing a mass cut below a resolution-dependent scale, as suggested by Wang and White, 2007:

$$M_{\rm lim} = 10.1\bar{\rho}dk_{\rm peak}^{-2}, \tag{90}$$

where d is the mean interparticle separation and $k_{\rm peak}$ is the spatial frequency at which the dimensionless power spectrum, $\Delta(k)^2$, has its maximum. However, we need to avoid removing the genuine haloes below this mass scale. Lovell et al., 2014 demonstrated that one can further discriminate between genuine and spurious subhaloes by making a cut based on the shapes of the initial Lagrangian regions from which WDM haloes form. They found that, compared to genuine haloes, spurious candidates tend to have much more flattened configurations in their initial positions. We follow the methodology developed by Lovell et al., 2014 to identify spurious haloes and exclude them from the halo catalogues of the WDM simulation; we describe this method briefly below.

The initial conditions specify the sphericity of haloes, which is defined as the axis ratio, $s = c/a$, of the minor to major axes in the diagonalized moment of inertia tensor of the initial particle load. The initial conditions sphericity is computed for all subhaloes in the simulation at all snapshots, so the initial conditions sphericity can be traced over time. The sphericity cut is then made such that 99 per cent of the CDM haloes containing more than 100 particles at the half-maximum mass snapshot lie above the threshold. We remove all haloes and subhaloes with the sphericity $s_{\rm half-max} < 0.2$ and $M_{\rm max} < M_{\rm cut} = 0.5M_{\rm lim}$, where $M_{\rm max}$ is the maximum mass attained by a halo during its evolution. Using Eq. 90 we find $M_{\rm cut}$ for this simulation to be $M_{\rm cut} = 1.6 \times 10^8$ $\rm M_\odot$. This is chosen so as to identify a halo at a time well before it falls into a larger host, after which point its particles are subject to tidal stripping, and thus, some information about the initial conditions region may be lost. The factor of 0.5 is calibrated by matching between resolutions in the WDM Aquarius simulations (Lovell et al., 2014).

5.2.3 The LG galaxy sample

Our primary source of LG galaxies is the most recent version of the LG catalogue of McConnachie, 2012, with the addition of Crater II (Torrealba et al., 2016a) and Antlia II (Torrealba et al., 2018) this catalogue gives 76 galaxies within 3 Mpc of the MW that have $M_* > 10^5$ $\rm M_\odot$. We extended the catalogue with galaxies from the online Extragalactic Distance database[6] (Tully et al., 2009). We use the *B*-band magnitude from the database and the stellar mass-to-light relations given in table 2 of Woo et al., 2008 to compute the stellar masses. This results in the addition of 12 dwarf galaxies to the LG, for a total of 88 dwarf galaxies.

One complication of the observations is that some ± 15 degrees of the sky is obscured by the Galactic Plane in a region known as the 'zone of avoidance'. We, therefore, implement the correction due to the zone of avoidance derived by Fattahi et al., 2020. This correction assumes that the dwarf galaxy number density in the zone of avoidance is the same as the outside region; it increases the

[6] edd.ifa.hawaii.edu

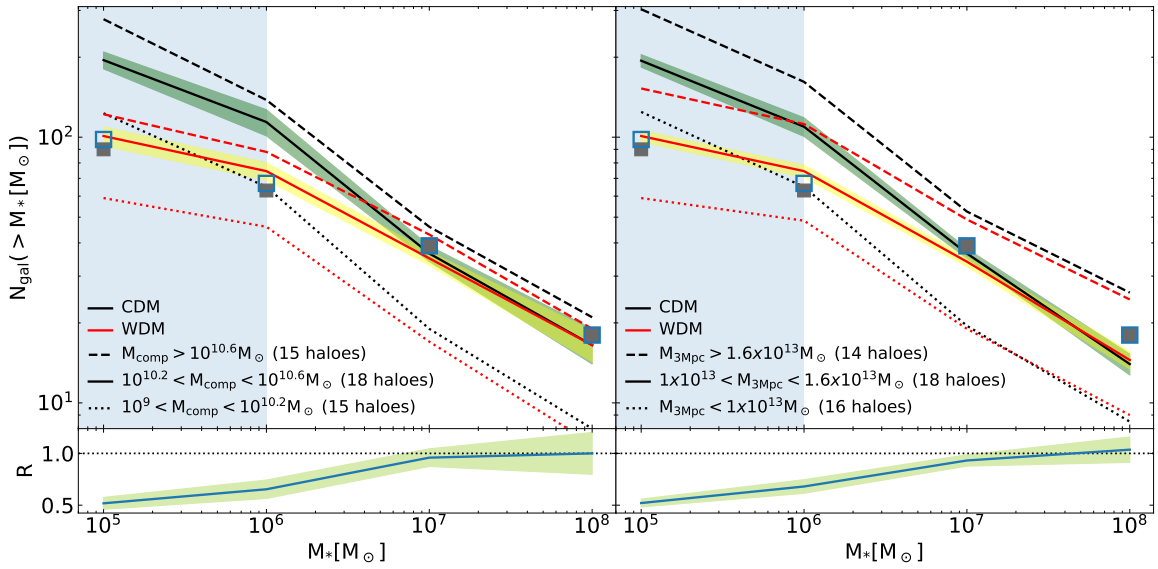

Figure 5.2: Cumulative stellar mass functions for MW-analogue haloes in different environments. The black and red lines correspond to the number of galaxies around MW-like haloes in CDM and WDM models, respectively. Grey solid squares represent the observed number of galaxies, while the open squares take into account the number of galaxies expected in the zone of avoidance. In the left-hand panel, different line styles indicate the highest mass companion of the main halo: $M_{\rm comp} = [10^{9.0}, 10^{10.2}]\,{\rm M}_\odot$ is shown as dotted lines, $M_{\rm comp} = [10^{10.2}, 10^{10.6}]\,{\rm M}_\odot$ are shown as solid lines and $M_{\rm comp} > 10^{10.6}\,{\rm M}_\odot$ are presented as dashed lines. In the right-hand panel, different styles of lines indicate the total mass within 3 Mpc of the main halo. Dotted lines indicate $M_{\rm 3Mpc} < 1 \times 10^{13}$ ${\rm M}_\odot$, solid lines represent the total mass in the range $M_{\rm 3Mpc} = [1, 1.6] \times 10^{13}$ ${\rm M}_\odot$ and $M_{\rm 3Mpc} > 1.6 \times 10^{13}$ ${\rm M}_\odot$ is shown as dashed lines. The shaded yellow and green regions represent the standard deviation of median values using the bootstrapping method. The shaded blue regions indicate the galaxies in simulations with up to 10-star particles. Solid lines in the bottom panels show the ratio of the WDM to CDM median relations for the middle $M_{\rm comp}$ and $M_{\rm 3Mpc}$ mass bins with the combination of standard deviations of the two medians shown as the shaded yellow-green area.

number of field dwarf galaxies by 8, to a total of 96 galaxies with $M_* > 10^5$ ${\rm M}_\odot$. Recent studies have provided further evidence that there is a significant number of undiscovered dwarf galaxies in the LG, using the HESTIA simulation suite (Newton et al., 2023) and the APOSTLE simulations (Santos-Santos et al., 2023).

5.3 Results

Our goal is to understand how the number of galaxies changes between the CDM and WDM models as a function of stellar mass and the local environment. As stated above, the cutoff in the WDM power spectrum causes not only a decrease in the number of low-mass haloes but also a delay in their formation time. The latter is related to where haloes are located, whether in cosmologically overdense or underdense regions (Lovell, 2024).

Our more specific interest is the impact of free-streaming on LG dwarfs and to understand how

the DM content changes from the overdense regions immediately surrounding the MW and M31 to the underdense LG outskirts. Within our MW-analogue-centred regions, the overdensity drops from 23 to 0.01 for the radial distance of 0.2 to 3 Mpc on average within a < 3Mpc radius. However, there is likely some additional scatter in the halo counts due to perturbations on scales > 3Mpc (Lovell, 2024), which will require large scale, constrained simulations like Sibelius (Sawala et al., 2022) and Hestia (Libeskind et al., 2020) to obtain a precise prediction. This is complicated by two factors: the low statistics of galaxy counts associated with low-density regions of the LG and also that we do not have a large set of LG analogues with MW-M31 halo pairs at the measured MW-M31 separation. Therefore, we approach this problem in two stages. First, in Section 5.3.1, we identify a series of MW-analogue haloes, broadly defined, and compute the galaxy counts in their vicinity. Second, we generate a series of randomly-positioned 3 Mpc-radius volumes with a variety of densities to identify how galaxy properties change from high-density regions to low-density regions, and present the results in Section 5.3.2.

5.3.1 LG dwarf galaxy counts in CDM and WDM

We begin by building a catalogue of MW-mass haloes in the simulations. Callingham et al., 2019 estimate the mass of the MW halo to be $M_{200}^{\rm MW} = 1.17^{+0.21}_{-0.15} \times 10^{12}$ M$_\odot$, and more broadly the mass is expected to be in the range $[0.8, 2.4] \times 10^{12}$ M$_\odot$ (Watkins et al., 2019, Fritz et al., 2020, Karukes et al., 2020), where the virial mass M_{200} of the halo defined as the mass contained within a sphere of radius r_{200} whose enclosed average density is 200 times the critical density. We are interested in systems that may contain a single MW-analogue halo or a MW-M31 pair within the parent FoF group therefore we select FoF catalogue haloes that have M_{200} in the range from the Callingham et al., 2019 1σ lower limit to $2\times$ the Callingham et al., 2019 1σ upper limit, which is $M_{200} = [1.02, 2.76] \times 10^{12}$ M$_\odot$. When applied to the CDM simulation, this criterion returns 48 individual haloes in the desired mass range. We draw spheres of radius 3 Mpc around these haloes and count the number of enclosed galaxies; we then identify these same 48 haloes in the WDM simulation and repeat the process.

We also follow Fattahi et al., 2020 and consider how the dwarf galaxy number density is affected by the presence of a massive companion galaxy like M31 in LG analogues, as well as by the overall mass of the LG. We therefore compute the total mass within each 3 Mpc volume, $M_{\rm 3Mpc}$, and identify each MW-analogue's most massive companion galaxy within 3 Mpc. We label the stellar mass of this companion $M_{\rm comp}$. We split the 48 haloes between 3 bins in $M_{\rm 3Mpc}$ and $M_{\rm comp}$, with the bins chosen to have roughly equal numbers of MW analogues per bin. We compute the cumulative radial stellar mass function for each of the 48 volumes, where the stellar mass, M_*, is defined as the gravitationally bound mass of all star particles associated with each galaxy, and then calculate the median cumulative radial mass function for each of the three $M_{\rm 3Mpc}$ and the three $M_{\rm comp}$ bins, then plot the results in Fig. 5.2. The cumulative number of observed galaxies in our observational sample is indicated with solid squares, and the correction for the zone-of-avoidance is indicated with open squares.

The simulations that we use have a star particle mass of $M_* = 10^5\,{\rm M}_\odot$, which is equivalent to the smallest galaxies that we consider in this paper. We, therefore, indicate the stellar mass range of galaxies with fewer than 10-star particles in Fig. 5.2 as shaded regions to show where resolution introduces a particularly strong degree of uncertainty in our results. However, many gas particles are required to form a star particle, and therefore, the presence of a galaxy in the relevant subhaloes, with the stellar mass $M_* > 10^5\,{\rm M}_\odot$, is well established; it is only the particular stellar mass that is uncertain. The utility of this plot is, therefore, in showing the general trend in the difference between CDM and WDM; we discuss the requirements for precise predictions later in this section.

As seen in the left panel of Fig. 5.2, the WDM model haloes that best match the observednumber density (of galaxies with $M_* > 10^7$ M$_\odot$) have $M_{\rm comp} = [10^{10.2}, 10^{10.6}]$ M$_\odot$ and $M_{\rm 3Mpc} = [1 - 1.6] \times 10^{13}$ M$_\odot$. The same is true for CDM, as in this regime, the number of predicted dwarfs is

nearly identical for the two models. However, below $M_* = 10^7$ $\mathrm{M}_\odot$, the number of galaxies in the CDM simulation increases almost linearly (in log-log space) while the WDM curve flattens markedly. Remarkably, the WDM turnover occurs at a very similar mass to that in which the observations diverge from CDM. For MW-analogues with a companion galaxy $M_{\rm comp} = [10^{10.2}, 10^{10.6}]\,\mathrm{M}_\odot$, the number of galaxies in the CDM simulation is 92 per cent and 53 per cent higher than in the WDM simulation at $M_* = 10^5$ $\mathrm{M}_\odot$ and $M_* = 10^6$ $\mathrm{M}_\odot$, respectively. We use bootstrap sampling to calculate the standard deviation of a median. The corresponding deviations on the stellar mass function at $M_* = 10^5$ $\mathrm{M}_\odot$ and $M_* = 10^6$ $\mathrm{M}_\odot$ are 8.2 and 5.8 in WDM and 14.1 and 12.7 in CDM. The relative uncertainty of R, the ratio of the WDM to CDM median relations is Δ_R given by $\Delta_R = N_{\rm wdm}/N_{\rm cdm} \times ((\sigma_{\rm wdm}/N_{\rm wdm})^2 + (\sigma_{\rm cdm}/N_{\rm cdm})^2)^{1/2}$. In the mass range, $M_{\rm comp} = [10^{10.2}, 10^{10.6}]$ $\mathrm{M}_\odot$, R values at ($M_* = 10^5, M_* = 10^6, M_* = 10^7, M_* = 10^8$ $\mathrm{M}_\odot$) are ($0.52\pm0.06, 0.65\pm0.09, 0.96\pm0.08, 1\pm0.2$).

The right-hand panel of Fig. 5.2 shows that for galaxies with total mass within 3 Mpc in the mass range $M_{\rm 3Mpc} = [1, 1.6] \times 10^{13}\,\mathrm{M}_\odot$, the CDM simulation yields 92 per cent and 46 per cent more galaxies than the WDM simulation at $M_* = 10^5$ $\mathrm{M}_\odot$ and at $M_* = 10^6$ $\mathrm{M}_\odot$, respectively. That the greatest difference between CDM and WDM is found for low stellar mass systems follows naturally from the familiar WDM suppression of small-scale perturbations, especially at mass scales around and below the half-mode mass, $M_{\rm hm}$. The corresponding bootstrap errors on the stellar mass function at $M_* = 10^5$ $\mathrm{M}_\odot$ and $M_* = 10^6$ $\mathrm{M}_\odot$ are 4.9 and 3.9 in WDM and 10.5 and 8.8 in CDM. Then the ratio, R, of the WDM to CDM median relations in the mass range, $M_{\rm 3Mpc} = [1, 1.6] \times 10^{13}\,\mathrm{M}_\odot$, are ($0.52 \pm 0.04, 0.68 \pm 0.07, 0.93 \pm 0.06, 1.04 \pm 0.13$).

We note that our CDM mass functions are somewhat steeper than those of Fattahi et al., 2020. Our simulations differ from theirs in two relevant ways: (i) their volumes are tailored specifically to the MW-M31 system while ours are restricted to what is available in the box, and (ii) their simulations used the EAGLE Reference galaxy formation model while ours use the Recal model. While recognising that the observational data may be incomplete, the primary takeaway from our result is simply that the WDM predictions very roughly track the observations, whereas the CDM predictions instead diverge, despite the fact that the WDM model was not tuned to reproduce this result. A much more careful treatment of both MW-M31 pair selection and the sub-kpc galaxy formation physics will be required to make precise predictions that could constrain either model.

5.3.2 Dwarfs and their environment

Having shown that the number of dwarf galaxies differs significantly between CDM and WDM simulations for a fixed galaxy formation model and that the divergence grows at a mass scale that is highly relevant for comparisons to observations, we next turn to an exploration of how the number of dwarf galaxies arises from the combination of the dwarf halo abundance, the impact of reionization in preventing galaxy formation, and the stellar mass–halo mass relation. We consider all of these factors as a function of the matter density within 3 Mpc.

We begin by analysing the impact of the different halo mass functions between the two models, specifically the change in the number of haloes as a function of the overdensity parameter, $\delta_{\rm 3Mpc} + 1 \equiv \rho_{\rm 3Mpc}/\rho_{\rm crit}$. We choose three dwarf halo mass bins: $[0.5, 2] \times M_{\rm hm}$, $[2, 8] \times M_{\rm hm}$, and $[8, 32] \times M_{\rm hm}$, which corresponds to halo mass bins of $[3.15\times10^8 - 1.26\times10^9]\,\mathrm{M}_\odot$, $[1.26\times10^9 - 5.04\times10^9]\,\mathrm{M}_\odot$ and $[5.04\times10^9 - 2.016\times10^{10}]\,\mathrm{M}_\odot$, respectively. For our definition of halo mass, we use the gravitationally bound mass including all mass species, otherwise known as the dynamical mass, $M_{\rm dyn}$. We use $M_{\rm dyn}$ instead of M_{200} here as our dwarf halo sample includes both isolated haloes and satellites. An even better approach would be to use the peak halo mass over time, $M_{\rm peak}$, as this quantity correlates more strongly with the galaxy formation probability than present day mass; this aspect should be explored further in future work. We count the number of haloes in 1000 randomly centred 3 Mpc-radius spheres in the WDM and CDM counterpart simulations. We include both isolated haloes and subhaloes and

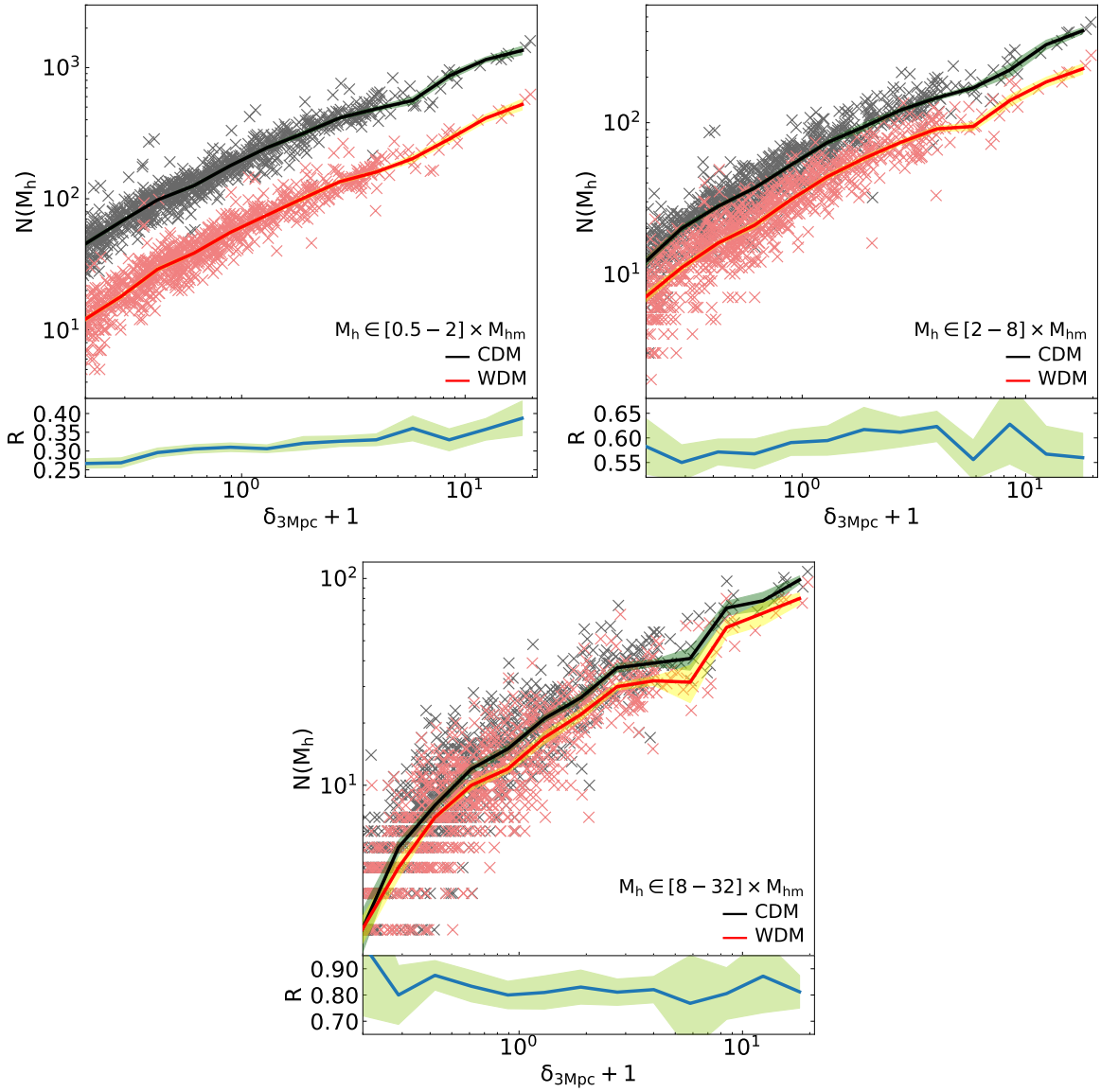

Figure 5.3: Number of haloes as a function of overdensity. The left, right and middle panels correspond to $[0.5, 2] \times M_{\rm hm}$, $[2, 8] \times M_{\rm hm}$, and $[8, 32] \times M_{\rm hm}$ halo mass ranges, which corresponds to halo mass bins of $[3.15\times10^8 - 1.26\times10^9]\,{\rm M}_\odot$, $[1.26\times10^9 - 5.04\times10^9]\,{\rm M}_\odot$ and $[5.04\times10^9 - 2.016\times10^{10}]\,{\rm M}_\odot$, respectively. Black and red colours indicate the CDM and the WDM counterparts, respectively. Crosses indicate the number of haloes in the randomly chosen 1000 volumes, and solid lines are the median relations. The shaded yellow and green regions represent the standard deviation of WDM and CDM median values, respectively, using the bootstrap method. Each bottom panel shows the ratio of the WDM and CDM median relations. The yellow–green shaded area represents the combination of standard deviations of the two medians. The left panel has the biggest slope of the ratio, while the right has a minor increase, and the middle panel is effectively flat. Note the vastly different y-axis ranges of the sub-panels.

make no distinction between them; for the remainder of this section, we refer to both types of objects as 'haloes' for brevity.

As shown in the left panel of Fig. 5.3, the number density of galaxies with mass around and below the half-mode mass is more strongly suppressed in the most underdense regions. The ratio $n_{\rm WDM}/n_{\rm CDM}$ is $\simeq 0.27 \pm 0.01$ at $\delta_{\rm 3Mpc} + 1 = 0.2$ but increases to $\simeq 0.34 \pm 0.03$ at $\delta_{\rm 3Mpc} + 1 = 10$. In the middle and the high mass ranges, shown in the centre and right-hand panels, the number of haloes in the two cosmogonies is similar, particularly so for the most massive haloes, where the WDM-to-CDM number density ratio is 0.85 ± 0.06 and 0.84 ± 0.12 at $\delta_{\rm 3Mpc} + 1 = 0.5$ and $\delta_{\rm 3Mpc} + 1 = 10$, respectively. The difference between WDM and CDM, therefore, widens with decreasing local density, especially for halo masses around (or less than) the half-mode mass. We next consider the variation in the fraction of luminous haloes given our resolution limit, $f_{*,5}$, which we define as the ratio of the number of haloes hosting at least one star particle, with the mass of $M_* = 10^5\,{\rm M}_\odot$, to the total number of haloes within a given mass bin. We follow the template of Fig. 5.3 and show the results in Fig. 5.4 as a function of $\delta_{\rm 3Mpc} + 1$ for low-, intermediate- and high-mass haloes in the left, centre and right-hand panels, respectively. In CDM, $f_{*,5}$ for the highest overdensities sampled by the simulations is 1.2, 0.55 and 1 in the low, middle and high-mass ranges, respectively. These fractions then decrease monotonically from overdense to underdense regions. The ratio of the WDM-to-CDM relations in the middle and upper halo masses ranges becomes smaller towards less dense regions to the ratio of 0.56 ± 0.05 at $\delta_{\rm 3Mpc} + 1 = 0.8$ for the middle mass range and 0.80 ± 0.02 at the same underdensity for the higher mass range. This behaviour results from the interplay of the delay in WDM halo formation and the impact of reionization: the delay in formation shifts the halo collapse time past the end of the reionization epoch, inhibiting and preventing the cooling of gas and the formation of a galaxy above a stellar mass threshold of $M_* = 10^5\,{\rm M}_\odot$. Note that we adopt a temporally-varying but spatially-uniform UV/X-ray background and therefore neglect local reionization sources; adopting an inhomogeneous field may lead to higher dwarf halo galaxy formation efficiencies in both WDM and CDM (Shen et al., 2023). The picture in the lowest halo mass bin is somewhat different, with a higher $f_{*,5}$ in WDM than CDM at all overdensities. This result can be explained by the width of the halo mass bin and the shape of the halo mass function. The $f_{*,5}$ in both the CDM and WDM models for haloes at $2 \times M_{\rm hm}$ is higher than that at $0.5 \times M_{\rm hm}$, but the abundance of CDM haloes at the lower end of the bracket is much larger than that of either WDM haloes at that mass or of either model at $2 \times M_{\rm hm}$.

We have shown that the transition to lower-density regions decreases both the relative total number of haloes and the relative fraction of luminous haloes between WDM and CDM. The final property to consider is the stellar mass–halo mass relation. For those haloes that do form a galaxy at least above a stellar mass threshold of $M_* = 10^5\,{\rm M}_\odot$, how many stars do they form? The monolithic collapse of WDM haloes (Lovell et al., 2019) suggests that they may lose less of their gas to stellar feedback at very early times than is the case in CDM and thus yield a higher stellar mass–to–halo mass ratio. We, therefore, compute this ratio for all haloes with at least one star particle, and in Fig. 5.5 show the median of this ratio as a function of overdensity and halo mass, as per previous figures.

The median stellar-to-halo mass ratios in WDM are consistently greater than those in CDM in the low and intermediate-mass bins, while the two are similar in the high-mass bin. Remarkably, the median ratio of the WDM to CDM stellar mass–halo mass relation increases from overdense to underdense regions. In the low-mass bin, the ratio of WDM to CDM median stellar mass per unit halo mass increases from 1.4 ± 0.13 to 1.8 ± 0.37 between $\delta_{\rm 3Mpc} + 1 = 5$ and $\delta_{\rm 3Mpc} + 1 = 0.4$; in the intermediate-mass bin the ratio increases from 1.4 ± 0.14 to 1.8 ± 0.18 for $\delta_{\rm 3Mpc} + 1 = 10$ to $\delta_{\rm 3Mpc} + 1 = 0.7$. We caution that many haloes in the low mass case only host a single particle and that the value of M_* for any individual galaxy is highly unreliable for the reasons discussed in Section 5.2. However, a similar result has been inferred from the same data set using mock HI surveys (Oman et al., 2024) and has also been shown for a power spectrum cutoff at high redshift in an independent

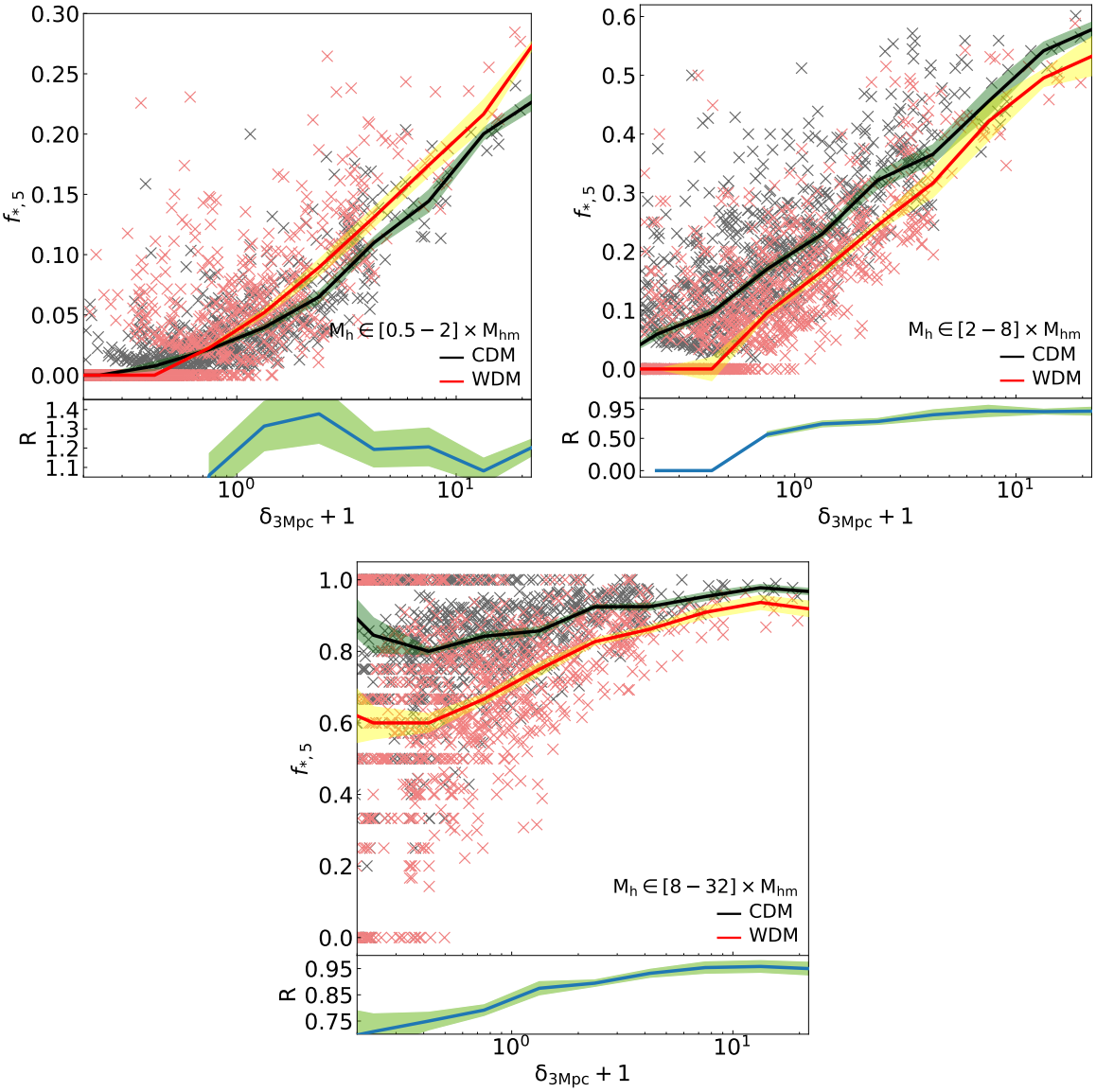

Figure 5.4: The fraction of luminous haloes, $f_{*,5}$, as a function of overdensity. The left, right and middle panels correspond to $[0.5, 2] \times M_{\rm hm}$, $[2, 8] \times M_{\rm hm}$, and $[8, 32] \times M_{\rm hm}$ halo mass ranges, which corresponds to halo mass bins of $[3.15 \times 10^8 - 1.26 \times 10^9]\,\mathrm{M}_\odot$, $[1.26 \times 10^9 - 5.04 \times 10^9]\,\mathrm{M}_\odot$ and $[5.04 \times 10^9 - 2.016 \times 10^{10}]\,\mathrm{M}_\odot$, respectively. Crosses indicate $f_{*,5}$, in the randomly chosen 1000 volumes, and solid lines correspond to the median relations as a function of overdensity $\delta_{3\mathrm{Mpc}}+1$. The shaded yellow and green regions represent the standard deviation of WDM and CDM median values, respectively, using the bootstrap method. Each bottom panel shows the ratio of the WDM and CDM median relations, while the yellow–green shaded area shows the combination of standard deviations of the two medians.

galaxy formation model (Lovell et al., 2019). This result supports the hypothesis that star formation in WDM haloes in underdense regions can quickly catch up and surpass the CDM through a strong late-time ($z \sim 8$) starburst (Bose et al., 2016b), which leads to a population of dwarf galaxies that is brighter than would otherwise be the case, including in underdense regions.

We have the three components that combine to provide the stellar mass function: the halo mass function, the fraction of luminous haloes with stellar mass $> 10^5\,\mathrm{M}_\odot$ and the stellar mass–halo mass relation. We now analyse how the stellar mass function itself changes from high-density regions to low-density regions. We therefore consider the number density of luminous galaxies as a function of overdensity, now split into three stellar mass bins rather than three halo mass bins: $\left[10^5 - 10^6\right]$, $\left[10^6 - 10^7\right]$, and $\left[10^7 - 10^8\right]\ \mathrm{M}_\odot$. We present the results in Fig. 5.6.

The decreasing ratio of the WDM to CDM galaxy abundance at the highest sampled overdensities is more pronounced for low-mass galaxies, being 0.85 ± 0.06 in the highest mass bin and 0.60 ± 0.03 at $[10^6, 10^7]\ \mathrm{M}_\odot$ and 0.30 ± 0.02 at $[10^5, 10^6]\ \mathrm{M}_\odot$. Of greater interest is the fact that this suppression differs from the halo abundance by remaining constant with decreasing overdensity rather than increasing, down to the regime where the resolution has a significant impact. Part of this result can likely be explained by the large $f_{*,5}$ for halo masses $8M_{\mathrm{hm}}$ across all environments. However, even this class of haloes exhibits a large difference in $f_{*,5}$ between CDM and WDM in underdense regions. Instead, we have a picture where the increase in the WDM stellar mass-halo mass relation with decreasing local density balances the impact of greater halo number density suppression and lower $f_{*,5}$. The details of this process will be strongly dependent on the details of dwarf galaxy astrophysics at high redshift (Shen et al., 2023), including how reionization proceeds on small scales and how gas cools into low-mass haloes. We have shown that free-streaming can, in principle, lead to changes in galaxy counts with the local density. However, the degree of the change will depend strongly on astrophysical processes, and the magnitudes of their effects are poorly understood.

5.4 Conclusions

Experimental detection and consistency with galaxy observations are needed to claim that we have an authoritative description of DM. The CDM model has yet to be verified through any experimental detection of its DM candidate, and tensions remain with dwarf galaxy observations, including the abundance of dwarf galaxies in the LG. The WDM model may offer a remedy for both elements of this problem in that its sterile neutrino particle physics candidate has been potentially detected in X-ray emission (Boyarsky et al., 2014, Bulbul et al., 2014, Hofmann and Wegg, 2019), and this detection sets a characteristic scale that can impact dwarf galaxy properties in a manner that becomes more pronounced in underdense regions.

In this paper, we examine how the switch from CDM to WDM changes the properties of dwarfs in underdense regions for a fixed galaxy formation model (one calibrated using CDM simulations). We select a WDM candidate sterile neutrino with a mass $M_{\mathrm{s}} = 7.1\ \mathrm{keV}$, mixing angle $\sin^2(2\theta_1) = 2 \times 10^{-11}$, and the lepton asymmetry $L_6 = 11.2$ as computed using Laine and Shaposhnikov, 2008 and Lovell et al., 2016. We identify MW-mass haloes broadly defined – $M_{200} = [1 - 2] \times \mathrm{M}^{\mathrm{MW}}$ – which yields 48 haloes with the virial mass in the range $M_{200} \in [1.02 - 2.76] \times 10^{12}\,\mathrm{M}_\odot$ in CDM.

We measured the abundance of galaxies within 3 Mpc of each MW-analogue halo (Fig. 5.2) and found that the cumulative stellar mass function is nearly identical between WDM and CDM at $M_* > 10^7\,\mathrm{M}_\odot$. However, below this mass, the cumulative mass function becomes shallower for WDM, where this model predicts a smaller number of dwarf galaxies than CDM, at 50 per cent of the CDM value for $M_* > 10^5\ \mathrm{M}_\odot$. Curiously, the turnover in WDM occurs at a similar mass scale to where the observations depart from the CDM prediction. Two factors contribute to the lower number

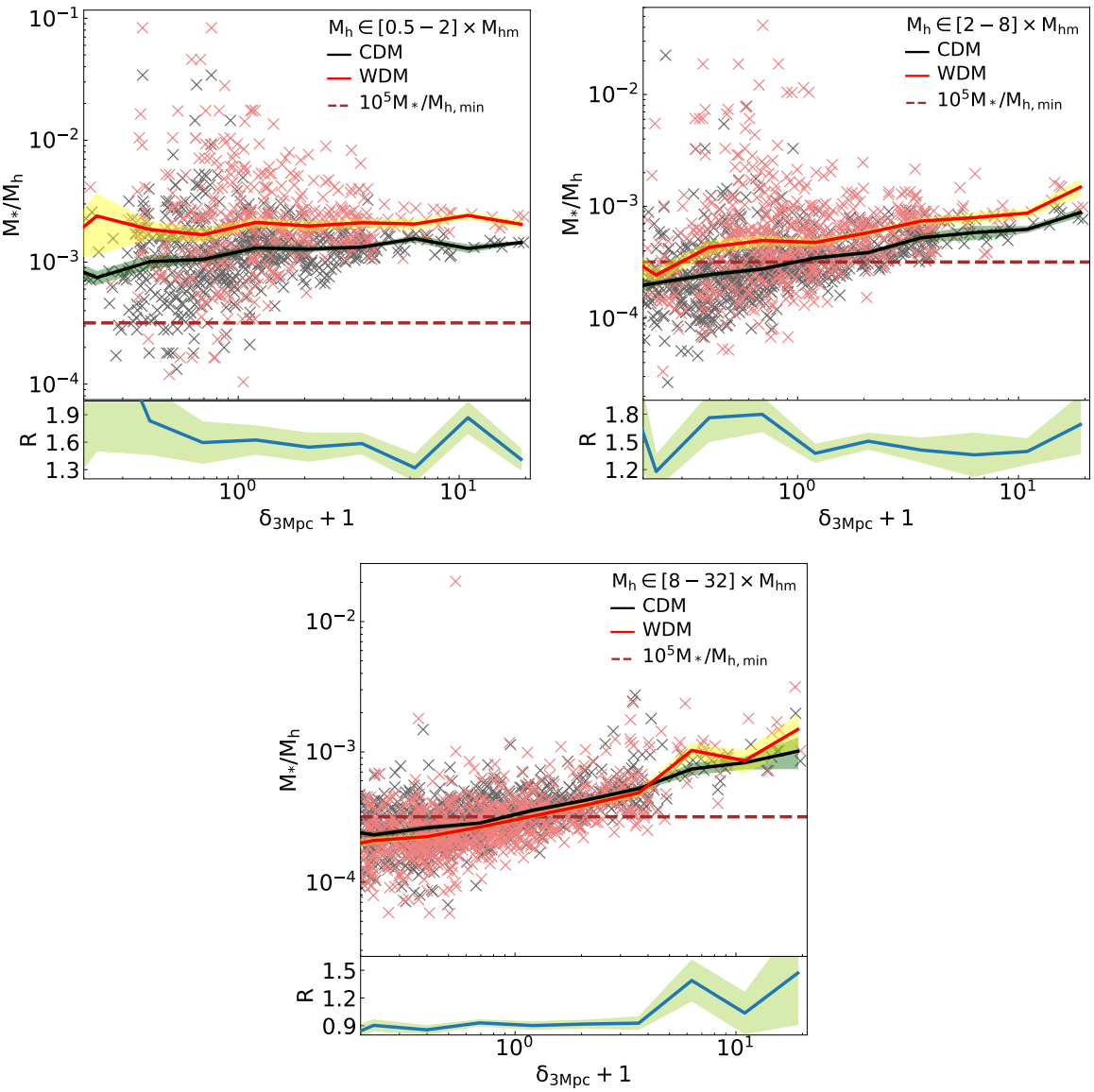

Figure 5.5: The stellar mass-halo mass relation as a function of overdensity. The left, right and middle panels correspond to $[0.5, 2] \times M_{\rm hm}$, $[2, 8] \times M_{\rm hm}$, and $[8, 32] \times M_{\rm hm}$ halo mass ranges, which corresponds to halo mass bins of $[3.15 \times 10^8 - 1.26 \times 10^9]\,{\rm M}_\odot$, $[1.26 \times 10^9 - 5.04 \times 10^9]\,{\rm M}_\odot$ and $[5.04 \times 10^9 - 2.016 \times 10^{10}]\,{\rm M}_\odot$, respectively. Crosses indicate the median values of the stellar mass-halo mass relation in the randomly chosen 1000 volumes, and solid lines correspond to the median relations. The horizontal dashed lines indicate the mass ratio associated with a single particle. The shaded yellow and green regions represent the standard deviation of WDM and CDM median values, respectively, as computed using the bootstrapping method. Each bottom panel shows the ratio of the WDM and CDM median relations, while the yellow-green shaded area shows the combination of standard deviations of the two medians.

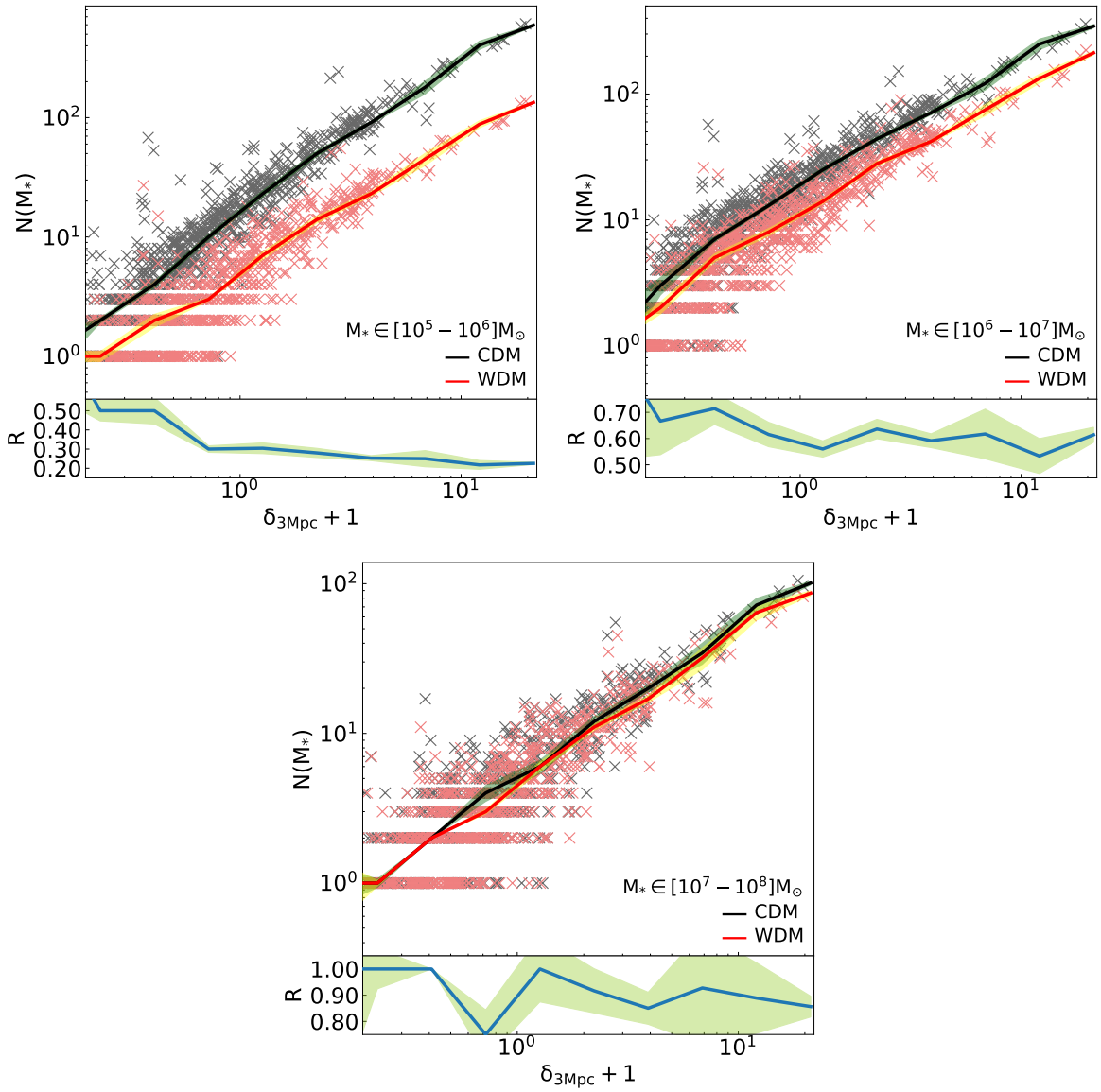

Figure 5.6: Number of galaxies as a function of overdensity. The left, right and middle panels correspond to $[10^5 - 10^6]\,\mathrm{M}_\odot$, $[10^6 - 10^7]\,\mathrm{M}_\odot$, and $[10^7 - 10^8]\,\mathrm{M}_\odot$ stellar mass ranges, respectively. Crosses indicate the number of galaxies in the corresponding 3Mpc radius volume. Solid red and black lines correspond to the medians in WDM and CDM counterparts according to the overdensity, $\delta_{\mathrm{3Mpc}} + 1$ values. The shaded yellow and green regions represent the standard deviation of WDM and CDM median values, respectively, computed using the bootstrapping method. Each bottom panel shows the ratio of the WDM and CDM median relations, while the yellow-green shaded area shows the combination of standard deviations of the two medians.

of dwarf galaxies in WDM: the suppression of halo number and later halo collapse times compared to CDM. Our results suggest that in the WDM model, the total mass within 3 Mpc is roughly in the range $[1 - 1.6] \times 10^{13}$ $\mathrm{M}_\odot$, and the MW's most massive companion halo has a stellar mass higher than $> 10^{10.2}$ $\mathrm{M}_\odot$, although careful simulations of MW-M31 pair analogues are required to confirm this result. For the latter, we consider the $[10^{10.2} - 10^{10.6}]$ $\mathrm{M}_\odot$ and $> 10^{10.6}$ $\mathrm{M}_\odot$ mass bins together since they are within the region-to-region scatter. Furthermore, the EAGLE model predicts a $\mathrm{M}_*/\mathrm{M}_\mathrm{h}$ relation for these mass ranges lower than is expected from observations (Schaye et al., 2015), thus an improved model may revise the values of M_comp upward. This result is within an order of magnitude of the inferred stellar mass of M31 estimated using optical and near-infrared imaging data (Tamm et al., 2012), and considering the correction, it can potentially return a better match to the observations.

One of the uncertainties in measuring the full population of LG dwarfs is depth completeness: could there be distant galaxies in the lower-local-density parts of the LG that we have not yet detected? The evolution of dwarf haloes between CDM and WDM is a function of local density: therefore, we study how the properties of dwarfs change in a series of 1000 randomly centred spheres or radius 3 Mpc. The ratio of halo number in WDM relative to CDM decreases significantly from high-density regions to low-density regions (Fig. 5.3), from 0.40 ± 0.05 at $\delta_\mathrm{3Mpc} + 1 = 20$ to 0.27 ± 0.01 at $\delta_\mathrm{3Mpc} + 1 = 0.2$ for haloes in the region of the half-mode mass $[3.2, 12.6] \times 10^8$ $\mathrm{M}_\odot$.

The fraction of luminous haloes, for galaxies with the stellar mass $> 10^5$ $\mathrm{M}_\odot$, $f_{*,5}$, in the two models also diverges from the top of the density range to the bottom for $M_{\{}rmdyn > 2M_\mathrm{hm}$, as the increased collapse delay at small densities pushes the collapse to after the reionization threshold (Fig. 5.4). However, we find that the stellar mass–halo mass relation of WDM haloes relative to CDM *increases* towards lower density regions for haloes of mass $< 8M_\mathrm{hm}$ (Fig. 5.5), which we posit is due to the absence of energy injection from stellar feedback at $z > 9$ as is the case in CDM. The net result is that the relative number of galaxies in the two models does not change between overdense and underdense regions: while both the relative number of haloes and the relative fraction of luminous haloes decrease towards lower densities, the concurrent increase in the stellar mass-halo mass relation compensates for the prior effects.

We have demonstrated in this paper that the 7.1 keV sterile neutrino DM candidate has the potential to explain the purported deficit of faint LG dwarfs and that the population of these dwarfs should be the same between the two models independent of the local density. While we were able to take advantage of a pair of high-resolution simulations sufficiently large to yield a reasonably representative galaxy population, we did not select specifically for LG-analogue volumes in that they did not feature a pair of MW and M31-analogue haloes at their precise separation; therefore future work will need to focus on APOSTLE-style volumes to check that low-density regions in the LG do exhibit the expected behaviour in WDM. Moreover, our results were obtained for a specific sterile neutrino model and a specific galaxy formation model, and it will be crucial to relax these conditions in future work. First, uncertainties in both the measured value of $\sin^2(2\theta)$ and in the particle physics calculations lead to a factor of 6 uncertainty in the 3.55 keV line-compliant M_hm value. Second, the EAGLE galaxy formation model was calibrated to reproduce the key properties of the present-day galaxy population and hence does not focus specifically on the particular challenge of dwarf galaxy formation during the epoch of reionization. The latter problem is beginning to be addressed with new simulations that follow early dwarf formation with radiative transfer (e.g. Shen et al., 2023), while the former will require a dedicated particle physics phenomenology effort. Should the *XRISM* mission detect a series of X-ray emission lines at an energy of 3.55 keV with the properties predicted for DM decay, this will provide compelling extra motivation to pursue this kind of particle physics work in addition to modelling the faintest galaxies in the Universe in the WDM cosmology.

Acknowledgements

We thank Jesús Zavala for the helpful discussions and comments on the draft. TM and MRL acknowledge support by a Project Grant from the Icelandic Research Fund (grant number 206930). RAC was supported by a Royal Society University Research Fellowship during the initial development of this study. JP is supported by the Australian government through the Australian Research Council's Discovery Projects funding scheme (DP220101863).

Data Availability

Researchers interested in access to the simulations used in this paper should contact R. A. Crain at R.A.Crain@ljmu.ac.uk.

6 Summary and Outlook

This thesis investigates the nature of dark matter within the context of structure formation and galaxy evolution (in the regime of dwarf galaxies), focusing on alternative models beyond the standard ΛCDM paradigm. Self-interacting dark matter (SIDM) and Warm Dark Matter (WDM) models are explored as potential modifications to address discrepancies between the predictions of ΛCDM and observations of the dwarf galaxy population.

In Article 2 (chapter 5), we study a WDM model candidate, the resonantly produced sterile neutrino, and its impact on the abundance and structure of low-mass dark matter (sub)haloes using high-resolution hydrodynamical simulations, which include full baryonic physics with the EAGLE galaxy formation and evolution model. We concentrate on looking at the statistics of the galaxy population across both CDM and WDM models and demonstrate that a 7.1 keV sterile neutrino has the potential to explain the purported deficit of faint Local Group dwarfs. We measure the abundance of galaxies within 3 Mpc of Milky Way-analogue haloes in the simulation and found that the cumulative stellar mass function is nearly identical between WDM and CDM at $M_* > 10^7\,\mathrm{M}_\odot$. However, it becomes shallower for WDM, where this model predicts a smaller number of dwarf galaxies than CDM, at 50 per cent of the CDM value for $M_* > 10^5\,\mathrm{M}_\odot$, with the turnover of WDM at a similar mass scale where the observations deviate from the CDM prediction. We also find that the suppression of galaxies with $M_* > 10^5\,\mathrm{M}_\odot$ between WDM and CDM is independent of the local environment since the suppression of halo counts and the luminous fraction is balanced by an enhancement in the stellar mass–halo mass relation. In order to broaden our research, we must relax the condition that centres around a particular sterile neutrino model. This will require further studies with a focus on particle physics phenomenology. In addition, we need to adopt more comprehensive models of galaxy formation for dwarf galaxies that will describe their evolution from the epoch of reionization to the present day.

In Article 1 (chapter 3), we study the effects of dark matter self-interactions on the formation and evolution of dwarf-size haloes, particularly focusing on the phenomenon of the gravothermal catastrophe in SIDM haloes and its potential to explain the observed diversity of the inner dark matter densities in the Milky Way satellites. We develop an analytical framework to predict the timescales for triggering the gravothermal collapse of the SIDM core as a function of halo mass and for a broad range in the parameter space of velocity-dependent SIDM cross sections. In addition, we also estimate the mass scales for the formation of intermediate-mass black holes in the SIDM haloes that undergo collapse. As a result, we show that dark matter haloes with a mass greater than $10^{12}\,\mathrm{M}_\odot$ in allowed SIDM cross sections cannot reach the core-collapse phase by today and can only have small cores; likewise, haloes with mass in the range of a few times $10^{10}\,\mathrm{M}_\odot$ to $10^{12}\,\mathrm{M}_\odot$ have not had time to reach the core-collapse phase but develop a significant spherical isothermal core; more importantly, for those in the range of dwarf galaxy scales - up to few times $10^{10}\,\mathrm{M}_\odot$, we find that a fraction of dwarf galaxies should be embedded in collapsed SIDM haloes with cuspy density profiles, and hosting SIDM-generated intermediate black holes with the mass in range $[0.2 - 10^3]\,\mathrm{M}_\odot$. Since the transition between cored SIDM haloes and those that have collapsed depends on halo mass and concentration, we bracket the parameter space of SIDM models that are predicted to have a bi-modality (cusps and cores) in the (sub)haloes that host the Local Group galaxy population and can thus provide a promising solution for the diversity problem with a unique signature of the SIDM nature (the presence

of intermediate-mass black holes). Possible avenues of future research include verifying the results of our analytical framework with a suite of SIDM simulations representative of the broad range of parameter space we explored. In addition, we could apply our framework to SIDM models with cross sections with phenomenology different to the classical plasma-physics inspired formula 16, for example, to study models with resonant behaviour.

In Chapter 4 (Article 3 in preparation), we extend our study of the gravothermal collapse in SIDM haloes by looking at its impact on stellar systems within these haloes. Using the gravothermal fluid model described in section 2.2, we calculate the evolution of the gravitational potential of a SIDM halo as it goes from the cusp-core transformation phase to the long-lived cored phase and finally to the core-collapse phase. By comparing the local timescale for the change in the gravitational potential to the typical orbital timescale of tracer particles (stars), we demonstrate that the tracers should evolve adiabatically throughout the entire evolution of the SIDM halo. Under this assumption, we follow an analytical method based on adiabatic invariants to calculate the evolution of the central density of an isothermal stellar distribution during the initial cusp-core transformation phase. As an example, we apply this formalism to the central globular cluster in the dwarf galaxy Eridanus II and find that for a constant cross section $\sigma_T/m_\chi = 100\mathrm{cm}^2\mathrm{g}^{-1}$, the central density in the globular cluster is predicted to decrease by up to a factor of 20 during the cusp-core transformation of the parent halo of Eridanus II. The analysis connected to this Chapter is ongoing and is the basis of an article in preparation. We plan to extend our analysis to a broader range of stellar systems, from globular clusters to dSphs, where the assumptions of the model should be applicable. We also plan to make predictions for the second phase in the evolution of the SIDM haloes, the core-collapse phase, which we have also found to be adiabatic.

In another ongoing project (complementary to that in Chapter 4), which I have been working on during my Thesis but that is still in the preparatory phase, we are incorporating baryonic processes into SIDM simulations. The ultimate goal is to provide insights into the interplay between dark matter and baryons in shaping the central dynamics of galaxies within the SIDM framework. The main objective of this ongoing project is to understand the impact of gravothermal collapse on the formation and evolution of dwarf-size galaxies with idealised/controlled simulations using the AREPO code. For consistency, we are using the same dark matter halo and its parameters as presented in the analytic work in Chapter 4. This dark matter halo corresponds to a typical dwarf galaxy with an average concentration. For our initial analysis, we have chosen the velocity-independent cross section equal to $\sigma_T/m_\chi = 100\mathrm{cm}^2\mathrm{g}^{-1}$. We are studying how the gravothermal core-collapse affects the formation and dynamics of a gaseous disk. For this purpose, we have set initial conditions for a spherically symmetric dark matter halo with a hot gas corona in hydrostatic equilibrium and with non-zero angular momentum. We are studying the disk formation phase by switching on radiative atomic cooling in a configuration where the cooling timescale is comparable to the core-collapse timescale. Our first goal is to explore the dynamical response of the disk to the core collapse of the SIDM halo and how its structure differs from a CDM simulation with the same configuration. We then plan to include star formation and feedback processes to have a more realistic but still controlled setting where we can more easily separate the physics of the SIDM collapse from the baryonic physics. In such a setting, we plan to study not only the dynamic impact on the stellar distribution in the baryonic galaxy (which we will then compare to the analytic results in Chapter 4) but also the impact on the star formation and feedback cycles. This could result in indirect but distinct signatures of the gravothermal collapse that could be potentially observable in dwarf galaxies.

In conclusion, this thesis advances our understanding of alternative dark matter models and their implications for dwarf galaxy formation and evolution. Our findings underscore the potential of WDM and SIDM models to address the shortcomings of the ΛCDM paradigm, particularly in explaining the observed properties of dwarf galaxies. Results of Article 2 (chapter 5) suggest that the sterile neutrino WDM model better explains the deficit of faint Local Group dwarf galaxies than CDM. Results of

Article 1 (chapter 3) provide evidence that SIDM can account for the diversity of dark matter density profiles in the Milky Way satellites and predict the existence of intermediate-mass black holes in these galaxies. Moving forward, the next generation of surveys, such as the Vera C. Rubin Observatory's Legacy Survey of Space and Time, will be instrumental in testing these predictions and refining our models. Additionally, incorporating more detailed baryonic processes in simulations will enhance our understanding of the interplay between dark matter and baryons. The challenges ahead lie in further refining these models, expanding the parameter space, and improving the observational techniques needed to detect the subtle signatures of dark matter's true nature. Ultimately, this research paves the way for a deeper exploration into the fundamental properties of dark matter, offering new avenues for discovering the hidden structure of our universe. Moreover, this work sets the stage for future investigations into the interplay between dark matter and baryonic physics. By utilizing cutting-edge simulation codes like AREPO and focusing on the unique signatures of SIDM and WDM, we are poised to make significant strides in our quest to understand galaxy formation and evolution.

References

F. Zwicky. Die Rotverschiebung von extragalaktischen Nebeln. *Helv. Phys. Acta*, 6:110–127, 1933. doi: 10.1007/s10714-008-0707-4.

F. Zwicky. Republication of: The redshift of extragalactic nebulae. *General Relativity and Gravitation*, 41(1):207–224, January 2009. doi: 10.1007/s10714-008-0707-4.

U. G. Briel and J. P. Henry. An X-ray temperature map of Coma. In A. Mazure, F. Casoli, F. Durret, and D. Gerbal, editors, *Untangling Coma Berenices: A New Vision of an Old Cluster*, page 170, January 1998. doi: 10.48550/arXiv.astro-ph/9711237.

Vera C. Rubin and Jr. Ford, W. Kent. Rotation of the Andromeda Nebula from a Spectroscopic Survey of Emission Regions. , 159:379, February 1970. doi: 10.1086/150317.

V. C. Rubin, Jr. Ford, W. K., and N. Thonnard. Extended rotation curves of high-luminosity spiral galaxies. IV. Systematic dynamical properties, Sa -> Sc. , 225:L107–L111, November 1978. doi: 10.1086/182804.

Edwin Hubble. A Relation between Distance and Radial Velocity among Extra-Galactic Nebulae. *Proceedings of the National Academy of Science*, 15(3):168–173, March 1929. doi: 10.1073/pnas.15.3.168.

S. Perlmutter, G. Aldering, B. J. Boyle, P. G. Castro, W. J. Couch, S. Deustua, S. Fabbro, R. S. Ellis, A. V. Filippenko, A. Fruchter, G. Goldhaber, A. Goobar, D. E. Groom, I. M. Hook, M. Irwin, A. G. Kim, M. Y. Kim, R. A. Knop, J. C. Lee, T. Matheson, R. G. McMahon, H. J. M. Newberg, C. Lidman, P. Nugent, N. J. Nunes, R. Pain, N. Panagia, C. R. Pennypacker, R. Quimby, P. Ruiz-Lapuente, B. Schaefer, N. Walton, and Supernova Cosmology Project. Measurements of Omega and Lambda from 42 High-Redshift Supernovae. In J. Paul, T. Montmerle, and E. Aubourg, editors, *19th Texas Symposium on Relativistic Astrophysics and Cosmology*, page 146, December 1998.

Adam G. Riess, Alexei V. Filippenko, Peter Challis, Alejandro Clocchiatti, Alan Diercks, Peter M. Garnavich, Ron L. Gilliland, Craig J. Hogan, Saurabh Jha, Robert P. Kirshner, B. Leibundgut, M. M. Phillips, David Reiss, Brian P. Schmidt, Robert A. Schommer, R. Chris Smith, J. Spyromilio, Christopher Stubbs, Nicholas B. Suntzeff, and John Tonry. Observational Evidence from Supernovae for an Accelerating Universe and a Cosmological Constant. , 116(3):1009–1038, September 1998. doi: 10.1086/300499.

Craig J. Copi, David N. Schramm, and Michael S. Turner. Big-Bang Nucleosynthesis and the Baryon Density of the Universe. *Science*, 267(5195):192–199, January 1995. doi: 10.1126/science.7809624.

A. A. Penzias and R. W. Wilson. A Measurement of Excess Antenna Temperature at 4080 Mc/s. , 142: 419–421, July 1965. doi: 10.1086/148307.

A. D. Miller, R. Caldwell, M. J. Devlin, W. B. Dorwart, T. Herbig, M. R. Nolta, L. A. Page, J. Puchalla,

E. Torbet, and H. T. Tran. A Measurement of the Angular Power Spectrum of the Cosmic Microwave Background from L = 100 to 400. , 524(1):L1–L4, October 1999. doi: 10.1086/312293.

Planck Collaboration. Planck 2018 results. I. Overview and the cosmological legacy of Planck. , 641: A1, September 2020. doi: 10.1051/0004-6361/201833880.

Daniel J. Eisenstein et al. Detection of the Baryon Acoustic Peak in the Large-Scale Correlation Function of SDSS Luminous Red Galaxies. , 633(2):560–574, November 2005. doi: 10.1086/466512.

Éric Aubourg, others, and BOSS Collaboration. Cosmological implications of baryon acoustic oscillation measurements. , 92(12):123516, December 2015. doi: 10.1103/PhysRevD.92.123516.

Matteo Viel, George D. Becker, James S. Bolton, and Martin G. Haehnelt. Warm dark matter as a solution to the small scale crisis: New constraints from high redshift Lyman-α forest data. , 88(4): 043502, August 2013. doi: 10.1103/PhysRevD.88.043502.

G. Jungman, M. Kamionkowski, and K. Griest. Supersymmetric dark matter. , 267:195–373, March 1996. doi: 10.1016/0370-1573(95)00058-5.

Francesca Chadha-Day, John Ellis, and David J. E. Marsh. Axion dark matter: What is it and why now? *Science Advances*, 8(8):eabj3618, February 2022. doi: 10.1126/sciadv.abj3618.

E. Aprile et al. Dark Matter Search Results from a One Ton-Year Exposure of XENON1T. *Phys. Rev. Lett.*, 121(11):111302, 2018. doi: 10.1103/PhysRevLett.121.111302.

Gaia Lanfranchi, Maxim Pospelov, and Philip Schuster. The Search for Feebly Interacting Particles. *Annual Review of Nuclear and Particle Science*, 71:279–313, September 2021. doi: 10.1146/annurev-nucl-102419-055056.

Leslie J. Rosenberg. Dark-matter QCD-axion searches. *Proceedings of the National Academy of Science*, 112(40):12278–12281, October 2015. doi: 10.1073/pnas.1308788112.

N. Du, N. Force, R. Khatiwada, E. Lentz, R. Ottens, L. J. Rosenberg, G. Rybka, G. Carosi, N. Woollett, D. Bowring, A. S. Chou, A. Sonnenschein, W. Wester, C. Boutan, N. S. Oblath, R. Bradley, E. J. Daw, A. V. Dixit, J. Clarke, S. R. O'Kelley, N. Crisosto, J. R. Gleason, S. Jois, P. Sikivie, I. Stern, N. S. Sullivan, D. B. Tanner, G. C. Hilton, and ADMX Collaboration. Search for Invisible Axion Dark Matter with the Axion Dark Matter Experiment. , 120(15):151301, April 2018. doi: 10.1103/PhysRevLett.120.151301.

Sean Tulin and Hai-Bo Yu. Dark matter self-interactions and small scale structure. , 730:1–57, February 2018. doi: 10.1016/j.physrep.2017.11.004.

A. Boyarsky, M. Drewes, T. Lasserre, S. Mertens, and O. Ruchayskiy. Sterile neutrino Dark Matter. *Progress in Particle and Nuclear Physics*, 104:1–45, January 2019. doi: 10.1016/j.ppnp.2018.07.004.

Margaret J. Geller and John P. Huchra. Mapping the Universe. *Science*, 246(4932):897–903, November 1989. doi: 10.1126/science.246.4932.897.

III Gott, J. Richard, Mario Jurić, David Schlegel, Fiona Hoyle, Michael Vogeley, Max Tegmark, Neta Bahcall, and Jon Brinkmann. A Map of the Universe. , 624(2):463–484, May 2005. doi: 10.1086/428890.

Volker Springel, Simon D. M. White, Adrian Jenkins, Carlos S. Frenk, Naoki Yoshida, Liang Gao, Julio Navarro, Robert Thacker, Darren Croton, John Helly, John A. Peacock, Shaun Cole, Peter Thomas, Hugh Couchman, August Evrard, Jörg Colberg, and Frazer Pearce. Simulations of the

formation, evolution and clustering of galaxies and quasars. , 435(7042):629–636, June 2005a. doi: 10.1038/nature03597.

M. Vogelsberger, J. Zavala, and A. Loeb. Subhaloes in self-interacting galactic dark matter haloes. , page 3127, May 2012a. doi: 10.1111/j.1365-2966.2012.21182.x.

A. A. Klypin and S. F. Shandarin. Three-dimensional numerical model of the formation of large-scale structure in the Universe. , 204:891–907, September 1983. doi: 10.1093/mnras/204.3.891.

Josh Barnes and Piet Hut. A hierarchical O(N log N) force-calculation algorithm. , 324(6096):446–449, December 1986. doi: 10.1038/324446a0.

Volker Springel. E pur si muove: Galilean-invariant cosmological hydrodynamical simulations on a moving mesh. , 401(2):791–851, January 2010. doi: 10.1111/j.1365-2966.2009.15715.x.

Volker Springel. The cosmological simulation code GADGET-2. , 364(4):1105–1134, December 2005. doi: 10.1111/j.1365-2966.2005.09655.x.

William H. Press and Paul Schechter. Formation of Galaxies and Clusters of Galaxies by Self-Similar Gravitational Condensation. , 187:425–438, February 1974. doi: 10.1086/152650.

J. R. Bond, S. Cole, G. Efstathiou, and N. Kaiser. Excursion Set Mass Functions for Hierarchical Gaussian Fluctuations. , 379:440, October 1991. doi: 10.1086/170520.

Richard G. Bower. The evolution of groups of galaxies in the Press-Schechter formalism. , 248: 332–352, January 1991. doi: 10.1093/mnras/248.2.332.

Cedric Lacey and Shaun Cole. Merger rates in hierarchical models of galaxy formation. , 262(3): 627–649, June 1993. doi: 10.1093/mnras/262.3.627.

Michael Boylan-Kolchin, Volker Springel, Simon D. M. White, Adrian Jenkins, and Gerard Lemson. Resolving cosmic structure formation with the Millennium-II Simulation. , 398(3):1150–1164, September 2009. doi: 10.1111/j.1365-2966.2009.15191.x.

Till Sawala, Carlos S. Frenk, Azadeh Fattahi, Julio F. Navarro, Tom Theuns, Richard G. Bower, Robert A. Crain, Michelle Furlong, Adrian Jenkins, Matthieu Schaller, and Joop Schaye. The chosen few: the low-mass haloes that host faint galaxies. , 456(1):85–97, February 2016a. doi: 10.1093/mnras/stv2597.

Julio F. Navarro, Carlos S. Frenk, and Simon D. M. White. A Universal Density Profile from Hierarchical Clustering. , 490(2):493–508, December 1997. doi: 10.1086/304888.

Julio F. Navarro, Carlos S. Frenk, and Simon D. M. White. The Structure of Cold Dark Matter Halos. , 462:563, May 1996a. doi: 10.1086/177173.

J. Wang, S. Bose, C. S. Frenk, L. Gao, A. Jenkins, V. Springel, and S. D. M. White. Universal structure of dark matter haloes over a mass range of 20 orders of magnitude. , 585(7823):39–42, September 2020. doi: 10.1038/s41586-020-2642-9.

Aaron D. Ludlow, Julio F. Navarro, Raúl E. Angulo, Michael Boylan-Kolchin, Volker Springel, Carlos Frenk, and Simon D. M. White. The mass-concentration-redshift relation of cold dark matter haloes. , 441(1):378–388, June 2014. doi: 10.1093/mnras/stu483.

J. S. Bullock, T. S. Kolatt, Y. Sigad, R. S. Somerville, A. V. Kravtsov, A. A. Klypin, J. R. Primack, and A. Dekel. Profiles of dark haloes: evolution, scatter and environment. , 321(3):559–575, March 2001. doi: 10.1046/j.1365-8711.2001.04068.x.

Angelo F. Neto, Liang Gao, Philip Bett, Shaun Cole, Julio F. Navarro, Carlos S. Frenk, Simon D. M. White, Volker Springel, and Adrian Jenkins. The statistics of Λ CDM halo concentrations. , 381(4): 1450–1462, November 2007. doi: 10.1111/j.1365-2966.2007.12381.x.

Aaron D. Ludlow, Sownak Bose, Raúl E. Angulo, Lan Wang, Wojciech A. Hellwing, Julio F. Navarro, Shaun Cole, and Carlos S. Frenk. The mass-concentration-redshift relation of cold and warm dark matter haloes. , 460(2):1214–1232, August 2016. doi: 10.1093/mnras/stw1046.

M. R. Lovell, C. S. Frenk, V. R. Eke, A. Jenkins, L. Gao, and T. Theuns. The properties of warm dark matter haloes. , 439:300–317, March 2014. doi: 10.1093/mnras/stt2431.

Stelios Kazantzidis, Lucio Mayer, Chiara Mastropietro, Jürg Diemand, Joachim Stadel, and Ben Moore. Density Profiles of Cold Dark Matter Substructure: Implications for the Missing-Satellites Problem. , 608(2):663–679, June 2004. doi: 10.1086/420840.

M. Geha, M. R. Blanton, R. Yan, and J. L. Tinker. A Stellar Mass Threshold for Quenching of Field Galaxies. , 757(1):85, September 2012. doi: 10.1088/0004-637X/757/1/85.

Kristine Spekkens, Natasha Urbancic, Brian S. Mason, Beth Willman, and James E. Aguirre. The Dearth of Neutral Hydrogen in Galactic Dwarf Spheroidal Galaxies. , 795(1):L5, November 2014. doi: 10.1088/2041-8205/795/1/L5.

A. J. Benson, C. S. Frenk, C. G. Lacey, C. M. Baugh, and S. Cole. The effects of photoionization on galaxy formation - II. Satellite galaxies in the Local Group. , 333(1):177–190, June 2002. doi: 10.1046/j.1365-8711.2002.05388.x.

W. J. G. de Blok and S. S. McGaugh. The dark and visible matter content of low surface brightness disc galaxies. , 290(3):533–552, September 1997. doi: 10.1093/mnras/290.3.533.

Deidre A. Hunter, Dana Ficut-Vicas, Trisha Ashley, Elias Brinks, Phil Cigan, Bruce G. Elmegreen, Volker Heesen, Kimberly A. Herrmann, Megan Johnson, Se-Heon Oh, Michael P. Rupen, Andreas Schruba, Caroline E. Simpson, Fabian Walter, David J. Westpfahl, Lisa M. Young, and Hong-Xin Zhang. Little Things. , 144(5):134, November 2012. doi: 10.1088/0004-6256/144/5/134.

Se-Heon Oh, Deidre A. Hunter, Elias Brinks, Bruce G. Elmegreen, Andreas Schruba, Fabian Walter, Michael P. Rupen, Lisa M. Young, Caroline E. Simpson, Megan C. Johnson, Kimberly A. Herrmann, Dana Ficut-Vicas, Phil Cigan, Volker Heesen, Trisha Ashley, and Hong-Xin Zhang. High-resolution Mass Models of Dwarf Galaxies from LITTLE THINGS. , 149(6):180, June 2015. doi: 10.1088/0004-6256/149/6/180.

Matthew G. Walker and Jorge Peñarrubia. A Method for Measuring (Slopes of) the Mass Profiles of Dwarf Spheroidal Galaxies. , 742(1):20, November 2011a. doi: 10.1088/0004-637X/742/1/20.

Anatoly Klypin, Andrey V. Kravtsov, Octavio Valenzuela, and Francisco Prada. Where Are the Missing Galactic Satellites? , 522(1):82–92, September 1999. doi: 10.1086/307643.

B. Moore, S. Ghigna, F. Governato, G. Lake, Thomas R. Quinn, J. Stadel, and P. Tozzi. Dark matter substructure within galactic halos. *Astrophys. J. Lett.*, 524:L19–L22, 1999. doi: 10.1086/312287.

James S. Bullock, Andrey V. Kravtsov, and David H. Weinberg. Reionization and the Abundance of Galactic Satellites. , 539(2):517–521, August 2000. doi: 10.1086/309279.

Michael Boylan-Kolchin, James S. Bullock, and Manoj Kaplinghat. Too big to fail? The puzzling darkness of massive Milky Way subhaloes. , 415(1):L40–L44, July 2011. doi: 10.1111/j.1745-3933.2011.01074.x.

Michael Boylan-Kolchin, James S. Bullock, and Manoj Kaplinghat. The Milky Way's bright satellites as an apparent failure of ΛCDM. , 422(2):1203–1218, May 2012. doi: 10.1111/j.1365-2966.2012.20695.x.

Shea Garrison-Kimmel, Michael Boylan-Kolchin, James S. Bullock, and Evan N. Kirby. Too big to fail in the Local Group. , 444(1):222–236, October 2014. doi: 10.1093/mnras/stu1477.

E. Papastergis, R. Giovanelli, M. P. Haynes, and F. Shankar. Is there a "too big to fail" problem in the field? , 574:A113, February 2015. doi: 10.1051/0004-6361/201424909.

Kyle A. Oman, Julio F. Navarro, Azadeh Fattahi, Carlos S. Frenk, Till Sawala, Simon D. M. White, Richard Bower, Robert A. Crain, Michelle Furlong, Matthieu Schaller, Joop Schaye, and Tom Theuns. The unexpected diversity of dwarf galaxy rotation curves. , 452(4):3650–3665, October 2015. doi: 10.1093/mnras/stv1504.

Nicole C. Relatores, Andrew B. Newman, Joshua D. Simon, Richard S. Ellis, Phuongmai Truong, Leo Blitz, Alberto Bolatto, Christopher Martin, Matt Matuszewski, Patrick Morrissey, and James D. Neill. The Dark Matter Distributions in Low-mass Disk Galaxies. II. The Inner Density Profiles. , 887(1):94, December 2019. doi: 10.3847/1538-4357/ab5305.

Isabel M. E. Santos-Santos, Julio F. Navarro, Andrew Robertson, Alejandro Benítez-Llambay, Kyle A. Oman, Mark R. Lovell, Carlos S. Frenk, Aaron D. Ludlow, Azadeh Fattahi, and Adam Ritz. Baryonic clues to the puzzling diversity of dwarf galaxy rotation curves. , 495(1):58–77, June 2020. doi: 10.1093/mnras/staa1072.

Azadeh Fattahi, Julio F. Navarro, Carlos S. Frenk, Kyle A. Oman, Till Sawala, and Matthieu Schaller. Tidal stripping and the structure of dwarf galaxies in the Local Group. , 476(3):3816–3836, May 2018. doi: 10.1093/mnras/sty408.

Jesús Zavala, Mark R. Lovell, Mark Vogelsberger, and Jan D. Burger. Diverse dark matter density at sub-kiloparsec scales in Milky Way satellites: Implications for the nature of dark matter. *Phys. Rev. D*, 100(6):063007, 2019. doi: 10.1103/PhysRevD.100.063007.

Raphaël Errani, Jorge Peñarrubia, and Matthew G. Walker. Systematics in virial mass estimators for pressure-supported systems. , 481(4):5073–5090, December 2018. doi: 10.1093/mnras/sty2505.

Julio F. Navarro, Vincent R. Eke, and Carlos S. Frenk. The cores of dwarf galaxy haloes. , 283(3): L72–L78, December 1996b. doi: 10.1093/mnras/283.3.L72.

F. Governato, C. Brook, L. Mayer, A. Brooks, G. Rhee, J. Wadsley, P. Jonsson, B. Willman, G. Stinson, T. Quinn, and P. Madau. Bulgeless dwarf galaxies and dark matter cores from supernova-driven outflows. , 463(7278):203–206, January 2010. doi: 10.1038/nature08640.

Alejandro Benítez-Llambay, Carlos S. Frenk, Aaron D. Ludlow, and Julio F. Navarro. Baryon-induced dark matter cores in the EAGLE simulations. , 488(2):2387–2404, September 2019. doi: 10.1093/mnras/stz1890.

Aaron A. Dutton, Tobias Buck, Andrea V. Macciò, Keri L. Dixon, Marvin Blank, and Aura Obreja. NIHAO - XXV. Convergence in the cusp-core transformation of cold dark matter haloes at high star formation thresholds. , 499(2):2648–2661, December 2020. doi: 10.1093/mnras/staa3028.

Jorge Peñarrubia, Andrew Pontzen, Matthew G. Walker, and Sergey E. Koposov. The Coupling between the Core/Cusp and Missing Satellite Problems. , 759(2):L42, November 2012. doi: 10.1088/2041-8205/759/2/L42.

N. C. Amorisco, J. Zavala, and T. J. L. de Boer. Dark Matter Cores in the Fornax and Sculptor Dwarf

Galaxies: Joining Halo Assembly and Detailed Star Formation Histories. , 782(2):L39, February 2014. doi: 10.1088/2041-8205/782/2/L39.

J. I. Read, O. Agertz, and M. L. M. Collins. Dark matter cores all the way down. , 459(3):2573–2590, July 2016. doi: 10.1093/mnras/stw713.

Sownak Bose, Carlos S. Frenk, Adrian Jenkins, Azadeh Fattahi, Facundo A. Gómez, Robert J. J. Grand, Federico Marinacci, Julio F. Navarro, Kyle A. Oman, Rüdiger Pakmor, Joop Schaye, Christine M. Simpson, and Volker Springel. No cores in dark matter-dominated dwarf galaxies with bursty star formation histories. , 486(4):4790–4804, July 2019. doi: 10.1093/mnras/stz1168.

Victor H. Robles, James S. Bullock, Oliver D. Elbert, Alex Fitts, Alejandro González-Samaniego, Michael Boylan-Kolchin, Philip F. Hopkins, Claude-André Faucher-Giguère, Dušan Kereš, and Christopher C. Hayward. SIDM on FIRE: hydrodynamical self-interacting dark matter simulations of low-mass dwarf galaxies. , 472(3):2945–2954, December 2017. doi: 10.1093/mnras/stx2253.

Andrea V. Macciò, Jonas Frings, Tobias Buck, Camilla Penzo, Aaron A. Dutton, Marvin Blank, and Aura Obreja. The edge of galaxy formation - I. Formation and evolution of MW-satellite analogues before accretion. , 472(2):2356–2366, December 2017. doi: 10.1093/mnras/stx2048.

Anna Genina, Justin I. Read, Azadeh Fattahi, and Carlos S. Frenk. Can tides explain the low dark matter density in Fornax? , 510(2):2186–2205, February 2022. doi: 10.1093/mnras/stab3526.

Coral Wheeler, Philip F. Hopkins, Andrew B. Pace, Shea Garrison-Kimmel, Michael Boylan-Kolchin, Andrew Wetzel, James S. Bullock, Dušan Kereš, Claude-André Faucher-Giguère, and Eliot Quataert. Be it therefore resolved: cosmological simulations of dwarf galaxies with 30 solar mass resolution. , 490(3):4447–4463, December 2019. doi: 10.1093/mnras/stz2887.

Matthew D. A. Orkney, Justin I. Read, Martin P. Rey, Imran Nasim, Andrew Pontzen, Oscar Agertz, Stacy Y. Kim, Maxime Delorme, and Walter Dehnen. EDGE: two routes to dark matter core formation in ultra-faint dwarfs. , 504(3):3509–3522, July 2021. doi: 10.1093/mnras/stab1066.

David N. Spergel and Paul J. Steinhardt. Observational evidence for self-interacting cold dark matter. *Phys. Rev. Lett.*, 84:3760–3763, Apr 2000. doi: 10.1103/PhysRevLett.84.3760. URL https://link.aps.org/doi/10.1103/PhysRevLett.84.3760.

Romeel Davé, David N. Spergel, Paul J. Steinhardt, and Benjamin D. Wandelt. Halo Properties in Cosmological Simulations of Self-interacting Cold Dark Matter. , 547(2):574–589, February 2001. doi: 10.1086/318417.

Miguel Rocha, Annika H. G. Peter, James S. Bullock, Manoj Kaplinghat, Shea Garrison-Kimmel, Jose Oñorbe, and Leonidas A. Moustakas. Cosmological simulations with self-interacting dark matter – I. Constant-density cores and substructure. *Monthly Notices of the Royal Astronomical Society*, 430(1):81–104, 01 2013. ISSN 0035-8711. doi: 10.1093/mnras/sts514. URL https://doi.org/10.1093/mnras/sts514.

Joshua D. Simon. The Faintest Dwarf Galaxies. , 57:375–415, August 2019. doi: 10.1146/annurev-astro-091918-104453.

Stacy Y. Kim, Annika H. G. Peter, and Jonathan R. Hargis. Missing Satellites Problem: Completeness Corrections to the Number of Satellite Galaxies in the Milky Way are Consistent with Cold Dark Matter Predictions. , 121(21):211302, November 2018. doi: 10.1103/PhysRevLett.121.211302.

A. Drlica-Wagner, others, and DES Collaboration. Milky Way Satellite Census. I. The Observational Selection Function for Milky Way Satellites in DES Y3 and Pan-STARRS DR1. , 893(1):47, April 2020. doi: 10.3847/1538-4357/ab7eb9.

Laura V. Sales, Andrew Wetzel, and Azadeh Fattahi. Baryonic solutions and challenges for cosmological models of dwarf galaxies. *Nature Astronomy*, 6:897–910, June 2022. doi: 10.1038/s41550-022-01689-w.

Shea Garrison-Kimmel, Andrew Wetzel, James S. Bullock, Philip F. Hopkins, Michael Boylan-Kolchin, Claude-André Faucher-Giguère, Dušan Kereš, Eliot Quataert, Robyn E. Sanderson, Andrew S. Graus, and Tyler Kelley. Not so lumpy after all: modelling the depletion of dark matter subhaloes by Milky Way-like galaxies. , 471(2):1709–1727, October 2017. doi: 10.1093/mnras/stx1710.

Gregory A. Dooley, Annika H. G. Peter, Mark Vogelsberger, Jesús Zavala, and Anna Frebel. Enhanced tidal stripping of satellites in the galactic halo from dark matter self-interactions. , 461(1):710–727, September 2016. doi: 10.1093/mnras/stw1309.

Adi Zolotov, Alyson M. Brooks, Beth Willman, Fabio Governato, Andrew Pontzen, Charlotte Christensen, Avishai Dekel, Tom Quinn, Sijing Shen, and James Wadsley. Baryons Matter: Why Luminous Satellite Galaxies have Reduced Central Masses. , 761(1):71, December 2012. doi: 10.1088/0004-637X/761/1/71.

Till Sawala, Carlos S. Frenk, Azadeh Fattahi, Julio F. Navarro, Richard G. Bower, Robert A. Crain, Claudio Dalla Vecchia, Michelle Furlong, John. C. Helly, Adrian Jenkins, Kyle A. Oman, Matthieu Schaller, Joop Schaye, Tom Theuns, James Trayford, and Simon D. M. White. The APOSTLE simulations: solutions to the Local Group's cosmic puzzles. , 457(2):1931–1943, April 2016b. doi: 10.1093/mnras/stw145.

Azadeh Fattahi, Julio F. Navarro, Till Sawala, Carlos S. Frenk, Laura V. Sales, Kyle Oman, Matthieu Schaller, and Jie Wang. The cold dark matter content of Galactic dwarf spheroidals: no cores, no failures, no problem. *arXiv e-prints*, art. arXiv:1607.06479, July 2016a. doi: 10.48550/arXiv.1607.06479.

E. O. Nadler and DES Collaboration. Milky Way Satellite Census. II. Galaxy-Halo Connection Constraints Including the Impact of the Large Magellanic Cloud. , 893(1):48, April 2020. doi: 10.3847/1538-4357/ab846a.

Viraj Manwadkar and Andrey V. Kravtsov. Forward-modelling the luminosity, distance, and size distributions of the Milky Way satellites. , 516(3):3944–3971, November 2022. doi: 10.1093/mnras/stac2452.

Shea Garrison-Kimmel, Philip F. Hopkins, Andrew Wetzel, James S. Bullock, Michael Boylan-Kolchin, Dušan Kereš, Claude-André Faucher-Giguère, Kareem El-Badry, Astrid Lamberts, Eliot Quataert, and Robyn Sanderson. The Local Group on FIRE: dwarf galaxy populations across a suite of hydrodynamic simulations. , 487(1):1380–1399, July 2019a. doi: 10.1093/mnras/stz1317.

Pedro Colín, Vladimir Avila-Reese, and Octavio Valenzuela. Substructure and Halo Density Profiles in a Warm Dark Matter Cosmology. , 542(2):622–630, October 2000. doi: 10.1086/317057.

Paul Bode, Jeremiah P. Ostriker, and Neil Turok. Halo Formation in Warm Dark Matter Models. , 556 (1):93–107, July 2001. doi: 10.1086/321541.

Sownak Bose, Wojciech A. Hellwing, Carlos S. Frenk, Adrian Jenkins, Mark R. Lovell, John C. Helly, and Baojiu Li. The Copernicus Complexio: statistical properties of warm dark matter haloes. , 455 (1):318–333, January 2016a. doi: 10.1093/mnras/stv2294.

Mark R. Lovell, Jesús Zavala, and Mark Vogelsberger. ETHOS - an effective theory of structure formation: formation of the first haloes and their stars. , 485(4):5474–5489, June 2019. doi: 10.1093/mnras/stz766.

Annika H. G. Peter, Miguel Rocha, James S. Bullock, and Manoj Kaplinghat. Cosmological simulations with self-interacting dark matter - II. Halo shapes versus observations. , 430(1):105–120, March 2013. doi: 10.1093/mnras/sts535.

Andrew Robertson, David Harvey, Richard Massey, Vincent Eke, Ian G. McCarthy, Mathilde Jauzac, Baojiu Li, and Joop Schaye. Observable tests of self-interacting dark matter in galaxy clusters: cosmological simulations with SIDM and baryons. , 488(3):3646–3662, September 2019. doi: 10.1093/mnras/stz1815.

Joshua D. Simon and Marla Geha. The Kinematics of the Ultra-faint Milky Way Satellites: Solving the Missing Satellite Problem. , 670(1):313–331, November 2007. doi: 10.1086/521816.

Matthew G. Walker, Mario Mateo, and Edward W. Olszewski. Stellar Velocities in the Carina, Fornax, Sculptor, and Sextans dSph Galaxies: Data From the Magellan/MMFS Survey. , 137(2):3100–3108, February 2009. doi: 10.1088/0004-6256/137/2/3100.

G. Torrealba, S. E. Koposov, V. Belokurov, and M. Irwin. The feeble giant. Discovery of a large and diffuse Milky Way dwarf galaxy in the constellation of Crater. , 459:2370–2378, July 2016a. doi: 10.1093/mnras/stw733.

G. Torrealba, V. Belokurov, S. E. Koposov, T. S. Li, M. G. Walker, J. L. Sanders, A. Geringer-Sameth, D. B. Zucker, K. Kuehn, N. W. Evans, and W. Dehnen. The hidden giant: discovery of an enormous Galactic dwarf satellite in Gaia DR2. , 488(2):2743–2766, September 2019a. doi: 10.1093/mnras/stz1624.

Raphaël Errani, Julio F. Navarro, Rodrigo Ibata, and Jorge Peñarrubia. Structure and kinematics of tidally limited satellite galaxies in LCDM. , 511(4):6001–6018, April 2022. doi: 10.1093/mnras/stac476.

Alexandra Borukhovetskaya, Julio F. Navarro, Raphaël Errani, and Azadeh Fattahi. Galactic tides and the Crater II dwarf spheroidal: a challenge to LCDM? , 512(4):5247–5257, June 2022. doi: 10.1093/mnras/stac653.

Alexander P. Ji, Sergey E. Koposov, Ting S. Li, Denis Erkal, Andrew B. Pace, Joshua D. Simon, Vasily Belokurov, Lara R. Cullinane, Gary S. Da Costa, Kyler Kuehn, Geraint F. Lewis, Dougal Mackey, Nora Shipp, Jeffrey D. Simpson, Daniel B. Zucker, Terese T. Hansen, Joss Bland-Hawthorn, and S5 Collaboration. Kinematics of Antlia 2 and Crater 2 from the Southern Stellar Stream Spectroscopic Survey (S^5). , 921(1):32, November 2021. doi: 10.3847/1538-4357/ac1869.

Kyle A. Oman, Antonino Marasco, Julio F. Navarro, Carlos S. Frenk, Joop Schaye, and Alejandro Benítez-Llambay. Non-circular motions and the diversity of dwarf galaxy rotation curves. , 482(1):821–847, January 2019. doi: 10.1093/mnras/sty2687.

M. R. Lovell, V. Eke, C. S. Frenk, L. Gao, A. Jenkins, T. Theuns, J. Wang, S. D. M. White, A. Boyarsky, and O. Ruchayskiy. The haloes of bright satellite galaxies in a warm dark matter universe. , 420:2318–2324, March 2012. doi: 10.1111/j.1365-2966.2011.20200.x.

Mark R. Lovell and Jesús Zavala. Matching the mass function of Milky Way satellites in competing dark matter models. , 520(1):1567–1589, March 2023. doi: 10.1093/mnras/stad216.

J. Zavala, M. Vogelsberger, and M. G. Walker. Constraining self-interacting dark matter with the Milky way's dwarf spheroidals. , 431:L20–L24, April 2013. doi: 10.1093/mnrasl/sls053.

Ethan O. Nadler, Daneng Yang, and Hai-Bo Yu. A Self-interacting Dark Matter Solution to the Extreme Diversity of Low-mass Halo Properties. , 958(2):L39, December 2023. doi: 10.3847/2041-8213/ad0e09.

Camila A. Correa. Constraining velocity-dependent self-interacting dark matter with the Milky Way's dwarf spheroidal galaxies. , 503(1):920–937, May 2021. doi: 10.1093/mnras/stab506.

Felix Kahlhoefer, Manoj Kaplinghat, Tracy R. Slatyer, and Chih-Liang Wu. Diversity in density profiles of self-interacting dark matter satellite halos. , 2019(12):010, December 2019. doi: 10.1088/1475-7516/2019/12/010.

Manoj Kaplinghat, Mauro Valli, and Hai-Bo Yu. Too Big To Fail in Light of Gaia. *Mon. Not. Roy. Astron. Soc.*, 490(1):231–242, 2019. doi: 10.1093/mnras/stz2511.

Omid Sameie, Hai-Bo Yu, Laura V. Sales, Mark Vogelsberger, and Jesús Zavala. Self-Interacting Dark Matter Subhalos in the Milky Way's Tides. , 124(14):141102, April 2020. doi: 10.1103/PhysRevLett.124.141102.

Daneng Yang, Ethan O. Nadler, and Hai-Bo Yu. Strong Dark Matter Self-interactions Diversify Halo Populations within and surrounding the Milky Way. , 949(2):67, June 2023a. doi: 10.3847/1538-4357/acc73e.

Peter Creasey, Omid Sameie, Laura V. Sales, Hai-Bo Yu, Mark Vogelsberger, and Jesús Zavala. Spreading out and staying sharp - creating diverse rotation curves via baryonic and self-interaction effects. , 468(2):2283–2295, June 2017. doi: 10.1093/mnras/stx522.

Camila A. Correa, Matthieu Schaller, Sylvia Ploeckinger, Noemi Anau Montel, Christoph Weniger, and Shin'ichiro Ando. TangoSIDM: tantalizing models of self-interacting dark matter. , 517(2):3045–3063, December 2022. doi: 10.1093/mnras/stac2830.

Tamar Meshveliani, Jesús Zavala, and Mark R. Lovell. Gravothermal collapse of self-interacting dark matter halos as the origin of intermediate mass black holes in Milky Way satellites. *Phys. Rev. D*, 107(8):083010, 2023. doi: 10.1103/PhysRevD.107.083010.

Dark Energy Survey Collaboration. The Dark Energy Survey: more than dark energy - an overview. , 460(2):1270–1299, August 2016. doi: 10.1093/mnras/stw641.

K. Bechtol, others, and DES Collaboration. Eight New Milky Way Companions Discovered in First-year Dark Energy Survey Data. , 807(1):50, July 2015. doi: 10.1088/0004-637X/807/1/50.

A. Drlica-Wagner, others, and DES Collaboration. Eight Ultra-faint Galaxy Candidates Discovered in Year Two of the Dark Energy Survey. , 813(2):109, November 2015. doi: 10.1088/0004-637X/813/2/109.

Benjamin P. M. Laevens, Nicolas F. Martin, Rodrigo A. Ibata, Hans-Walter Rix, Edouard J. Bernard, Eric F. Bell, Branimir Sesar, Annette M. N. Ferguson, Edward F. Schlafly, Colin T. Slater, William S. Burgett, Kenneth C. Chambers, Heather Flewelling, Klaus W. Hodapp, Nicholas Kaiser, Rolf-Peter Kudritzki, Robert H. Lupton, Eugene A. Magnier, Nigel Metcalfe, Jeffrey S. Morgan, Paul A. Price, John L. Tonry, Richard J. Wainscoat, and Christopher Waters. A New Faint Milky Way Satellite Discovered in the Pan-STARRS1 3π Survey. , 802(2):L18, April 2015a. doi: 10.1088/2041-8205/802/2/L18.

Benjamin P. M. Laevens, Nicolas F. Martin, Edouard J. Bernard, Edward F. Schlafly, Branimir Sesar, Hans-Walter Rix, Eric F. Bell, Annette M. N. Ferguson, Colin T. Slater, William E. Sweeney, Rosemary F. G. Wyse, Avon P. Huxor, William S. Burgett, Kenneth C. Chambers, Peter W. Draper, Klaus W. Hodapp, Nicholas Kaiser, Eugene A. Magnier, Nigel Metcalfe, John L. Tonry, Richard J. Wainscoat, and Christopher Waters. Sagittarius II, Draco II and Laevens 3: Three New Milky Way Satellites Discovered in the Pan-STARRS 1 3π Survey. , 813(1):44, November 2015b. doi: 10.1088/0004-637X/813/1/44.

Željko Ivezić et al. LSST: from Science Drivers to Reference Design and Anticipated Data Products. *Astrophys. J.*, 873(2):111, 2019. doi: 10.3847/1538-4357/ab042c.

James S. Bullock and Michael Boylan-Kolchin. Small-Scale Challenges to the ΛCDM Paradigm. , 55 (1):343–387, August 2017a. doi: 10.1146/annurev-astro-091916-055313.

Donald G. York and SDSS Collaboration. The Sloan Digital Sky Survey: Technical Summary. , 120 (3):1579–1587, September 2000. doi: 10.1086/301513.

B. Flaugher, others, and DES Collaboration. The Dark Energy Camera. , 150(5):150, November 2015. doi: 10.1088/0004-6256/150/5/150.

Satoshi Miyazaki et al. Hyper Suprime-Cam: System design and verification of image quality. , 70:S1, January 2018. doi: 10.1093/pasj/psx063.

Jin Koda, Masafumi Yagi, Hitomi Yamanoi, and Yutaka Komiyama. Approximately a Thousand Ultra-diffuse Galaxies in the Coma Cluster. , 807(1):L2, July 2015. doi: 10.1088/2041-8205/807/1/L2.

Paul Eigenthaler, Thomas H. Puzia, Matthew A. Taylor, Yasna Ordenes-Briceño, Roberto P. Muñoz, Karen X. Ribbeck, Karla A. Alamo-Martínez, Hongxin Zhang, Simón Ángel, Massimo Capaccioli, Patrick Côté, Laura Ferrarese, Gaspar Galaz, Eva K. Grebel, Maren Hempel, Michael Hilker, Ariane Lançon, Steffen Mieske, Bryan Miller, Maurizio Paolillo, Mathieu Powalka, Tom Richtler, Joel Roediger, Yu Rong, Ruben Sánchez-Janssen, and Chelsea Spengler. The Next Generation Fornax Survey (NGFS). II. The Central Dwarf Galaxy Population. , 855(2):142, March 2018. doi: 10.3847/1538-4357/aaab60.

Pieter G. van Dokkum, Roberto Abraham, Allison Merritt, Jielai Zhang, Marla Geha, and Charlie Conroy. Forty-seven Milky Way-sized, Extremely Diffuse Galaxies in the Coma Cluster. , 798(2): L45, January 2015. doi: 10.1088/2041-8205/798/2/L45.

Kyle A. Oman. The ALFALFA H I velocity width function. , 509(3):3268–3284, January 2022. doi: 10.1093/mnras/stab3164.

Bärbel S. Koribalski et al. WALLABY – an SKA Pathfinder H i survey. *Astrophys. Space Sci.*, 365(7): 118, 2020. doi: 10.1007/s10509-020-03831-4.

A. Drlica-Wagner et al. The DECam Local Volume Exploration Survey: Overview and First Data Release. *Astrophys. J. Supp.*, 256(1):2, 2021. doi: 10.3847/1538-4365/ac079d.

A. Drlica-Wagner et al. The DECam Local Volume Exploration Survey Data Release 2. *Astrophys. J. Supp.*, 261(2):38, 2022. doi: 10.3847/1538-4365/ac78eb.

Rodrigo A. Ibata, Alan McConnachie, et al. The Canada-France Imaging Survey: First Results from the u-Band Component. , 848(2):128, October 2017. doi: 10.3847/1538-4357/aa855c.

S. Mau, W. Cerny, A. B. Pace, Y. Choi, A. Drlica-Wagner, et al. Two Ultra-faint Milky Way Stellar Systems Discovered in Early Data from the DECam Local Volume Exploration Survey. , 890(2): 136, February 2020. doi: 10.3847/1538-4357/ab6c67.

W. Cerny and Delve Collaboration. Pegasus IV: Discovery and Spectroscopic Confirmation of an Ultra-faint Dwarf Galaxy in the Constellation Pegasus. , 942(2):111, January 2023a. doi: 10.3847/1538-4357/aca1c3.

W. Cerny and Delve Collaboration. Six More Ultra-faint Milky Way Companions Discovered in the DECam Local Volume Exploration Survey. , 953(1):1, August 2023b. doi: 10.3847/1538-4357/acdd78.

Simon E. T. Smith et al. Discovery of a New Local Group Dwarf Galaxy Candidate in UNIONS: Boötes V. , 166(2):76, August 2023. doi: 10.3847/1538-3881/acdd77.

Gaia Collaboration et al. The Gaia mission. , 595:A1, November 2016. doi: 10.1051/0004-6361/201629272.

Gaia Collaboration et al. Gaia Early Data Release 3. Summary of the contents and survey properties. , 649:A1, May 2021. doi: 10.1051/0004-6361/202039657.

Andrew B. Pace and Ting S. Li. Proper Motions of Milky Way Ultra-faint Satellites with Gaia DR2 × DES DR1. , 875(1):77, April 2019. doi: 10.3847/1538-4357/ab0aee.

Alan W. McConnachie and Kim A. Venn. Revised and New Proper Motions for Confirmed and Candidate Milky Way Dwarf Galaxies. , 160(3):124, September 2020a. doi: 10.3847/1538-3881/aba4ab.

Alan W. McConnachie and Kim A. Venn. Updated Proper Motions for Local Group Dwarf Galaxies Using Gaia Early Data Release 3. *Research Notes of the American Astronomical Society*, 4(12):229, December 2020b. doi: 10.3847/2515-5172/abd18b.

G. Torrealba, V. Belokurov, and S. E. Koposov. Nine tiny star clusters in Gaia DR1, PS1, and DES. , 484(2):2181–2197, April 2019b. doi: 10.1093/mnras/stz071.

Andrew B. Pace, Sergey E. Koposov, Matthew G. Walker, Nelson Caldwell, Mario Mateo, Edward W. Olszewski, Ian U. Roederer, John I. Bailey, Vasily Belokurov, Kyler Kuehn, Ting S. Li, and Daniel B. Zucker. The kinematics, metallicities, and orbits of six recently discovered Galactic star clusters with Magellan/M2FS spectroscopy. , 526(1):1075–1094, November 2023. doi: 10.1093/mnras/stad2760.

Federico Lelli, Stacy S. McGaugh, and James M. Schombert. SPARC: Mass Models for 175 Disk Galaxies with Spitzer Photometry and Accurate Rotation Curves. , 152(6):157, December 2016. doi: 10.3847/0004-6256/152/6/157.

Se-Heon Oh, Chris Brook, Fabio Governato, Elias Brinks, Lucio Mayer, W. J. G. de Blok, Alyson Brooks, and Fabian Walter. The Central Slope of Dark Matter Cores in Dwarf Galaxies: Simulations versus THINGS. , 142(1):24, July 2011. doi: 10.1088/0004-6256/142/1/24.

Jürgen Ott, Adrienne M. Stilp, Steven R. Warren, Evan D. Skillman, Julianne J. Dalcanton, Fabian Walter, W. J. G. de Blok, Bärbel Koribalski, and Andrew A. West. VLA-ANGST: A High-resolution H I Survey of Nearby Dwarf Galaxies. , 144(4):123, October 2012. doi: 10.1088/0004-6256/144/4/123.

Matthew Frosst, Stéphane Courteau, Nikhil Arora, Connor Stone, Andrea V. Macciò, and Marvin Blank. The diversity of spiral galaxies explained. , 514(3):3510–3531, August 2022. doi: 10.1093/mnras/stac1497.

Martin P. Rey, Matthew D. A. Orkney, Justin I. Read, Payel Das, Oscar Agertz, Andrew Pontzen, Anastasia A. Ponomareva, Stacy Y. Kim, and William McClymont. EDGE - Dark matter or astrophysics? Breaking dark matter heating degeneracies with H I rotation in faint dwarf galaxies. , 529(3):2379–2398, April 2024. doi: 10.1093/mnras/stae718.

Jiangang Kang, Ming Zhu, Mei Ai, Haiyang Yu, and Chun Sun. Extragalactic H I Survey with FAST: First Look at the Pilot Survey Results. *Research in Astronomy and Astrophysics*, 22(6):065019, June 2022. doi: 10.1088/1674-4527/ac6796.

W. J. G. de Blok, Athanassoula, et al. MeerKAT HI commissioning observations of MHONGOOSE galaxy ESO 302-G014. , 643:A147, November 2020. doi: 10.1051/0004-6361/202038894.

N. Maddox et al. MIGHTEE-HI: The H I emission project of the MeerKAT MIGHTEE survey. , 646: A35, February 2021. doi: 10.1051/0004-6361/202039655.

Alex Drlica-Wagner, Yao-Yuan Mao, Susmita Adhikari, et al. Probing the Fundamental Nature of Dark Matter with the Large Synoptic Survey Telescope. *arXiv e-prints*, art. arXiv:1902.01055, February 2019. doi: 10.48550/arXiv.1902.01055.

Joshua Simon, Simon Birrer, Keith Bechtol, Sukanya Chakrabarti, Francis-Yan Cyr-Racine, Ian Dell'Antonio, Alex Drlica-Wagner, Chris Fassnacht, Marla Geha, Daniel Gilman, Yashar D. Hezaveh, Dongwon Kim, Ting S. Li, Louis Strigari, and Tommaso Treu. Testing the Nature of Dark Matter with Extremely Large Telescopes. , 51(3):153, May 2019. doi: 10.48550/arXiv.1903.04742.

Jonathan L. Feng, Manoj Kaplinghat, Huitzu Tu, and Hai-Bo Yu. Hidden charged dark matter. , 2009 (7):004, July 2009. doi: 10.1088/1475-7516/2009/07/004.

Abraham Loeb and Neal Weiner. Cores in Dwarf Galaxies from Dark Matter with a Yukawa Potential. , 106(17):171302, April 2011. doi: 10.1103/PhysRevLett.106.171302.

Sean Tulin, Hai-Bo Yu, and Kathryn M. Zurek. Beyond collisionless dark matter: Particle physics dynamics for dark matter halo structure. , 87(11):115007, June 2013. doi: 10.1103/PhysRevD.87.115007.

Susmita Adhikari, Arka Banerjee, Kimberly K. Boddy, Francis-Yan Cyr-Racine, Harry Desmond, Cora Dvorkin, Bhuvnesh Jain, Felix Kahlhoefer, Manoj Kaplinghat, Anna Nierenberg, Annika H. G. Peter, Andrew Robertson, Jeremy Sakstein, and Jesús Zavala. Astrophysical Tests of Dark Matter Self-Interactions. *arXiv e-prints*, art. arXiv:2207.10638, July 2022. doi: 10.48550/arXiv.2207.10638.

Oliver D. Elbert, James S. Bullock, Shea Garrison-Kimmel, Miguel Rocha, Jose Oñorbe, and Annika H. G. Peter. Core formation in dwarf haloes with self-interacting dark matter: no fine-tuning necessary. , 453(1):29–37, October 2015. doi: 10.1093/mnras/stv1470.

Ayuki Kamada, Manoj Kaplinghat, Andrew B. Pace, and Hai-Bo Yu. Self-Interacting Dark Matter Can Explain Diverse Galactic Rotation Curves. , 119(11):111102, September 2017. doi: 10.1103/PhysRevLett.119.111102.

Giulia Despali, Martin Sparre, Simona Vegetti, Mark Vogelsberger, Jesús Zavala, and Federico Marinacci. The interplay of self-interacting dark matter and baryons in shaping the halo evolution. , 484(4):4563–4573, April 2019. doi: 10.1093/mnras/stz273.

Manoj Kaplinghat, Sean Tulin, and Hai-Bo Yu. Dark Matter Halos as Particle Colliders: Unified Solution to Small-Scale Structure Puzzles from Dwarfs to Clusters. , 116(4):041302, January 2016. doi: 10.1103/PhysRevLett.116.041302.

Oliver D. Elbert, James S. Bullock, Manoj Kaplinghat, Shea Garrison-Kimmel, Andrew S. Graus, and Miguel Rocha. A Testable Conspiracy: Simulating Baryonic Effects on Self-interacting Dark Matter Halos. , 853(2):109, February 2018. doi: 10.3847/1538-4357/aa9710.

Andrew Robertson, Richard Massey, and Vincent Eke. What does the Bullet Cluster tell us about self-interacting dark matter? , 465(1):569–587, February 2017. doi: 10.1093/mnras/stw2670.

Andrew Robertson, Richard Massey, Vincent Eke, Sean Tulin, Hai-Bo Yu, Yannick Bahé, David J. Barnes, Richard G. Bower, Robert A. Crain, Claudio Dalla Vecchia, Scott T. Kay, Matthieu Schaller, and Joop Schaye. The diverse density profiles of galaxy clusters with self-interacting dark matter plus baryons. , 476(1):L20–L24, May 2018. doi: 10.1093/mnrasl/sly024.

Zhichao Carton Zeng, Annika H. G. Peter, Xiaolong Du, Andrew Benson, Stacy Kim, Fangzhou Jiang,

Francis-Yan Cyr-Racine, and Mark Vogelsberger. Core-collapse, evaporation and tidal effects: The life story of a self-interacting dark matter subhalo. , April 2022. doi: 10.1093/mnras/stac1094.

Maya Silverman, James S. Bullock, Manoj Kaplinghat, Victor H. Robles, and Mauro Valli. Motivations for a Large Self-Interacting Dark Matter Cross Section from Milky Way Satellites. *arXiv e-prints*, art. arXiv:2203.10104, March 2022.

Hiroya Nishikawa, Kimberly K. Boddy, and Manoj Kaplinghat. Accelerated core collapse in tidally stripped self-interacting dark matter halos. *Phys. Rev. D*, 101(6):063009, 2020. doi: 10.1103/PhysRevD.101.063009.

Hannah C. Turner, Mark R. Lovell, Jesús Zavala, and Mark Vogelsberger. The onset of gravothermal core collapse in velocity-dependent self-interacting dark matter subhaloes. *Mon. Not. Roy. Astron. Soc.*, 505(4):5327–5339, 2021. doi: 10.1093/mnras/stab1725.

Jan D. Burger, Jesús Zavala, Laura V. Sales, Mark Vogelsberger, Federico Marinacci, and Paul Torrey. Kinematic signatures of impulsive supernova feedback in dwarf galaxies. *Phys. Rev. Lett.*, 129: 191103, Nov 2022. doi: 10.1103/PhysRevLett.129.191103. URL `https://link.aps.org/doi/10.1103/PhysRevLett.129.191103`.

Christian Maulbetsch, Vladimir Avila-Reese, Pedro Colín, Stefan Gottlöber, Arman Khalatyan, and Matthias Steinmetz. The Dependence of the Mass Assembly History of Cold Dark Matter Halos on Environment. , 654(1):53–65, January 2007. doi: 10.1086/509706.

Wojciech A. Hellwing, Marius Cautun, Rien van de Weygaert, and Bernard T. Jones. Caught in the cosmic web: Environmental effect on halo concentrations, shape, and spin. , 103(6):063517, March 2021. doi: 10.1103/PhysRevD.103.063517.

Takehiko Asaka and Mikhail Shaposhnikov. The @nMSM, dark matter and baryon asymmetry of the universe [rapid communication]. *Physics Letters B*, 620(1-2):17–26, July 2005. doi: 10.1016/j.physletb.2005.06.020.

Alexey Boyarsky, Oleg Ruchayskiy, and Mikhail Shaposhnikov. The Role of Sterile Neutrinos in Cosmology and Astrophysics. *Annual Review of Nuclear and Particle Science*, 59(1):191–214, November 2009. doi: 10.1146/annurev.nucl.010909.083654.

Aurel Schneider. Astrophysical constraints on resonantly produced sterile neutrino dark matter. , 2016 (4):059, April 2016. doi: 10.1088/1475-7516/2016/04/059.

John F. Cherry and Shunsaku Horiuchi. Closing in on resonantly produced sterile neutrino dark matter. , 95(8):083015, April 2017. doi: 10.1103/PhysRevD.95.083015.

Vid Iršič, Matteo Viel, Martin G. Haehnelt, James S. Bolton, Stefano Cristiani, George D. Becker, Valentina D'Odorico, Guido Cupani, Tae-Sun Kim, Trystyn A. M. Berg, Sebastian López, Sara Ellison, Lise Christensen, Kelly D. Denney, and Gábor Worseck. New constraints on the free-streaming of warm dark matter from intermediate and small scale Lyman-α forest data. , 96(2): 023522, July 2017. doi: 10.1103/PhysRevD.96.023522.

Vid Iršič, Matteo Viel, Martin G. Haehnelt, James S. Bolton, Margherita Molaro, Ewald Puchwein, Elisa Boera, George D. Becker, Prakash Gaikwad, Laura C. Keating, and Girish Kulkarni. Unveiling dark matter free streaming at the smallest scales with the high redshift Lyman-alpha forest. , 109(4): 043511, February 2024. doi: 10.1103/PhysRevD.109.043511.

J. W. Hsueh, W. Enzi, S. Vegetti, M. W. Auger, C. D. Fassnacht, G. Despali, L. V. E. Koopmans, and J. P. McKean. SHARP - VII. New constraints on the dark matter free-streaming properties and

substructure abundance from gravitationally lensed quasars. , 492(2):3047–3059, February 2020. doi: 10.1093/mnras/stz3177.

Daniel Gilman, Simon Birrer, Anna Nierenberg, Tommaso Treu, Xiaolong Du, and Andrew Benson. Warm dark matter chills out: constraints on the halo mass function and the free-streaming length of dark matter with eight quadruple-image strong gravitational lenses. , 491(4):6077–6101, February 2020. doi: 10.1093/mnras/stz3480.

Nilanjan Banik, Jo Bovy, Gianfranco Bertone, Denis Erkal, and T. J. L. de Boer. Novel constraints on the particle nature of dark matter from stellar streams. , 2021(10):043, October 2021. doi: 10.1088/1475-7516/2021/10/043.

E. O. Nadler and DES Collaboration. Constraints on Dark Matter Properties from Observations of Milky Way Satellite Galaxies. , 126(9):091101, March 2021. doi: 10.1103/PhysRevLett.126.091101.

Ethan O. Nadler, Simon Birrer, Daniel Gilman, Risa H. Wechsler, Xiaolong Du, Andrew Benson, Anna M. Nierenberg, and Tommaso Treu. Dark Matter Constraints from a Unified Analysis of Strong Gravitational Lenses and Milky Way Satellite Galaxies. , 917(1):7, August 2021a. doi: 10.3847/1538-4357/abf9a3.

Wolfgang Enzi, Riccardo Murgia, Oliver Newton, Simona Vegetti, Carlos Frenk, Matteo Viel, Marius Cautun, Christopher D. Fassnacht, Matt Auger, Giulia Despali, John McKean, Léon V. E. Koopmans, and Mark Lovell. Joint constraints on thermal relic dark matter from strong gravitational lensing, the Ly α forest, and Milky Way satellites. , 506(4):5848–5862, October 2021. doi: 10.1093/mnras/stab1960.

Oliver Newton, Matteo Leo, Marius Cautun, Adrian Jenkins, Carlos S. Frenk, Mark R. Lovell, John C. Helly, Andrew J. Benson, and Shaun Cole. Constraints on the properties of warm dark matter using the satellite galaxies of the Milky Way. , 2021(8):062, August 2021. doi: 10.1088/1475-7516/2021/08/062.

Ioana A. Zelko, Tommaso Treu, Kevork N. Abazajian, Daniel Gilman, Andrew J. Benson, Simon Birrer, Anna M. Nierenberg, and Alexander Kusenko. Constraints on Sterile Neutrino Models from Strong Gravitational Lensing, Milky Way Satellites, and the Lyman-α Forest. , 129(19):191301, November 2022. doi: 10.1103/PhysRevLett.129.191301.

Bruno Villasenor, Brant Robertson, Piero Madau, and Evan Schneider. New constraints on warm dark matter from the Lyman-α forest power spectrum. , 108(2):023502, July 2023. doi: 10.1103/PhysRevD.108.023502.

Mark R. Lovell. Anticipating the XRISM search for the decay of resonantly produced sterile neutrino dark matter. , 524(4):6345–6357, October 2023a. doi: 10.1093/mnras/stad2237.

Manoj Kaplinghat, Sean Tulin, and Hai-Bo Yu. Direct detection portals for self-interacting dark matter. , 89(3):035009, February 2014. doi: 10.1103/PhysRevD.89.035009.

Jordan Smolinsky and Philip Tanedo. Dark photons from captured inelastic dark matter annihilation: Charged particle signatures. , 95(7):075015, April 2017. doi: 10.1103/PhysRevD.95.075015.

Jonathan L. Feng, Manoj Kaplinghat, and Hai-Bo Yu. Halo Shape and Relic Density Exclusions of Sommerfeld-Enhanced Dark Matter Explanations of Cosmic Ray Excesses. *Phys. Rev. Lett.*, 104: 151301, 2010. doi: 10.1103/PhysRevLett.104.151301.

S. A. Khrapak, A. V. Ivlev, G. E. Morfill, and S. K. Zhdanov. Scattering in the attractive yukawa potential in the limit of strong interaction. *Phys. Rev. Lett.*, 90:225002, Jun

2003. doi: 10.1103/PhysRevLett.90.225002. URL https://link.aps.org/doi/10.1103/PhysRevLett.90.225002.

D. Lynden-Bell and Roger Wood. The gravo-thermal catastrophe in isothermal spheres and the onset of red-giant structure for stellar systems. , 138:495, January 1968a. doi: 10.1093/mnras/138.4.495.

D. Lynden-Bell and P. P. Eggleton. On the consequences of the gravothermal catastrophe. , 191: 483–498, May 1980. doi: 10.1093/mnras/191.3.483.

Shmuel Balberg, Stuart L. Shapiro, and Shogo Inagaki. Selfinteracting dark matter halos and the gravothermal catastrophe. *Astrophys. J.*, 568:475–487, 2002. doi: 10.1086/339038.

Shmuel Balberg and Stuart L. Shapiro. Gravothermal collapse of selfinteracting dark matter halos and the origin of massive black holes. *Phys. Rev. Lett.*, 88:101301, 2002. doi: 10.1103/PhysRevLett.88.101301.

Jason Pollack, David N. Spergel, and Paul J. Steinhardt. Supermassive Black Holes from Ultra-Strongly Self-Interacting Dark Matter. *Astrophys. J.*, 804(2):131, 2015. doi: 10.1088/0004-637X/804/2/131.

Jun Koda and Paul R. Shapiro. Gravothermal collapse of isolated self-interacting dark matter haloes: N-body simulation versus the fluid model. , 415(2):1125–1137, August 2011. doi: 10.1111/j.1365-2966.2011.18684.x.

Stuart L. Shapiro. Star clusters, self-interacting dark matter halos, and black hole cusps: The fluid conduction model and its extension to general relativity. , 98(2):023021, July 2018. doi: 10.1103/PhysRevD.98.023021.

Nadav Joseph Outmezguine, Kimberly K. Boddy, Sophia Gad-Nasr, Manoj Kaplinghat, and Laura Sagunski. Universal gravothermal evolution of isolated self-interacting dark matter halos for velocity-dependent cross sections. *arXiv e-prints*, art. arXiv:2204.06568, April 2022.

Daneng Yang, Ethan O. Nadler, Hai-Bo Yu, and Yi-Ming Zhong. A parametric model for self-interacting dark matter halos. , 2024(2):032, February 2024. doi: 10.1088/1475-7516/2024/02/032.

Rouven Essig, Samuel D. McDermott, Hai-Bo Yu, and Yi-Ming Zhong. Constraining Dissipative Dark Matter Self-Interactions. , 123(12):121102, September 2019. doi: 10.1103/PhysRevLett.123.121102.

Sophia Gad-Nasr, Kimberly K. Boddy, Manoj Kaplinghat, Nadav Joseph Outmezguine, and Laura Sagunski. On the Late-Time Evolution of Velocity-Dependent Self-Interacting Dark Matter Halos. *arXiv e-prints*, art. arXiv:2312.09296, December 2023. doi: 10.48550/arXiv.2312.09296.

Daneng Yang and Hai-Bo Yu. Gravothermal evolution of dark matter halos with differential elastic scattering. , 2022(9):077, September 2022. doi: 10.1088/1475-7516/2022/09/077.

Shengqi Yang, Xiaolong Du, Zhichao Carton Zeng, Andrew Benson, Fangzhou Jiang, Ethan O. Nadler, and Annika H. G. Peter. Gravothermal Solutions of SIDM Halos: Mapping from Constant to Velocity-dependent Cross Section. , 946(1):47, March 2023b. doi: 10.3847/1538-4357/acbd49.

Volker Springel, Simon D. M. White, Adrian Jenkins, Carlos S. Frenk, Naoki Yoshida, Liang Gao, Julio Navarro, Robert Thacker, Darren Croton, John Helly, John A. Peacock, Shaun Cole, Peter Thomas, Hugh Couchman, August Evrard, Jörg Colberg, and Frazer Pearce. Simulations of the formation, evolution and clustering of galaxies and quasars. , 435(7042):629–636, June 2005b. doi: 10.1038/nature03597.

James S. Bullock and Michael Boylan-Kolchin. Small-Scale Challenges to the ΛCDM Paradigm. , 55 (1):343–387, August 2017b. doi: 10.1146/annurev-astro-091916-055313.

Matthew G. Walker and Jorge Peñarrubia. A Method for Measuring (Slopes of) the Mass Profiles of Dwarf Spheroidal Galaxies. , 742(1):20, November 2011b. doi: 10.1088/0004-637X/742/1/20.

A. Agnello and N. W. Evans. A Virial Core in the Sculptor Dwarf Spheroidal Galaxy. , 754(2):L39, August 2012. doi: 10.1088/2041-8205/754/2/L39.

Maarten A. Breddels, A. Helmi, R. C. E. van den Bosch, G. van de Ven, and G. Battaglia. Orbit-based dynamical models of the Sculptor dSph galaxy. , 433(4):3173–3189, August 2013. doi: 10.1093/mnras/stt956.

G. Torrealba, S. E. Koposov, V. Belokurov, and M. Irwin. The feeble giant. Discovery of a large and diffuse Milky Way dwarf galaxy in the constellation of Crater. , 459(3):2370–2378, July 2016b. doi: 10.1093/mnras/stw733.

J. I. Read, M. G. Walker, and P. Steger. Dark matter heats up in dwarf galaxies. , 484(1):1401–1420, March 2019. doi: 10.1093/mnras/sty3404.

Andrew Pontzen and Fabio Governato. How supernova feedback turns dark matter cusps into cores. , 421(4):3464–3471, April 2012. doi: 10.1111/j.1365-2966.2012.20571.x.

Jan D. Burger and Jesús Zavala. The nature of core formation in dark matter haloes: adiabatic or impulsive? , 485(1):1008–1028, May 2019. doi: 10.1093/mnras/stz496.

Jan D. Burger and Jesús Zavala. Supernova-driven Mechanism of Cusp-core Transformation: an Appraisal. , 921(2):126, November 2021. doi: 10.3847/1538-4357/ac1a0f.

Arianna Di Cintio, Chris B. Brook, Andrea V. Macciò, Greg S. Stinson, Alexander Knebe, Aaron A. Dutton, and James Wadsley. The dependence of dark matter profiles on the stellar-to-halo mass ratio: a prediction for cusps versus cores. , 437(1):415–423, January 2014a. doi: 10.1093/mnras/stt1891.

Pedro Colín, Vladimir Avila-Reese, Octavio Valenzuela, and Claudio Firmani. Structure and Subhalo Population of Halos in a Self-interacting Dark Matter Cosmology. , 581(2):777–793, December 2002. doi: 10.1086/344259.

Mark Vogelsberger, Jesus Zavala, and Abraham Loeb. Subhaloes in self-interacting galactic dark matter haloes. , 423(4):3740–3752, July 2012b. doi: 10.1111/j.1365-2966.2012.21182.x.

Miguel Rocha, Annika H. G. Peter, James S. Bullock, Manoj Kaplinghat, Shea Garrison-Kimmel, Jose Oñorbe, and Leonidas A. Moustakas. Cosmological simulations with self-interacting dark matter - I. Constant-density cores and substructure. , 430(1):81–104, March 2013. doi: 10.1093/mnras/sts514.

Victor H. Robles, Tyler Kelley, James S. Bullock, and Manoj Kaplinghat. The Milky Way's halo and subhaloes in self-interacting dark matter. , 490(2):2117–2123, December 2019. doi: 10.1093/mnras/stz2345.

Mark Vogelsberger, Jesús Zavala, Katelin Schutz, and Tracy R. Slatyer. Evaporating the Milky Way halo and its satellites with inelastic self-interacting dark matter. , 484(4):5437–5452, April 2019. doi: 10.1093/mnras/stz340.

Tao Ren, Anna Kwa, Manoj Kaplinghat, and Hai-Bo Yu. Reconciling the Diversity and Uniformity of Galactic Rotation Curves with Self-Interacting Dark Matter. *Physical Review X*, 9(3):031020, July 2019. doi: 10.1103/PhysRevX.9.031020.

David Harvey, Andrew Robertson, Richard Massey, and Ian G. McCarthy. Observable tests of self-interacting dark matter in galaxy clusters: BCG wobbles in a constant density core. , 488(2):1572–1579, September 2019. doi: 10.1093/mnras/stz1816.

Kevin E. Andrade, Jackson Fuson, Sophia Gad-Nasr, Demao Kong, Quinn Minor, M. Grant Roberts, and Manoj Kaplinghat. A stringent upper limit on dark matter self-interaction cross-section from cluster strong lensing. , 510(1):54–81, February 2022. doi: 10.1093/mnras/stab3241.

D. Eckert, S. Ettori, A. Robertson, R. Massey, E. Pointecouteau, D. Harvey, and I. G. McCarthy. Constraints on dark matter self-interaction from the internal density profiles of X-COP galaxy clusters. , 666:A41, October 2022. doi: 10.1051/0004-6361/202243205.

Xuejian Shen, Thejs Brinckmann, David Rapetti, Mark Vogelsberger, Adam Mantz, Jesús Zavala, and Steven W. Allen. X-ray morphology of cluster-mass haloes in self-interacting dark matter. , 516(1): 1302–1319, October 2022. doi: 10.1093/mnras/stac2376.

Giulia Despali, Levi G. Walls, Simona Vegetti, Martin Sparre, Mark Vogelsberger, and Jesús Zavala. Constraining SIDM with halo shapes: Revisited predictions from realistic simulations of early-type galaxies. , 516(3):4543–4559, November 2022. doi: 10.1093/mnras/stac2521.

Mauro Valli and Hai-Bo Yu. Dark matter self-interactions from the internal dynamics of dwarf spheroidals. *Nature Astronomy*, 2:907–912, August 2018. doi: 10.1038/s41550-018-0560-7.

J. I. Read, M. G. Walker, and P. Steger. The case for a cold dark matter cusp in Draco. , 481(1): 860–877, November 2018. doi: 10.1093/mnras/sty2286.

Stacy Y. Kim and Annika H. G. Peter. The Milky Way satellite velocity function is a sharp probe of small-scale structure problems. *arXiv e-prints*, art. arXiv:2106.09050, June 2021.

Matthew R. Buckley and Patrick J. Fox. Dark matter self-interactions and light force carriers. , 81(8): 083522, April 2010. doi: 10.1103/PhysRevD.81.083522.

Piet Hut, Steve McMillan, Jeremy Goodman, Mario Mateo, E. S. Phinney, Carlton Pryor, Harvey B. Richer, Frank Verbunt, and Martin Weinberg. Binaries in Globular Clusters. , 104:981, November 1992. doi: 10.1086/133085.

D. Lynden-Bell and Roger Wood. The gravo-thermal catastrophe in isothermal spheres and the onset of red-giant structure for stellar systems. , 138:495, January 1968b. doi: 10.1093/mnras/138.4.495.

Mark Vogelsberger, Jesus Zavala, Christine Simpson, and Adrian Jenkins. Dwarf galaxies in CDM and SIDM with baryons: observational probes of the nature of dark matter. , 444(4):3684–3698, November 2014. doi: 10.1093/mnras/stu1713.

Sebastian Bohr, Jesús Zavala, Francis-Yan Cyr-Racine, and Mark Vogelsberger. The halo mass function and inner structure of ETHOS haloes at high redshift. , 506(1):128–138, September 2021. doi: 10.1093/mnras/stab1758.

Stelios Kazantzidis, Andrew R. Zentner, and Andrey V. Kravtsov. The Robustness of Dark Matter Density Profiles in Dissipationless Mergers. , 641(2):647–664, April 2006. doi: 10.1086/500579.

Michael Boylan-Kolchin and Chung-Pei Ma. Major mergers of galaxy haloes: cuspy or cored inner density profile? , 349(3):1117–1129, April 2004. doi: 10.1111/j.1365-2966.2004.07585.x.

Kyungjin Ahn and Paul R. Shapiro. Formation and evolution of self-interacting dark matter haloes. , 363(4):1092–1110, November 2005. doi: 10.1111/j.1365-2966.2005.09492.x.

Onsi Fakhouri, Chung-Pei Ma, and Michael Boylan-Kolchin. The merger rates and mass assembly histories of dark matter haloes in the two Millennium simulations. , 406(4):2267–2278, August 2010. doi: 10.1111/j.1365-2966.2010.16859.x.

Ewa L. Łokas and Gary A. Mamon. Properties of spherical galaxies and clusters with an NFW density profile. , 321(1):155–166, February 2001. doi: 10.1046/j.1365-8711.2001.04007.x.

Mihael Petač, Piero Ullio, and Mauro Valli. On velocity-dependent dark matter annihilations in dwarf satellites. , 2018(12):039, December 2018. doi: 10.1088/1475-7516/2018/12/039.

Mark Vogelsberger and Jesus Zavala. Direct detection of self-interacting dark matter. , 430(3): 1722–1735, April 2013. doi: 10.1093/mnras/sts712.

Huangyu Xiao, Xuejian Shen, Philip F. Hopkins, and Kathryn M. Zurek. SMBH seeds from dissipative dark matter. , 2021(7):039, July 2021. doi: 10.1088/1475-7516/2021/07/039.

Jeremie Choquette, James M. Cline, and Jonathan M. Cornell. Early formation of supermassive black holes via dark matter self-interactions. , 2019(7):036, July 2019. doi: 10.1088/1475-7516/2019/07/036.

Wei-Xiang Feng, Hai-Bo Yu, and Yi-Ming Zhong. Seeding Supermassive Black Holes with Self-interacting Dark Matter: A Unified Scenario with Baryons. , 914(2):L26, June 2021. doi: 10.3847/2041-8213/ac04b0.

Wei-Xiang Feng, Hai-Bo Yu, and Yi-Ming Zhong. Dynamical instability of collapsed dark matter halos. , 2022(5):036, May 2022. doi: 10.1088/1475-7516/2022/05/036.

Miguel Rocha, Annika H. G. Peter, and James Bullock. Infall times for Milky Way satellites from their present-day kinematics. , 425(1):231–244, September 2012. doi: 10.1111/j.1365-2966.2012.21432.x.

Jorge Peñarrubia, Andrew J. Benson, Matthew G. Walker, Gerard Gilmore, Alan W. McConnachie, and Lucio Mayer. The impact of dark matter cusps and cores on the satellite galaxy population around spiral galaxies. , 406(2):1290–1305, August 2010. doi: 10.1111/j.1365-2966.2010.16762.x.

Lilian Jiang, Shaun Cole, Till Sawala, and Carlos S. Frenk. Orbital parameters of infalling satellite haloes in the hierarchical ΛCDM model. , 448(2):1674–1686, April 2015. doi: 10.1093/mnras/stv053.

Miguel A. Sánchez-Conde and Francisco Prada. The flattening of the concentration-mass relation towards low halo masses and its implications for the annihilation signal boost. , 442(3):2271–2277, August 2014. doi: 10.1093/mnras/stu1014.

A. Marasco, G. Cresci, L. Posti, F. Fraternali, F. Mannucci, A. Marconi, F. Belfiore, and S. M. Fall. A universal relation between the properties of supermassive black holes, galaxies, and dark matter haloes. , 507(3):4274–4293, November 2021. doi: 10.1093/mnras/stab2317.

M. J. Bustamante-Rosell, Eva Noyola, Karl Gebhardt, Maximilian H. Fabricius, Ximena Mazzalay, Jens Thomas, and Greg Zeimann. Dynamical Analysis of the Dark Matter and Central Black Hole Mass in the Dwarf Spheroidal Leo I. , 921(2):107, November 2021. doi: 10.3847/1538-4357/ac0c79.

John R. Jardel and Karl Gebhardt. The Dark Matter Density Profile of the Fornax Dwarf. , 746(1):89, February 2012. doi: 10.1088/0004-637X/746/1/89.

V. Lora, F. J. Sánchez-Salcedo, A. C. Raga, and A. Esquivel. An Upper Limit on the Mass of the Black Hole in Ursa Minor Dwarf Galaxy. , 699(2):L113–L117, July 2009. doi: 10.1088/0004-637X/699/2/L113.

Jesús Zavala and Carlos S. Frenk. Dark matter haloes and subhaloes. *Galaxies*, 7(4):81, 2019. doi: 10.3390/galaxies7040081.

Ayuki Kamada, Hee Jung Kim, and Takumi Kuwahara. Maximally self-interacting dark matter: models and predictions. *Journal of High Energy Physics*, 2020(12):202, December 2020. doi: 10.1007/JHEP12(2020)202.

Jenny E. Greene, Jay Strader, and Luis C. Ho. Intermediate-Mass Black Holes. , 58:257–312, August 2020. doi: 10.1146/annurev-astro-032620-021835.

Morgan MacLeod, James Guillochon, Enrico Ramirez-Ruiz, Daniel Kasen, and Stephan Rosswog. Optical Thermonuclear Transients from Tidal Compression of White Dwarfs as Tracers of the Low End of the Massive Black Hole Mass Function. , 819(1):3, March 2016. doi: 10.3847/0004-637X/819/1/3.

Victor H. Robles, J. L. Zagorac, and N. Padmanabhan. Scalar Field Dark Matter: Impact of Supernovae-driven blowouts on the soliton structure of low mass dark matter halos. *arXiv e-prints*, art. arXiv:2308.14691, August 2023. doi: 10.48550/arXiv.2308.14691.

David J. E. Marsh and Jens C. Niemeyer. Strong Constraints on Fuzzy Dark Matter from Ultrafaint Dwarf Galaxy Eridanus II. , 123(5):051103, August 2019. doi: 10.1103/PhysRevLett.123.051103.

E. M. Lifshitz and L. P. Pitaevskii. *Physical kinetics*. 1981.

James Binney and Scott Tremaine. *Galactic Dynamics: Second Edition*. 2008.

A. A. Williams, N. W. Evans, and A. D. Bowden. Hamiltonians of spherical Galaxies in action-angle coordinates. , 442(2):1405–1410, August 2014. doi: 10.1093/mnras/stu892.

N. C. Amorisco and N. W. Evans. Phase-space models of the dwarf spheroidals. , 411(4):2118–2136, March 2011. doi: 10.1111/j.1365-2966.2010.17715.x.

Daniel R. Weisz, Alessandro Savino, and Andrew E. Dolphin. On the reionization-era globular cluster in the low-mass galaxy eridanus ii. *The Astrophysical Journal*, 948(1):50, may 2023. doi: 10.3847/1538-4357/acc328. URL https://dx.doi.org/10.3847/1538-4357/acc328.

Joshua D. Simon, Thomas M. Brown, Alex Drlica-Wagner, Ting S. Li, Roberto J. Avila, Keith Bechtol, Gisella Clementini, Denija Crnojević, Alessia Garofalo, Marla Geha, David J. Sand, Jay Strader, and Beth Willman. Eridanus II: A Fossil from Reionization with an Off-center Star Cluster. , 908 (1):18, February 2021. doi: 10.3847/1538-4357/abd31b.

Michael Boylan-Kolchin. The globular cluster-dark matter halo connection. , 472(3):3120–3130, December 2017. doi: 10.1093/mnras/stx2164.

Planck Collaboration. Planck 2013 results. i. overview of products and scientific results. *A&A*, 571: A1, 2014. doi: 10.1051/0004-6361/201321529. URL https://doi.org/10.1051/0004-6361/201321529.

A. Di Cintio, C. B. Brook, A. V. Macciò, G. S. Stinson, A. Knebe, A. A. Dutton, and J. Wadsley. The dependence of dark matter profiles on the stellar-to-halo mass ratio: a prediction for cusps versus cores. , 437:415–423, January 2014b. doi: 10.1093/mnras/stt1891.

E. Polisensky and M. Ricotti. Constraints on the dark matter particle mass from the number of Milky Way satellites. , 83(4):043506, February 2011. doi: 10.1103/PhysRevD.83.043506.

B. Bozek, M. Boylan-Kolchin, S. Horiuchi, S. Garrison-Kimmel, K. Abazajian, and J. S. Bullock. Resonant sterile neutrino dark matter in the local and high-z Universe. , 459:1489–1504, June 2016. doi: 10.1093/mnras/stw688.

S. Horiuchi, B. Bozek, K. N. Abazajian, M. Boylan-Kolchin, J. S. Bullock, S. Garrison-Kimmel, and J. Onorbe. Properties of resonantly produced sterile neutrino dark matter subhaloes. , 456: 4346–4353, March 2016. doi: 10.1093/mnras/stv2922.

Oliver Newton, Marius Cautun, Adrian Jenkins, Carlos S. Frenk, and John C. Helly. The total satellite population of the Milky Way. , 479(3):2853–2870, Sep 2018. doi: 10.1093/mnras/sty1085.

Andrea V. Macciò, Jonas Frings, Tobias Buck, Aaron A. Dutton, Marvin Blank, Aura Obreja, and Keri L. Dixon. The edge of galaxy formation III: the effects of warm dark matter on Milky Way satellites and field dwarfs. , 484(4):5400–5408, Apr 2019. doi: 10.1093/mnras/stz327.

Ethan O. Nadler, Simon Birrer, Daniel Gilman, Risa H. Wechsler, Xiaolong Du, Andrew Benson, Anna M. Nierenberg, and Tommaso Treu. Dark Matter Constraints from a Unified Analysis of Strong Gravitational Lenses and Milky Way Satellite Galaxies. , 917(1):7, August 2021b. doi: 10.3847/1538-4357/abf9a3.

F. Governato, A. Zolotov, A. Pontzen, C. Christensen, S. H. Oh, A. M. Brooks, T. Quinn, S. Shen, and J. Wadsley. Cuspy no more: how outflows affect the central dark matter and baryon distribution in Λ cold dark matter galaxies. , 422(2):1231–1240, May 2012. doi: 10.1111/j.1365-2966.2012.20696.x.

T. Sawala, C. S. Frenk, A. Fattahi, J. F. Navarro, T. Theuns, R. G. Bower, R. A. Crain, M. Furlong, A. Jenkins, M. Schaller, and J. Schaye. The chosen few: the low-mass haloes that host faint galaxies. , 456:85–97, February 2016c. doi: 10.1093/mnras/stv2597.

Mark R. Lovell, Violeta Gonzalez-Perez, Sownak Bose, Alexey Boyarsky, Shaun Cole, Carlos S. Frenk, and Oleg Ruchayskiy. Addressing the too big to fail problem with baryon physics and sterile neutrino dark matter. , 468(3):2836–2849, July 2017. doi: 10.1093/mnras/stx621.

A. Fattahi, J. F. Navarro, T. Sawala, C. S. Frenk, K. A. Oman, R. A. Crain, M. Furlong, M. Schaller, J. Schaye, T. Theuns, and A. Jenkins. The APOSTLE project: Local Group kinematic mass constraints and simulation candidate selection. , 457:844–856, March 2016b. doi: 10.1093/mnras/stv2970.

Azadeh Fattahi, Julio F. Navarro, and Carlos S. Frenk. The missing dwarf galaxies of the Local Group. , 493(2):2596–2605, April 2020. doi: 10.1093/mnras/staa375.

Alyson M. Brooks, Michael Kuhlen, Adi Zolotov, and Dan Hooper. A Baryonic Solution to the Missing Satellites Problem. , 765(1):22, March 2013. doi: 10.1088/0004-637X/765/1/22.

Andrew R. Wetzel, Philip F. Hopkins, Ji-hoon Kim, Claude-André Faucher-Giguère, Dušan Kereš, and Eliot Quataert. Reconciling Dwarf Galaxies with ΛCDM Cosmology: Simulating a Realistic Population of Satellites around a Milky Way-mass Galaxy. , 827(2):L23, August 2016. doi: 10.3847/2041-8205/827/2/L23.

Shea Garrison-Kimmel, Philip F. Hopkins, Andrew Wetzel, James S. Bullock, Michael Boylan-Kolchin, Dušan Kereš, Claude-André Faucher-Giguère, Kareem El-Badry, Astrid Lamberts, Eliot Quataert, and Robyn Sanderson. The Local Group on FIRE: dwarf galaxy populations across a suite of hydrodynamic simulations. , 487(1):1380–1399, July 2019b. doi: 10.1093/mnras/stz1317.

Morad Aaboud et al. Search for dark matter and other new phenomena in events with an energetic jet and large missing transverse momentum using the ATLAS detector. *JHEP*, 01:126, 2018. doi: 10.1007/JHEP01(2018)126.

A. M. Sirunyan and CMS Collaboration. Search for new physics in final states with an energetic jet or a hadronically decaying W or Z boson and transverse momentum imbalance at $\sqrt{\{s\}}$=13 TeV. , 97 (9):092005, May 2018. doi: 10.1103/PhysRevD.97.092005.

Dan Hooper and Lisa Goodenough. Dark matter annihilation in the Galactic Center as seen by the Fermi Gamma Ray Space Telescope. *Physics Letters B*, 697(5):412–428, March 2011. doi: 10.1016/j.physletb.2011.02.029.

A. Albert et al. Searching for Dark Matter Annihilation in Recently Discovered Milky Way Satellites with Fermi-LAT. *Astrophys. J.*, 834(2):110, 2017. doi: 10.3847/1538-4357/834/2/110.

Xiangdong Shi and George M. Fuller. New dark matter candidate: Nonthermal sterile neutrinos. *Phys. Rev. Lett.*, 82:2832–2835, Apr 1999. doi: 10.1103/PhysRevLett.82.2832. URL https://link.aps.org/doi/10.1103/PhysRevLett.82.2832.

Esra Bulbul, Maxim Markevitch, Adam Foster, Randall K. Smith, Michael Loewenstein, and Scott W. Randall. Detection of an unidentified emission line in the stacked x-ray spectrum of galaxy clusters. *The Astrophysical Journal*, 789(1):13, jun 2014. doi: 10.1088/0004-637X/789/1/13. URL https://dx.doi.org/10.1088/0004-637X/789/1/13.

A. Boyarsky, O. Ruchayskiy, D. Iakubovskyi, and J. Franse. Unidentified line in x-ray spectra of the andromeda galaxy and perseus galaxy cluster. *Phys. Rev. Lett.*, 113:251301, Dec 2014. doi: 10.1103/PhysRevLett.113.251301. URL https://link.aps.org/doi/10.1103/PhysRevLett.113.251301.

F. Hofmann and C. Wegg. 7.1 keV sterile neutrino dark matter constraints from a deep Chandra X-ray observation of the Galactic bulge Limiting Window. , 625:L7, May 2019. doi: 10.1051/0004-6361/201935561.

Michael E. Anderson, Eugene Churazov, and Joel N. Bregman. Non-detection of X-ray emission from sterile neutrinos in stacked galaxy spectra. , 452(4):3905–3923, October 2015. doi: 10.1093/mnras/stv1559.

Tesla Jeltema and Stefano Profumo. Deep XMM observations of Draco rule out at the 99 per cent confidence level a dark matter decay origin for the 3.5 keV line. , 458(4):3592–3596, June 2016. doi: 10.1093/mnras/stw578.

Christopher Dessert, Nicholas L. Rodd, and Benjamin R. Safdi. The dark matter interpretation of the 3.5-keV line is inconsistent with blank-sky observations. *Science*, 367(6485):1465–1467, March 2020. doi: 10.1126/science.aaw3772.

Christopher Dessert, Joshua W. Foster, Yujin Park, and Benjamin R. Safdi. Was There a 3.5 keV Line? *arXiv e-prints*, art. arXiv:2309.03254, September 2023. doi: 10.48550/arXiv.2309.03254.

Mark R. Lovell. Anticipating the XRISM search for the decay of resonantly produced sterile neutrino dark matter. , 524(4):6345–6357, October 2023b. doi: 10.1093/mnras/stad2237.

Mark R. Lovell. Halo assembly in cold and warm dark matter during the JWST frontier epoch. , 527(2):3029–3037, January 2024. doi: 10.1093/mnras/stad3415.

Sownak Bose, Carlos S. Frenk, Jun Hou, Cedric G. Lacey, and Mark R. Lovell. Reionization in sterile neutrino cosmologies. , 463(4):3848–3859, December 2016b. doi: 10.1093/mnras/stw2288.

Robert A. Crain and Freeke van de Voort. Hydrodynamical Simulations of the Galaxy Population: Enduring Successes and Outstanding Challenges. , 61:473–515, August 2023. doi: 10.1146/annurev-astro-041923-043618.

Joop Schaye, Robert A. Crain, Richard G. Bower, Michelle Furlong, Matthieu Schaller, Tom Theuns, Claudio Dalla Vecchia, Carlos S. Frenk, I. G. McCarthy, John C. Helly, Adrian Jenkins, Y. M. Rosas-Guevara, Simon D. M. White, Maarten Baes, C. M. Booth, Peter Camps, Julio F. Navarro, Yan Qu, Alireza Rahmati, Till Sawala, Peter A. Thomas, and James Trayford. The EAGLE project: simulating the evolution and assembly of galaxies and their environments. , 446(1):521–554, January 2015. doi: 10.1093/mnras/stu2058.

R. A. Crain, J. Schaye, R. G. Bower, M. Furlong, M. Schaller, T. Theuns, C. Dalla Vecchia, C. S. Frenk, I. G. McCarthy, J. C. Helly, A. Jenkins, Y. M. Rosas-Guevara, S. D. M. White, and J. W.

Trayford. The EAGLE simulations of galaxy formation: calibration of subgrid physics and model variations. , 450:1937–1961, June 2015. doi: 10.1093/mnras/stv725.

Nate Bastian, Joel Pfeffer, J. M. Diederik Kruijssen, Robert A. Crain, Sebastian Trujillo-Gomez, and Marta Reina-Campos. The globular cluster system mass-halo mass relation in the E-MOSAICS simulations. , 498(1):1050–1061, October 2020. doi: 10.1093/mnras/staa2453.

Andrew C. Mason, Robert A. Crain, Ricardo P. Schiavon, David H. Weinberg, Joel Pfeffer, Joop Schaye, Matthieu Schaller, and Tom Theuns. Realistic simulated galaxies form [α/Fe]-[Fe/H] knees due to a sustained decline in their star formation rates. *arXiv e-prints*, art. arXiv:2311.00041, October 2023. doi: 10.48550/arXiv.2311.00041.

Joel Pfeffer, J. M. Diederik Kruijssen, Robert A. Crain, and Nate Bastian. The E-MOSAICS project: simulating the formation and co-evolution of galaxies and their star cluster populations. , 475(4): 4309–4346, April 2018. doi: 10.1093/mnras/stx3124.

J. M. Diederik Kruijssen, Joel L. Pfeffer, Robert A. Crain, and Nate Bastian. The E-MOSAICS project: tracing galaxy formation and assembly with the age-metallicity distribution of globular clusters. , 486(3):3134–3179, July 2019. doi: 10.1093/mnras/stz968.

Kyle A. Oman, Carlos S. Frenk, Robert A. Crain, Mark R. Lovell, and Joel Pfeffer. A warm dark matter cosmogony may yield more low-mass galaxy detections in 21-cm surveys than a cold dark matter one. *arXiv e-prints*, art. arXiv:2401.11878, January 2024. doi: 10.48550/arXiv.2401.11878.

Mark R. Lovell, Wojciech Hellwing, Aaron Ludlow, Jesús Zavala, Andrew Robertson, Azadeh Fattahi, Carlos S. Frenk, and Jennifer Hardwick. Local group star formation in warm and self-interacting dark matter cosmologies. , 498(1):702–717, October 2020. doi: 10.1093/mnras/staa2525.

J. Ghiglieri and M. Laine. Improved determination of sterile neutrino dark matter spectrum. *Journal of High Energy Physics*, 2015:171, November 2015. doi: 10.1007/JHEP11(2015)171.

Tejaswi Venumadhav, Francis-Yan Cyr-Racine, Kevork N. Abazajian, and Christopher M. Hirata. Sterile neutrino dark matter: Weak interactions in the strong coupling epoch. , 94(4):043515, August 2016. doi: 10.1103/PhysRevD.94.043515.

Mark R. Lovell, Sownak Bose, Alexey Boyarsky, Shaun Cole, Carlos S. Frenk, Violeta Gonzalez-Perez, Rachel Kennedy, Oleg Ruchayskiy, and Alex Smith. Satellite galaxies in semi-analytic models of galaxy formation with sterile neutrino dark matter. , 461(1):60–72, September 2016. doi: 10.1093/mnras/stw1317.

Mikko Laine and Mikhail Shaposhnikov. Sterile neutrino dark matter as a consequence of νMSM-induced lepton asymmetry. , 2008(6):031, June 2008. doi: 10.1088/1475-7516/2008/06/031.

A. Lewis, A. Challinor, and A. Lasenby. Efficient Computation of Cosmic Microwave Background Anisotropies in Closed Friedmann-Robertson-Walker Models. , 538:473–476, August 2000. doi: 10.1086/309179.

Matteo Viel, Julien Lesgourgues, Martin G. Haehnelt, Sabino Matarrese, and Antonio Riotto. Constraining warm dark matter candidates including sterile neutrinos and light gravitinos with WMAP and the Lyman-α forest. , 71(6):063534, March 2005. doi: 10.1103/PhysRevD.71.063534.

M. R. Lovell. The halo mass function in alternative dark matter models. , 493(1):L11–L15, March 2020. doi: 10.1093/mnrasl/slaa005.

Jie Wang and Simon D. M. White. Discreteness effects in simulations of hot/warm dark matter. *Monthly Notices of the Royal Astronomical Society*, 380(1):93–103, 08 2007. ISSN 0035-

8711. doi: 10.1111/j.1365-2966.2007.12053.x. URL https://doi.org/10.1111/j.1365-2966.2007.12053.x.

A. W. McConnachie. The Observed Properties of Dwarf Galaxies in and around the Local Group. , 144:4, July 2012. doi: 10.1088/0004-6256/144/1/4.

G. Torrealba, V. Belokurov, S. E. Koposov, T. S. Li, M. G. Walker, J. L. Sanders, A. Geringer-Sameth, D. B. Zucker, K. Kuehn, N. W. Evans, and W. Dehnen. The hidden giant: discovery of an enormous Galactic dwarf satellite in Gaia DR2. *arXiv e-prints*, art. arXiv:1811.04082, Nov 2018.

R. B. Tully, L. Rizzi, E. J. Shaya, H. M. Courtois, D. I. Makarov, and B. A. Jacobs. The Extragalactic Distance Database. , 138:323–331, August 2009. doi: 10.1088/0004-6256/138/2/323.

J. Woo, S. Courteau, and A. Dekel. Scaling relations and the fundamental line of the local group dwarf galaxies. , 390:1453–1469, November 2008. doi: 10.1111/j.1365-2966.2008.13770.x.

Oliver Newton, Arianna Di Cintio, Salvador Cardona-Barrero, Noam I. Libeskind, Yehuda Hoffman, Alexander Knebe, Jenny G. Sorce, Matthias Steinmetz, and Elmo Tempel. The Undiscovered Ultradiffuse Galaxies of the Local Group. , 946(2):L37, April 2023. doi: 10.3847/2041-8213/acc2bb.

Isabel M. E. Santos-Santos, Julio F. Navarro, and Alan McConnachie. Anisotropies in the spatial distribution and kinematics of dwarf galaxies in the Local Group and beyond. *arXiv e-prints*, art. arXiv:2310.02464, October 2023. doi: 10.48550/arXiv.2310.02464.

Till Sawala, Stuart McAlpine, Jens Jasche, Guilhem Lavaux, Adrian Jenkins, Peter H. Johansson, and Carlos S. Frenk. The SIBELIUS Project: E Pluribus Unum. , 509(1):1432–1446, January 2022. doi: 10.1093/mnras/stab2684.

Noam I. Libeskind, Edoardo Carlesi, Robert J. J. Grand, Arman Khalatyan, Alexander Knebe, Ruediger Pakmor, Sergey Pilipenko, Marcel S. Pawlowski, Martin Sparre, Elmo Tempel, Peng Wang, Hélène M. Courtois, Stefan Gottlöber, Yehuda Hoffman, Ivan Minchev, Christoph Pfrommer, Jenny G. Sorce, Volker Springel, Matthias Steinmetz, R. Brent Tully, Mark Vogelsberger, and Gustavo Yepes. The HESTIA project: simulations of the Local Group. , 498(2):2968–2983, October 2020. doi: 10.1093/mnras/staa2541.

Thomas M. Callingham, Marius Cautun, Alis J. Deason, Carlos S. Frenk, Wenting Wang, Facundo A. Gómez, Robert J. J. Grand, Federico Marinacci, and Ruediger Pakmor. The mass of the Milky Way from satellite dynamics. , 484(4):5453–5467, Apr 2019. doi: 10.1093/mnras/stz365.

Laura L. Watkins, Roeland P. van der Marel, Sangmo Tony Sohn, and N. Wyn Evans. Evidence for an Intermediate-mass Milky Way from Gaia DR2 Halo Globular Cluster Motions. , 873(2):118, March 2019. doi: 10.3847/1538-4357/ab089f.

T. K. Fritz, A. Di Cintio, G. Battaglia, C. Brook, and S. Taibi. The mass of our Galaxy from satellite proper motions in the Gaia era. , 494(4):5178–5193, June 2020. doi: 10.1093/mnras/staa1040.

E. V. Karukes, M. Benito, F. Iocco, R. Trotta, and A. Geringer-Sameth. A robust estimate of the Milky Way mass from rotation curve data. , 2020(5):033, May 2020. doi: 10.1088/1475-7516/2020/05/033.

Xuejian Shen, Josh Borrow, Mark Vogelsberger, Enrico Garaldi, Aaron Smith, Rahul Kannan, Sandro Tacchella, Jesús Zavala, Lars Hernquist, Jessica Y. C. Yeh, and Chunyuan Zheng. THESAN-HR: Galaxies in the Epoch of Reionization in warm dark matter, fuzzy dark matter and interacting dark matter. *arXiv e-prints*, art. arXiv:2304.06742, April 2023. doi: 10.48550/arXiv.2304.06742.

A. Tamm, E. Tempel, P. Tenjes, O. Tihhonova, and T. Tuvikene. Stellar mass map and dark matter distribution in M 31. , 546:A4, October 2012. doi: 10.1051/0004-6361/201220065.